UAB
Universitat Autònoma de Barcelona

Gamma-Rays and Multi-Messenger Signatures from Transient Phenomena

Manuel David Artero

Universitat Autònoma
de Barcelona

Universitat Autònoma de Barcelona

Departament de Física

A dissertation submitted for the degree of
Doctor of Philosophy (PhD)

Gamma-Rays and Multi-Messenger Signatures from Transient Phenomena

---

Author	*Tutor*	*Director*
Artero	Prof. Delfino Reznicek	Dr. Blanch Bigas
Manuel David	Manuel Carlos	Oscar
martero@ifae.es	*delfino@pic.es*	*blanch@ifae.es*

May 2023

Abstract

The cosmos is populated by astrophysical objects that can undergo once-in-a-lifetime transient astrophysical phenomena. In the most dramatic cases, the involved object can exhibit luminosities that surpass what our nearby Sun produces over its entire lifetime, in time spans of seconds. Observatories that detect various cosmic messengers, such as neutrinos and Gravitational Waves (GW), have opened up new possibilities to study these transient events in the framework of Multi-Messenger (MM) astronomy. The aim of the research conducted in this dissertation is to leverage open data streams and computational methods in order to facilitate the co-detection of cosmic messengers.

When confronted with the MM approach, ground-based Imaging Atmospheric Cerenkov Telescope systems face certain obstacles. Working on a feasible strategy for the follow-up of MM alerts with the Major Atmospheric Gamma-ray Imaging Cherenkov Telescope (MAGIC) and the first deployed Large-Sized Telescope (LST-1), I adopted/elaborated a set of methodologies that allowed to implement tailored strategies for the generic small field of view instrument. The underlying algorithm culminated in an open-source software (ToOpy) and allows to execute time-critical follow-up observations on triggers from neutrino, GW, and Gamma-Ray Burst (GRB) alerts.

Using ToOpy, real-time and archival data streams from observatories such as IceCube, *Fermi*, and LIGO-Virgo were accessed in order to isolate potential co-detections of multiple messengers. The proposal of ToOpy being valuable for this task was validated by recovering the spatio-temporal coincidences of the two major cornerstones of MM astronomy, namely TXS0506+056/IC-170922A as well as GRB170817A/GW170817. Along this line, ToOpy triggered follow-up observations of an IceCube TRACK alert by both the MAGIC and the LST-1 telescopes in March of 2021, but no excess very-high-energy gamma emission was recorded. Furthermore, ToOpy allowed to elaborate a catalog of host galaxies that serve as potential electromagnetic counterparts to CASCADE alerts issued by IceCube. Finally, digging through extensive GW event catalogs as well as GRB trigger data from *Fermi*-GBM, four unprecedented spatio-temporal coincidences were detected. While a bootstrapped approach lowers the significance of these novel associations, further study with *Fermi*-LAT data shows an interesting hint for an unrepeated (on a 10-year basis) high-energy gamma-ray flare from within the combined uncertainty region of the GRB and GW localization errors.

On a different note, in the context of a Multi-Wavelength (MWL) study, I elaborate on my efforts to study the flaring TeV blazar VER J0521+211, which was observed by the MAGIC telescopes and other instruments during the spring of 2020. Leveraging therein extensive MWL coverage allowed to model the broadband spectral energy distribution by adopting time-evolving parameters for leptonic and leptohadronic emission mechanisms. Alongside these results, the combined gamma-ray spectra from MAGIC and *Fermi*-LAT allowed to constrain the unknown redshift for this particular blazar to a range of $0.18 \leq z \leq 0.243$.

Declaration

I herewith declare that I have produced this thesis without the prohibited assistance of third parties and without making use of aids other than those specified; notions taken over directly or indirectly from other sources have been identified as such. This paper has not previously been presented in identical or similar form to any other Spanish or foreign examination board.

The thesis work was conducted from September 2019 to May 2023 under the supervision of Oscar Blanch Bigas at Barcelona.

Manuel David Artero

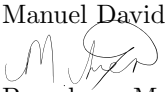

Barcelona, May 12th, 2023.

Acknowledgements

I would like to take the opportunity to express my deepest gratitude to Oscar Blanch. PhD students know that during their studies, academic supervisors represent a key figure in one's scientific and personal life. In this sense, I couldn't have wished for a better supervisor to guide me through this critical career stage. Being a true gem, Oscar is not only an excellent scientist but also characterized by such humanity. Thank you so much for your guidance, confidence, and support throughout this journey. I am also extremely grateful to Prof. Manel Martinez (and Prof. Mario Martínez, as a matter of fact) for giving me the chance to start my academic journey as a high-energy researcher at IFAE.

I would like to thank all the seniors from the gamma-ray and gravitational wave groups for the fruitful discussions during our meetings. Special shoutouts to Abelardo for patiently walking me through the analysis of MAGIC data with flute. Daniel holds a special role amongst the seniors to receive my gratitude. Not only would I like to thank you for taking a big chunk out of your time (during an almost French Revolution) to proofread my thesis with such care, but also for working on various projects with me. It was such a pleasure to work and teach with the most positive and upbeat person I've met in a long time.

I would also like to give a shoutout to all the former and current Post-Docs, and of course the past and present PhD and Master students and visitors with whom I shared the office during these extraordinary couple of years. Special thanks go to Merve and Daniele for patiently teaching me to become a MAGICian myself, to Juan for shielding me from "El taller" (you'll do great!), and Jelena for helping with teaching the next generation of "critical thinkers" ;D. A major thank you is also due to the administration, tech-support, and engineers at IFAE, especially mentioning Marta, Cristina, Jordi, and Laura. Along this line, I would like to thank the staff and visitors of the ICRR, and especially Koji for the interesting project and discussions, as well as Midori for making this exchange possible and such a smooth experience.

Special thanks goes to my entire MAGIC family and LST collaborators, and especially to those people with whom I embark on projects and spend countless nights at the ORM. There are many other people whom I did not directly mention here. So, to them, I say thank you for sharing your most valuable resource (speaking of time, not coffee, by the way ;D).

As a closing line, I would like to thank the most important people in my life without whom I could not have embarked on this journey called life. Thank you Katy, Esteban, Benja and family for your endless support, and to Nancy for making me a better person and turning my weaknesses into strengths.

CONTENTS

CHAPTER 1

INTRODUCTION

Contents

1.1 Closing in on Multi-Messenger Astronomy

Since the dawn of modern astronomy (∼17th century), breakthroughs in instrumentation and observational methodology laid the foundations for discoveries that would dramatically alter our understanding of the Universe. The most recent one, being the opening of an observational window to gravitational astronomy. The discovery of Cosmic Rays (CRs) in 1912 tells no different story. This epochal moment marked an inflection point that was followed by discoveries of exotic particle species, which resulted in the emergence of an entire field devoted to the study of particle physics. The development of sophisticated accelerator technologies and related instrumentation allowed to formulate the current Standard Model (SM) of particle physics and its experimental verification. Over time these novel detector designs would mature into systems that are capable of detecting signatures from a wealth of cosmic messengers; charged particles, photons, neutrinos and eventually Gravitational Waves (GW). Reaching a level of sophistication when it comes to instrumentational designs and observational strategies the past decade has been pivotal for Multi-Messenger (MM) astronomy. Upon detecting for the first time a GW signal from a Binary Black Hole (BBH) system on September 14th, 2015, it only took two more years to probe the first spatio-temporal coincidence of GWs and photons. The co-detection of a GW from a merging Binary Neutron Star (BNS) system along with Electromagnetic (EM) transient signatures from a Gamma-Ray Burst (GRB) on August 17th, 2017 indicate for many astronomers the birth of MM astronomy. The very same year was marked with the exciting discovery of a spatio-temporal coincidence of a High-Energy

(HE) neutrino with a gamma-ray flare from an Active Galactic Nucleus (AGN). This in turn brings us today to the doorstep of a new era in which we are capable of studying multiple messengers in order to probe regions of space-time that were previously inaccessible, e.g. proximity of Black Holes (BH) and beyond the Cosmic Microwave Background (CMB). Being able for the first time to study astrophysical processes at the highest energies through different lenses indicates that truly exciting times are ahead for the field of astronomy.

1.2 Towards data driven Multi-Messenger Astronomy

In order to facilitate the study of potential spatio-temporal coincidences between cosmic messengers, it remains a pending task to elaborate data processing tools and related analysis techniques that are widely accessible to the astronomical community. Only then would this allow to filter through numerous alerts in order to pick out a needle from a haystack fast enough to detect a potential counterpart signal, which in the case of the EM domain might be fainting by the second. With various next-generation observatories being designed and currently built (see also Figure 1.1), these issues are about to be exacerbated in the short-term, especially when it comes to avalanches of alerts. Hence, there is an incentive for the development of techniques that allow dealing with the wealth of data that we are going to be able to collect in the near future. At the heart of these efforts will be to design and develop tools that allow astronomers to keep up with the increasing data flux and are at the same time capable of bridging various observational communities, thus facilitating efficient information exchange between them.

1.3 VHE Gamma-Ray Astronomy and Principal Efforts of this Work

Thanks to the fast-paced evolution in the MM approach, the astronomical community is gaining momentum when it comes to reacting to short-lived astrophysical phenomena, which are commonly also referred to as transient astrophysical events or "transients". These kinds of events pool phenomena such as Supernovae (SN), GRBs, Compact Binary Coalescence (CBC), AGN flares, Fast Radio Bursts (FRBs), Tidal Disruption Events (TDEs) as well others. When it comes to the study of these phenomena, there is no doubt that the observatories outlined in Figure 1.1, will play crucial roles in performing time-domain astronomy, and in particular to the study of short-lived transient astrophysical phenomena. However, for the most cataclysmic astrophysical events, instruments that target Very-High-Energy (VHE) gamma-rays will play a key role. They probe photons of the highest energies and could exploit a direct link to a parental particle population that branches off to neutrinos as well. In the framework of this thesis project, I will elaborate on my efforts to facilitate Imaging Atmospheric Cerenkov Telescope (IACT) systems with a capacity to perform time-domain astronomy. Having already motivated the prospects of using IACT systems to perform MM astronomy, i.e. targeting the most energetic photons, there are certain drawbacks to be taken into account. On one hand, IACTs have a limited duty cycle which is a severe drawback when considering facilities such as neutrino and GW observatories that can have continuous uptime. Furthermore and more importantly, the small Field of View (FoV) of IACTs limits their capacity

for follow-ups. The principal aim of this thesis is to provide IACT systems with adequate strategies to react to triggers from both neutrino and GW events in order to detect promising transient signals. The underlying approach is to pinpoint host environments that might provide adequate conditions to initiate and maintain processes that result in signatures of messengers related to transient phenomena. Based on this approach, the follow-up would then be performed on specific galaxy/sky region, commonly performed as Target of Opportunity (ToO) observations. Furthermore, using the same tools, we elaborate a methodology that allows for performing archival searches. This allows checking for past spatio-temporal coincidences in Multi-Wavelength (MWL) as well as MM datasets.

Thesis Overview This dissertation is divided into chapters, with the first two serving as introductory and the remaining five reporting on the scientific achievements obtained throughout this work.

◇ **Chapters 2-3;** aim to introduce the reader to processes occurring in the non-thermal Universe.

- **Chapter 2;** introduces the field of high-energy astrophysics, along with a variety of instrumentation that allows studying the main messengers of interest for my work, namely gamma-rays, neutrinos and GWs. As MM studies correspond to a principal goal of this thesis, synergies between observations of the various messenger particles are presented.
- **Chapter 3;** provides an overview of transient astrophysical phenomena that have proven to be interesting for studies involving the different messenger particles.

◇ **Chapters 4-7;** outline the scientific achievements that were obtained throughout this thesis project.

- **Chapter 4;** details on the flaring BL Lacertae blazar VER J0521+211 as observed during a MWL campaign in spring 2020.
- **Chapter 5;** introduces my open-source tool ToOpy, which aims at providing small FoV instruments with personalized ToO strategies in order to enable autonomous EM counterpart searches for a given set of MM alerts.
- **Chapter 6;** reports on using ToOpy in order to isolate and execute searches for EM counterparts to neutrino alerts issued by the IceCube Observatory. Furthermore, I elaborate on a methodology of merging archival datasets from various instruments to search for spatio-temporal coincidences using *Fermi*-GBM triggers and LIGO/Virgo candidate events.
- **Chapter 7;** elaborates on my efforts to obtain a revised Gamma-Ray Follow Up (GFU) list in order for the Large-Sized Telescope (LST) to react to multiplet neutrino alerts from IceCube.
- **Chapter 8;** concludes this thesis and provides guidance for further investigations.

◇ **Appendix A;** presents results from the commissioning of the LST-1 camera.

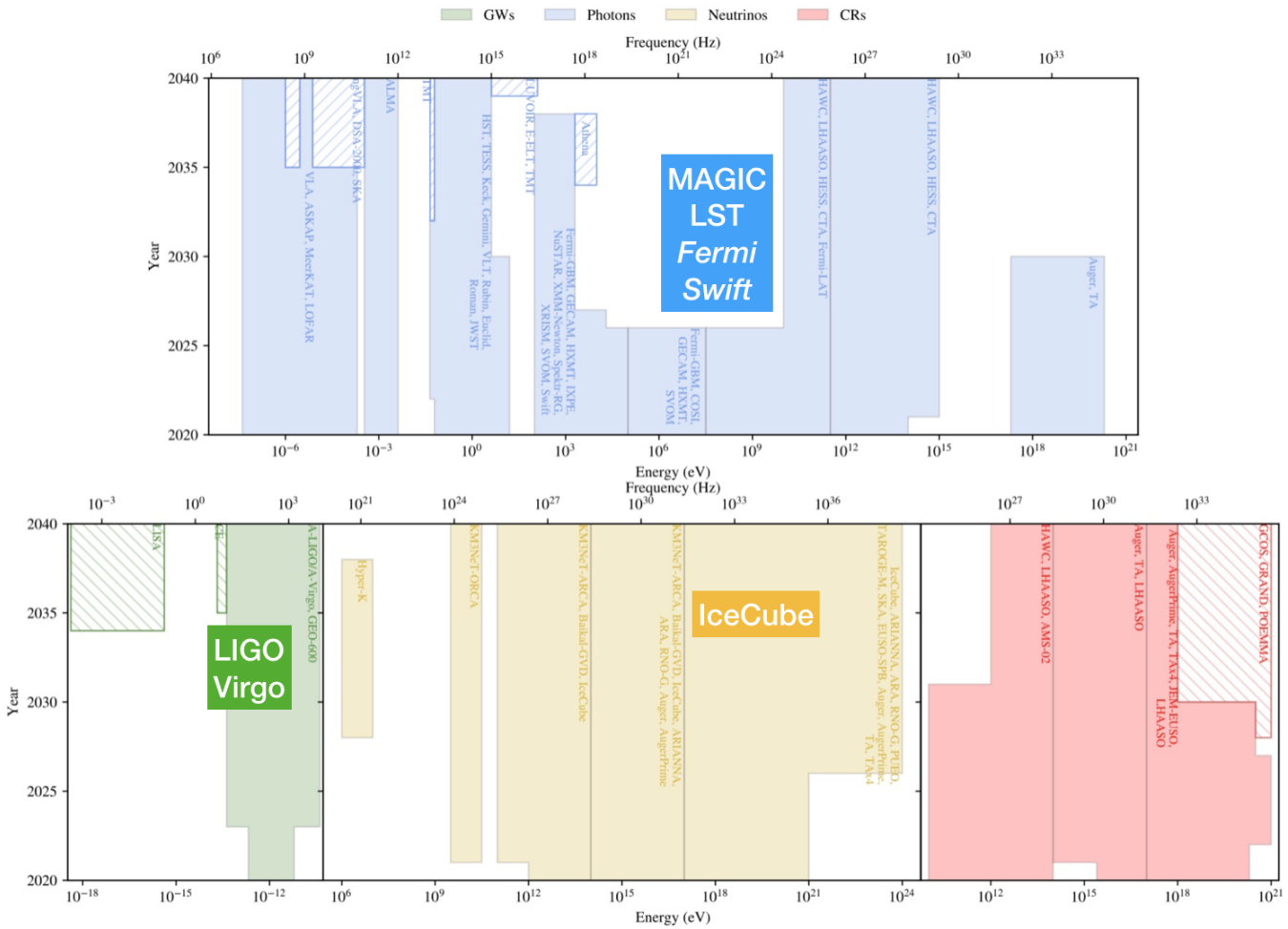

Figure 1.1: Operational schedule (albeit outdated and not complete) for some of the current and future facilities that are targeting the various cosmic messengers. Note that the experiments and observatories that are visually enhanced, e.g. photons (MAGIC, LST, *Fermi, Swift*), neutrino (IceCube) and GW (LIGO/Virgo), show the instruments from which this dissertation uses datasets. Image Credit: Adapted from Engel et al. (2022)

1.4 Summary Technical Research Activity

My principal effort with respect to technical research was the development of strategies in order to perform counterpart searches of MM alerts. Over time these efforts led to the development of ToOpy, which effectively combines the working principle of data brokers and schedulers. This tool enables its users to perform automatic ToO observations for a variety of MM alert streams. Additionally, the obtained output allows to take into account observability criteria and technical limitations. During the elaboration of ranking methodologies that would be implemented into the broker, I managed to develop a method that allows to perform archival searches with a variety of datasets. Furthermore, getting acquainted with galaxy catalogs, I would also contribute to the revision of GFU target list that might be contributing towards future efforts of the IceCube and LST collaborations.

- ◇ **ToOpy:** Details on a tool that combines the working principle of a data broker and observations scheduler in order to enable autonomous ToO observations. It is elaborated in Chapter 5 with the main achievements:
  - **Broker;** which combines various data streams and provides the basis for ToO strategies.
  - **ToO Strategies;** elaborated for both galaxy-targeted and tiling-based approaches. Thus allowing the follow-up of alerts with large localization errors.
  - **Scheduler;** that is customizable in order to provide users with an autonomous selection of pointing sequences based on several criteria that can be selected by the user.
- ◇ **GFU List:** Details on the elaboration of a galaxy-targeted list to be implemented by IceCube in order to select and share multiplet events with the LST collaboration. It is elaborated in Chapter 7 with main achievements:
  - **Catalogs;** the use of a variety of catalogs and therein information in order to motivate a galaxy-targeted approach for neutrino triggers.
- ◇ **Archival Searches:** Details on the elaboration of an algorithm to search for coincident triggers from low latency alerts, namely GWs and GRBs. It is elaborated in Chapter 6 with main achievements:
  - **Low-latency Alerts;** combined with other triggers and MWL dataset allow to find galaxies or sky regions that could harbor potential sites of previous BNS mergers.

Aside from these principal technical investigations, I also contributed to the commissioning efforts of the four LST cameras that will be deployed within the northern Cherenkov Telescope Array (CTA) (see also Appendix A).

1.5 Summary Physics Research Activity

The principal scientific aim of my thesis work was the study of transient astrophysical phenomena, namely AGN flares, GRBs and CBCs, at the highest photon energies, i.e. VHE gamma-rays. Adopting

the assumption that these transient events can manifest themselves by a variety of cosmic messengers, allowed me to benefit from inherent connections between the various messengers, i.e. photon and neutrino emission from AGNs, or photon and GW emission from merging BNS systems. This would allow me to leverage the MWL and MM approach in order to elaborate strategies for ToO observations. Prior to attaining results in favour of a specific ToO strategy, I was already involved in a MWL study of a flaring blazar. Therein progress resulted to be essential in order to develop strategies to be implemented in ToOpy. Attaining a mature version of my algorithm, allowed me to diversify into a variety of research avenues, which resulted in taking the initiative to perform ToO observations (see also 6.1 and 6.2) as well as obtain results from low-latency alerts and archival datasets (see also 6.3).

- ◇ **VER J0521+211:** Details on the flaring BL Lacertae blazar VER J0521+211 as observed during a MWL campaign in spring 2020. Discussed in Chapter 4 with main achievements:
  - **VHE Analysis;** performed using the data analysis chain from the Major Atmospheric Gamma-ray Imaging Cherenkov Telescope (MAGIC).
  - **High-Energy (HE) Analysis;** performing the analysis of *Fermi*-LAT data using the fermipy data analysis chain.
  - **Spectral Energy Distribution (SED) Modeling;** performing the modeling of MWL data.
- ◇ **ToO Observations:** Details on the emergence of ToO opportunities from MM coincidences found by ToOpy, e.g. from neutrino- as well as GRB-triggers in the epoch 2020-2023. Discussed in Chapter 6 with main achievements:
  - **IceCube TRACK Alert;** initiating the follow-up of IceCube-220303A by the MAGIC and LST collaborations.
  - **EM Counterpart Catalog for CASCADE alerts;** using *Fermi*-LAT data in order to elaborate a catalog of galaxy-targeted ToO opportunities for IceCube CASCADE alerts. Note that this catalog focuses on flaring AGNs in order to identify progenitor systems for neutrino triggers and thus remains biased to HE gamma-ray emitters.
- ◇ **Archival Searches:** Details on the usage and results when combining low-latency alerts with various archival MWL datasets from instruments operating within the EM domain. Discussed in Chapter 6 with main achievements:
  - **MM Reference Results;** proof that ToOpy motivates one of the main reference coincidences of MM astronomy (GW170817/GRB170817A).
  - **HE and Low-latency Alerts;** The combination of HE gamma-ray and GW astronomy presents a powerful tool for studying short-duration GRBs.

Bibliography

Engel, K., Lewis, T., Muzio, M. S., Venters, T. M., Ahlers, M., Albert, A., Allen, A., Solares, H. A. A., Anandagoda, S., Andersen, T. et al. (2022). Advancing the landscape of multimessenger science in the next decade, *arXiv preprint arXiv:2203.10074* .

CHAPTER 2

HIGH ENERGY ASTROPHYSICS

Resume: Aiming to introduce the reader to processes occurring in the non-thermal Universe and elaborate on performing astronomy using different cosmic messengers.

Contents

High-energy astrophysics encompasses a broad area of research involving a plethora of physics. Historically, experimental advances required to study photons across the EM spectrum, which includes radio waves, infrared (IR), visible light, ultraviolet (UV), X-rays, and gamma rays. However, since there are limitations to the propagation of photons, this so-called MWL approach does not allow to obtain a complete picture of the underlying mechanisms that govern the physical processes occurring in that energetic landscape. Fast forwarding from the initial discovery of CRs in the 20th century, today we can study a variety of cosmic messengers such as photons, charged particles, neutrinos and GW and hence follow a MM approach that has high prospects when studying extreme astrophysical processes related to high-energy astrophysics.

Going through this chapter, I will start by discussing CRs (Section 2.1), their inherent limitations for astrophysical studies and crucial links between neutrino and photon messengers. We then provide an extensive discussion on gamma-ray astronomy (Section 2.2): where I elaborate on underlying physics and different instrumentation required in order to access different energy regimes. Upon providing a lightning introduction to neutrino (Section 2.3) and gravitational wave (Section 2.4) astronomy I then elaborate in (Section 2.5) on synergies between the different messengers

2.1 Cosmic-Ray Astronomy

The mystery why isolated electroscopes discharged (seemingly spontaneously) puzzled various generations of scientists but eventually could be attributed to background radiation that over time caused the discharge of the device. Regarding the source of that radiation, there were several hypotheses. One assumption was that there was radioactivity stemming from the Earth's crust and/or the atmosphere. Another option was that there could perhaps be an extraterrestrial component (the Sun due to its proximity being the most viable candidate). After several experiments performed underwater and in increasing altitudes the debate was eventually settled by a series of balloon flights performed by Victor Hess. His air-born experiments allowed to measure an increase in the ionisation rate for increasing altitudes, therefore concluding that the earth' atmosphere is exposed to a flux of energetic particles that originate from outer space and were later called "Cosmic Rays". A wealth of experiments carried out throughout the prior century led to the discovery of new particle species, e.g. positron, muon, kaon, pion, thus yielding the experimental formulation of the SM of physics. The study of CR was furthermore pushed by designing specialized satellite missions as well as the construction of various extended surface detectors, thus eventually reaching a broad understanding with respect to the spectral energy distribution of CRs as well as their composition. Nevertheless, the accelerators of CRs and how they manage to accelerate therein particles to the highest observed energies remain elusive to this day.

2.1.1 Spectrum and Composition

Gathering data from a wealth of air-born and ground-based experiments allowed to deduce the composition of the generic CR population to roughly 86% protons, 11% helium, 1% heavier nuclei, and 2% electrons. The resulting all-particle spectrum is depicted in Figure 2.1.

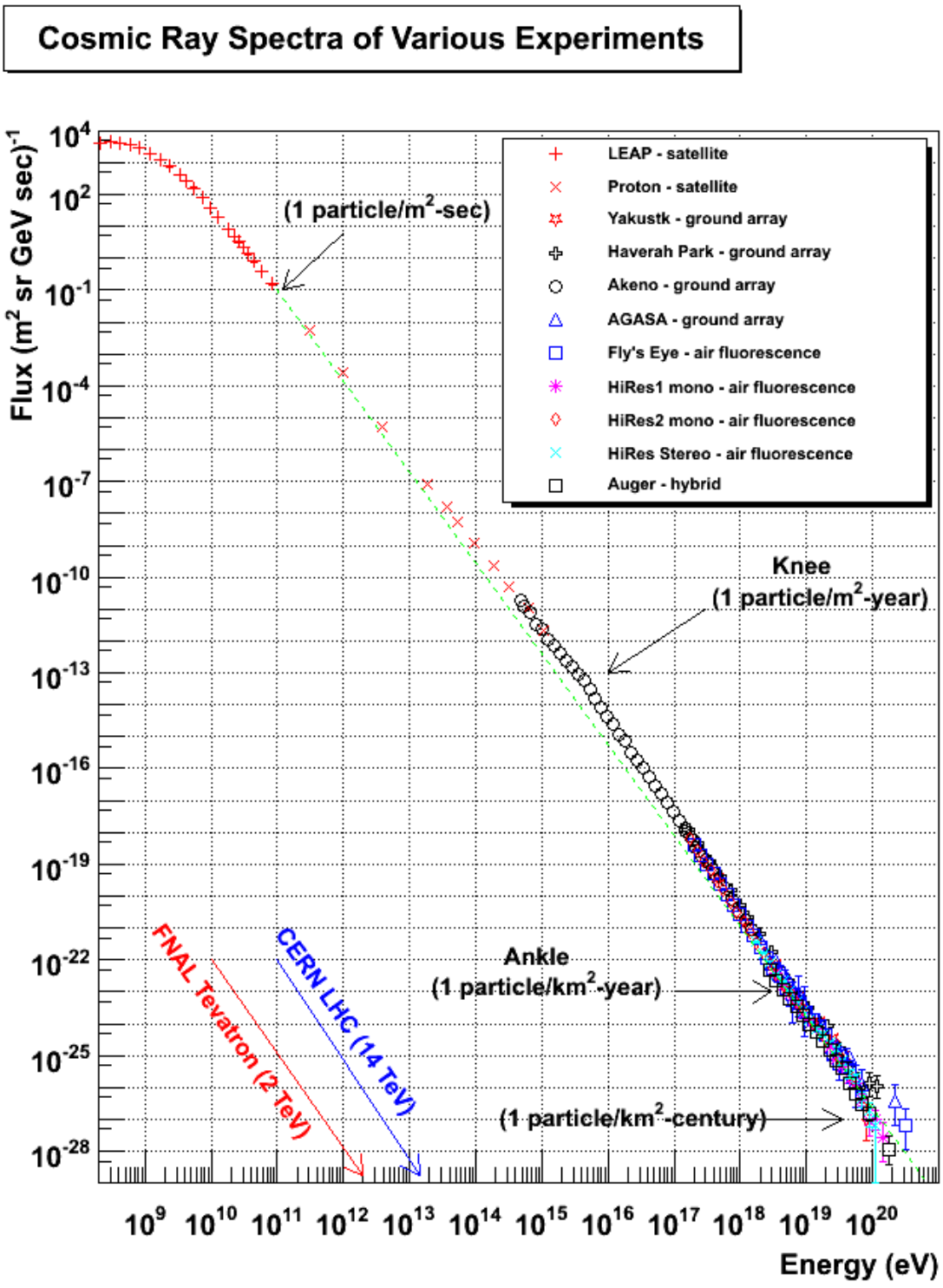

Figure 2.1: The CR all-particle spectrum measured by a non-exhaustive list of experiments The location of the knee and the ankle are depicted by arrows. Image Credit: W. Hanlon https://web.physics.utah.edu/∼whanlon/spectrum.html

It shows an almost featureless spectrum that spans 13 decades in energy from 10^8 to 10^{21} eV. The CR flux at energies below 10^9 eV is attributed to emissions from our Sun, thus reflecting chemical abundances consistent with those prevalent in solar winds. Above that threshold, the spectrum can be fitted by a simple power–law:

$$\frac{dF}{dE} \propto E^{-\alpha} \tag{2.1}$$

with constant spectral indices for three distinct energy ranges:

$$\alpha = \begin{cases} \sim 2.7 & 100 \text{ MeV} < \text{E} < 5 \text{ PeV for } \mathbf{I} \\ \sim 3 & 5 \text{ PeV} < \text{E} < 3 \text{ EeV for } \mathbf{II} \\ \sim 2.6 & 3 \text{ EeV} < \text{E} < 30 \text{ EeV for } \mathbf{III} \end{cases} \tag{2.2}$$

- ◇ **I;** CR likely to be of galactic origin, with supernovae remnant (SNR) as prime candidate for being the main accelerator. Upper limit ($E \sim 10^{16}$ eV) is a transition region coined as "knee" and known to be charge-dependent.
- ◇ **II;** Transition region between the "knee" and the so-called "ankle" ($E \sim 10^{18}$ eV) where CRs are likely to be a mixture of galactic and extragalactic origin.
- ◇ **III;** The "ankle" marks the conditions where the extragalactic component of the CR starts to dominate the flux. Also the galactic magnetic fields are not able to confine particles at these energies.

It remains highly debated whether changes in the spectral index are related to the origin of CRs themselves. Also, at energies beyond $E \sim 10^{20}$ eV there is a sharp cutoff, which stems either from a limit of the maximum energy attainable in the accelerators, or the attenuation of the CR flux due to the interaction of its constituents with the CMB (see also Section 2.1.3).

2.1.2 High Energy Cosmic-Ray Accelerators

Since there are so few features visible in the CR spectrum the question arises what kind of simplistic acceleration mechanism could provide these cosmic messengers with the ability to attain such high energies and whether there is a maximum energy they can reach. In the literature the discussion tends to follow two scenarios, whereas the "Top-Down" scenario requires the existence of exotic particles and new physics, the "Bottom-Up" scenario boils down to a shock acceleration mechanism coined by Fermi in 1949. In this later scenario, the initial seed particles can be accelerated by repeatedly crossing a shock region prevalent around various cosmic sources.

Acceleration of charged CR or "Bottom-Up" Scenario Following the elaboration of Fermi and others, it was found that astrophysical sources could achieve a generic CR flux resulting in "powerlaw-like" spectrum by reducing the treatment to a mechanism that involves particles moving through regions that contain shock waves and magnetic field inhomogeneities, resulting in stochastic shock acceleration of the initial seed particles. In this scenario the charged CRs that primarily stem from ejecta of various astrophysical sources can be accelerated if their trajectories cross turbulent magnetic fields. Undergoing

stochastic collisions these CRs could eventually attain relativistic speeds that allow them to escape the confinement of the magnetic field lines.

Possible Sites of Acceleration Based on the assumption that CRs are accelerated through the previously described Fermi mechanism, the main ingredients for our accelerators are magnetic fields and extensive shock waves, which happen to prevail in a variety of astrophysical sources, e.g. AGNs, SN, GRBs, etc.. According to calculations by Hillas, CRs are confined to an acceleration region if their gyroradius does not exceed the size of their confinement. Hence the maximum energy (E_{max}) a CR can reach reduces to a balance between magnetic field strength (B) and accelerator size (R) as:

$$E_{max} \simeq 10^{18} eV q \frac{R}{kpc} \frac{B}{\mu G} \tag{2.3}$$

and is known as the "Hillas-criterion", effectively limiting the potential sources of CRs to a handful of astrophysical objects depicted in Figure 2.2. The following information can be extracted from this criterion:

- **Take Away 1;** Since particles with E above the "ankle" would have a gyroradius larger than size of milky way, the bulk of CR we detect at energies below the "ankle" must be of galactic origin.
- **Take Away 2;** Particles with E above the "ankle" are of extragalactic origin, stemming from sources such as AGNs and GRBs.

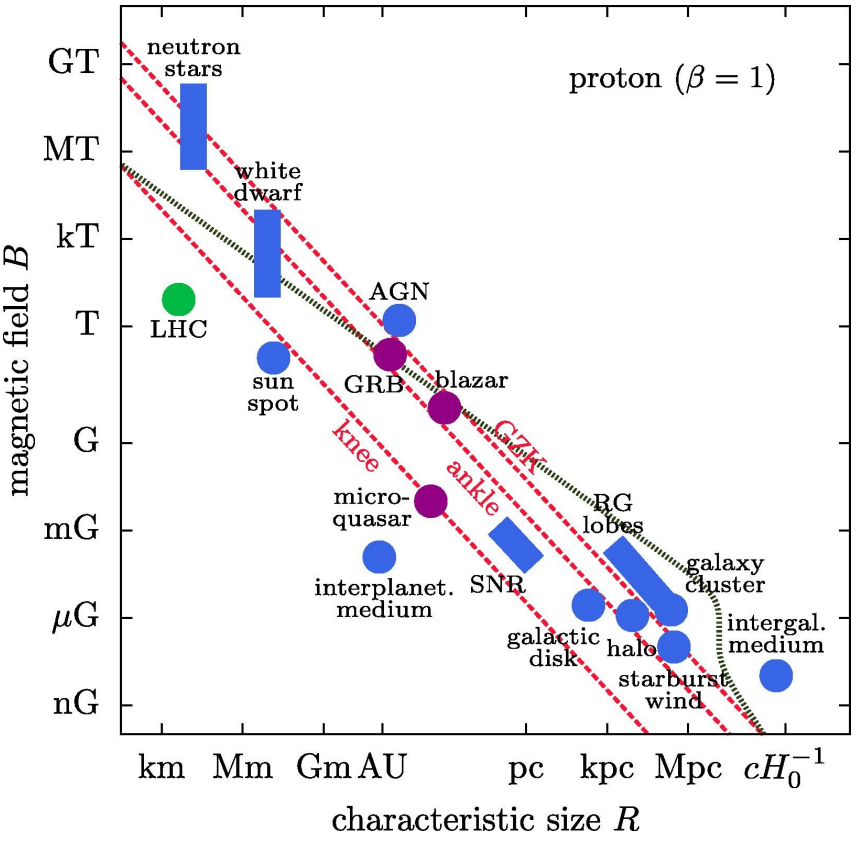

Figure 2.2: Astrophysical objects that could act as potential CR accelerators according to the "Hillas-criterion". The magnetic field strenght is plotted vs the size of each object. Various boundaries for CR acceleration are marked accordingly ("knee", "ankle"). Image Credit: Aartsen et al. (2018)

2.1.3 Limitations to Cosmic-Ray Astronomy

Propagation of charged CRs Once CRs manage to escape their magnetic prison, the prevalence of magnetic fields becomes somewhat of a double-edged sword. On one hand, one needs them to accelerate them, but once CRs attain speeds that allow them to eventually escape their confinement (balance between centrifugal and Lorentz force), they encounter interstellar and intergalactic space filled with magnetic fields that over the long journey of the CR trajectory affect their propagation apart from additional interactions with populations of photons and matter.

Greisen-Zatsepin-Kuzmin cutoff For CRs energetic enough to not be significantly deflected by the magnetic field lines, there is another effect kicking in at energies above $E > 5 * 10^{19}$ eV, where their flux is strongly attenuated due to the CMB photons interacting with the protons.

$$p + \gamma_{CMB} \rightarrow \Delta^+ \rightarrow \begin{cases} p + \pi^0 & \textbf{with branching ratio} \sim 2/3 \\ n + \pi^+ & \textbf{with branching ratio} \sim 1/3 \end{cases} \tag{2.4}$$

This particular effect is termed as the Greisen-Zatsepin-Kuzmin (GZK) cutoff. It implicates that sources

which lie at distances above 200 Mpc are not able to be detected by CR ($E > 5 * 10^{19}$ eV) since their flux will decrease exponentially as visible in Figure 2.3.

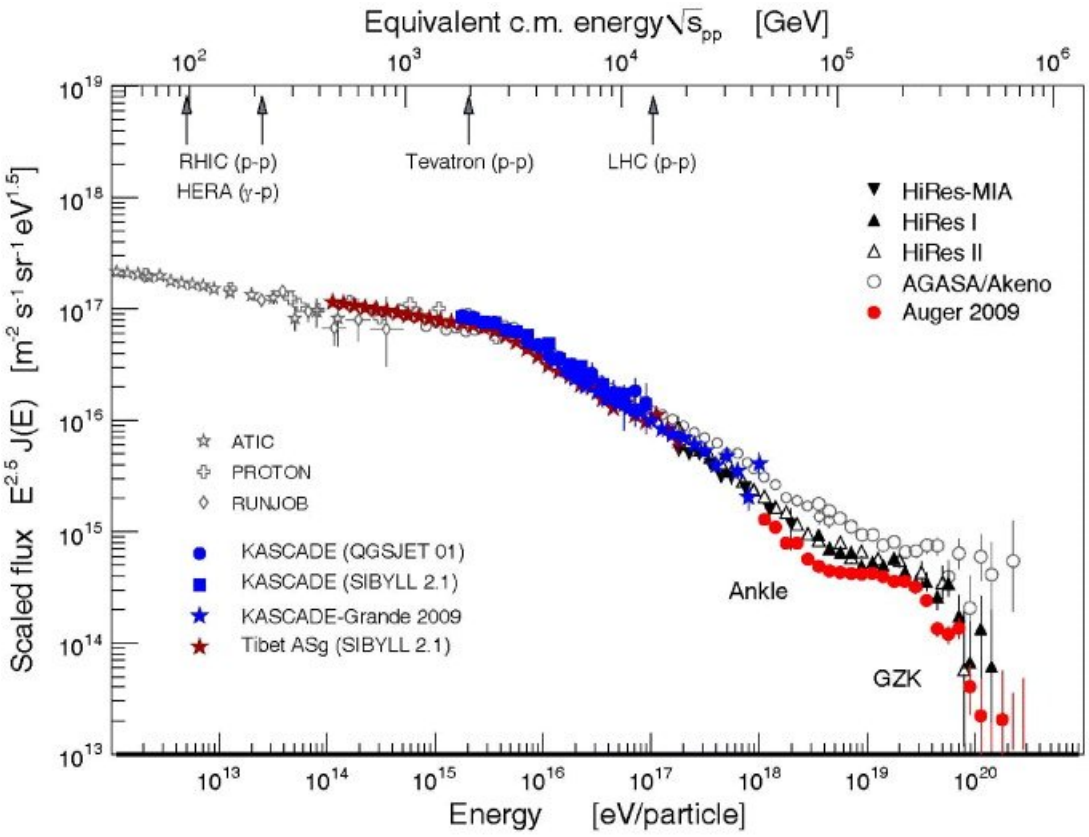

Figure 2.3: CR spectrum showing how the GZK cutoff drastically attenuates the CR flux at the highest energies, i.e. $E > 5 * 10^{19}$ eV. Image Credit: Blümer et al. (2009)

Major limitations when performing CR Astronomy Following the previous section, it would be tempting to provide a list of astrophysical CR sources, such as the objects in Figure 2.2. However, first of all the "Hillas criterion" follows a very simplistic argument with an optimized accelerator geometry, unlikely to have a nature-made counterpart. On top of that, due to the charged nature of the CRs there is no way to pinpoint their accelerators.

Nevertheless, even if the "Hillas-criterion" holds, emitted close-by emitted charged heavy particles with energies around the GZK barrier should remain unaffected by magnetic fields. This would allow obtaining directional information from the reconstructed events, thus allowing to pinpoint of the regions where the particles were accelerated. As a matter of fact, the Pierre Auger Observatory reported on a potential correlation between the position of close-by AGNs ($\sim$ 75 Mpc) and the arrival direction of CR events with reproduced energies $E > 8 * 10^{18}$ eV (Collaboration et al.; 2017). Nevertheless, concerns were raised that therein used galaxy catalog might be affected by a biased distribution (Erdoğdu et al.; 2006).

2.2 Gamma-Ray Astronomy

Astrophysical processes generate photons of all sorts of energies. For each energy range there exist different experimental set-ups that allow to study the different wavebands (see also Figure 2.4). Photons in the high energy regime of the spectrum, i.e. gamma-rays, are particularly useful messengers to study the most extreme astrophysical environments. They are generated through non-thermal processes and their neutral electric charge allow them to move on a straight trajectory through space without being affected by magnetic fields in the intergalactic space (unlike their parental CR origins). Thus, making them promising targets to study their place of origin that share ties with the still elusive accelerators of CRs. However, in order to fully appreciate the intimate connection between gamma rays and CRs, we need to first understand the mechanisms that are able to generate these highly energetic photons.

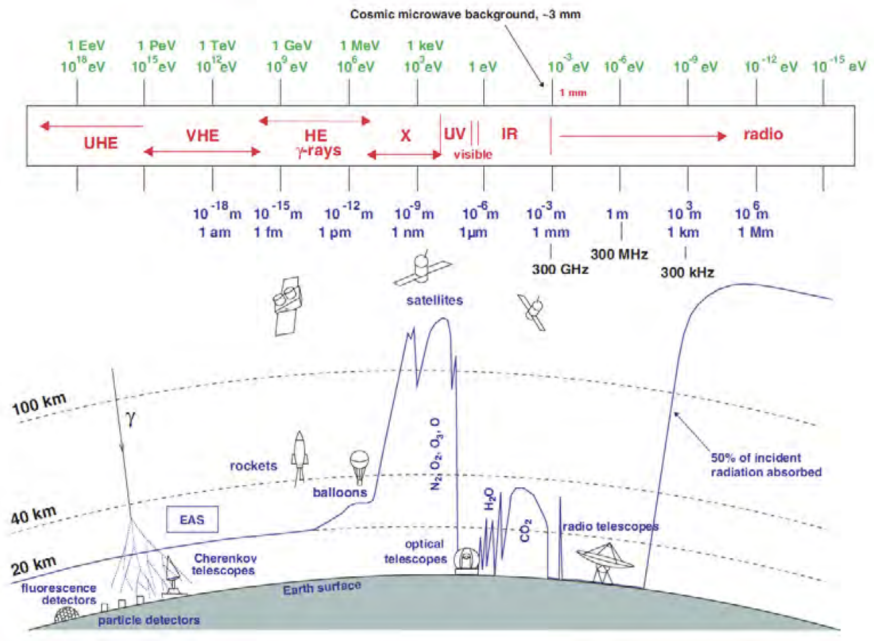

Figure 2.4: Overview of instruments and observational techniques in the broader EM domain. Depending on the photon energies the atmosphere is more or less transparent (indicated by a blue line). Image Credit: Longair (1992)

2.2.1 High-Energy Gamma Ray Generation and Absorption Processes

As we learned, CR trajectories are scrambled through interactions with magnetic and electric fields that permeate the Universe. But in order to study the very accelerators that can power high-energy astrophysical phenomena, we are in need of a messenger that can point straight back to these sources and thus allow us to identify them. As we will see these radiation fields, as well as other matter fields (e.g. molecular clouds), allow the production of high-energy photons through processes and thus allow gamma-ray sources to manifest their presence via photonic messengers (see also Figure 2.5). Hence the necessity arises to shed light on a few basic radiative and collisional mechanisms that are capable of

yielding a significant amount of gamma rays. In favor of simplicity, I will split the discussion into leptonic and hadronic processes and give a brief recital of the underlying mechanism, but refer to the literature for more elaborate treatment Grupen (2005); Longair (1992); Aharonian (2004); Angelis and Pimenta (2018).

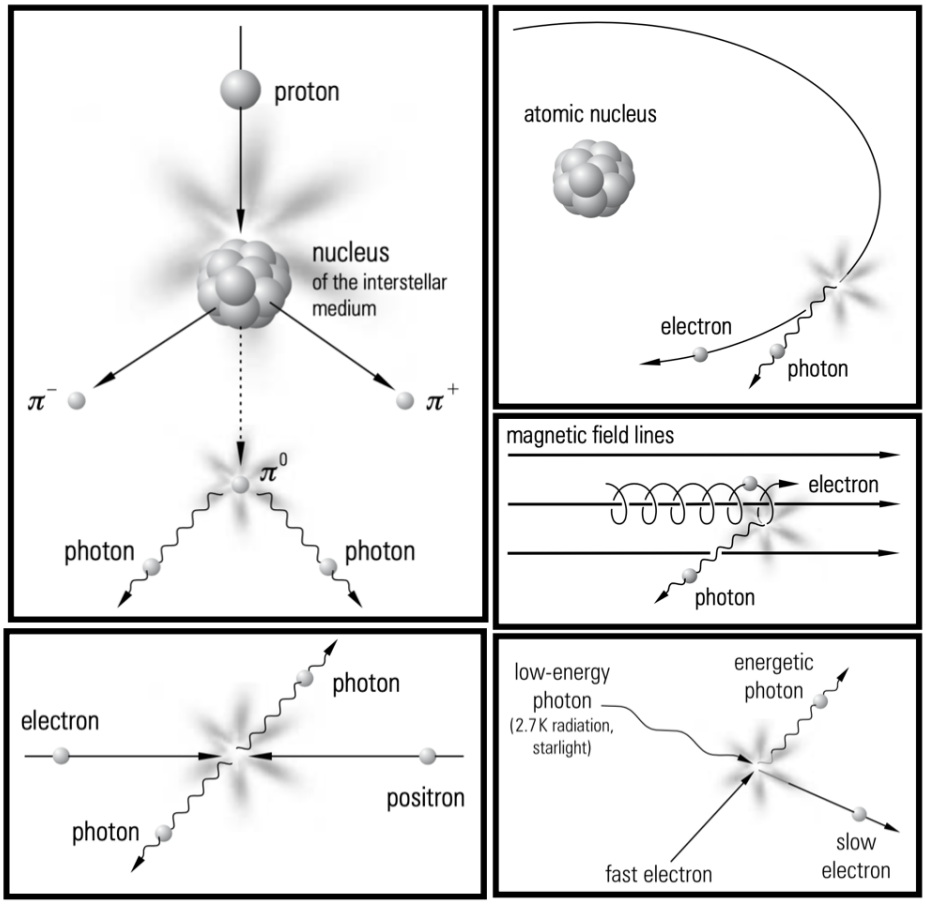

Figure 2.5: Main processes considered to contribute towards gamma-ray emission. Image Credit: Adapted from Grupen (2005)

Leptonic Models; Radiative processes Since the electron is a particle that has the capacity to undergo certain mechanisms that result in significant emission of high-energy photons, we will keep it as the main constituent for the following radiative processes:

- ◇ **Synchrotron radiation;** This kind of radiation is produced when a relativistic, charged particle encounters magnetic field lines along its trajectory. Due to the Lorentz force, the charged particle will be forced to spiral around the magnetic field lines and emit radiation.
- ◇ **Inverse-Compton (IC) scattering;** Highly energetic photons can be generated through an up-scattering of an initial low energetic photon with a relativistic charged particle.

$$e^-_{HE} + \gamma_{LE} \rightarrow e^-_{LE} + \gamma_{HE} \tag{2.5}$$

Note *that the inverse can also occur, e.g. low energetic electron gaining energy from a high energetic photon, also denoted as direct Compton scattering.*

- ◇ **Bremsstrahlung;** Gamma-ray radiation can be generated along the deflection of a relativistic charged particle that encounters the Coulomb field of a nearby nucleus.
- ◇ **Electron/Positron annihilation;** Gamma-ray photons could in principle also stem from annihilation events of particles with their own antiparticle.

$$e^- + e^+ \rightarrow \gamma + \gamma \tag{2.6}$$

Note *that the inverse can also occur, e.g. two photons that undergo pair production.*

Synchrotron Self-Compton (SSC); The final spectra of accelerated photons can be produced by a combination of the phenomena described above. As for instance with the SSC constitutes for the coupling of two fundamental processes that can lead to the generation of VHE gamma rays (see also Figure 2.6).

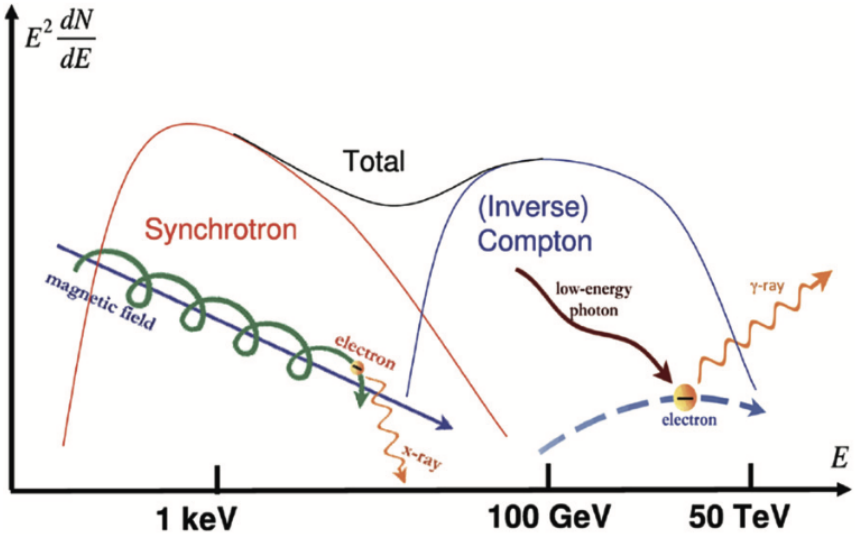

Figure 2.6: Toy model of the SSC process where the photons that were generated thorugh radiation become the targets for a subsequent IC intercation with their parental electrons. Image Credit: Angelis and Pimenta (2018)

Hadronic Models; Colissional processes On the other hand, when it comes to gamma-ray emission through collisional processes, a hadron should be taken into main consideration, where protons usually constitute as bulk material (also due to their abundance in CRs):

- ◇ **Pion Decay;** Through proton-proton collisions, neutral and charged pions can be produced:

$$p + p \rightarrow k^*[\pi^0 + \pi^{\pm}] + \chi \tag{2.7}$$

where k^* denotes the pion multiplicity and χ accounts for the resulting hadronic cascade. The neutral pion then decays mostly into two gamma-ray photons:

$$\pi^0 \rightarrow \begin{cases} \gamma + \gamma & \textbf{with branching ratio } 99\% \\ e^- + e^+ + \gamma & \textbf{with branching ratio } 1\% \end{cases} \tag{2.8}$$

Note also that the charged pions are able to decay into muons and neutrinos:

$$\pi^{\pm} \rightarrow \mu^{\pm} + \bar{\nu}_{\mu}(\nu_{\mu}) \tag{2.9}$$

We will revisit this decay channel in Section 2.3.

◇ **Hadrons and radiative processes;** Bremsstrahlung, Synchrotron and IC processes can in principle also occur with hadronic constituents undergoing alterations to their trajectories, however, the generation of gamma photons in such a way is not efficient.

Absorption Mechanisms Once produced, gamma rays are exposed to radiation fields that can lead to absorption and hence flux suppression. The main process being relevant for photon-photon interactions is the electron-positron pair production (kinematically allowed for $E_{\gamma\gamma} > 2m_e c^2$):

◇ **Classical pair production;**

$$\gamma + \gamma \rightarrow e^- + e^+ \tag{2.10}$$

Whilst the classical pair production is on one hand responsible for gamma-ray absorption in the atmosphere and hence of benefit for the working principle of IACTs, the latter is unfortunate for the propagation of VHE gammas and thus poses a significant challenge whose discussion will be revisited in Section 2.2.4.

2.2.2 Detection Techniques for Gamma-Ray Astronomy

Since the energy window of gamma-ray astronomy is quite wide, the literature usually adopts the following classification scheme:

Table 2.1: Energy ranges and corresponding detection techniques for gamma-ray astronomy.

Energy Range	Detection Technique	Instrument Examples
1 MeV - 30 MeV Low Energy (LE)	Compton Scattering	CGRO
30 MeV - 50 GeV High Energy (HE)	Pair-Production	*Fermi*-LAT
50 GeV - 100 TeV Very-High Energy (VHE)	Cerenkov$_{atmo}$	IACTs, i.e. MAGIC and LST
100 TeV - 100 PeV Ultra-High Energy (UHE)	Cerenkov$_{water}$	LHAASO, HAWC
$>$ 100 PeV Extremely-High Energy (EHE)	Fluorescence	JEM-EUSO

Compton Gamma Ray Observatory (CGRO), Large High Altitude Air Shower Observatory (LHAASO), High-Altitude Water Cherenkov (HAWC), Joint Experiment Missions for Extreme Universe Space Observatory (JEM-EUSO)

As shown in Table 2.1 the instrumentation needed to detect gamma-ray photons from astronomical sources is dependent on their energy. Narrowing in on the HE-UHE regimes, we can classify the required detectors into a "direct" or "indirect" type (depending on the fact that they detect the initial gamma ray or the products of its annihilation in the atmosphere). Whilst the small dimensions of the direct detectors, allow them to be placed into an earth-bound orbit aboard a satellite, the indirect detector types require large ground-based detector arrays of various kinds. In the following, we will give a brief overview of both detector types by elaborating on the various instrumental designs and then summarize the respective advantages and disadvantages of each of these detector classes.

Space-born Gamma-Ray Observatories, Direct Detection Detectors that are placed onboard satellites are most sensitive to gamma-rays in the LE-HE range and detect photons using different techniques. Whilst Compton scattering dominates the interactions in the LE range, in the HE range pair-production is prevalent:

- ◇ **Pair-production technique;** The *Fermi* Gamma-ray Space Telescope is an observatory that ever since it became operational in 2008 played key roles in both MWL and MM observations. Benefiting from its low-Earth orbit, both its onboard instruments the Gamma-ray Burst Monitor (GBM) and the Large Area Telescope (LAT), can monitor the whole sky with very low cadences, every ∼1 and ∼3 hours for GBM and LAT respectively, effectively covering eight decades in photon energy (Thompson and Wilson-Hodge; 2022). Instruments aboard the *Fermi* Satellite played a crucial role in both the discovery of a flaring state in TXS 0506+056 (Ansoldi et al.; 2018) and the association of GRB170817A to GW170817 (Abbott et al.; 2017).

  - **LAT;** The LAT instrument onboard the *Fermi* satellite is a pair-conversion telescope with a precision converter-tracker and calorimeter that allows the detection of gamma rays in the energy range between 20 MeV and more than 300 GeV (Atwood et al.; 2009).

  - **GBM;** The GBM instrument onboard the *Fermi* satellite is a survey instrument able to coarsely locate gamma-ray bursts (GRBs). Spanning an energy range of 8 keV–40 MeV (Meegan et al.; 2009) it is able to provide broad spectral information.

A major advantage of satellite detectors is the wide FoV along almost constant uptime (∼100% duty cycle), see also Table 2.2 for a characterization. Note There are numerous satellite instruments that are of utmost relevance for high energy astrophysics. The X-ray satellite *Swift* is routinely detecting GRBs. The INTEGRAL mission was essential in its contributions to the detection of GRB170817A. The AGILE mission made significant discoveries in gamma-ray astronomy, i.e. detection of gamma-ray emission from the Crab Nebula, from distant blazars and other extragalactic sources. Furthermore, the impact that future systems, i.e. those shown in Figure 1.1, will have on our understanding of high energy astrophysics can not be overstated. Nevertheless, for the results obtained in the thesis at hand the most relevant space-born instruments remain the payloads from the *Fermi* satellite.

Ground-based Gamma-Ray Observatories, Indirect Detection Hampered by limited payload capabilities onboard satellite missions, their collection area does limits the study of gamma rays at

energies in the VHE-band. Hence, the necessity arises to elaborate ground-based detectors that would allow studying higher energies gamma rays with sufficient statistics. Direct detection of gamma rays remains elusive due to an opaque atmosphere preventing such energetic photons to reach ground level. Fortunately, an indirect detection remains prospective thanks to the possibility of measuring the particle cascades, also called Extensive Air Showers (EAS) that are initiated due to the absorption processes occurring once the gamma rays enter the atmosphere. The inference of a primary gamma causing the EAS (along with an estimate for its energy and directional information) can be deduced either by collecting the Cerenkov radiation originating from the superluminal motion of secondary particles or by detection of the secondary particles themselves. Depending on one of these two strategies we distinguish on the following two techniques to measure the shower:

◇ **IACT technique;** Aims to measure the Cerenkov light that is emitted by the secondary particles that travel through the atmosphere. By imaging the EAS one can deduce whether the initial particle is a gamma ray using gamma/hadron separation algorithms. Shower (or event) reconstruction algorithms applied to data collected with this technique allow to obtain an estimate for both the direction and energy of the primary gamma ray. Whilst it has excellent angular and good energy resolution the FoV and duty cycle are rather limited (see also Table 2.2). The inclined reader is referred to the following references for further information on technical discussions of IACTs.

- **MAGIC;** The MAGIC Florian Goebel Telescopes are a stereoscopic system consisting of two IACTs with a 17 m diameter mirror each situated at an elevation of ∼2200 m above sea level and is located on the Canary Island of La Palma (28.7° N, 17.9° W) (Aleksić et al.; 2016). Thanks to its low trigger energy threshold of ∼ 50 GeV, a fast-repositioning design, MAGIC is among the third-generation IACTs particularly suited for blazar observations during flares as well as GRB follow-ups.

- **LST;** The LST-1, which since October 2018 is being commissioned, is the first of four telescopes to be deployed on the Canary Island of La Palma (Lopez-Coto et al.; 2021). Together with the Medium-Sized Telescopes (MST) the array will constitute the Northern site of the CTA observatory. The LSTs are designed in order to cover the lower energy ranges of the observatory, thus sensitive to gamma rays down to ∼ 20 GeV.

◇ **Water Cherenkov Arrays;** If gamma rays happen to exceed energies of ∼ 100 GeV, the secondary particles that are produced in the particle cascades are able to reach the ground where they can be measured with the water Cerenkov technique. Whilst the angular resolution is rather limited, they have the advantage of 100% duty cycles coupled with large FoV (see also Table 2.2).

Note The simplistic division of ground-based gamma ray observatories into two categories undermines the efforts and wit of multiple generations of astronomers that worked on a breadth of techniques. Also, the impact that future systems like the CTA observatory and LHAASO will have on our understanding of high-energy astrophysics can not be overstated. Nevertheless, once again, for the results obtained in the thesis at hand the most relevant ground-based gamma-ray instruments are the MAGIC experiment as well as the LST-1.

Table 2.2: Summary of pros and cons for instruments operating within the HE-UHE regime.

Instrument (Energy Range)	Advantage	Disadvantage
Satellites (HE)	FoV	angular resolution
	duty cycle	collection area
	γ/h separation	-
IACTs (VHE)	collection area	duty cycle
	angular resolution	FoV
	γ/h separation	-
Water Cerenkov Arrays (UHE)	duty cycle	energy resolution
	collection area	angular resolution
	FoV	γ/h separation

2.2.3 Sources/Transient Phenomena detected from Gamma-Ray Observations

Unlike for charged CR, where we were limited to imagine potential sources that might accelerate these messengers to high energies, with gamma-rays we have a messenger that points right back at its origin. Thanks to a wealth of detection techniques that allow estimating the energy and directions of the primary gamma photons, we can gather information on their astronomical origin and the environment of their source. In the following a brief outline of the known gamma-ray sources will be provided where the usual distinction will be made between galactic and extragalactic sources.

Galactic Objects:

◇ **Supernovae;** The observational phenomenology of the more generic class of supernovae is best described by classifying the dynamics that ultimately leads to an explosion and hence a clear distinction of progenitor systems:

- **Type 1a;** Once a star has burned all of its fuel and the equilibrium between radiation pressure and its gravitational pull tilts towards the latter it collapses into a compact neutron star or all the way to a singularity if the progenitor star is heavy enough. Shock waves accompany this collapse.
- **Type 1b;** Given a binary stellar system, one of the constituents can accrete matter overshooting a critical mass threshold which results in a thermonuclear explosion of the accreting star causing shock waves.

Within the shells of the expanding shock waves there occur processes of thermal and non-thermal origin, that in turn lead to photon emission over the entire EM domain, i.e. radio to gamma-ray band.

◇ **Pulsars;** These compact objects are the remaining core of a massive star that underwent supernova. Due to the conservation of angular momentum and magnetic field density the neutron star is rapidly spinning and exhibits very high magnetic fields.

- ◇ **Pulsar Wind Nebula (PWN);** When a gas nebula (or generic ISM) is located in proximity to a pulsar, VHE photons can be generated through IC scattering. One of the most relevant objects for VHE astronomy is the Crab Nebula.

- ◇ **Gamma-Ray Binaries;** Constitute a bound binary system that is composed of a massive star and a compact object of degenerate stellar matter, e.g. neutron star (NS) or black hole (BH). Accreting stellar mass from the companion, the compact object accumulates bulk amounts of matter that lead to conditions prone for gamma ray emission.

Extragalactic Objects:

- ◇ **AGNs;** They are among the most energetic sources hosted in our Universe. It is not uncommon that the region surrounding the nucleus outshines the remaining galaxy. Since transient phenomena related to this source class are among the main topics of the thesis at hand, the discussion of this source class type will be postponed to Section 3.1.

- ◇ **Starburst galaxies;** Galaxies with high star formation rate, hence with increased rates for SN explosion and CR density.

- ◇ **GRB;** Flares detected on a daily basis that last from a fractions of seconds to a few seconds. Studying the fluctuations in the burst durations allowed to define a measure that looks at the median timescale in which 90% of the total flux was collected, coined as the T_{90} statistic. Upon plotting a histogram of T_{90} a double peak structure is revealed (see Figure 2.7). Based on the flux evolution of the underlying GRB event one distinguishes them by assigning them to two classes: Long- (LGRB) and Short-type (SGRB). This classification is motivated in the sense that the host galaxies in which these pheonomena manifest have different characterization. This in turn leads to a hypothesis of separate progenitor populations. Since transient phenomena related to GRBs are among the main topics of the thesis at hand, a further discussion of this source class will be postponed to Sections 3.2, 3.3.

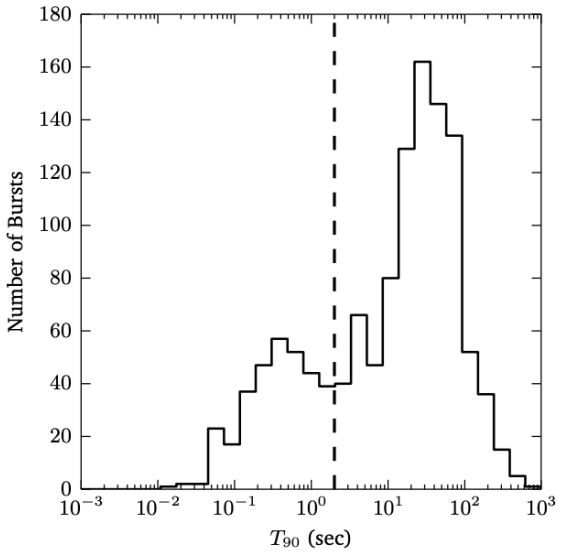

Figure 2.7: Histogram showing the distribution of the T_{90} statistic. It reveals the presence of two separate distributions, whose peaks are separated by ∼2 seconds. Image Credit: Urban (2016)

2.2.4 Limitations to Gamma-Ray Astronomy

Back in Section 2.1.3 we learned that CRs are not particularly useful to pinpoint the sites of CR acceleration due to their deflection by magnetic fields. Even though the uncharged photon seems a rich source of information, it comes with its own limitations. Astronomies that are performed in the classical EM domain, e.g. radio up to gamma-band, experience the disadvantage that their messenger particles are absorbed by matter and radiation fields. On one hand, this allows the observer to study the environment surrounding a source as well as the ISM between the source and the observer along the line of sight. However, this generally limits the attainable information to surface properties of the astronomical objects one intends to study. In the case of gamma-ray astronomy, an additional complication arises for photons that travel over large distances and undergo attenuation due to interactions with background photon fields that are summed along the history of the Universe.

Propagation of VHE Gamma-Ray Photons Photon-photon collisions are capable of producing electron-positron pairs, also known as "Breit-Wheeler" pair production:

$$\gamma + \gamma \rightarrow e^+ + e^- \tag{2.11}$$

Since the Universe is not opaque to photons in the HE-VHE regime, these are strongly affected by the Extragalactic Background Light (EBL). This significantly impairs the propagation of gamma rays and thus establishing sort of a gamma horizon (see also Figure 2.8) thus effectively limiting the reach of TeV astronomy:

$$\gamma_{TeV} + \gamma_{EBL} \rightarrow e^+ + e^- \tag{2.12}$$

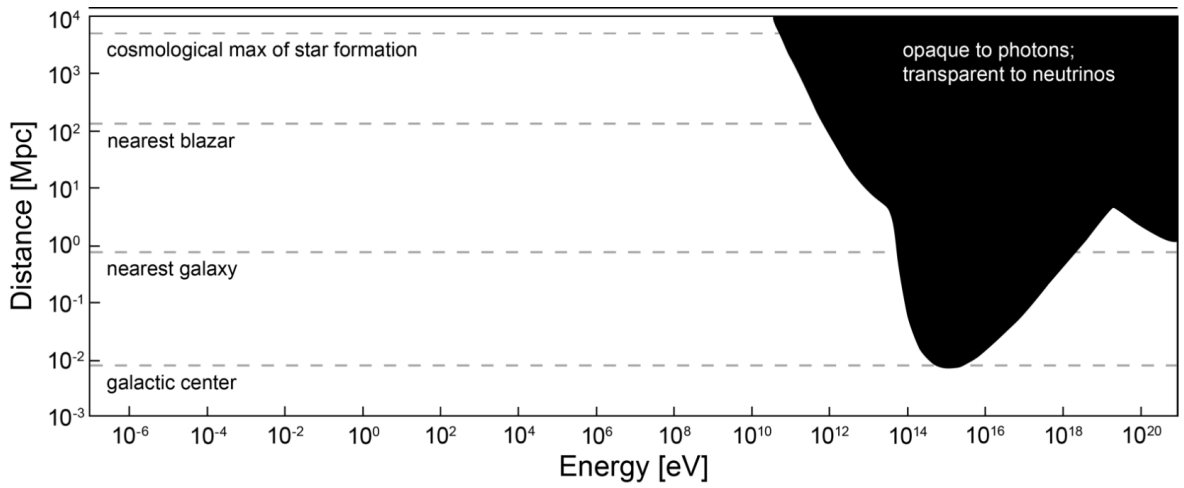

Figure 2.8: Qualitative energy and distance dependency of the opaqueness of our Universe to photons. The opaqueness of the Universe to a given gamma-ray is strongly dependent on its energy and the distance it has to travel in order to be observed. Image Credit: Adapted from the IceCube Collaboration

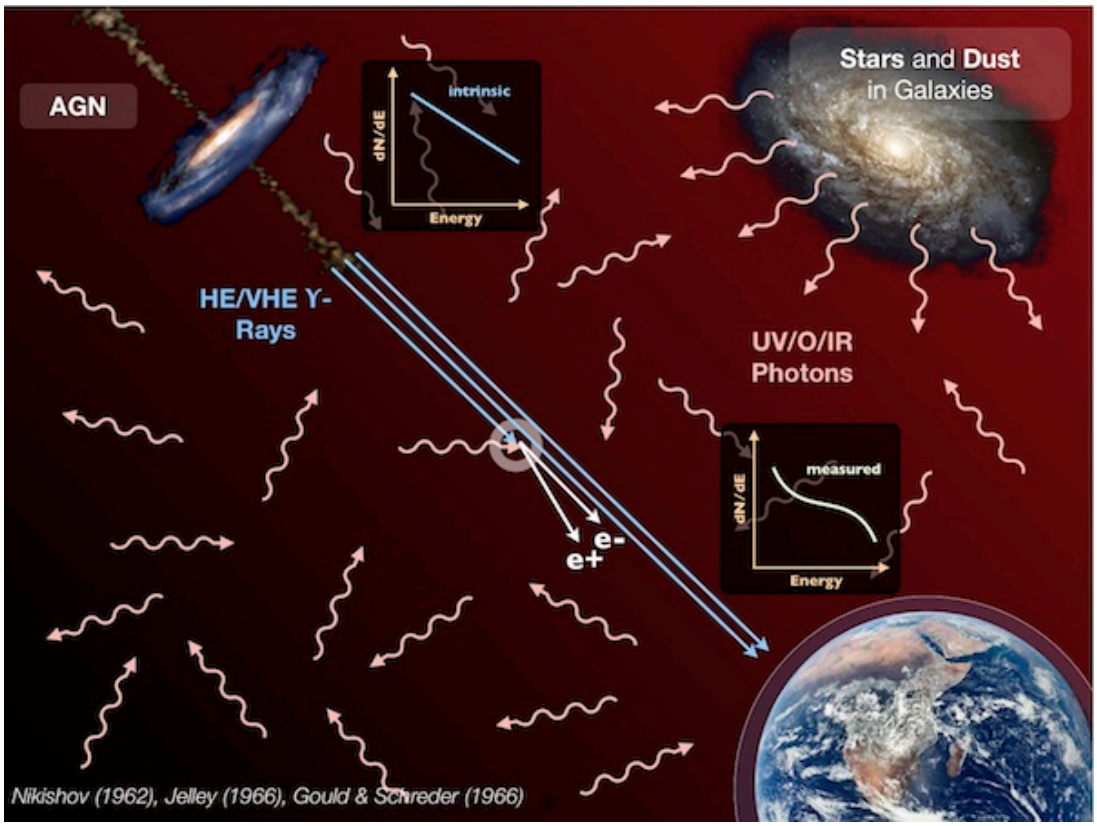

Figure 2.9: Attenuation of gamma-rays by EBL photons. Image Credit: Martin Raue 2011

Since the EBL impairs a correct measurement of the SED from a given source, one has to account for it in

order to derive the intrinsic source parameters (see also Figure 2.9). Due to its faint nature, obtaining an estimation of the EBL is hardly attainable by means of direct measurements in the different wavelength regimes. However, using combined results from various indirect measurements (such as studies of TeV emitters) allowed astronomers to establish a set of viable EBL models that are estimating the star formation history and AGN evolution in order to quantify for EBL attenuation at different epochs.

2.3 Neutrino Astronomy

The use of neutrinos as messenger particles in order to perform astronomy remains a fairly new and difficult task. Due to their very small cross-section, their role as cosmic messengers can not be overstated as they are capable of leaving their production site without undergoing any alterations. This in turn allows you to obtain direct information from the core region of a cosmic accelerator, unlike the case of gamma rays which suffer absorption along their propagation. Once again we have to understand their connection to CRs and the mechanisms that are able to generate these highly energetic neutrinos.

2.3.1 High-Energy Neutrino Generation via collisional Cosmic-Ray Processes

There are several processes from which one expects neutrinos to be produced, but when it comes to neutrino production through collisional processes involving CR the main processes are:

- **GZK Neutrinos:** Neutrino emission can be expected by hadronic mechanisms, such as the previously discussed GZK cutoff from proton-γ collisions:

$$p + \gamma \to \Delta^+ \to \begin{cases} p + \pi^0 & \textbf{with branching ratio } \sim 2/3 \\ n + \pi^+ & \textbf{with branching ratio } \sim 1/3 \end{cases} \tag{2.13}$$

  The intermediary pions will eventually lead to neutrinos emission (see equation 2.15 below).

- **Astrophysical Neutrinos:** There is a similar contribution expected from proton-proton collisions (or heavier nuclei):

$$p + p \to \Delta \to \begin{cases} p + p + \pi^0 & \textbf{with branching ratio } \sim 2/3 \\ p + n + \pi^+ & \textbf{with branching ratio } \sim 1/3 \end{cases} \tag{2.14}$$

  The intermediary pions will eventually lead to neutrinos emission (see equation 2.15 below).

- **Atmospheric Neutrinos:** Generated from CR interactions with molecules in the atmosphere (similar to equation 2.14 above) that lead to cascades of subatomic particles.

The intermediary charged pion species produced in these interactions eventually decay accordingly:

$$\begin{aligned} \pi^+ \to \mu^+ + \nu_\mu \to e^+ + \nu_e + \bar{\nu}_\mu + \nu_\mu & \quad \textbf{with branching ratio } > 99.9\% \\ \pi^- \to \mu^- + \bar{\nu}_\mu \to e^- + \bar{\nu}_e + \bar{\nu}_\mu + \nu_\mu & \quad \textbf{with branching ratio } > 99.9\% \\ \pi^0 \to \gamma + \gamma & \quad \textbf{with branching ratio } > 99\% \end{aligned} \tag{2.15}$$

One important take away from these mechanisms is that VHE gamma rays that are generated through hadronic collision processes are necessarily accompanied by high energetic neutrinos emission. As we learned, photons are affected both by matter and radiation fields, i.e. optically thick sources and EBL absorption, hence undergo substantial attenuation upon reaching the observer on Earth.

2.3.2 Detection Techniques for Neutrino Astronomy

Early attempts to design neutrino detectors aimed at leveraging the kinematics of the inverse beta decay in order to deduce the presence of a neutrino species by means of radiochemical or scintillator methods that rely on the following process for detection:

$$\bar{\nu}_e + p \rightarrow e^+ + n \tag{2.16}$$

Since these methods did not allow for a reconstruction of directional information from the neutrinos and were sensitive to energies around ∼MeV, their potential to perform neutrino astronomy was limited. Nevertheless, the findings from these pathfinder experiments confirm the possibility to detect neutrinos from astrophysical origin. Hence, the potential impact that neutrino astronomy could have on our understanding of the Universe can not be overstated.

Cerenkov Radiation Method Upon adopting the Cerenkov radiation method, one can take advantage of the presence of charged particles that result from neutrino-matter interactions. Since these charged particles generate Cerenkov radiation along their trajectory one can design experiments that gather these Cerenkov photons and based on their properties can deduce the direction of the charged particle as well as obtain an estimate of its energy. Depending on the experimental design this then allows the reconstruction of the properties of the initial neutrino. Thanks to the feasibility of this approach one can use large volumes of a transparent medium in order to detect Cerenkov photons by using devices such as PMTs. These media can range from liquid water (Kamiokande, KM3NeT) to glacial ice (IceCube, Baikal).

- ◇ **Pioneer Experiments;** Upon proposing the use of bulk volumes of natural media the use of the Cerenkov radiation method was pioneered by a variety of experiments such as the DUMAND, AMANDA, ANTARES, and Lake Baikal neutrino experiment.

- ◇ **IceCube Observatory;** The IceCube neutrino observatory is located at the South Pole and is currently the main player in neutrino astronomy (see also Figure 2.10). Its detector medium is made up of a cubic kilometer of transparent ice, in which 5160 Digital Optical Modules are attached on 86 strings that are placed on a hexagonal grid of 125m horizontal spacing. Benefiting from an additional air shower array that is built on top of the detector, denoted IceTop, there exists an additional CR detector as well as an effective veto system for atmospheric muon and neutrino events that are initialized by CR interactions within the atmosphere of the southern sky.

- ◇ **Future Observatories;** future facilities that are also based on the Cerenkov radiation technique are planned to become operational in the near term and will be built in the northern hemisphere using liquid water as detector medium, e.g. KM3NeT.

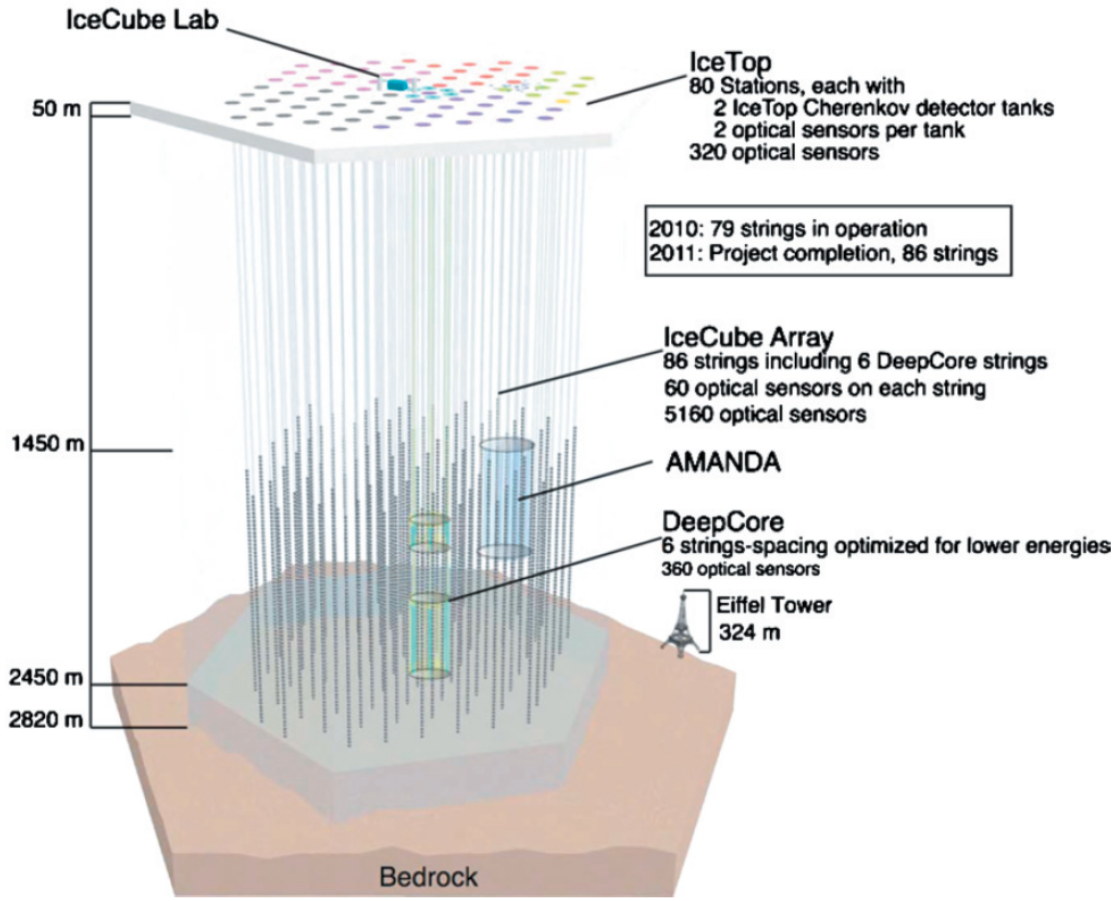

Figure 2.10: Experimental setup of the IceCube observatory at the South Pole. Image Credit: IceCube Collaboration

2.3.3 Astrophysical Neutrino Sources

Unlike for charged CRs, where we were limited to imagining potential sources that might accelerate these messengers to high energies, with neutrinos we have a messenger that points right back at its origin. In the following I briefly outline the known neutrino sources:

- ◇ **Stellar Neutrinos:** from our own Sun.
- ◇ **Supernova Neutrinos:** generated during the collapse of a massive star, i.e. SN1987A which occurred in the nearby Large Magellanic Cloud (Goldman et al.; 1988).
- ◇ **High-Energy Extragalactic Neutrinos:**
  - **TXS 0506+056 and IC-170922A;** The reconstructed direction of the high energy neutrino event that was detected by IceCube on the 22nd of September 2017 was found to be consistent with the location of the blazar TXS 0506+056 (Ansoldi et al.; 2018). This in turn triggered

MWL follow-up observations by 14 observatories across the EM domain. Both *Fermi*-LAT and the MAGIC telescopes found the blazar in a flaring state at HE and VHE respectively. The observation of VHE gamma performed by the MAGIC telescopes was groundbreaking since it confirmed that the jets of AGNs might be sites where one could expect hadronic processes, thus constituting AGNs as excellent laboratories for MM studies. This event made a significant impact to the astronomical community and marks together with the GRB170817A /GW170817 association a cornerstone for MM efforts.

- **NGC 1068:** Combining 10 years of IceCube muon neutrino data, the Seyfert-II-type galaxy corresponds to its most significant detection, which also coincides with the hotspot in the all-sky scan of the IceCube observatory (Collaboration*† et al.; 2022).

2.3.4 Limitations to Neutrino Astronomy

The small cross-section that makes neutrinos such valuable messengers for dense regions of space is what at the same time renders their detection such a difficult task and explain why so few sources were identifies to this day. When using the Cerenkov radiation method to detect these messengers a further complication arises from the extensive muon background that stems from showers initiated by CRs. This background can trigger signals in the detector which could be misinterpreted for actual neutrino signals (there are $\sim 10^6$ atmospheric muon events for each astrophysical neutrino event). One way to overcome this immense background is to operate the IceCube as a downward-looking telescope. This allows to use the Earth as a muon shield and therefore the events that generate an upgoing track must stem from neutrinos that traversed the Earth. Since IceCube operates at the South Pole its monitoring capabilities is limited to the northern northern hemisphere. However, once the BAIKAl and KM3NeT observatories become operational this will be an issue from the past.

2.4 Gravitational Wave Astronomy

The use of GWs as messengers in order to study the Universe constitutes the most recent window that was opened to perform astronomy. After three successful observing runs with ever-increasing detection rates, the prospects for future runs are very promising. Furthermore, with the imminent incorporation of a fourth interferometer, the MM community is excited about the upcoming findings of the upcoming fourth observation run dubbed O4.

2.4.1 Gravitational Wave Generation from Cosmic Sources

GWs are produced by any given mass that undergoes acceleration processes that include orbiting and spinning objects. Depending on the characteristics of the underlying system, e.g. the involved masses and orbital velocities as well as spin, therein generated GWs can attain large enough amplitudes in order to be detectable in certain frequency ranges covered by the currently deployed instrumentation. For our use, we focus on the lower scales, i.e. frequencies in the range $10^{-4} - 10^4$ Hz, which are expected to be caused by CBCs (see also Figure 2.11). These events tend to occur in systems composed of two compact objects that are composed of degenerate star matter, namely BHs and NSs.

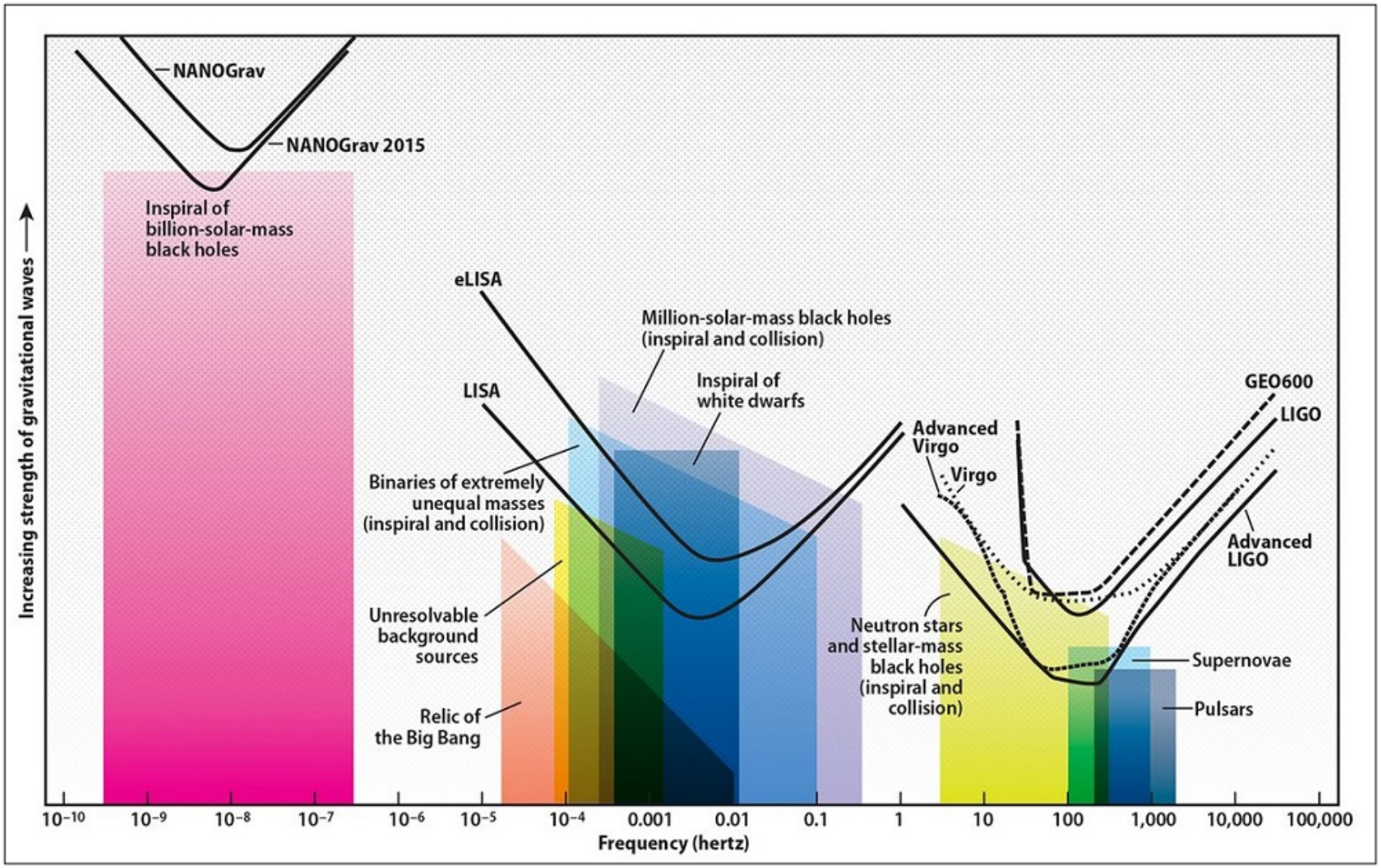

Figure 2.11: Frequency range and sensitivities of current and future GWs detectors for given progenitors. Image credit: (Moore et al.; 2014)

As we will see in Section 2.4.3, CBCs were successfully detected in large numbers, and their potential to be detectable in the EM domain as well, renders them prime targets for MM efforts. Nevertheless, for completeness there are also other potential sources of GWs that might be detectable by adopting novel detection designs and commissioning future detector technologies:

- ◇ **Stochastic GW:** relic signals from the early stages of the Universe.
- ◇ **Burst GW:** generated when SN explode asymmetrically
- ◇ **Continuous GW:** from spinning NS

2.4.2 Detection Techniques for Gravitational Wave Astronomy

Initial attempts to detect GWs were pioneered in the 1960s by J. Weber and the bar detector design. Whilst several detector systems were elaborated in the following decades, eventually, the "bar" design was replaced by a design that was derived from the interferometric technique having its origins in the late 19th century, namely the Michelson-Morley experiment.

Interferometric Technique Although the first experimental design was proposed in the 1960s, only with today's technology they are sensitive enough in order to detect the small amplitudes of signals from astrophysical origin. Whilst there were many steps and sophisticated methodologies implemented in order to attain the sensitivity of nowadays operating laser-powered GW interferometers, their core design remains a modified version of the Michelson interferometer. The working principle of this optical instrument is based on the phenomenon of interference. Therein two waves of light overlap and thereafter generate interference patterns that can be observed. This in turn allows measuring small differences in the lengths of paths of light. With respect to the intricacies of the GW use case, the inclined reader is referred to the literature for more details. In the following I provide a list of the current and future laser-powered interferometers that are used for detecting GWs:

- ◇ **LIGO and Virgo Detectors;** establish the current LIGO–Virgo Collaboration (LVC) constituting of the advanced LIGO (Aasi et al. 2015) and advanced Virgo (Acernese et al. 2014) interferometers. Note that in order to reduce the impact of geological perturbations interferometers must be spatially separated also allowing better localization of GW signals.
- ◇ **KAGRA;** employs a novel cryogenic design in order to reduce the background.
- ◇ **Next Generation Detectors;** mitigate limitations of the current design by introducing new experimental set-ups.
  - **Einstein Telescope;** adopting a triangular shape, one reduces the blind spots of the currently adopted L-shaped design. Containing three nested detectors that share three 10 km arms will constitute both a high-frequency and low-frequency interferometer, thus improving the sensitivity for CBCs at both ends of the frequency spectrum.
  - **Cosmic Explorer;** based on the currently adopted L-shaped design, the Cosmic Explorer will follow the lessons from the current 2nd generation detectors but have arms of 40 km, and therefore be more sensitive in the high-frequency range.

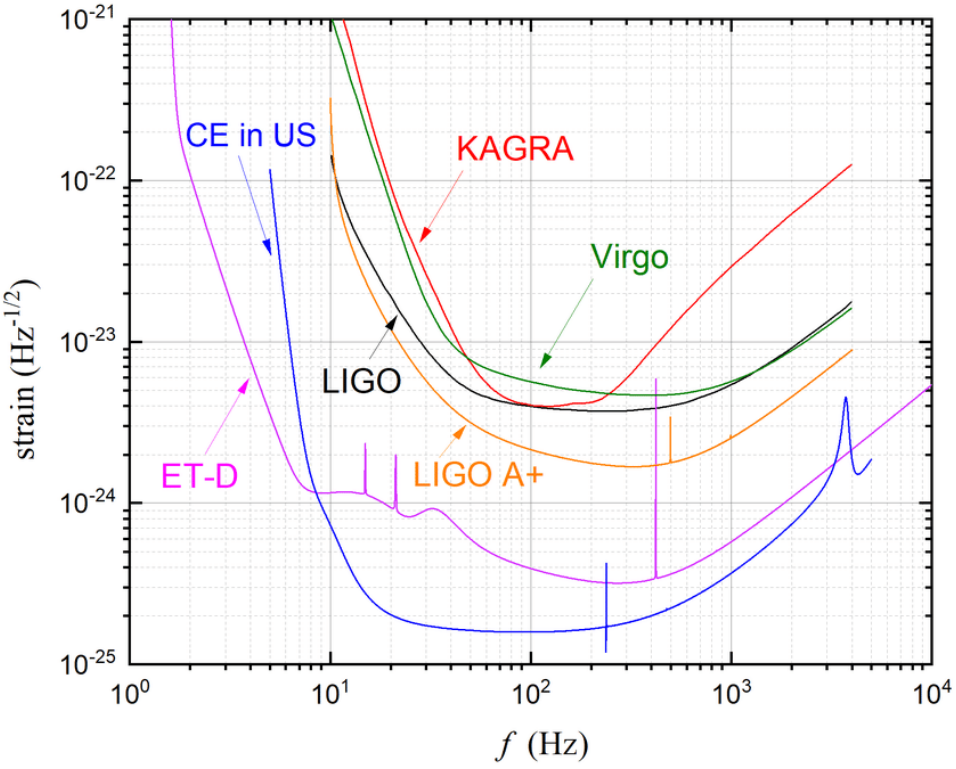

Figure 2.12: Operational frequency ranges for current and next generation GW interferometers. Image Credit: (Wang et al.; 2020)

2.4.3 Astrophysical Gravitational Wave Sources

In the following, I outline the currently experimentally verified GW sources. Discussion on their transient phenomena will be postponed to the upcoming chapter (see also Section 3.3).

- ◇ **PSR 1913+16:** This binary system composed of a pulsar and neutron star was for $\sim$ 100 years the sole experimental verification (albeit indirect) of the GWs predicted by Einstein's theory of General Relativity.

- ◇ **CBC Catalogs:** After three successful observing runs, the LIGO and Virgo interferometers managed to amass extensive catalogs of GW events. In these catalogs, they report on the binary system parameters for a total of 93 confident detections. Only for the case of a single NS-NS system (GW170817) there was a co-detection in the EM domain (GRB170817A). This co-detection inspired a growing effort in the MM community to use triggers from GW sub-threshold event catalogs in order to search for spatio-temporal coincidences in archival datasets of instruments operating in the EM domain.

2.4.4 Limitations to Gravitational Wave Astronomy

From an experimental point of view there are certain limitations to GW astronomy. Since the localization of sources that generate GW is characterized by large uncertainty (errors attributed to localization regions that for Ligo-Virgo are usually in the range of ∼20–1000 deg^2 Abbott et al. (2020)) the most significant limitations can associated to the difficulty of following-up on GW events. Additionally, but mostly attributed to limitations due to technical capabilities of the currently operating ground-based interferometers, for now, astronomers are only sensitive to a narrow frequency range that encompasses binary systems that are at close cosmological distances, i.e. distances of less than 200 Mpc. Once the next-generation instruments and space-based satellite systems will be online these distance and frequency limitations could be mitigated with improved technology.

2.5 Lessons to be learned from the different Messengers

As we have learned in the previous sections, each of the four messengers could in principle be used to deduce information about conditions and processes that occur in highly energetic environments (see Table 2.3). Such locations include regions around Supermassive Black Hole (SMBH), compact binaries as well as stellar evolution.

Table 2.3: Lessons to be learned from observing the different messengers.

Messenger	from Source	from Universe	from Fundamental Physics	new Physics
γ	Generation & Environment	EBL	LIV	DM & ALPs
ν	Generation & Thermodynamics	CνB	SM	-
GW	Dynamics & Mass	H_0	LIV	-
CR	Environment	CMB	LIV	DM

Lorentz Invariance Violation (LIV), Cosmic Neutrino Background (CνB),
Hubble Constant (H_0), Dark Matter (DM), Axion-like particles (ALPs)

Note from the latter two columns in Table 2.3, that each of the messengers also carries information that could be beneficial for studying the history of the Universe as well as some of the most fundamental questions at the frontiers of our current theoretical understanding. In order to elaborate on the innate synergies between the different messenger populations, it's worth taking into account a set of distinguished sources (see also Table 2.4). Their common denominator is that in recent times they proved to be promising targets for performing MM campaigns, e.g. TXS 0506+056, GW170817 and SN1987a.

Table 2.4: Distinguished set of progenitor systems for transient astrophysical phenomena.

Transient Astrophysical Source	EM (γ)	CR	ν	GW	Examples
Active Galactic Nuclei	yes	yes	yes	no	TXS 0506+056
Compact Binary Coalesence	yes	?	?	yes	GW170817
Core Colapse SN	yes ($\sim$ years?)	$\sim$ years?	yes	yes*	SN1987a

$*$ for sufficient spherical asymmetry

As we will see in the next chapter, combining information from the different cosmic messengers will be instrumental for our understanding of short-lived transient astrophysical phenomena, such as SN, CBC, Core-Colapse-SN (CCSN) (see also Chapter 3). Note that there are additional source classes that could in principle also be of interest to the MM community, e.g. X-ray Binaries, FRBs, TDEs and others. However, for the work at hand, we will restrain ourselves to discuss messenger pairs that in recent follow-up efforts yielded scientific results. Also given the frame of the work at hand, its focus will lie on the synergies between gamma-rays, neutrinos, and GWs.

Bibliography

Aartsen, M., Ackermann, M., Adams, J., Aguilar, J. A., Ahlers, M., Ahrens, M., Altmann, D., Andeen, K., Anderson, T., Ansseau, I. et al. (2018). Astrophysical neutrinos and cosmic rays observed by icecube, *Advances in Space Research* **62**(10): 2902–2930.

Aasi, J., Abbott, B., Abbott, R., Abbott, T., Abernathy, M., Ackley, K., Adams, C., Adams, T., Addesso, P., Adhikari, R. et al. (2015). Advanced ligo, *Classical and quantum gravity* **32**(7): 074001.

Abbott, B. P., Abbott, R., Abbott, T., Acernese, F., Ackley, K., Adams, C., Adams, T., Addesso, P., Adhikari, R., Adya, V. et al. (2017). Gravitational waves and gamma-rays from a binary neutron star merger: Gw170817 and grb 170817a, *The Astrophysical Journal Letters* **848**(2): L13.

Abbott et al. (2020). Prospects for observing and localizing gravitational-wave transients with advanced ligo, advanced virgo and kagra, *Living reviews in relativity* **23**(1): 1–69.

Acernese, F. a., Agathos, M., Agatsuma, K., Aisa, D., Allemandou, N., Allocca, A., Amarni, J., Astone, P., Balestri, G., Ballardin, G. et al. (2014). Advanced virgo: a second-generation interferometric gravitational wave detector, *Classical and Quantum Gravity* **32**(2): 024001.

Aharonian, F. A. (2004). *Very High Energy Cosmic Gamma Radiation Physics*, World Scientific Publishing Company.

Aleksić, J., Ansoldi, S., Antonelli, L. A., Antoranz, P., Babic, A., Bangale, P., Barceló, M., Barrio, J., González, J. B., Bednarek, W. et al. (2016). The major upgrade of the magic telescopes, part ii: A performance study using observations of the crab nebula, *Astroparticle Physics* **72**: 76–94.

Angelis, A. D. and Pimenta, M. (2018). *Introduction to Astroparticle Physics*, Springer.

Ansoldi, S., Antonelli, L. A., Arcaro, C., Baack, D., Babić, A., Banerjee, B., Bangale, P., De Almeida, U. B., Barrio, J. A., González, J. B. et al. (2018). The blazar txs 0506+ 056 associated with a high-energy neutrino: insights into extragalactic jets and cosmic-ray acceleration, *The Astrophysical Journal Letters* **863**(1): L10.

Atwood, W., Abdo, A. A., Ackermann, M., Althouse, W., Anderson, B., Axelsson, M., Baldini, L., Ballet, J., Band, D., Barbiellini, G. et al. (2009). The large area telescope on the fermi gamma-ray space telescope mission, *ApJ* **697**(2): 1071.

Blümer, J., Engel, R. and Hörandel, J. R. (2009). Cosmic rays from the knee to the highest energies, *Progress in Particle and Nuclear Physics* **63**(2): 293–338.

Collaboration, P. A., Aab, A., Abreu, P., Aglietta, M., Al Samarai, I., Albuquerque, I., Allekotte, I., Almela, A., Alvarez Castillo, J., Alvarez-Muñiz, J. et al. (2017). Observation of a large-scale anisotropy in the arrival directions of cosmic rays above 8× 1018 ev, *Science* **357**(6357): 1266–1270.

Collaboration*†, I., Abbasi, R., Ackermann, M., Adams, J., Aguilar, J., Ahlers, M., Ahrens, M., Alameddine, J., Alispach, C., Alves Jr, A. et al. (2022). Evidence for neutrino emission from the nearby active galaxy ngc 1068, *Science* **378**(6619): 538–543.

Erdoğdu, P., Huchra, J. P., Lahav, O., Colless, M., Cutri, R. M., Falco, E., George, T., Jarrett, T., Jones, D. H., Kochanek, C. S. et al. (2006). The dipole anisotropy of the 2 micron all-sky redshift survey, *Monthly Notices of the Royal Astronomical Society* **368**(4): 1515–1526.

Goldman, I., Aharonov, Y., Alexander, G. and Nussinov, S. (1988). Implications of the supernova sn1987a neutrino signals, *Physical review letters* **60**(18): 1789.

Grupen, C. (2005). *Astroparticle Physics*, Springer.

Longair, M. S. (1992). *Astrophysics*, Cambridge University Press.

Lopez-Coto, R., Moralejo, A., Artero, M., Baquero, A., Bernardos, M., Contreras, J., Di Pierro, F., García, E., Kerszberg, D., López-Moya, M. et al. (2021). Physics performance of the large-sized telescope prototype of the cherenkov telescope array, *arXiv preprint arXiv:2109.03515* .

Meegan, C., Lichti, G., Bhat, P., Bissaldi, E., Briggs, M. S., Connaughton, V., Diehl, R., Fishman, G., Greiner, J., Hoover, A. S. et al. (2009). The fermi gamma-ray burst monitor, *The Astrophysical Journal* **702**(1): 791.

Moore, C. J., Cole, R. H. and Berry, C. P. (2014). Gravitational-wave sensitivity curves, *Classical and Quantum Gravity* **32**(1): 015014.

Thompson, D. J. and Wilson-Hodge, C. A. (2022). Fermi gamma-ray space telescope, *Handbook of X-ray and Gamma-ray Astrophysics* .

Urban, A. L. (2016). *Monsters in the dark: High energy signatures of black hole formation with multi-messenger astronomy*, PhD thesis, The University of Wisconsin-Milwaukee.

Wang, B., Zhu, Z., Li, A. and Zhao, W. (2020). Comprehensive analysis of the tidal effect in gravitational waves and implication for cosmology, *The Astrophysical Journal Supplement Series* **250**: 6.

CHAPTER 3

TRANSIENT ASTROPHYSICAL PHENOMENA

Resume: Aiming to introduce the reader to transient astrophyiscal phenomena that are commonly studied in the framework of time-domain astronomy.

Contents

As seen in the previous chapter the Universe provides us with natural laboratories that are capable to produce various fundamental particles and signals (see also Table 2.4). Since therein conditions are not reproducible on Earth, e.g. density, temperature and magnetic fields, we are limited to hold the role of a passive observer that needs to understand the environmental settings in order to deduce the implications for the various science topics they allow us to study (see also Table 2.3). Nevertheless, studying the respective signatures and rates of these messengers allows gathering information about their acceleration sites, therein processes and the medium within they are propagating.

One of the most puzzling (and exciting) laboratories constitutes the so-called transient phenomena. Therein short-lived astrophysical phenomena manifest themselves at unpredictable times and seemingly arbitrary positions (although they are usually found in association with AGNs, compact binaries, and stellar evolution amongst others). Hence, since one can usually not predict when and where these events happen, attempting observations on them is very challenging and comes with a high risk-reward ratio. As discussed in the previous chapter (see also Table 2.4), these source classes exhibit connections between the different messenger particles. Hence by operating various observatories in synergy, the MM approach would allow to react to short-lived phenomena, therefore optimize the efficiency of triggering follow-up observations in the EM domain. While for the mentioned source classes there remain many open questions regarding their inner working and potential to be progenitor systems for transient phenomena, recent advances and co-detection in MM astronomy have brought optimism when it comes to answering them in the near future.

Going through this chapter, we will start by discussing AGNs (Section 3.1), for which we will discuss phenomenology and blazar subclass, in depth, as well as elaborating on a crucial link between neutrino and photon messengers. We then discuss CCSN (Section 3.2) and stellar mass compact object binaries (Section 3.3), for which after discussing their respective phenomenology we will elaborate on their connections to the two known GRB populations. We close this chapter with a brief discussion of a few other transient phenomena that are not targets for the studies at hand but also constitute interesting objects/phenomena (Section 3.4).

3.1 Active Galactic Nuclei

SMBH ($M > 10^5 M_\odot$), that are located in the core region of galaxies can, through matter accretion, lead to luminosities beyond typical star counts of their host galaxy (10^{42} to 10^{49} erg s^{-1}). These sources ($\sim 1\%$ of galaxies) are denoted as Active Galactic Nuclei (AGN). The broadband EM emission of these objects shows significant temporal variability ($\sim$ days and even up to minutes) and can reach up to the VHE gamma-ray regime. As one of the most numerous extragalactic sources detected at VHE, they significantly contribute to the energy budget of the Universe. Strong emission lines as well as continuum emission, that are detectable by various instruments operating in the EM domain, render these galaxies of interest for the general astronomical community.

3.1.1 Phenomenology and Unification Scheme

Even though the observational phenomenology of AGNs is quite rich, it can be boiled down to the following building blocks:

- ◇ **Super Massive Black Hole:** in the mass region of $10^3 M_\odot < M < 10^{10} M_\odot$, constituting the central engine that converts part of the potential energy from infalling matter into kinetic energy that power jet formation and emissions in general.
- ◇ **Accretion Disk:** formed by matter that is falling into the BH and is confined to a rotating accretion disk due to the conservation of its angular momentum. Depending on the accretion rate the physical state of the disk varies, e.g. thickness and opaqueness.
- ◇ **Jets:** powered by collimated plasma flows that shoot out at relativistic speeds perpendicular to the accretion disk and eject ultra-relativistic particles. Generally considered as one of the most powerful accelerators of CRs, these structures are present in $\sim 10\%$ of AGNs and can extend several kpc in distance. Therein shock acceleration and non-thermal processes, allow for generation of highly variable emissions (with measured variations on the timescale of minutes) over the entire EM domain.
- ◇ **Torus:** formed around the accretion disk, effectively obscuring the optical photons that are absorbed by the dust molecules and re-emited at IR and radio wavelengths.

Even though AGNs are all constituted of the same building blocks, they exhibit an astonishing diversity when it comes to observational phenomenology. Due to the large variety of spectral characteristics and temporal behaviours, AGNs are considered an inhomogeneous source class. Nevertheless, adopting the idea that the different sub-classes could be simply explained by different viewing angles (as depicted schematically in Figure 3.1) introduced a major paradigm shift in their understanding (Urry and Padovani, 1995).

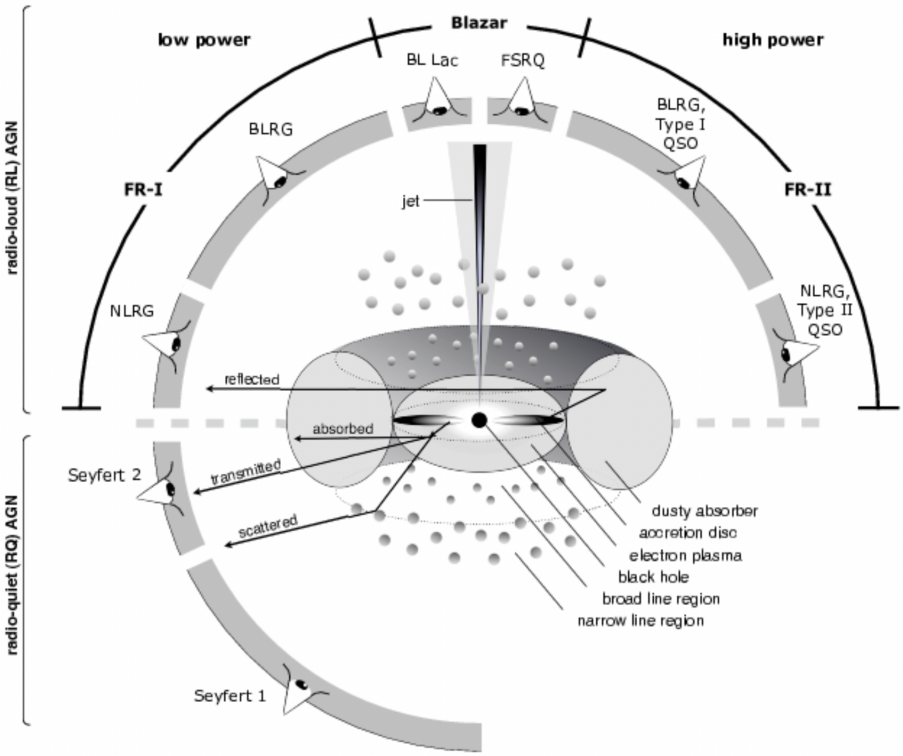

Figure 3.1: Unification of AGNs based on angle of view relative to the jet. Image Credit: (Beckmann and Shrader; 2013)

3.1.2 Blazar-like AGN Types

Blazars account for a particular subclass of AGNs, that are classified according to the observer's viewing angle onto their prominent jet. In blazars the jet axis is typically very closely aligned with the observer line of sight, leading to the non-thermal radiation originating from the jet often outshining the entire host galaxy. Therefore, this feature usually dominates the spectra over the entire EM domain, i.e. from radio up to the VHE band. The SEDs of blazars show a generic two-bump structure (see Figure 3.2), with the prior (also denoted as synchrotron bump) peaking between IR and X-ray frequencies whilst the latter does beyond the X-ray band (Ghisellini et al.; 2017). Based on optical emission line characteristics, a further sub-classification of the underlying blazar-like AGNs gives rise to a more refined classification:

- ◇ **FSRQ:** Strong emission lines accompanied by strong EM emission at optical/UV regime due to accretion processes close to the SMBH. Their SED is characterized by a low-energy bump that peaks at optical/IR wavelengths (see blue curve in Figure 3.2).
- ◇ **BL Lac:** No or weak presence of emission lines and commonly fainter than FSRQs but exhibiting SEDs with low energy bumps peaking at higher energies (up to the X-ray band). BL Lac objects are usually further classified based on the peak frequency of their lower energy synchrotron peak: low synchrotron peaked; $\nu_{syn} < 10^{14}$ Hz), intermediate synchrotron peaked; $10^{14} < \nu_{syn} < 10^{15}$ Hz

and high synchrotron peaked; $\nu_{syn} > 10^{15}$ Hz.

In theory, the extreme environments prevalent in these jets can power shock-accelearation of CRs. Thereafter these undergo hadronic collisional processes that through pion decay eventually can lead to significant fluxes in both neutrinos and gamma rays expected to exhibit similarities in their respective spectra.

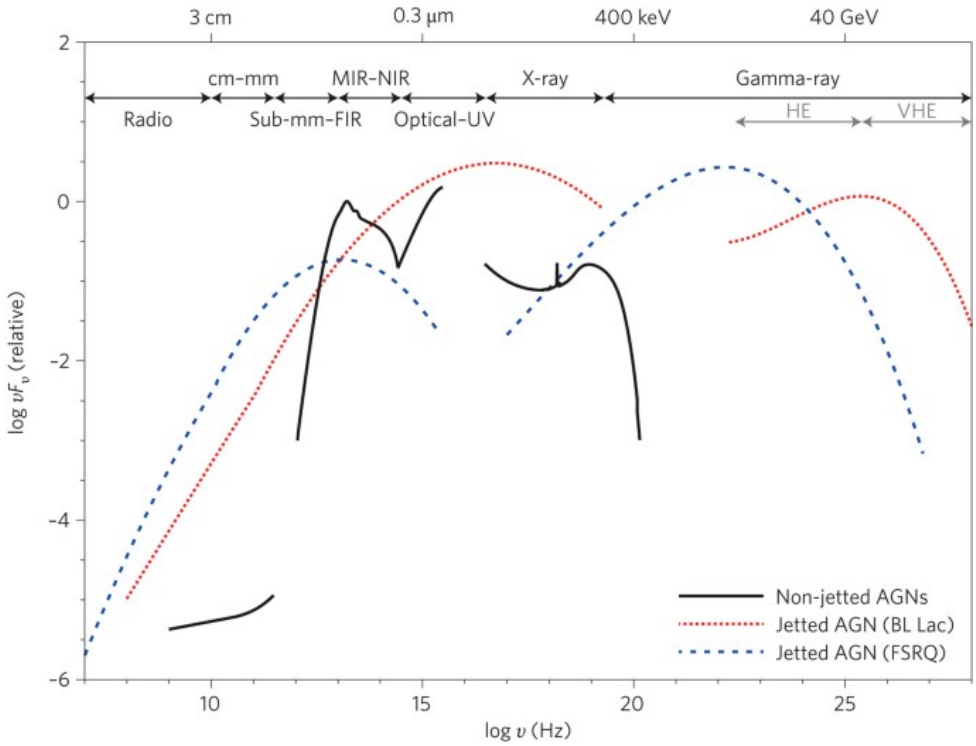

Figure 3.2: Expected SED measurements from different kinds of AGNs. Image Credit: (Padovani et al.; 2017)

3.1.3 Open Questions and Prospects for MM Astronomy

Open Questions Astronomers spent many decades theorising about the mechanism of jet formation, as well as performing observation campaigns that use instruments over the entire EM domain in order to attempt to answer what emission mechanisms prevail in AGNs and their jets. From a theoretical point of view, it was quite early understood that there were in principle simple mechanisms to extract energy from a BH (Penrose and Floyd; 1971; Blandford and Znajek; 1977). Nevertheless, despite extensive study of these jets, their formation and processes within remain active frontiers of contemporaneous research, and thus highly relevant for the MM astronomy approach. The detection of either CRs or neutrinos from structures associated to the jets would be a smoking gun for ongoing hadronic processes. This would allow to understand environmental conditions close to the SMBH and within the jets, which in turn could bolster our understanding of their respective composition and dynamical processes within.

Prospects for MM Astronomy

Neutrino and Gamma-ray Connection With the advent of the IceCube Neutrino Observatory, the successful detection of high-energy neutrinos indicates that these messengers can originate in stem from astrophysical sources and are hence of cosmic origin. Nevertheless, the identity of the principal hosts remain a mystery as of today. However, thanks to significant progress in the development and performance of neutrino observatories as well as synergies with observatories in the EM domain, astronomers are closing in on evidence for particle acceleration scenarios in AGNs.

One possible approach to pinpoint the accelerations sites of likely host environments, encompasses the swift coverage of neutrino triggers with observations carried out in the broader EM domain. Whilst for optical instruments one would benefit from large FoVs, focusing on VHE gamma rays one has the clear benefits from related production channels that involve hadronic interactions of cosmic rays. Originating from a common parental particle, the spectra of both gamma-rays and neutrino should exhibit similar shape and normalization. These similarities could be leveraged in future efforts to deduce characteristic of the host environments, constraints of hadronic emission models as well as obtain distance estimates of the involved host galaxies. This can be understood in the sense that whilst neutrinos can travel cosmic distances through dense environments without experiencing significant attenuation, this does not hold for gamma-rays. On their trajectory, the highest energetic photons experience effects induced by the EBL (as discussed in Section 2.2.4). However, whilst the measurement of neutrino spectra is still far in the future, one needs to address two principal issues on how to coordinate observations with gamma-ray instruments. On one hand, neutrino observatories are characterized by a large FoV which enables them to monitor continuously the entire sky at once (with different sensitivity for the two hemispheres, however). Gamma-ray telescopes, on the other hand, because of their small FoV require to point at single sources and have a duty cycle of $\sim 10\%$ (see also Table 2.2).

Neutrino Triggered Target of Opportunity (NToO) One way to operate IACTs and neutrino observatories in synergy is to perform follow-up observations of triggers issued by neutrino observatories. The main player when it comes to follow-up with MAGIC is IceCube. Due to its sensitivity to the entire northern hemisphere and a reported duty cycle of $\sim 99\%$. Once it detects events that are likely due to astrophysical origin, it alerts the astronomical community by sending out machine-readable messages, that can be used to perform follow-up observations. One program that is followed by several second-generation IACT systems is the NToO program. It comes in two main avenues, where it distinguishes between single high-energy neutrino candidate events or temporally clustered multiplets from pre-selected sky regions. These two approaches will be revisited in Chapter 5 and 7, respectively. Therein I will elaborate on an strategy and implementation regarding ToO observations of the prior case as well as elaboration of candidate galaxies that make up the pre-selected sky regions for the latter.

3.2 Core-Collapse Supernova

Once a massive star ($8\ M_\odot < M < 130\ M_\odot$) has burned off all its nuclear fuel, it enters its final stage of life. Unable to balance the gravitational force by means of pressure generated by nuclear fusion, results in a collapse of the core ultimately triggering a massive explosion. The last century was marked with the successful observation of photons and neutrinos from SN1987a, making a clear statement that these events are prime examples for the benefits of a MM approach. Furthermore, due to the potential emergence of asymmetries during the core collapse it has been theoretized that the same sort of source class could in principle generate detectable GWs. Hence, CCSN have the potential to be observable by up to three distinct cosmic messengers, and thus the occurence of a close-by SN (ideally in our own galaxy) would allow to obtain a very rich study sample potentially answering many open questions.

3.2.1 Phenomenology and Stellar Evolution

Stars are initially born by gravitational clumping of hydrogen-rich regions within molecular clouds. Once the pressure and temperature within the gravitational confinements increases to levels where it facilitate the fusion of hydrogen atoms to helium, the star enters its main-sequence phase, whose evolution depends on the mass accumulated during the clumping. As time goes by, the temperature and pressure continue to increase, and eventually, helium and heavier elements can initiate fusion processes, therefore producing heavier elements. The fusion products settle on the star in an "onion-like" fashion, eventually establishing an iron core that can't undergo further fusion. If the iron core happens to exceed a certain mass range ($\sim$1.5 $M_\odot$) it becomes unstable due to gravitational pressure becoming unbalanced by the pressure exerted from electron degeneracy pressure and fusion processes in the shells. This ultimately causes the core to collapse under its mass. Along the contraction of the iron core, therein electrons manage to break the Coulomb barrier and meet the protons of the iron core thereby producing neutrons and neutrinos via inverse beta decay. Undergoing this process, fuels a neutrino burst of immense intensity that accounts for 99 % of the energy which is liberated during the explosion ($\sim 10^{53}$ erg). Hence the main power is radiated away mainly by neutrinos and the remainder of the available energy is mostly transformed into photons and a very small fraction into GWs. Depending on the mass of the initial star the collapse might stop once a neutron star is formed or continue all the way to a singularity.

3.2.2 Collapsar Model Connection to long Gamma-Ray Bursts

If an evolved star has a high angular momentum and undergoes super-Eddington accretion whilst at the brink of a core-collapse event, it could in principle allow to power the formation of ultra-relativistic jets that shoot out perpendicular to the accretion disk. This class is denoted as collapsar and one of the most likely progenitors for LGRBs. The elaboration of a potential mechanism was performed by MacFadyen and Woosley (MacFadyen and Woosley; 1999), but there are various modifications involving Blandford-Znajek mechanism as well as magnetohydrodynamics processes. Note that the literature also commonly uses the term "Hypernova" in order to describe this sort of stellar explosion involving so-called Wolf-Rayet stars that weight up of tens of times the solar mass. One important takeaway from the collapsar model is that the timescales required for the entire mechanism to finis is $\sim$10 seconds. Hence they might

be the progenitor systems that could explain the LGRB-population.

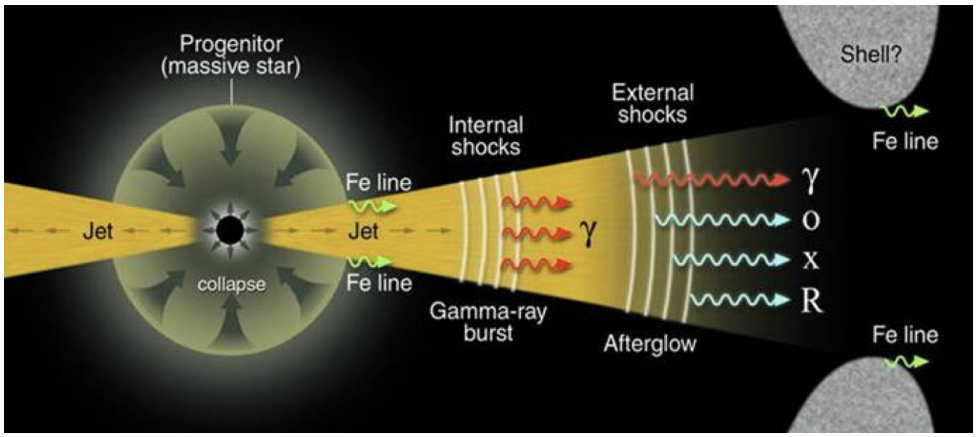

Figure 3.3: Collapsar model of the relativistically expanding fireball. Image Credit: (Frontera, 2019)

Observational confirmations A major consequence of the collapsar model is that LGRBs could be associated with the final stages of stellar evolution. Hence LGRBs should be prevalent in galaxies with active star formation, which from an observationally point of view is strongly supported. Furthermore, both the prompt and afterglow phase of LGRBs were detected in follow-up campagins:

- **Prompt Phase;** as the initial gamma-ray burst commonly detected by space-based observatories such as *Fermi*, *Swift*, INTEGRAL. In this phase the emission of photons up the TeV energies are expected (to be experimentally confirmed by IACTs).
- **Afterglow;** where over time photons of increasing frequencies are emitted. Follow-ups performed by optical observatories usually detect spectral features in the afterglow, therefore establishing clear CCSN-LGRB associations.

3.2.3 Open Questions and Prospects for MM Astronomy

Whilst it took an entire millennium to detect five supernovae (1006; 1054; 1181; 1572; 1604), nowadays a few hundred are detected each year. Even though there are decades worth of observational data from astronomical facilities (and neutrino experiments), only a single CCSN has been co-detected by photon and neutrino observations. SN1987a was observed in the close-by Large Magellanic Cloud ($\sim$50 kpc) and resulted in the observation of $\sim$25 neutrinos detected in the MeV range by different neutrino experiments. Interestingly, these neutrino events were recorded $\sim$3 hours prior to a detection in the EM domain. Since this has been so far a singular event many open questions remain about the engine of the CCSN itself:

- ◇ **Engine of core-collapse supernova:**
  - **Presence of asymmetries in the supernova engine;** In principle, the production of GWs requires that the source has no spherical symmetry. Hence, a single rotating star must be ruled out from the pool of GW emitters.
  - **Explosion Mechanism;** the mechanism of the explosion remains elusive. This so-called supernova problem, could in principle be resolved by obtaining constraints from studying the dynamics of the explosion by means of GW.

When it comes to the progenitors of the related LGRB population there are many unanswered questions:

- ◇ **LGRB:**
  - **Cosmic event rate of LGRBs;** might scale with cosmic star formation history. However, due to only a fraction of these events being visible (due to beaming of radiation into conical jets of angular width $1 - 10\,\mathrm{deg}$) there is a large uncertainty.
  - **Associated Neutrinos;** detected along with gamma-rays could prove that the highest energetic CRs could stem from LGRBs.

Answers to these questions (and many others) might be extractable from studying the signatures of multiple messengers from single CCSN events.

Prospects for MM Astronomy CCSN is a special case of transient phenomena due to its possibility to generate all of the four messengers along its stellar evolution. With this comes a wealth of information that could enable astronomers to study the dynamics of the core during the explosion. In particular, EM emission could help with the localisation of the source. Photons however, carry limited or no information about the collapse itself and are therefore not useful to study the dynamics of the core. Since along the stellar evolution, the messengers appear at different times they complement each other and help in designing follow-up strategies (see also Figure 3.4).

◇ **Neutrinos:** Carry information on the theromdynamics of the collapse

- **Pre-SN;** during silicon burning
- **SN;** Freed energy of a CCSN is $\sim 10^{53}$ erg from which 99% is carried away by neutrinos, majorly during the first $\sim$ 10 seconds following the collapse.

◇ **GWs:** Dynamics and properties of the central engine during the initial phase of the collapse.

◇ **CRs:** Hadronic processes that generate CR in the jets of LGRBs as well as years later due to shock acceleration in SNR. It is noteworthy that VHE astronomy verified that up to $\sim$ 90 % of galactic VHE gamma-ray emitters can be associated to SNR.

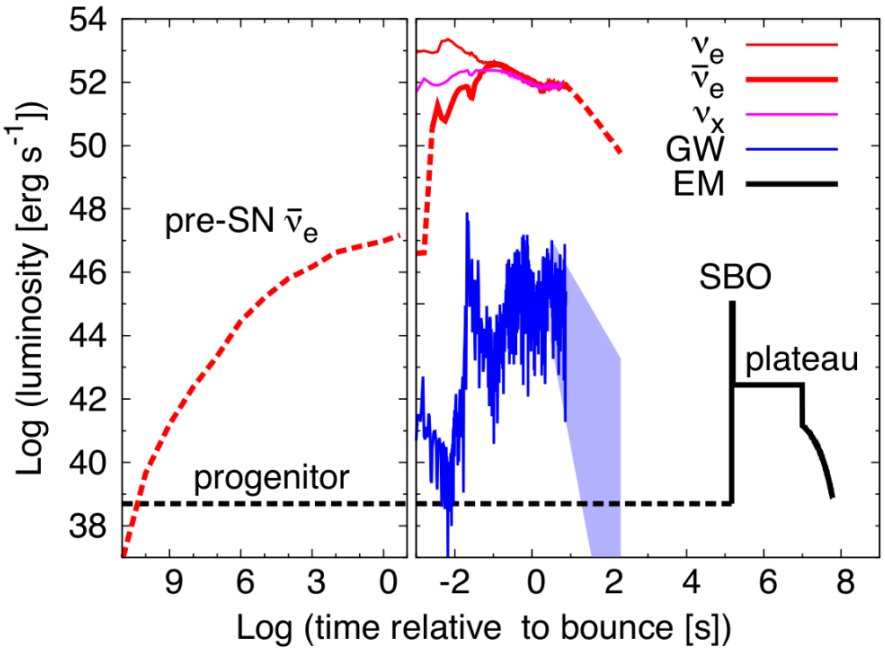

Figure 3.4: Expected time evolution of the luminosities of GW, optical and neutrino messengers from CCSN explosions. Image Credit: Nakamura et al. (2016)

Since there should be significant baryonic matter prevalent in the jets they are natural targets for CRs, neutrino, and gamma-ray observatories. On top of that, since CCSNs could be sources of GWs, this would allow studying LGRBs by means of GW interferometers as well. Nevertheless, there has been no clear neutrino association with LGRBs so far. We can only hope for a close-by CCSN (such as SN19787A) or for the next next-generation neutrino telescopes which would facilitate co-detection of neutrinos and gamma-rays.

3.3 Stellar Mass Compact Object Binaries

It is not a rare occurrence that NSs and BHs are found in bound-orbits around other objects that are compact objects themselves or made of non-degenerate stellar matter. Focusing on the generic case of a binary system that is composed of compact objects, it was long predicted that they can lose significant amounts of energy and angular momentum by means of emitting GWs. Early efforts of Taylor and Hulse to study the binary system PSR 1913+16 were up to very recently the sole experimental verification (albeit indirect) of the emission of GWs predicted by Einstein's theory of General Relativity (GR) (see also Figure 3.5).

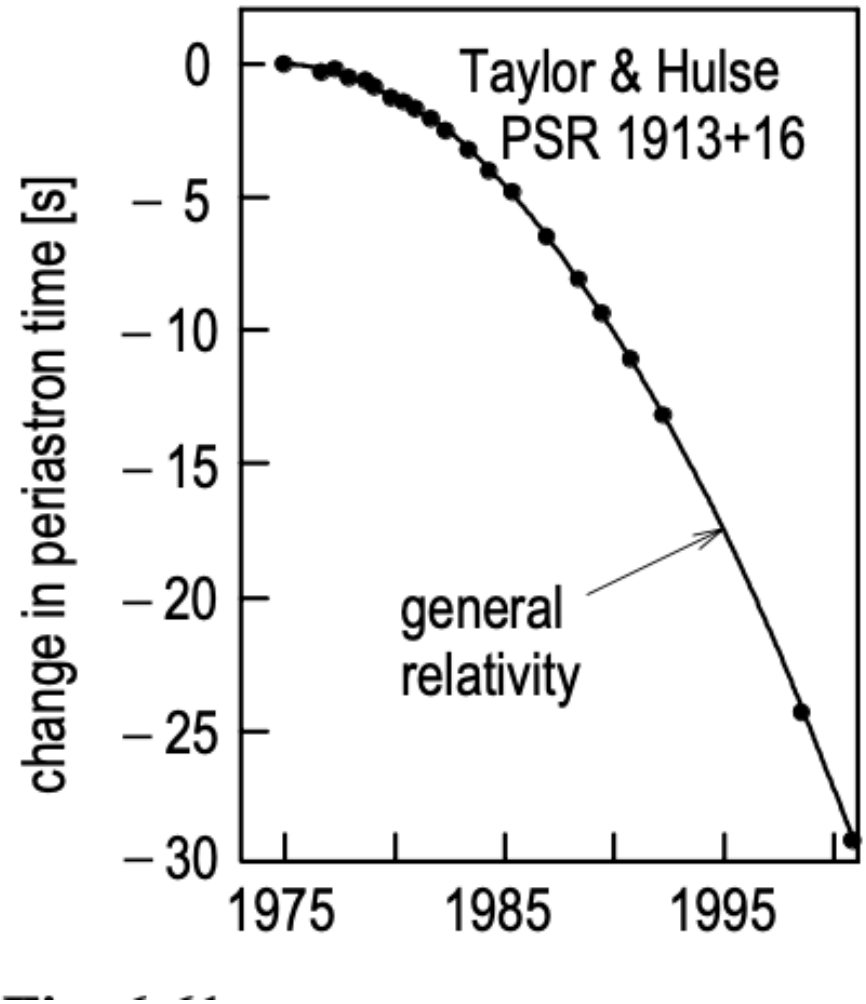

Figure 3.5: The changes in the periastron time of the binary system PSR 1913+16, which is composed of a pulsar and a NS. The measurements are in excellent agreement with the predictions from GR. Image Credit: Grupen (2005)

Once these systems reach the final stages of their orbital decay and are about to merge, they become prime targets for ground-based interferometers. In principle the inspiralling of the two neutron stars

that compose PSR 1913+16 would still takes about $\sim$ 300 million years, however, the GW community detected close to a hundred confident events in three observing runs of the LVC collaboration.

3.3.1 Phenomenology of Compact Object Coalescence

Binary Black Hole Systems Focusing on binary BH systems, astronomers can benefit from extensive work regarding the modeling of GW emissions thereof. Usually three phases characterize the whole merger process. The three phases are shown in Figure 3.6 for the first direct GW detected GW150914 and separated accordingly:

- ◇ **Inspiral:** Closing-in of the two BHs results in a slow-paced increase of the signal frequency related to GW radiation.
- ◇ **Merging:** Coalescence of the two BHs followed by a rapid increase of signal frequency and amplitude (also requires taking into account relativistic effects that are computed from numerical relativity calculations).
- ◇ **Ringdown:** Emission of so-called ringdown radiation of the remnant BH. Since the remnant has a much smaller mass than the sum of the two constituents, this serves as a measure of how much energy was radiated away by means of GWs.

The waveforms generated along these processes can be matched to an extensive database of simulated waveforms. Applying "matched filtering techniques" one can then deduce system parameters like spin, distance, and mass of each of the constituents that make up the binary system. After three successful observing runs, astronomers know that nature hosts a significant population of BBH system. Therefore future runs and next generation observatories are highly anticipated.

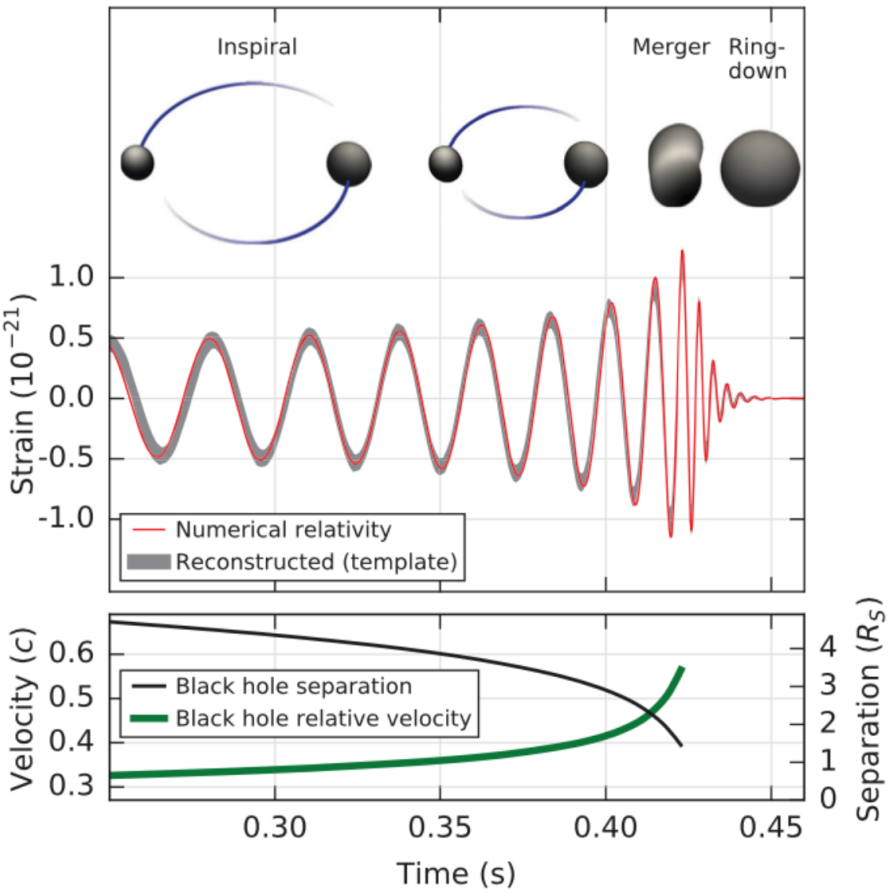

Figure 3.6: Obtained parameters for the progenitor system of GW150914, where **top half:** shows the gravitational-wave strain amplitude and **lower half:** shows the orbital dynamics of the BBH system, e.g. separation and orbital velocities. Image Credit: Crothers (2016)

Binary Neutron Star Systems Binary NS-NS systems on the other hand constitute a different scenario. Due to the presence of degenerate stellar mass, one needs to take into account fluid oscillations during the merger process:

- ◇ **Inspiral:** The constituents can undergo deformation due to tidal forces exerted during the inspiraling, resulting in a dephasing of the GW waveform.
- ◇ **Merging:** Strong dependence on masses of constituents as shown in Figure 3.7.

Since uncertainty regarding the neutron star equation of state has a significant impact on the outcome of modelling gravitational waveform, it is not surprising that current ground-based interferometers only managed to detect two NS-NS mergers: GW170817 and GW190425. Whilst the signal for GW170817 was followed ∼2 seconds later by a SGRB that was detected by Fermi-GBM and INTEGRAL, the latter did not yield the same result. Although the mass parameters of the progenitors from GW190425 are consistent with individual NS components, it cannot be ruled out that either one or both progenitors are BHs (Abbott et al.; 2020a).

Mixed Black Hole Neutron Star Systems Mixed systems are shown to be able to emit GW waves, and thus interesting targets for MM studies. Additionally, one must make a distinction whether the companion NS undergoes tidal disruption or not before it merges with the BH:

- ◇ **Tidal Disruption:** In the case that the NS is disrupted by tidal forces exerted by its BH companion, the resulting matter enriches the ISM with heavy elements and might also be able to power SGRBs.
- ◇ **Without Disruption:** On the other hand if the inspiral occurs without disrupting the integrity of the NS. It can merge with the BH resulting in waveform signals that resemble the ones from BBH.

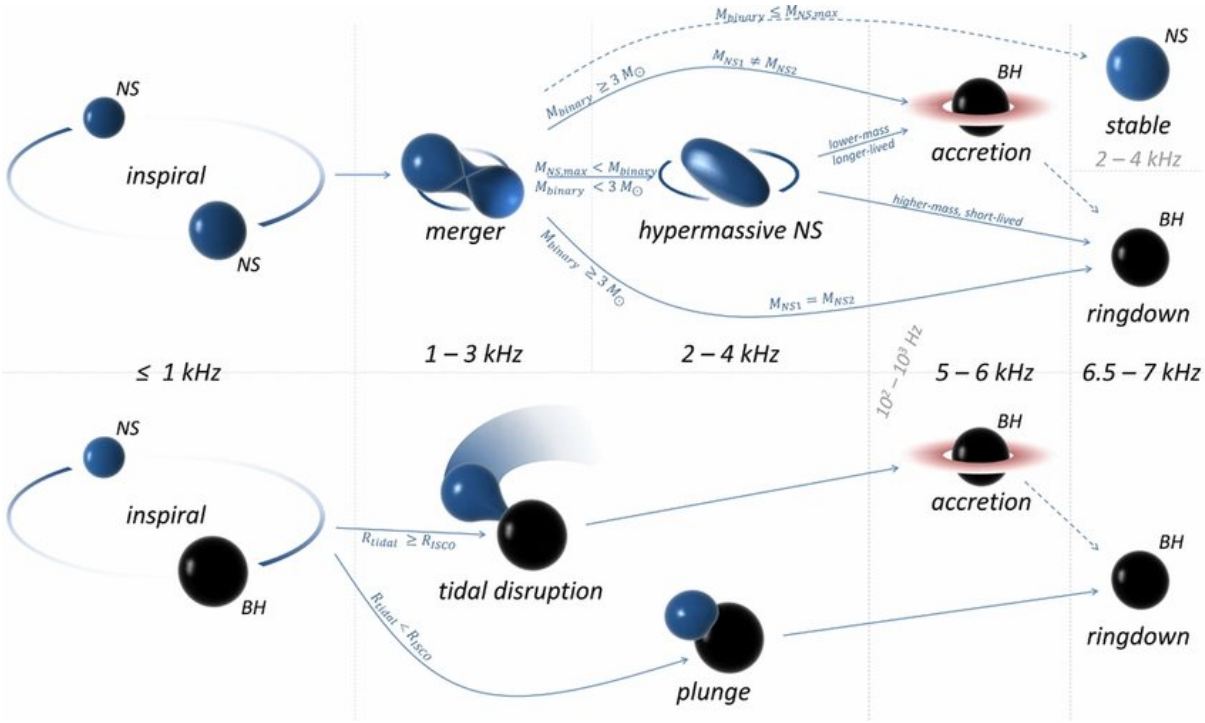

Figure 3.7: Schematic evolution of CBCs, where **top half:** shows the outcomes for BNS systems and **lower half:** shows the scenarios in case of a BHNS system. Image Credit: (Bartos et al.; 2013)

3.3.2 Connection to short Gamma-Ray Bursts

For compact object binaries that contain at least one NS, the merger process can result in the formation of a system that is composed of a central BH and an accretion disk of matter from the progenitor objects. Once the matter falls onto the BH, therein released potential energy can generate jets that serve as accelerators for highly energetic particles. Interestingly, these are almost identical ingredients as for the discussed collapsar model in Section 3.2.2. Nevertheless, the progenitor systems are different from those described previously.

- **NS-NS systems (upper half of Figure 3.7;** Upon conversion of the BNS system into a BH and accretion disk, fast accretion can facilitate the formation of jets fast enough in order to power SGRBs.
- **BH-NS systems (lower half of Figure 3.7;** Debris from the tidally disrupted NS is accreted at high rates onto the BH freeing the energy equivalent of an entire NS in order to power a SGRB.
- **Other systems;** Binary systems that are composed of a BH (or NS) and a white dwarf or non-degenerate star, e.g. massive giants or main sequence stars. In both cases the companion would be disintegrated during the in-spiraling, freeing up gravitational energy and thus powering GRBs through accretion. A caveat is that in these cases the time required to disrupt the companion star hint towards longer timescales (as well as low accretion rates), therefore favoring the formation of LGRBs.

Observational confirmations Unlike LGRBs that are accompanied with SN and found in active star forming regions, the short version seems to be found in old elliptical host galaxies that are located at smaller redshifts. As of the second run of the ground-based GW interferometers, NS-NS binaries have proven to constitute as an adecuate progenitor system of SGRBs. The clear association between GW170817 and GRB170817A triggered an extensive follow-up campaign that caught emission both from the prompt phase as well as the afterglow:

- **Prompt Phase;** the initial GRB, detected by *Fermi*-GBM and INTEGRAL $\sim$2 seconds after the GW signal.
- **Afterglow;** optical counterpart at 40 Mpc detected after $\sim$11 hours, UV counterpart detected after $\sim$15 hours, IR for a week, X-ray $\sim$9 days post-merger and eventually radio $\sim$16 days post-merger.

Note that the literature commonly uses the term "kilonova" in order to describe SGRBs. Optical and IR emissions are due to decay of heavy nuclei that are synthesised by "r-process" which is favourable in neutron rich environments.

3.3.3 Open Questions and Prospects for MM Astronomy

Open Questions With increasing experimental evidence for the existence of black holes (Abbott et al.; 2016; EHT-Collaboration et al.; 2019), it is crucial to extend our knowledge towards understanding possible formation channels of these objects and to study processes occurring in their gravitational field. The accumulation of stellar objects (such as NSs or other astrophysical BHs) in central regions of massive galaxies (Hailey et al. 2018)), can lead to interactions with each other. Over time these interactions can ultimately result in CBC, during which significant GWs are emitted. Their signatures can be detected by observatories such as the LVC. For particular combinations of merger progenitors, e.g. BNS- and NS-BH-systems, the actual merger can in principle be accompanied by EM signals as well as neutrino emission. However, whether BH-NS systems can power SGRBs or other post-merger EM transients remains unknown. In the context of MM astronomy, these are very interesting opportunities since the physical processes occurring during these merger events can be probed by a variety of messengers. Hence, once recorded by the GW observatories, these mergers trigger follow-up campaigns during which various high-energy, optical and radio telescope-system (space- and ground-based) are being deployed in order to detect associated counterpart signals. Even though the third observing run of GW observatories has added a significant fraction to the known population of observed CBCs, the pair GRB170817A and GW170817 remains the only association between a GW and its EM counterpart signal. Thus the astrophysical merger rates in the nearby Universe remains an open question which does not yet allow to probe whether their rate scales with cosmic star formation history.

Prospects for MM Astronomy

GW and Gamma-Ray Connection As mentioned previously, the detection of GW170817 followed by GRB170817A resulted in clear evidence that BNS mergers are progenitors of at least some of the SGRBs detected. Hence there is a clear connection between the emission of GW and high energetic gamma rays during the prompt phase of a SGRB, as well as photons in decreasing frequency in the evolution of the afterglow (see also Table 3.1).

Table 3.1: Overview of the temporal evolution of possible EM counterpart signatures originating from BNS- and NSBHs-type mergers in dependence of the observing angle θ_{obs}. Credit: adapted from Table 2.1 in Urban (2016)

EM Counterpart	Viewing Angle	Detectability Timescale	Bandpass
SGRB	$\theta_{obs} \lesssim \theta_{jet}$	∼seconds	gamma-ray/ hard X-ray
X-ray afterglow	$\theta_{obs} \lesssim \theta_{jet}$	∼minutes-hours	X-ray
optical afterglow	$\theta_{obs} \lesssim 2\theta_{jet}$	∼minutes-days	optical
kilonova	isotropic	∼days	optical/near-IR
radio afterglow	isotropic	∼weeks-years	radio

θ_{jet}: Opening jet angles ∼ 20 deg D'Avanzo (2015)

GW Triggered Target of Opportunity (GWToO) One of the main stepping stones can be attributed to large localisation regions inferred from the GW-signal (∼20–1000 deg^2 Abbott et al. (2020b). Further complications arise from the necessity to localise counterparts fast enough in order to get a glimpse of its rapidly decaying EM signals. On the other hand, there could be an advantage in the sense that GW interferometers can detect signatures during the inspiraling phase, thus predicting the 3-dimensional position along with an approximated time of the actual merger-phase. This in turn would allow to a priory predict SGRBs. Nevertheless, the lower latency comes off-course with a trade-off on localisation uncertainty as qualitatively visible in Figure 3.8. This approach as well as other details will be revisited in Chapter 5; where we discuss a possible implementation in order to react to alerts for the highly anticipated fourth observing run of the GW interferometers.

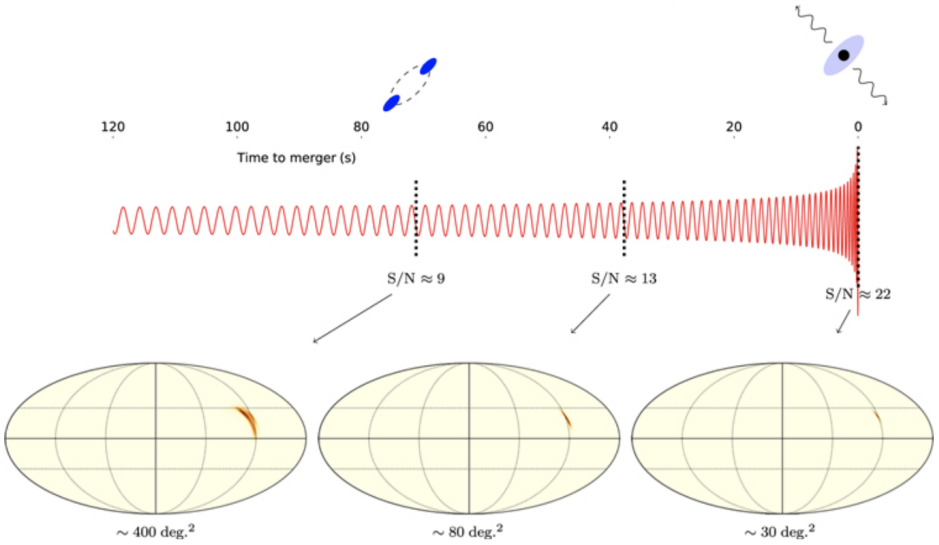

Figure 3.8: Qualitative evolution of the waveform and uncertainty localization for BNS system prior to merger phase. Image Credit: Magee et al. (2021)

3.4 Other Transient Phenomena

The following subsections introduce the phenomenology of additional transient phenomena. They are highly interesting on their own behalf and address relevant physics questions, but are currently beyond the reach of the algorithm developed throughout the thesis at hand. The inclined reader is referred to Engel et al. (2022) for further phenomena and discussions thereof.

3.4.1 Fast Radio Bursts

From a phenomenological point of view, FRBs could be somewhat described as a radio-analog of the GRB class. However, with the modification that their short-duration bursts manifest high fluences at radio wavelengths and that apart from single-burst events there seems to be a source class that shows repeated flaring activity. Initially discovered in 2007, observations from various experiments identified close to a thousand of these bursts. Various MWL observations were successful in identifying potential host galaxies that could harbor FRB sources (from optical follow-ups) as well as insights into the mechanism that governs these sources (from X-ray follow-ups). The co-detection of FRB200428 along with an X-ray burst from the direction of SGR 1935+2154 (Palmer (2020)) established a milestone in the study of these new phenomena. Further MWL campaigns as well as MM efforts should be able to bolster our understanding of their progenitor systems.

3.4.2 Tidal Disruption Events

Stellar objects that happen to be on eccentric orbits around their host SMBH can be exposed to tidal forces that ultimately cause the star to disintegrate and undergo TDE. Upon accretion of the stellar mass onto the SMBH, this leads to a flaring activity similar to AGNs which in principle could generate a variety of the discussed MM particles, e.g. photons, CRs and neutrinos. TDEs being theoretically proposed towards the end of the last century, nowadays the scientific community is gaining expertise when performing MM-observational campaigns.

Bibliography

Abbott, B. P., Abbott, R., Abbott, T., Abernathy, M., Acernese, F., Ackley, K., Adams, C., Adams, T., Addesso, P., Adhikari, R. et al. (2016). Gw150914: The advanced ligo detectors in the era of first discoveries, *Physical review letters* **116**(13): 131103.

Abbott et al. (2020a). Gw190425: Observation of a compact binary coalescence with total mass 3.4 m, *The Astrophysical Journal* **892**(1): L3.

Abbott et al. (2020b). Prospects for observing and localizing gravitational-wave transients with advanced ligo, advanced virgo and kagra, *Living reviews in relativity* **23**(1): 1–69.

Bartos, I., Brady, P. and Márka, S. (2013). How gravitational-wave observations can shape the gamma-ray burst paradigm, *Classical and Quantum Gravity* **30**.

Beckmann, V. and Shrader, C. R. (2013). The agn phenomenon: open issues, *arXiv preprint arXiv:1302.1397* .

Blandford, R. D. and Znajek, R. L. (1977). Electromagnetic extraction of energy from kerr black holes, *Monthly Notices of the Royal Astronomical Society* **179**(3): 433–456.

Crothers, S. J. (2016). A critical analysis of ligo's recent detection of gravitational waves caused by merging black holes, *Hadronic Journal* **39**: 1.

D'Avanzo, P. (2015). Short gamma-ray bursts: A review, *Journal of High Energy Astrophysics* **7**: 73–80.

EHT-Collaboration et al. (2019). First m87 event horizon telescope results. ii. array and instrumentation, *arXiv preprint arXiv:1906.11239* .

Engel, K., Lewis, T., Muzio, M. S., Venters, T. M., Ahlers, M., Albert, A., Allen, A., Solares, H. A. A., Anandagoda, S., Andersen, T. et al. (2022). Advancing the landscape of multimessenger science in the next decade, *arXiv preprint arXiv:2203.10074* .

Frontera, F. (2019). The key role of bepposax in the grb history, *Rendiconti Lincei. Scienze Fisiche e Naturali* **30**(Suppl 1): 171–184.

Ghisellini, G., Righi, C., Costamante, L. and Tavecchio, F. (2017). The Fermi blazar sequence, *Monthly Notices of the Royal Astronomical Society* **469**(1): 255–266.
URL: *https://doi.org/10.1093/mnras/stx806*

Grupen, C. (2005). *Astroparticle Physics*, Springer.

Hailey, C. J., Mori, K., Bauer, F. E., Berkowitz, M. E., Hong, J. and Hord, B. J. (2018). A density cusp of quiescent x-ray binaries in the central parsec of the galaxy, *Nature* **556**(7699): 70–73.

MacFadyen, A. and Woosley, S. (1999). Collapsars: Gamma-ray bursts and explosions in "failed supernovae", *The Astrophysical Journal* **524**(1): 262.

Magee, R., Chatterjee, D., Singer, L. P., Sachdev, S., Kovalam, M., Mo, G., Anderson, S., Brady, P., Brockill, P., Cannon, K. et al. (2021). First demonstration of early warning gravitational-wave alerts, *The Astrophysical Journal Letters* **910**(2): L21.

Nakamura, K., Horiuchi, S., Tanaka, M., Hayama, K., Takiwaki, T. and Kotake, K. (2016). Multimessenger signals of long-term core-collapse supernova simulations: synergetic observation strategies, *Monthly Notices of the Royal Astronomical Society* **461**(3): 3296–3313.

Padovani, P., Alexander, D., Assef, R., De Marco, B., Giommi, P., Hickox, R., Richards, G., Smolčić, V., Hatziminaoglou, E., Mainieri, V. et al. (2017). Active galactic nuclei: what's in a name?, *The Astronomy and Astrophysics Review* **25**: 1–91.

Palmer, D. M. (2020). A forest of bursts from sgr 1935+ 2154, *The Astronomer's Telegram* **13675**: 1.

Penrose, R. and Floyd, R. (1971). Extraction of rotational energy from a black hole, *Nature Physical Science* **229**: 177–179.

Urban, A. L. (2016). *Monsters in the dark: High energy signatures of black hole formation with multi-messenger astronomy*, PhD thesis, The University of Wisconsin-Milwaukee.

Urry, C. M. and Padovani, P. (1995). Unified schemes for radio-loud active galactic nuclei, *Publications of the Astronomical Society of the Pacific* **107**(715): 803.

CHAPTER 4

MULTI-WAVELENGTH OBSERVATIONS ON VER J0521+211

Contributions: The content of the chapter at hand is based on a publication of the MAGIC collaboration currently ongoing the latest step of the internal review defined in the collaboration, for which I am a corresponding author. J. Jormanien along with myself were performing the MAGIC analysis while the F-test was performed by V. Fallah Ramazani. M. Nievas Rosillo along with myself were performing the Fermi-LAT analysis.
An upper limit on redshift was obtained by myself and cross-checked by J. Jormanien.
Swift-XRT data were obtained and analyzed by V. Fallah Ramazani.
Swift-UVOT data were obtained and analyzed by M. Cerruti.
MWL Datasets were gathered and analyzed by J. Jormanien and V. Fallah Ramazani.
SED Modeling was performed by M. Nievas Rosillo, A. Omeliukh, X. Rodrigues and myself.

Contents

As discussed in the previous chapter on transient phenomena, AGNs are interesting objects that observationally manifest themselves with a large diversity. In the particular case that their relativistic jets are aligned with Earth's line of sight, they are classified as blazars (also introduced in Section 3.1.2). Therein BL Lac subtype is among the most studied AGNs at VHE. However, due to the common absence of emission lines (or too weak to be detected), establishing distance estimates of the underlying object are prone to large uncertainties.

In the broader context of the MM efforts of this manuscript, we note that the study of MM signals from AGNs was in recent years catalyzed by events such as the apparent correlation between the arrival directions of UHE CRs and nearby AGNs, as well as the detection of a flaring state in TXS 0506+056 along with a HE neutrino detected IC-170922A. These two associations raise the possibility of AGNs being accelerators of HE CRs. Whilst for now these two MM examples seem to be isolated, there still remains the MWL approach to study AGNs. This allows deepening our understanding by testing various emission models and comparing them to the observed broadband spectra.

Going through this chapter, we will start by outlining the observational history of the BL Lac-type object VER J0521+211 (Section 4.1). After reporting on the broadband MWL observations of a flaring state in VER J0521+211 along the 2020 campaign (Section 4.2), we elaborate on the instruments that were used during that period as well as the data taken, along with corresponding analysis methods and specific results from selected waveband regimes are discussed in Section 4.3. Section 4.4 reports on the MWL characterization of the source along with an estimate for an upper limit of its redshift, as well as results from time-dependent modeling of the broadband emission for VER J0521+211 during different phases of this particular flaring state. Section 4.5 draws the conclusion on the most important findings.

4.1 Observational History

VER J0521+211 is located at R.A. [J2000]: 05h 21m 45.9s. Dec. [J2000]: +21° 12' 51" and was initially discovered by the Very Energetic Radiation Imaging Telescope Array System (VERITAS) collaboration at TeV energies in 2009 and later on also spatially associated with the radio and X-ray source RGB J0521.8+2112 (Archambault et al.; 2013). The source was observed by MAGIC and VERITAS in a high state in the VHE band between 2013 and 2014 (VERITAS&MAGIC et al.; 2022). Classified as a BL Lac-type object, VER J0521+211 lacks, as many of its peers, any distinctive optical emission features. This inherently gives rise to a large uncertainty regarding the true distance of the host galaxy. Several redshift-measurement attempts were conducted, however a clear consensus has not yet been reached. Thus, for the time being a lower-limit on its redshift, $z > 0.18$, was established in (Paiano et al.; 2017), along with a recently published upper-limit at $z \leq 0.31$ (VERITAS&MAGIC et al.; 2022).

4.2 MWL Campain during 2020 Flaring State of VER J0521+211

In the framework of a recent MWL campaign, VER J0521+211 was observed once again by the MAGIC telescopes in February and March 2020. This was following an ATel published by the VERITAS collaboration on February 25th, 2020[1], alerting of renewed activity from the source in the VHE band. Significant detection of the source by MAGIC in the VHE gamma-ray band led to an observational campaign of six consecutive nights from February 26th to March 01 2020. These efforts were accompanied by an extensive contemporaneous MWL campaign, allowing to observe the source in different energy bands, that range from radio to VHE gamma rays, covered by various observational facilities and experiments.

4.3 Data Analysis and MWL Coverage

VER J0521+211 was observed between February and March of 2020 by a variety of instruments sensitive within the broader electromagnetic domain (ranging from radio up to VHE gamma rays). Whilst for several of these instruments the observations were conducted in the framework of regular monitoring programs (e.g. Tuorla Blazar Monitoring, KAIT *Fermi* AGN monitoring, Boston University blazar monitoring, OVRO radio monitoring), several facilities and instruments used a target-of-opportunity (ToO) scheduling, in order to detect that particular flaring state in VER J0521+211 (e.g. MAGIC, *Swift*).

4.3.1 VHE Gamma Rays (MAGIC)

VER J0521+211 is observable from the MAGIC site at zenith angles culminating at 55° deg between mid-September and mid-March. It was previously observed during fall 2013 (MJD 56580-56627) following a long-lasting enhanced state in the gamma-ray band detected by *Fermi*-LAT (also denoted in Fig 4.2 as reference for archival VHE flux). For the study at hand, we report on observations that were performed during six consecutive nights (MJD=58905-58910) initially triggered on the 26th of February 2020 by an elevated state in VHE gamma rays as reported by the VERITAS collaboration[1]. The corresponding observations were carried out for low to high zenith angles, ranging from 13° to 55° during both dark time (3.9 hours) as well as under moonlight conditions (2.1 hours, impacting the data analysis due to the higher night sky background (Ahnen et al.; 2017)). The data was analysed using the MAGIC Standard Analysis Software MARS (Zanin et al.; 2013) and since part of the data were partially affected by passing high altitude clouds, atmospheric transmission corrections were applied, based on the information obtained with the MAGIC elastic LIDAR (Fruck and Gaug; 2015).

The observations of VER J0521+211 performed by MAGIC led to significant detection at VHE energies for six consecutive nights. Individual exposures along with their respective significance are reported in Table 4.1 and shown in Figure 4.1. The night-wise TeV gamma-ray flux evolution at energies above 200 GeV is shown in the top panel of Figure 4.2. Significant detection during each exposure, allowed to reconstruct night-wise VHE gamma-ray spectra, that were further analysed by assuming both a power-law model (PWL; Eq. 4.1) as well as log-parabola model (LP; Eq. 4.2):

[1] https://www.astronomerstelegram.org/?read=13522

$$\frac{dF}{dE}(E) = F_0 \left(\frac{E}{E_0}\right)^{-\Gamma} \tag{4.1}$$

$$\frac{dF}{dE}(E) = F_0 \left(\frac{E}{E_0}\right)^{-\Gamma-\beta(\log_{10}(E/E_0))} \tag{4.2}$$

where:

- $\frac{dF}{dE}$ is the differential flux
- F_0 is the normalization constant
- E_0 is the normalization energy
- Γ is the photon index
- β is the curvature

The results of our spectral analysis for the VHE gamma-ray band are summarised in Table 4.1. As mentioned previously, the redshift of VER J0521+211 remains unknown. Hence, obtained spectral parameters were derived from observed spectra, and therefore do not take into account effects that stem from EBL absorption.

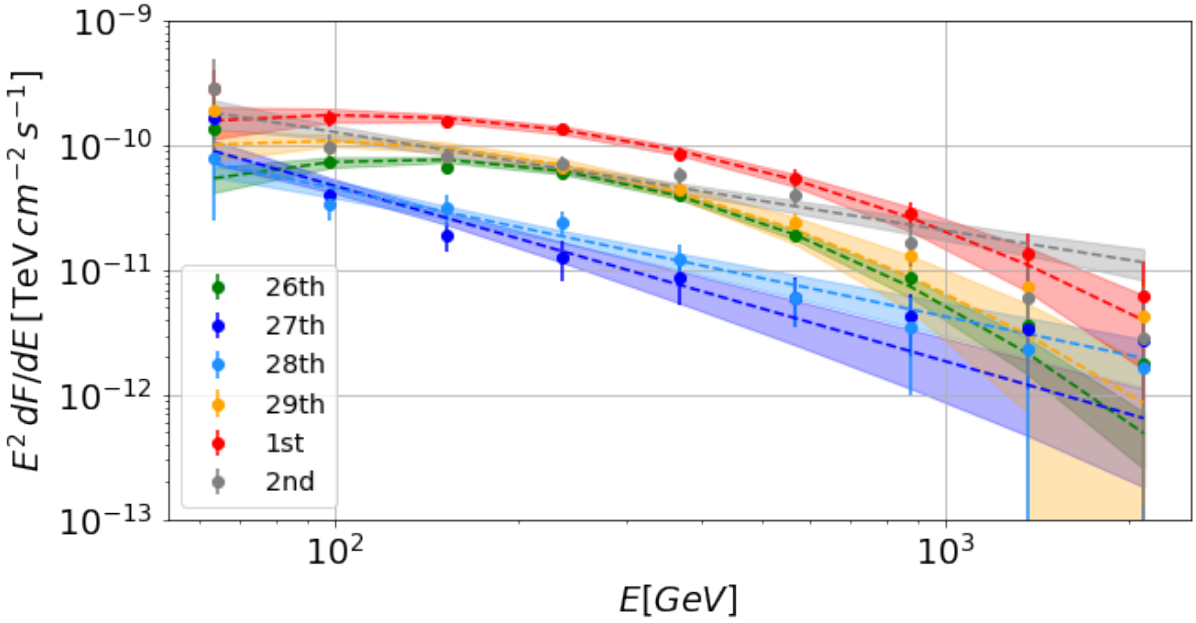

Figure 4.1: Night-wise SEDs for the VHE-range as obtained by MAGIC during the MWL campaign (Feb-March 2020).

State (see 4.4.1)	Epoch [MJD]	T_{eff} [hrs]	Significance [σ]	Model	F-Test	Flux at 300 GeV [$\times 10^{-11}$cm^{-2}s^{-1}TeV^{-1}]	Γ	β
Acciari et al. (2020)	56580-56627	4.50	30.47	LP	-	27.43 ± 0.51	2.69 ± 0.02	-0.47 ± 0.07
A	58903.5-58905.5	2.43	38.45	LP	5.08×10^{-5}	5.12 ± 0.31	3.07 ± 0.08	-1.47 ± 0.28
B	58905.5-58906.5	0.66	10.34	PWL	1.38×10^{-1}	0.02 ± 0.01	3.07 ± 0.08	-
B	58906.5-58907.5	0.65	11.58	PWL	6.95×10^{-2}	0.04 ± 0.01	3.05 ± 0.18	-
C	58907.5-58908.5	0.73	22.94	LP	1.25×10^{-5}	6.23 ± 0.64	3.35 ± 0.23	-1.72 ± 0.54
D	58908.5-58909.5	0.72	30.46	LP	1.18×10^{-3}	11.10 ± 0.90	3.04 ± 0.12	-0.88 ± 0.34
-	58909.5-58910.5	0.70	20.82	PWL	3.75×10^{-3}	0.22 ± 0.03	2.69 ± 0.10	-

Table 4.1: Results of the night-wise VHE gamma-ray spectral analysis for VER J0521+211. The LP model, (LP; Eq. 4.2), is preferred over the PWL model, (PWL; Eq. 4.1) at 3-σ confidence level if the F-test probability value was less than 0.27% (i.e. $< 2.7 \times 10^{-3}$). Columns: (1) State; (2) observation epoch; (3) effective time; (4) significance; (5) best-fitted model; (6) F-test; (7) flux at normalisation energy; (8) and (9) spectral index and the curvature parameter (when LP was preferred over PWL).

4.3.2 HE Gamma Rays (*Fermi*-LAT)

VER J0521+211 is associated with the gamma-ray source 4FGL J0521.7+2112 (Abdollahi et al.; 2020), for which the HE gamma-ray (HE, > 100 MeV) flux reported in the 4FGL is (1.132 ± 0.087) × 10^{-7} cm^{-2} s^{-1} along with a corresponding photon index of 1.965 ± 0.029. In order to analyse *Fermi*-LAT data, the Python package fermipy (Wood et al.; 2017) was employed. In this work I use publicly available *Fermi*-LAT data from a ∼2 year window, that ranges from July 2018 up to the flare in February/-March 2020 (MJD 58300-58912), where I focus on selected photons that are contained in the Pass 8 SOURCE class data (Atwood et al.; 2013). For the analysis, I limit the region of interest (ROI) to a circle centered at the position of the target source with a radius of 15°. Adopting the instrument response functions "P8R3_SOURCE_V2", a binned likelihood analysis (0.08° binning in RA and Dec) with 8 bins per decade in energy (range 0.1–300 GeV) was performed, where a correction for energy dispersion is included for all sources in the model. Furthermore, the standard quality cuts ("DATA_QUAL 0 && LAT_CONFIG==1") as well as a zenith cut of (Zd < 90°) is applied in order to limit contamination from the Earth's limb. I use standard galactic (Acero et al.; 2016) and isotropic diffuse emission models "gll_iem_v06.fits" and "iso_P8R3_SOURCE_V2_v1.txt", respectively, as well as all sources listed in the fourth source catalog of *Fermi*-LAT (4FGL) (Thompson; 2019) that are contained within 15° from the ROI center. During the fitting procedure, the parameters of both diffuse components are left free to vary, along with the spectral parameters of all sources contained within a radius of 5° around the source of interest. The remaining parameters for sources within the ROI are fixed to the values published in the 4FGL-catalog. In order to obtain the long- and short-term HE gamma-ray light curves of VER J0521+211, two sets of dedicated likelihood analyses with different time binnings were performed. For the long-term case, I use a monthly-binned *Fermi*-LAT data set, that includes events from July 2018 up to the flare. For the short-term case, I focus on a time window of temporal coincidence with MAGIC observations (MJD 58902.5-58911.5), and perform a daily-binned analysis with each of the time bins centred at midnight.

Fermi-LAT monitoring performed contemporaneous to MAGIC data taking shows significant detection for each of our defined epochs (see also Table 4.3). This allows to obtain night-wise spectra, described by a PWL model (see Eq. 4.1). The obtained parameters and test statistic (TS) values are summarised in Table 4.2.

State (see 4.4.1)	Epoch [MJD]	TS	Model	Γ_{LP} [$\times 10^{-7} cm^{-2} s^{-1}$]	$F_{0.1-300\ GeV}$
A	58903.5-58905.5	77	LP	1.64 ± 0.18	2.60 ± 1.01
B	58905.5-58907.5	29	LP	2.00 ± 0.29	2.27 ± 1.39
C	58907.5-58908.5	55	LP	1.47 ± 0.28	2.46 ± 1.27
D	58908.5-58909.5	90	LP	1.78 ± 0.29	3.86 ± 1.82

Table 4.2: Summary of the fit parameters to the *Fermi*-LAT spectra in each given epoch.

4.3.3 Multi-Wavelength Data Set

In the following sub-sections, we outline various MWL instruments along with their respective data analysis procedures, in order of decreasing frequencies: X-rays (*Swift*-XRT), optical and UV (*Swift*-UVOT), optical photometry and polarization (Perkins, NOT) and finally radio (VLBA, OVRO, Metsähovi).

X-Rays The X-ray Telescope (XRT, Burrows et al.; 2004) on-board the *Swift* satellite performed four contemporaneous observations (MJD 58904.1-58908.8) of VER J0521+211. The multi-epoch events list of the *Swift*-XRT for the given period entails a total exposure time of ~ 1.1 h, and they are obtained via the publicly available *Swift*-XRLOG (*Swift*-XRT Instrument Log)[2]. Following the procedure described in Fallah Ramazani et al. (2017), the data set is processed assuming a fixed equivalent Galactic hydrogen column density of $N_H = 4.38 \times 10^{21}$ cm^{-2} as reported by Willingale et al. (2013).

Optical UV The Ultraviolet/Optical Telescope (UVOT) instrument on board the *Swift* satellite (Poole et al.; 2008) observed VER J0521+211 on five occasions (MJD 58904.1-58908.8) along this campaign, where four out of five pointings were performed simultaneously with *Swift*-XRT. Observations were performed on two occasions with several optical (V, B and U) and UV (W1, W2 and W2) onboard filter combinations (Poole et al.; 2008; Breeveld et al.; 2010). Further observations with individual filters were obtained on three occasions. In addition, for the evaluation of the long-term MWL observations, archival data in the optical and UV bands were collected between MJD 55131-59283. The data was analysed using the `uvotmaghist`-task included in the HEAsoft package (v6.28) with the 20201026 release of the *Swift*/UVOTA CALDB. Source counts belonging to VER J0521+211 were isolated from a circular region (5 arcsec radius) centred on the source, whilst the background was estimated using a nearby source-free region (20 arcsec radius). The UVOT fluxes were corrected for galacting extinction with an E(B-V) value of 0.605 Schlafly and Finkbeiner (2011).

Optical Photometry and Polarization

- ◇ **Tuorla blazar monitoring program:** Optical R-band long-term and short-term light curves shown in Figure 4.2 extend through the period between MJD 58366.2 - 58906.3. These data were obtained through the Tuorla blazar monitoring program[3] (Takalo et al.; 2008), monitoring by the Boston University Blazar Group[4] (Jorstad and Marscher; 2016), KAIT *Fermi* AGN Light-curve Reservoir[5], Nordic Optical Telescope (NOT), and Belogradchik Observatory. The Tuorla monitoring program includes the following telescopes: the 50-cm Searchlight Observatory Network telescope (San Pedro de Atacama, Chile), the 40-cm Searchlight Observatory Network telescope (New Mexico, USA), the 60-cm telescope at Belogradchik (Bulgaria), and the Kungliga Vetenskapsakademien (KVA) telescope (ORM, La Palma, Canary islands, Spain), with most data taken with the KVA telescope. The data from the Boston University Blazar Group have been obtained with the 1.83-meter-diameter Perkins telescope (Arizona, USA). The data from KAIT *Fermi* AGN Light-curve

[2] `https://heasarc.gsfc.nasa.gov/W3Browse/swift/swiftxrlog.html`
[3] `https://users.utu.fi/kani/1m/index.html`
[4] `http://www.bu.edu/blazars/BEAM-ME.html`
[5] `http://herculesii.astro.berkeley.edu/kait/agn/`

Reservoir have been obtained with a 76-cm robotic Katzman Automatic Imaging Telescope at the Lick Observatory (California, USA). NOT is a 2.56-meter-diameter telescope located at the ORM, La Palma, Canary Islands, Spain. Further, an extended light curve with data spanning MJD 55494 - 59229 shown in Figure 4.3 use additional data from the Tuorla monitoring program, the NOT observatory, the KAIT Reservoir, and the Boston University Blazar Group.

- ◇ **Belogradchik and Perkins:** Additional multi-band optical data was collected from the time of the flare. These data include V- and I-bands from the Belogradchik Observatory, and B-, V-, and I-bands from the Perkins Observatory.

The data from the Tuorla monitoring program and NOT telescope were analysed following Nilsson et al. (2018). The same method of differential photometry was performed for the flat-, bias-, and dark-reduced images of the source from the Belogradchik Observatory. The analysis procedures of the data from the Boston University Blazar Group, and the data from KAIT Reservoir are described in (Jorstad and Marscher; 2016) and in (Li et al.; 2003), respectively. Additionally, all bands were corrected for galactic extinction along with corrections of the R- and I-bands for host emission. The host galaxy contribution to the source flux was estimated by assuming an elliptical galaxy with an absolute magnitude $M = -22.8$ at a redshift of $z = 0.18$ (lower-limit from (Paiano et al.; 2017)) with the aperture of $5''$ and an effective radius of 8 kpc.

Radio

- ◇ **OVRO:** Radio coverage between MJD 58360 - 58907 was facilitated by the Owens Valley Radio Telescope (OVRO, 15 GHz).
- ◇ **Metsähovi:** Further data provided by the 13.7-meter-diameter Metsähovi radio telescope (37 GHz).

The analysis methods for these instruments are detailed in Richards et al. (2011) and Teräsranta et al. (1998), respectively.

4.4 Results and Discussion

In this section, we describe the results of our study divided into different topics that played a role in characterising the possible emission scenarios within the jet of VER J0521+211. Past attempts have brought us closer to determining the redshift of this source (Paiano et al.; 2017; VERITAS&MAGIC et al.; 2022) and the two-zone emission model was suggested for this source already in Acciari et al. (2020), but in this study we approach this source with even more detailed methods in an attempt to answer the open questions about the emission mechanisms.

4.4.1 Multi-Wavelength Variability

When combining the information from several different wavelengths it is important to gather as much data as possible and look at the variability of the source not only at the time of the flare but also during

a longer period of time to get a clear picture of the source. In this section, we assess both the long-term and the short-term MWL variability of this source. In order to understand the evolution of the emission observed from blazars in general, it is important to compare the state of the source in the long term in other bands as the source has been observed in the VHE gamma rays only during flares. The long-term variability of this source was already studied in Lindfors et al. (2016) where they reported a trend of increasing flux both in radio and optical R-band data sets between 2010 and 2013. In addition, Acciari et al. (2020) performed the same analysis for the data between 2013 and 2018 and found that the flux level in the optical and in the radio band had become decreasing instead. In our study, we have collected the long-term data from 2018 onward to estimate whether the emission from these bands are still following the common trend. It would support the fact that the emission from these wavelengths stems from the same region within the jet as concluded in Lindfors et al. (2016). These MWL data are presented in Figure 4.2 where on the left panels we have the long-term light curve up to the start of the VHE gamma-ray flare and on the right panels we have the flare divided into four epochs. The common trends reported in Lindfors et al. (2016) and Acciari et al. (2020) are not clearly visible in the long-term radio and optical light curves between 2018 and 2020. Therefore, we have collected all the radio and optical R-band data from between 2009 and 2021 with additional data from the VLBI radio observations between 2009 and 2019 as well as optical and UV data from *Swift*-UVOT between 2009 and 2021 to inspect this more closely. The combined data sets are shown in Figure 4.3 and we can see that the long-term radio-to-UV variability follows closely similar trends compared to the core component observed with the VLBI whereas the radio knot does not follow the same trends (Lister et al.; 2018). The flares on top of the long-term trend follow the same decreasing pattern until 2021.

Comparing the long-term behaviour with the behaviour seen at the time of the flaring episode in spring 2020, we can see that in the HE gamma-rays (second panels from the top in Fig. 4.2) and in the X-rays (third panels from the top) VER J0521+211 was in an elevated flux state at the time of the VHE gamma-ray flare (top panels). Instead, we do not see a similar enhancement in the radio-to-UV bands, and when comparing the long-term part of these light curves to that shown in Figure 4.3 we can see that the flare is only observed in the energies in the X-ray regime and beyond (see also Table 4.3). In this light, this VHE gamma-ray flare is different in nature compared to the one analysed in Acciari et al. (2020) where at the time of the VHE-gamma-ray flare, high flux was observed across all bands from radio to VHE gamma-rays. This could indicate that the global state of the jet across these two flaring episodes was different. Thus, if we assume that the two-component scenario is true, the fact that we observe this 2020 flare only in the higher energies would hint that the contribution of the "jet" component has gotten weaker since the 2013 flare that was observed in all wavebands. When we zoom into the MWL variability observed during the 2020 flare, we see that the VHE gamma-ray light curve consists of two local maximums, between which there is a local minimum. Based on TeV gamma ray flux levels, we define four epochs (hereafter denoted as A, B, C, D) as elaborated in Table 4.3. For the HE and VHE band, the data of periods A and B are summed. Furthermore, based on the assumption that there is no short-term variability in the radio band, the corresponding data points in A, B, and C are summed and used for all four epochs. Focusing on the short-term evolution of VER J0521+211 over those four epochs allows to perform a time-dependent modeling of the broadband SEDs whose details and findings are reported in Section 4.4.3.

Campaign and State	Epoch [MJD]	Instrumental-Coverage	State with respect to long-term LC ; Fig 4.2		
			VHE and HE	X-Ray	UV, Optical and Radio
2013 Acciari et al. (2020)	56580-56627	MAGIC, VERITAS *Fermi*-LAT, *Swift*, Steward	enhanced	enhanced	archival and low
2020 A	58903.5-58905.5	MAGIC, *Fermi*-LAT, *Swift*, Belgradochik, Perkins OVRO, Metsahovi	flaring	enhanced	archival and low
2020 B	58905.5-58907.5	MAGIC, *Fermi*-LAT, *Swift* Belgradochik, Perkins OVRO, Metsahovi	enhanced	enhanced	archival and low
2020 C	58907.5-58908.5	MAGIC, *Fermi*-LAT, *Swift* Belgradochik, Perkins, KVA OVRO, Metsahovi	increasing	increasing	archival and low
2020 D	58908.5-58909.5	MAGIC, *Fermi*-LAT, *Swift*, NOT OVRO, Metsahovi	flaring	flaring	archival and low

Table 4.3: Selected states (A, B, C and D) for the time-dependent SED modeling (colours correspond to the ones used in tables and figures of this work).

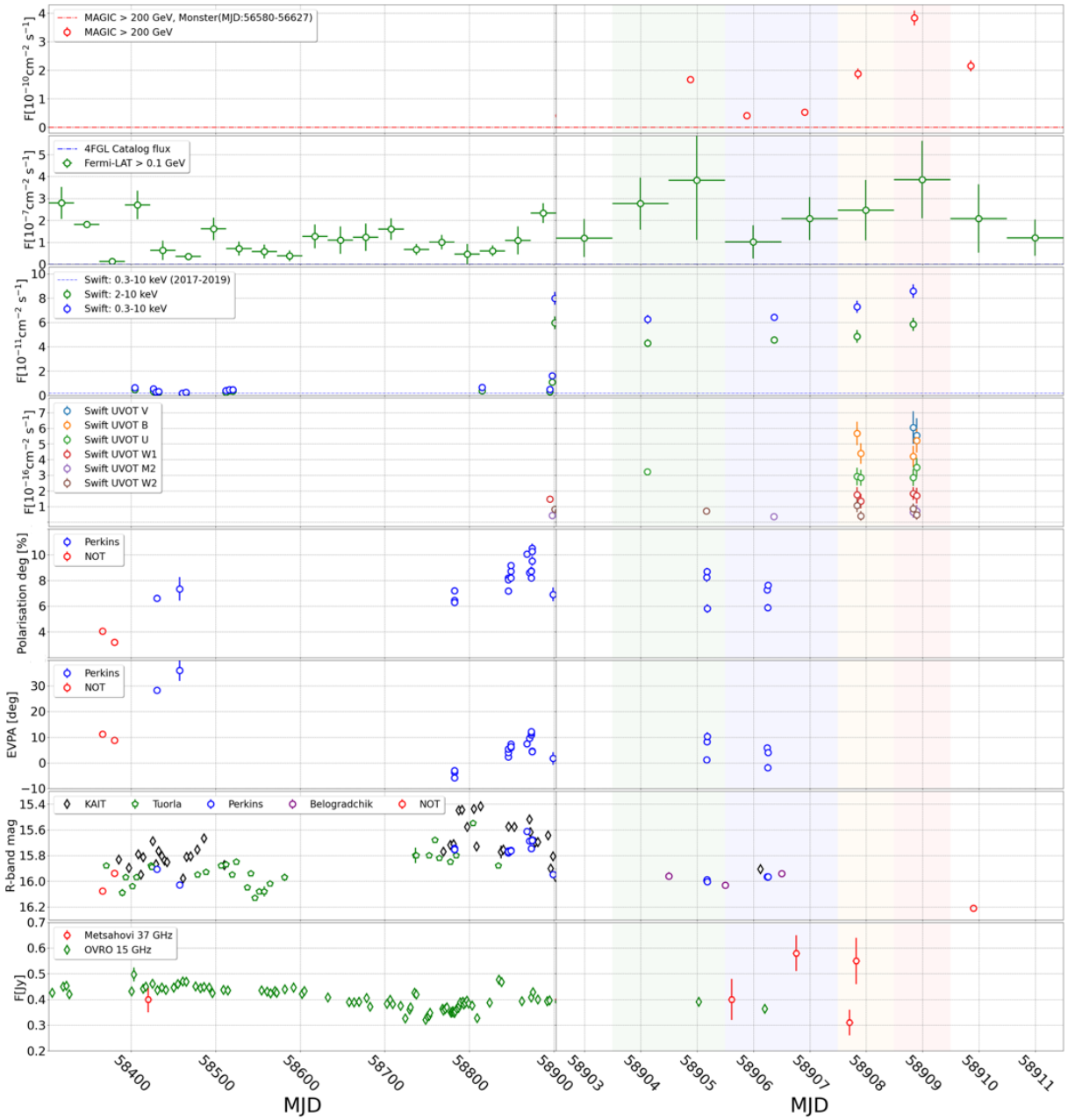

Figure 4.2: VER J0521+211 MWL light curve where the **left half** shows the long term (2017-2020) and the **right half** shows the short term (Feb-March 2020) evolution of the source. The individual energy bands are ordered in order of decreasing frequencies from top to bottom: VHE gamma-rays from MAGIC (E > 200 GEV) (with a reference value from Acciari et al. (2020)), HE gamma-ray flux (0.1-300 GeV) from *Fermi*-LAT (with the reference flux from the 4FGL), X-ray flux between 2-10 keV (blue) and 0.3-10 keV (blue) by *Swift*-XRT (indicating flux for non-active low state from 2017-2019), UV and optical in various bands from *Swift*-UVOT, R-band magnitudes from various optical telescopes as well as evolution of the long-term polarisation and EVPA. Radio flux densities at 15 GHz (green) and 37 GHz (red) from OVRO and Metsähovi, respectively.

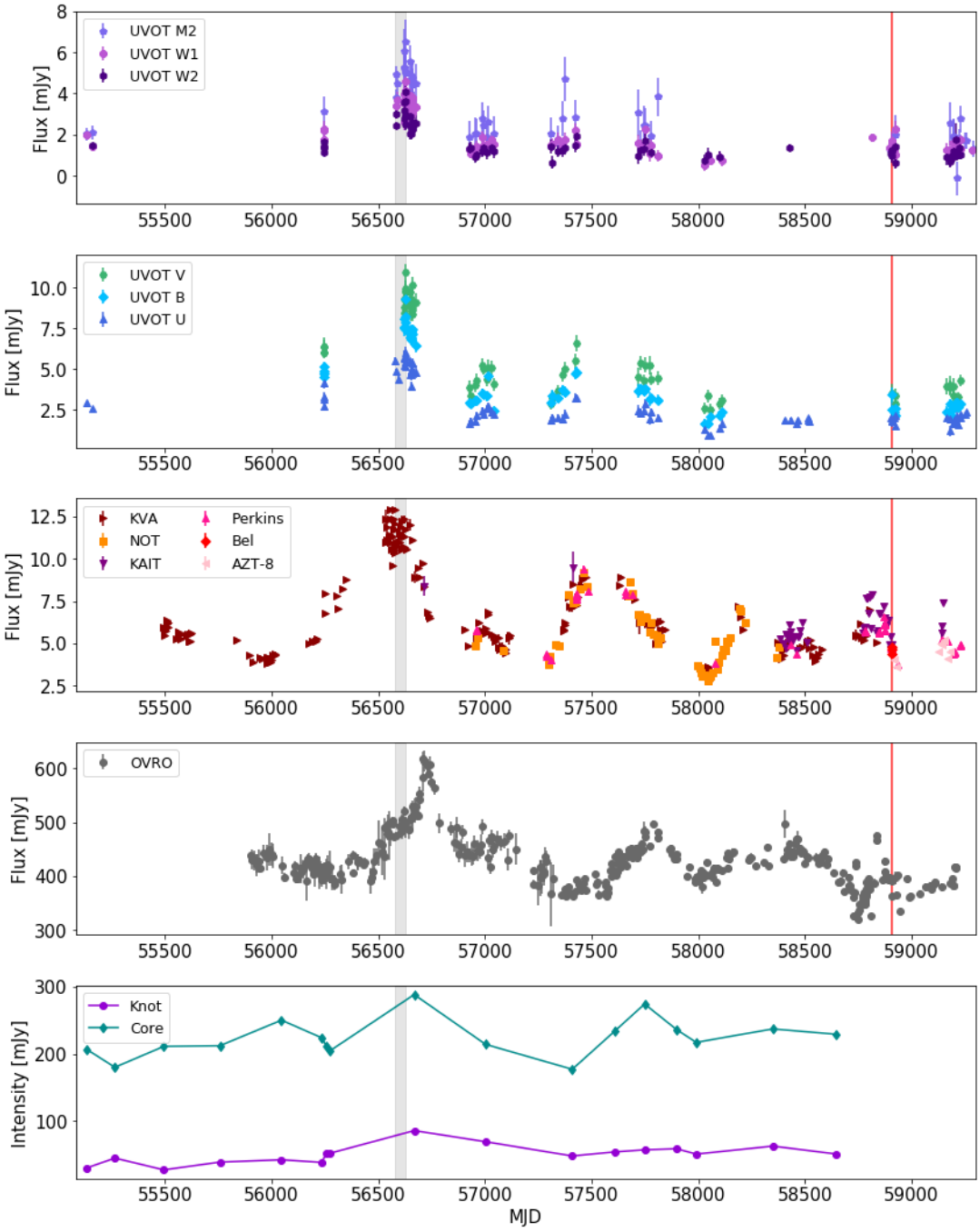

Figure 4.3: Long-term MWL light-curve with the UV bands (UVOT; M2, W1, W2), optical (UVOT; V, B, U), R-band (KVA, NOT, KAIT, Perkins, Belogradchik, AZT-8), radio (OVRO; 15 GHz), and VLBI intensity (MOJAVE; 15 GHz). The red vertical line indicates the epoch of the VHE gamma-ray flare observed during the spring of 2020, and the grey-shaded area indicates the epoch of the previous VHE gamma-ray flare reported in Prokoph et al. (2015).

4.4.2 Redshift Upper Limit

An accurate distance estimate for VER J0521+211 remains elusive. Nevertheless, a lower-limit estimate to its redshift could be established at z ≈ 0.18 (Paiano et al.; 2017). The uncertainty on its distance stems from a lack of emission lines in the optical emission spectrum of VER J0521+211 itself, thus making it challenging to obtain a proper estimate for this particular blazar. On the other hand, there is a possibility to study VHE gamma ray spectra the footprint induced by the EBL. Following the methodology described in (Acciari; 2019), I obtained an estimate of the upper limits of the redshift using a maximum likelihood fit with a concave log-parabola as the spectral model of the HE- and VHE-datasets (*Fermi*-LAT and MAGIC) of each epoch (A-D). Using all of the EBL models reported in (Acciari; 2019), we found that the uncertainties due to EBL model selection are negligible compared to the instrumental uncertainties. Thus we use the model described in (Dominguez et al.; 2011) to obtain 95% confidence level upper-limits on the source redshift. The instrumental uncertainties are estimated by tuning the simulated total light throughput with increments of ±15%. As shown in Figure 4.4, each period would in principle provide constraints for the upper limit. Nevertheless, the most stringent constraint comes from epoch D yielding a redshift upper limit with 95% confidence level of $z \leq 0.243$, which is consistent with the lower limit reported in (Paiano et al.; 2017). Our results allow to limit the parameter space of the redshift value to the range $0.18 \leq z \leq 0.243$. In order to calculate intrinsic properties of VER J0521+211 we use the lower limit established by (Paiano et al.; 2017) (see also results in Section 4.4.3).

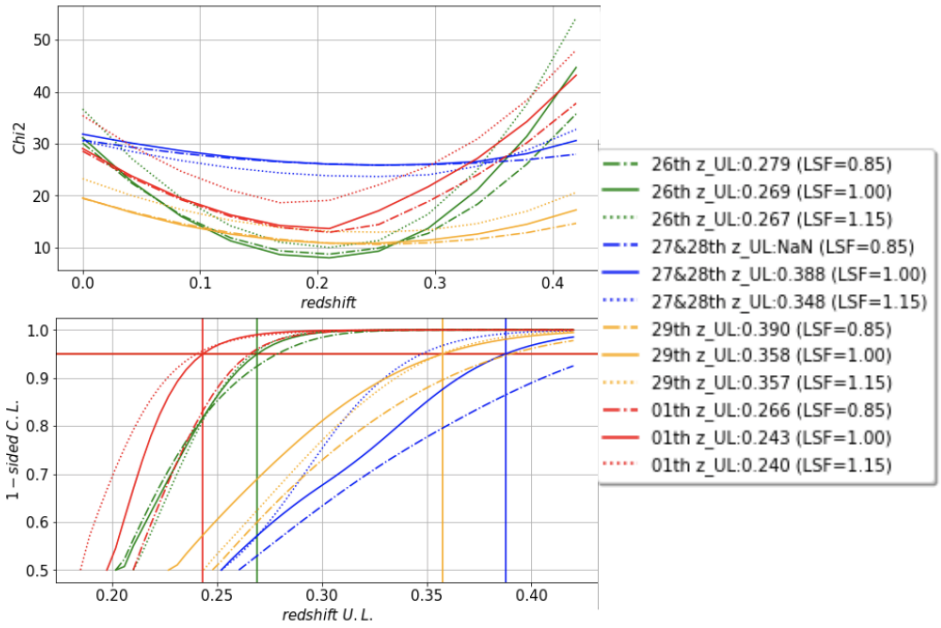

Figure 4.4: Findings when performing redshift scan in each period by using constraints from *Fermi*-LAT and varying the light throughput. The **upper plot** shows the minima of the chi-2 estimates, whereas the **lower plot** marks the 95% confidence level upper limits on the source redshift.

4.4.3 Spectral Energy Distribution Modeling

The 2020 MWL campaign on a flaring state of VER J0521+211, allowed to perform several measurements for its respective broadband SED. Based on the assumption of different emission scenarios, this eventually allowed to compare the predictions of several emission models with the obtained data. Also, the short-term variability in the recorded photon flux (shown at energies above the X-ray band) permits to elaborate sets of parameters for each emission model, where each one can adequately describe the night-wise evolution for that particular flaring state.

Considered Emission Models In order to fit the observational data, we assumed different emission models, which we outline in order of elaboration:

- **One-Zone leptonic SSC model;** The simplified case of a one-zone leptonic SSC model was excluded from our model list. Although, it remains very successful in describing a plethora of flaring blazars (Acciari et al.; 2020), in our case it is not possible to obtain a set of parameters that adequately model the short-term variability of VER J0521+211. Moreover, for this particular flaring state, the one-zone SSC model does not agree with the observations, since radio and optical bands show no notable short-term flux variability (see also Table 4.3).

- **Two-zone non-interacting leptonic SSC model;** In the framework of the two-zone SSC model, the steady low radio and optical fluxes stem from a larger region ("core") whose parameters remain constant over time, whilst the flare is constrained to a small emission region ("blob") whose parameters are time-dependent. Depending on the potential interaction of these two zones, one can specify whether or not there is interaction (photon feedback) between their underlying leptonic populations. For example, photons generated during synchrotron and/or SSC processes from one region could act as seed photons for the other region. In principle one could distinguish between these two case, however, this study is beyond the scope of this work.

- **One-zone lepto-hadronic model;** If we allow for leptohadronic interactions the obtained parameters of our one-zone leptohadronic model describe very accurately the short-term variability of VER J0521+211.

Used Emission Models In order to fit the observational data, we eventually elaborated three different emission models:

- Two-zone non-interacting leptonic SSC model (one by myself, one by Nievas Rosillo)

- One zone leptohadronic model (one by Omelikuh and Rodrigues)

Two-zone non-interacting leptonic SSC model Since for this particular flaring state of VER J0521+211 the various energy bands seem to follow two sorts of general trends (see also Table 4.3), individually time-constrained SEDs were modelled with non-interacting two-zone SSC models. These models are composed of two differently sized spherical regions, both filled with a population of relativistic electrons with energy distributions given by their respective broken power laws. Based on the assumption that both regions are physically well separated and that there is no significant interaction (in the form of photon feedback) between their underlying leptonic populations, we assume that photons generated by the synchrotron and/or SSC processes in one region are not subject to Compton up-scattering in the other region. Furthermore, we assume that 'self-absorption' due to pair production in the other region can be neglected.

- **Parameter-set I by M. Artero;** Starting from a previously obtained set of modeling parameters, as reported in (Acciari et al.; 2020) I elaborated a two-component models that successfully describe the time-constrained spectral data from radio frequencies up to the VHE band (as shown in Figure 4.5) with model parameters given in Table 4.4. We note that such a simple 2-zone model almost successfully (see mismatch at X-ray frequencies in Period B and at VHE energies in Period A and C) reproduces the evolving spectra with minor parameter changes, i.e. Lorentz factors $\gamma_{\mathrm{min,break,max}}$, as shown on the left half of Figure 4.5. Note that the γ-factors seem to undergo a similar temporal evolution as the photon fluxes of the different energy bands in the MWL light-curve (see Figure 4.2 and Table 4.3).

- **Parameter set II by M. Nievas;** Starting from a previously obtained set of modeling parameters, as reported in (Acciari et al.; 2020) we elaborated a two-component models that successfully describe the time-constrained spectral data from radio frequencies up to the VHE band (as shown in Figure 4.7) with model parameters given in Table 4.5. We note that such a simple 2-zone model successfully reproduces the evolving spectra with just changes in the Lorentz factors $\gamma_{\mathrm{min,break,max}}$, the magnetic field intensity B and the electron density $N*$. The time-resolved broadband SEDs are shown in Figure 4.7 with the considered emission models that we are going to discuss in the following subsections.

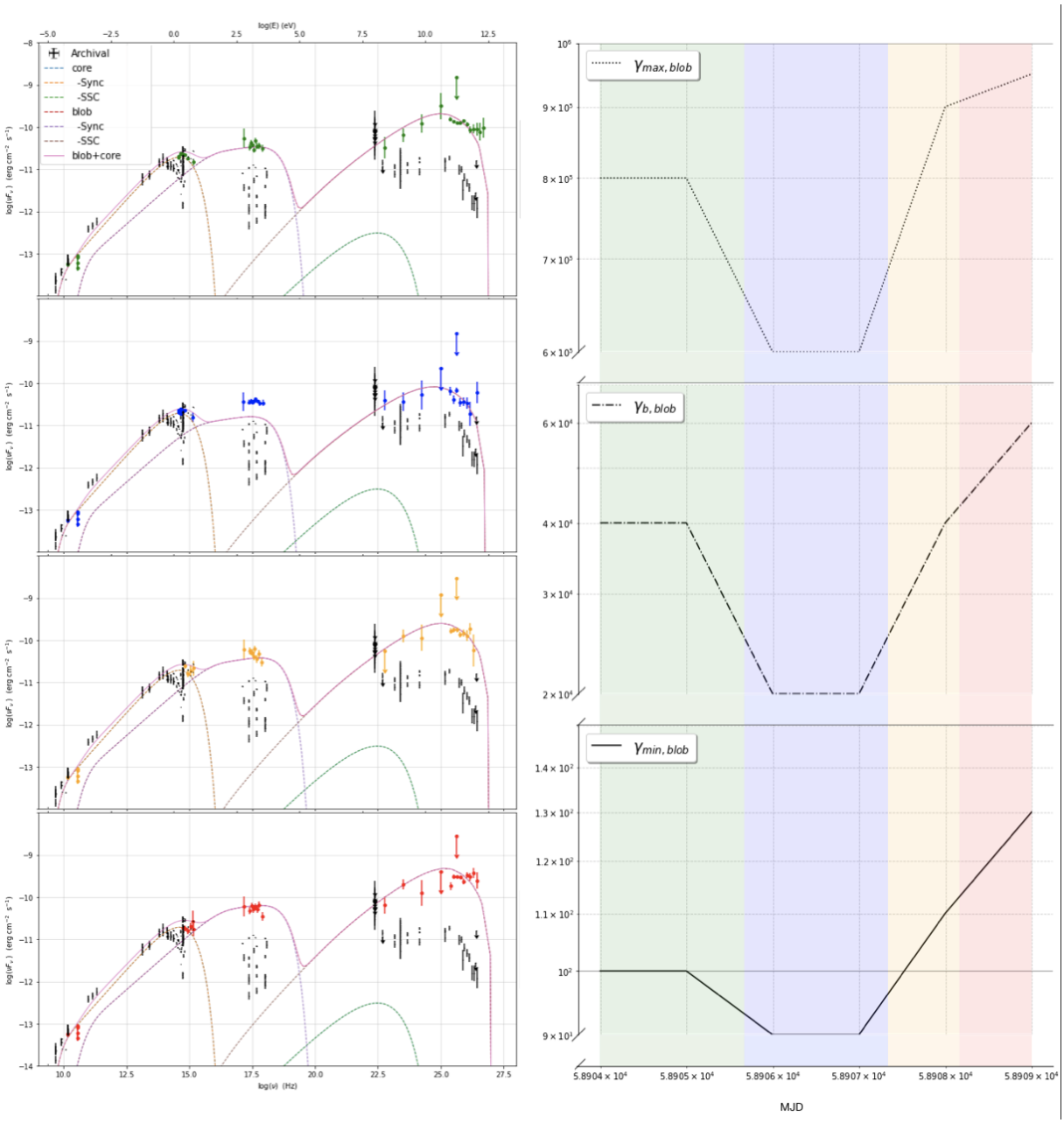

Figure 4.5: Broadband SEDs of the four observation epochs listed in Table 4.3. The **left plot** shows the obtained flux predictions from the two-zone leptonic models of each period, whereas the **right plot** shows the temporal evolution of the γ-factors along the four states. Note that in both plots the colors match with the states defined in Table 4.3.

Campaign State	Epoch [MJD]	Model (region)	$\gamma_{\rm min}$ [$\times 10^3$]	$\gamma_{\rm b}$ [$\times 10^4$]	$\gamma_{\rm max}$ [$\times 10^5$]	n_1	n_2	B [G]	N^* [cm^{-3}]	R [$\times 10^{15}$ cm]	δ
2020	58903.5-58905.5	2-zone (blob)	0.1	4.0	8.0	1.95	2.8	0.15	200	13	12
A		2-zone (core)	0.001	0.8	0.15	1.65	2.9	0.15	0.6	370	11
2020	58905.5-58907.5	2-zone (blob)	0.09	2.0	6.0	1.95	2.8	0.15	200	13	12
B		2-zone (core)	0.001	0.8	0.15	1.65	2.9	0.15	0.6	370	11
2020	58907.5-58908.5	2-zone (blob)	0.11	4.0	9.0	1.95	2.8	0.15	200	13	12
C		2-zone (core)	0.001	0.8	0.15	1.65	2.9	0.15	0.6	370	11
2020	58908.5-58909.5	2-zone (blob)	0.13	6.0	9.5	1.95	2.8	0.15	200	13	12
D		2-zone (core)	0.001	0.8	0.15	1.65	2.9	0.15	0.6	370	11

Table 4.4: Best-fit parameters of the non-interacting two-zone model. Columns: (1) state; (2) epoch; (3) model (emission region); (4), (5) and (6) minimum, break, and maximum electron Lorentz factor, respectively; (7) and (8) slopes of electron distribution below and above γ_b, respectively; (9) magnetic field strength; (10) electron density; (11) emission-region size; (12) Doppler factor.

One-zone leptohadronic model We show in this section that the four observed activity states of the source can be explained in the framework of a one-zone leptohadronic model. To test this scenario, we simulate the interactions of protons and electrons accelerated in the jet using the time-dependent code AM^3 (Gao et al., 2017). AM^3 numerically solves the system of differential equations describing the spectra of protons, electrons, photons and secondary particles, in a fully time-dependent and self-consistent approach. The emission region parameters of the source and of the accelerated particles are then optimized to provide the best fit for the observations in each of the four states, assuming each of them to originate from the steady-state emission.

The best-fit SEDs for each of the four activity states are shown as solid curves in Fig. 4.7. As we can see, each state can be explained in a one-zone paradigm where protons are co-accelerated with electrons. As detailed in Tab. 4.6, the emitting region is predicted to be an order of magnitude smaller in size compared to that of the purely leptonic case, while the magnetic field is stronger, of the order of $\sim G$ compared to $\sim mG$ in the leptonic case. The Doppler factor is slightly higher, but still within the limits put by observational constraints, as discussed previously. These three parameters have similar best-fit values among the four observed states, suggesting the same emitting region throughout the observational campaign. Differences in the SED between the four observation epochs are explained by variations in the number and maximum energy of protons and electrons injected into the emission region. On the other hand, the spectral indices seem to undergo almost no variation at all, as would be expected if the same acceleration mechanism is at play in the different epochs.

As shown in more detail in Figure 4.6, in this model the low-energy fluxes (radio to optical) are dominated by leptonic emission from the accelerated electrons, while the MAGIC flux is mainly of hadronic origin (from the interactions of the accelerated protons with the low-energy photon fields in the jet). The GeV range corresponds to the transition region from electron- to proton-dominated emission, and therefore in this model the *Fermi*-LAT fluxes are explained by a superposition of both emission mechanisms.
The photon-proton interactions undergone by the protons also lead to the emission of high-energy neutrinos, mainly from the decay of secondary charged pions. The expected neutrino fluxes are shown in Fig. 4.7 as dash-dotted curves. Because the neutrinos follow the maximum energy of the accelerated protons, their predicted flux in the observer's frame peaks in the ~ 10 PeV range. We can then estimate the predicted number of neutrinos observed by the IceCube observatory from the source during the four epochs. We do this by integrating the emitted neutrino flux spectra over the entire duration of states A, B, C and D, and convolving the resulting fluence with the IceCube effective area in the source's declination band. We obtain a prediction of 0.05, 0.02, 0.03, and 0.10 neutrino events during the respective states. Assuming Poisson statistics, these numbers are compatible with the non-observation of neutrinos from the source reported by Aartsen et al. (2020). This means the leptohadronic model cannot be excluded by current upper limits on the neutrino flux from the IceCube experiment. However, the continued monitoring of the neutrino sky by IceCube and future neutrino telescopes may be able to eventually constrain the lepto-hadronic emission scenario, especially if the source is detected again in the VHE regime.

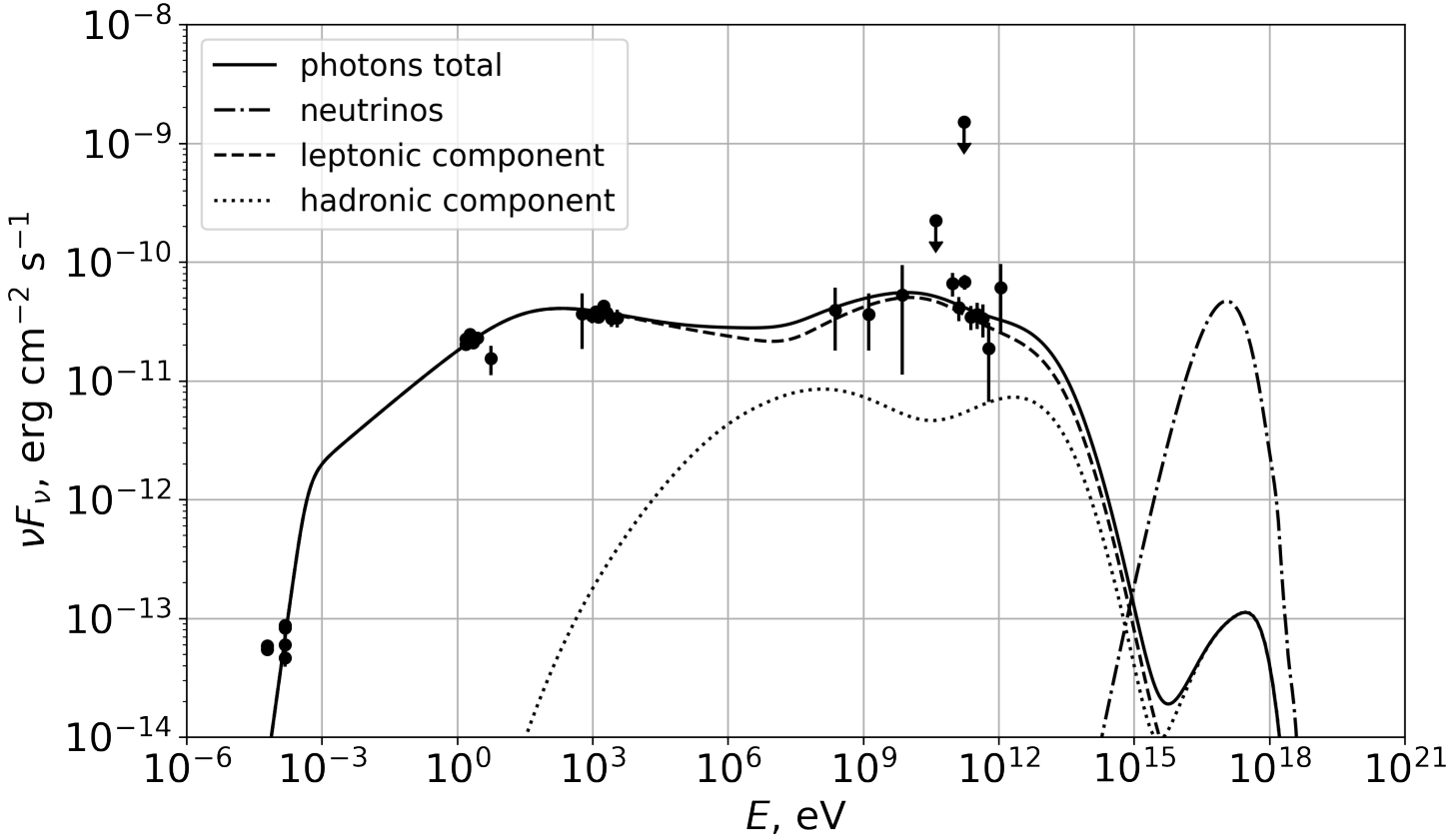

Figure 4.6: Contributions from different radiative processes to the SED of VER J0521+211 (epoch B), in a leptohadronic scenario where protons are accelerated to $\gtrsim$ 10 PeV. Leptonic: synchrotron + IC of injeced electrons, same for electrons from gamma-gamma annihilation Hadronic: synchrotron + IC of injected protons, same for electrons from p-gamma cascades, same for electrons/positrons from charged pion decays; small peak at around $1e^{17}$ eV due to neutral pions decaying into two gamma rays.

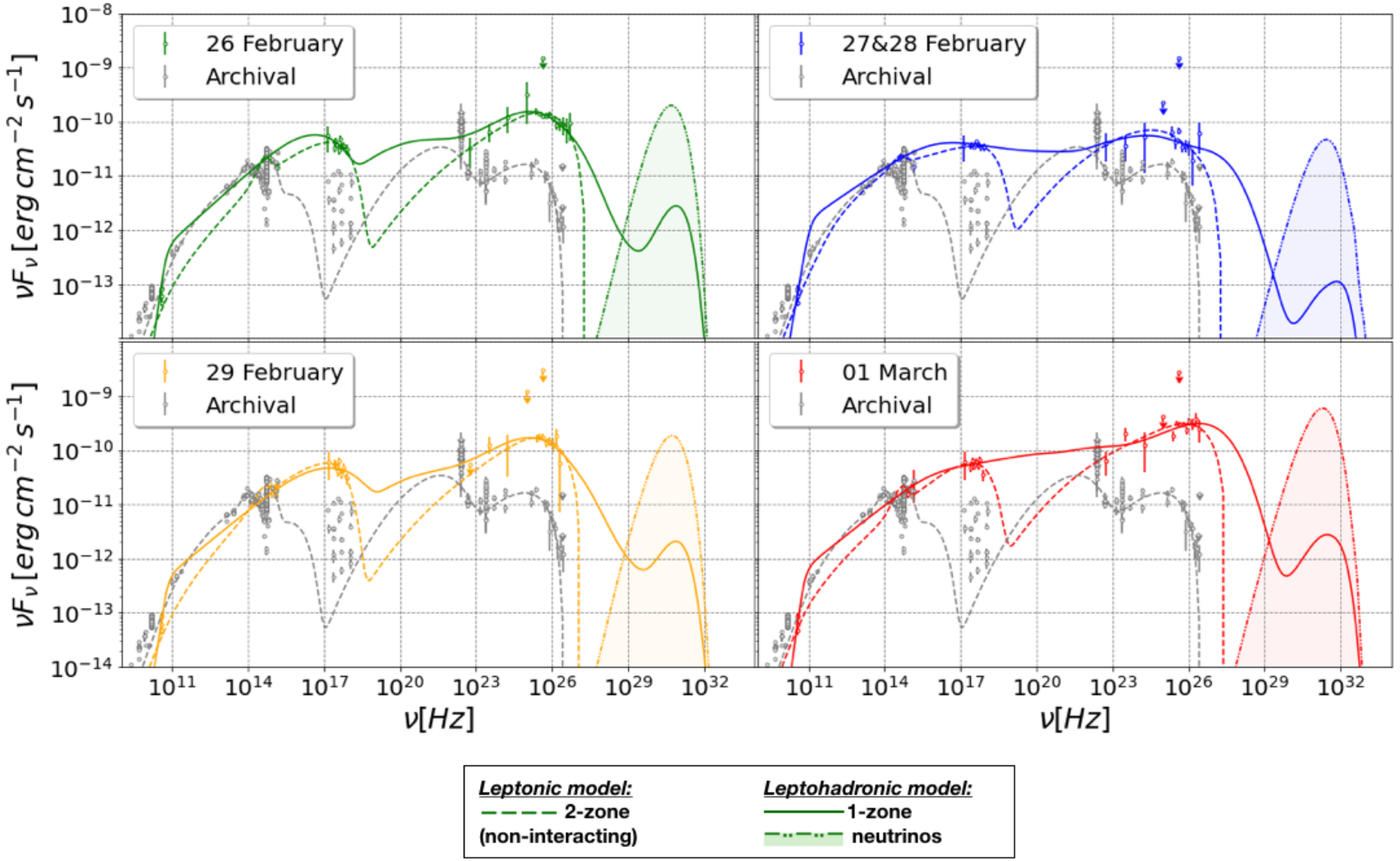

Figure 4.7: Broadband SEDs of the four observation epochs listed in Tab. 4.3. Archival data are shown in grey, while the data contemporary to the four epochs are shown in their respective colours. The fluxes fitted by the two-zone leptonic model (Nievas Rosillo) are shown dashed, while the predictions of the one-zone leptohadronic model are shown as solid lines. The spectra of emitted neutrinos predicted by the leptohadronic model are shown as dash-dotted lines.

State	Epoch [MJD]	Model (region)	$\gamma_{\rm min}$ [$\times 10^3$]	$\gamma_{\rm b}$ [$\times 10^4$]	$\gamma_{\rm max}$ [$\times 10^6$]	n_1	n_2	B [$\times 10^{-3}$G]	N^* [cm^{-3}]	R [$\times 10^{17}$ cm]	$R_{\rm H}$ [$\times 10^{18}$ cm]	δ
A	58903.5-58905.5	2-zone (blob)	1.0	8.0	2.0	1.4	1.4	6.5	0.65	3.7	8.0	11
		2-zone (core)	1.0	1.0	0.2	1.4	1.4	1.5	14.0	3.7	2.0	11
B	58905.5-58907.5	2-zone (blob)	1.0	8.0	2.0	1.4	1.4	17.0	1.8	3.7	8.0	11
		2-zone (core)	1.0	1.0	0.2	1.4	1.4	1.5	14.0	3.7	2.0	11
C	58907.5-58908.5	2-zone (blob)	1.0	7.0	1.4	1.4	1.4	9.0	0.62	3.7	8.0	11
		2-zone (core)	1.0	1.0	0.2	1.4	1.4	1.5	14.0	3.7	2.0	11
D	58908.5-58909.5	2-zone (blob)	1.0	20.0	3.0	1.4	1.4	4.0	0.65	3.7	8.0	11
		2-zone (core)	1.0	1.0	0.2	1.4	1.4	1.5	25.0	3.7	2.0	11

Table 4.5: Best-fit parameters of the non-interacting two-zone model.
Columns: (1) state; (2) epoch; (3) model (emission region); (4), (5) and (6) minimum, break, and maximum electron Lorentz factor, respectively; (7) and (8) slopes of electron distribution below and above γ_b, respectively; (9) magnetic field strength; (10) electron density; (11) emission-region size; (12) Doppler factor.

State	Epoch [MJD]	R_{blob} [$\times 10^{16}$ cm]	δ	B [G]	n_e n_p	γ_e^{min} γ_e^{max}	γ_p^{min} γ_p^{max}	L_e [erg/s] L_p [erg/s]
A	58903.5-58905.5	2.3	14.9	0.2	2.2	1.3×10^1	1.7×10^3	9.6×10^{42}
					1.5	6.1×10^4	1.6×10^7	9.1×10^{46}
B	58905.5-58907.5	1.5	15.6	0.2	2.4	5.7×10^1	3.7×10^3	8.9×10^{42}
					1.5	7.5×10^5	8.5×10^7	3.9×10^{45}
C	58907.5-58908.5	1.9	14.2	0.1	2.2	4.0×10^1	1.8×10^5	1.3×10^{43}
					1.5	8.0×10^5	2.2×10^7	7.5×10^{46}
D	58908.5-58909.5	2.0	14.3	0.2	2.3	1.7×10^1	4.5×10^4	1.1×10^{42}
					1.5	3.1×10^5	6.9×10^7	8.7×10^{46}

Table 4.6: Best-fit parameters of the leptohadronic one-zone model. Columns: (1) state, (2) epoch, (3) blob radius, (4) Doppler factor of the blob (5) magnetic field strength, (6) power-law spectral indexes for electron and proton distribution, (7) minimum and maximum energy for electrons, (8) minimum and maximum energy for protons, (9) electron and proton luminosity.

4.5 Conclusions

In this chapter we reported on the short-term evolution for an active state of the blazar VER J0521+211. Observations were carried out during the spring of 2020, shortly after VER J0521+211 entered into an enhanced flux state. Numerous instruments carried out observations in their respective wavebands, thus covering the broader EM domain. Benefiting from extensive MWL efforts over a time span of four consecutive nights, we study the broadband emission for this particular blazar. Along the MWL campaign, emissions at optical and radio frequencies show no variability and conform to low flux level as reported in archival data sets. On the other hand, for higher photon frequencies, i.e. beyond X-ray energies night-wise variability was measured. Despite VER J0521+211 being a well studied object, a redshift has not been measured yet. Recent observations allowed to obtain lower- and upper-limits to its redshift. Benefiting from our MAGIC VHE-dataset with both contemporaneous HE coverage from *Fermi*-LAT, we manage to determine a conservative 95% confidence level upper limit and constrain the distance of VER J0521+211 to a range of $0.18 \leq z \leq 0243$.

Finally, assuming emission scenarios that are purely based on leptonic models with two emission regions allowed to reproduce the measured broadband SED of VER J0521+211 in a broad frequency range (from radio up to VHE gamma rays). Furthermore, by allowing hadronic interactions, the predictions from the broadband modeling were extended to frequencies beyond the ones observed in this particular MWL campaign. This resulted in predictions for enhanced photon and neutrino fluxes at VHE energies $\sim 10^{31}$ Hz, where the flux enhancement in photons can be accounted for by a decaying π^0 population. Benefiting again from the high cadence of the underlying MWL observations, the modeling was performed for four consecutive epochs. This allowed to measure the temporal evolution of our respective model-parameters.

Bibliography

Aartsen, M. G. et al. (2020). Time-Integrated Neutrino Source Searches with 10 Years of IceCube Data, *Phys. Rev. Lett.* **124**(5): 051103.

Abdollahi, S., Acero, F., Ackermann, M., Ajello, M., Atwood, W., Axelsson, M., Baldini, L., Ballet, J., Barbiellini, G., Bastieri, D. et al. (2020). Fermi large area telescope fourth source catalog, *ApJS* **247**(1): 33.

Acciari, V. A., Ansoldi, S., Antonelli, L. A., Arbet Engels, A., Baack, D., Babić, A., Banerjee, B., Barres de Almeida, U., Barrio, J. A. and et al. (2020). Testing two-component models on very high-energy gamma-ray-emitting bl lac objects, *Astronomy Astrophysics* **640**: A132.
URL: *http://dx.doi.org/10.1051/0004-6361/202037811*

Acciari, V. A. e. a. (2019). Measurement of the extragalactic background light using MAGIC and Fermi-LAT gamma-ray observations of blazars up to z = 1, **486**(3): 4233–4251.

Acero, F., Ackermann, M., Ajello, M., Albert, A., Baldini, L., Ballet, J., Barbiellini, G., Bastieri, D., Bellazzini, R., Bissaldi, E. et al. (2016). Development of the model of galactic interstellar emission for

standard point-source analysis of fermi large area telescope data, *The Astrophysical Journal Supplement Series* **223**(2): 26.

Ahnen, M., Ansoldi, S., Antonelli, L., Arcaro, C., Babić, A., Banerjee, B., Bangale, P., Barres de Almeida, U., Barrio, J., Becerra González, J. and et al. (2017). Performance of the magic telescopes under moonlight, *Astroparticle Physics* **94**: 29–41.
URL: *http://dx.doi.org/10.1016/j.astropartphys.2017.08.001*

Archambault, S., Arlen, T., Aune, T., Behera, B., Beilicke, M., Benbow, W., Bird, R., Bouvier, A., Buckley, J., Bugaev, V. et al. (2013). Discovery of a new tev gamma-ray source: Ver j0521+ 211, *ApJ* **776**(2): 69.

Atwood, W., Albert, A., Baldini, L., Tinivella, M., Bregeon, J., Pesce-Rollins, M., Sgrò, C., Bruel, P., Charles, E., Drlica-Wagner, A. et al. (2013). Pass 8: toward the full realization of the fermi-lat scientific potential, *arXiv preprint arXiv:1303.3514* .

Breeveld, A., Curran, P., Hoversten, E., Koch, S., Landsman, W., Marshall, F., Page, M., Poole, T., Roming, P., Smith, P. et al. (2010). Further calibration of the swift ultraviolet/optical telescope, *MNRAS* **406**(3): 1687–1700.

Burrows, D. N., Hill, J. E., Nousek, J. A., Wells, A. A., Chincarini, G., Abbey, A. F., Beardmore, A. P., Bosworth, J., Bräuninger, H. W., Burkert, W., Campana, S., Capalbi, M., Chang, W., Citterio, O., Freyberg, M. J., Giommi, P., Hartner, G. D., Killough, R., Kittle, B., Klar, R., Mangels, C., McMeekin, M., Miles, B. J., Moretti, A., Mori, K., Morris, D. C., Mukerjee, K., Osborne, J. P., Short, A. D. T., Tagliaferri, G., Tamburelli, F., Watson, D. J., Willingale, R. and Zugger, M. E. (2004). The Swift X-Ray Telescope, *in* K. A. Flanagan and O. H. W. Siegmund (eds), *X-Ray and Gamma-Ray Instrumentation for Astronomy XIII*, Vol. 5165 of , pp. 201–216.

Dominguez, A., Primack, J. R., Rosario, D., Prada, F., Gilmore, R., Faber, S., Koo, D., Somerville, R., Pérez-Torres, M., Pérez-González, P. et al. (2011). Extragalactic background light inferred from aegis galaxy-sed-type fractions, *Monthly Notices of the Royal Astronomical Society* **410**(4): 2556–2578.

Fallah Ramazani, V., Lindfors, E. and Nilsson, K. (2017). Empirical multi-wavelength prediction method for very high energy gamma-ray emitting BL Lacertae objects, **608**: A68.

Fruck, C. and Gaug, M. (2015). Atmospheric monitoring in magic and data corrections.

Gao, S., Pohl, M. and Winter, W. (2017). On the direct correlation between gamma-rays and pev neutrinos from blazars, *ApJ* **843**(2): 109.

Jorstad, S. and Marscher, A. (2016). The vlba-bu-blazar multi-wavelength monitoring program, *Galaxies* **4**(4).
URL: *https://www.mdpi.com/2075-4434/4/4/47*

Li, W., Filippenko, A. V., Chornock, R. and Jha, S. (2003). The katzman automatic imaging telescope gamma-ray burst alert system, and observations of GRB 020813, *Publications of the Astronomical*

Society of the Pacific **115**(809): 844–853.
URL: *https://doi.org/10.1086/376432*

Lindfors, E., Hovatta, T., Nilsson, K., Reinthal, R., Ramazani, V. F., Pavlidou, V., Max-Moerbeck, W., Richards, J., Berdyugin, A., Takalo, L. et al. (2016). Optical and radio variability of the northern vhe gamma-ray emitting bl lacertae objects, *Astronomy & Astrophysics* **593**: A98.

Lister, M. L., Aller, M. F., Aller, H. D., Hodge, M. A., Homan, D. C., Kovalev, Y. Y., Pushkarev, A. B. and Savolainen, T. (2018). MOJAVE. XV. VLBA 15 GHz Total Intensity and Polarization Maps of 437 Parsec-scale AGN Jets from 1996 to 2017, **234**(1): 12.

Nilsson, K., Lindfors, E., Takalo, L. O., Reinthal, R., Berdyugin, A., Sillanpää, A., Ciprini, S., Halkola, A., Heinämäki, P., Hovatta, T., Kadenius, V., Nurmi, P., Ostorero, L., Pasanen, M., Rekola, R., Saarinen, J., Sainio, J., Tuominen, T., Villforth, C., Vornanen, T. and Zaprudin, B. (2018). Long-term optical monitoring of TeV emitting blazars. I. Data analysis, **620**: A185.

Paiano, S., Landoni, M., Falomo, R., Treves, A., Scarpa, R. and Righi, C. (2017). On the redshift of tev bl lac objects, *ApJ* **837**(2): 144.

Poole, T., Breeveld, A., Page, M., Landsman, W., Holland, S., Roming, P., Kuin, N., Brown, P., Gronwall, C., Hunsberger, S. et al. (2008). Photometric calibration of the swift ultraviolet/optical telescope, *MNRAS* **383**(2): 627–645.

Prokoph, H., Schultz, C. and Da Vela, P. (2015). Time-resolved multiwavelength observations of the blazar VER J0521+211 from radio to gamma-ray energies, *34th International Cosmic Ray Conference (ICRC2015)*, Vol. 34 of *International Cosmic Ray Conference*, p. 864.

Richards, J. L., Max-Moerbeck, W., Pavlidou, V., King, O. G., Pearson, T. J., Readhead, A. C., Reeves, R., Shepherd, M. C., Stevenson, M. A., Weintraub, L. C. et al. (2011). Blazars in the fermi era: the ovro 40 m telescope monitoring program, *ApJS* **194**(2): 29.

Schlafly, E. F. and Finkbeiner, D. P. (2011). Measuring reddening with sloan digital sky survey stellar spectra and recalibrating sfd, *ApJ* **737**(2): 103.

Takalo, L. O., Nilsson, K., Lindfors, E., Sillanpää, A., Berdyugin, A. and Pasanen, M. (2008). Tuorla Blazar Monitoring Program, *in* F. A. Aharonian, W. Hofmann and F. Rieger (eds), *American Institute of Physics Conference Series*, Vol. 1085 of *American Institute of Physics Conference Series*, pp. 705–707.

Teräsranta, H., Tornikoski, M., Mujunen, A., Karlamaa, K., Valtonen, T., Henelius, N., Urpo, S., Lainela, M., Pursimo, T., Nilsson, K. et al. (1998). Fifteen years monitoring of extragalactic radio sources at 22, 37 and 87 ghz, *A&AS* **132**(3): 305–331.

Thompson, D. J. (2019). The fourth fermi lat source catalog (4fgl), *AAS/High Energy Astrophysics Division* **17**: 109–33.

VERITAS&MAGIC et al. (2022). Multiwavelength observations of the blazar ver j0521+ 211 during an elevated tev gamma-ray state, *arXiv preprint arXiv:2205.02808* .

Willingale, R., Starling, R. L. C., Beardmore, A. P., Tanvir, N. R. and O'Brien, P. T. (2013). Calibration of X-ray absorption in our Galaxy, **431**(1): 394–404.

Wood, M., Caputo, R., Charles, E., Di Mauro, M., Magill, J. and Perkins, J. (2017). Fermipy: An open-source python package for analysis of fermi-lat data.
URL: *https://arxiv.org/abs/1707.09551*

Zanin, R., Carmona, E., Sitarek, J., Colin, P., Frantzen, K., Gaug, M., Lombardi, S., Lopez, M., Moralejo, A., Satalecka, K., Scapin, V. and Stamatescu, V. (2013). MARS, The MAGIC Analysis and Reconstruction Software, *International Cosmic Ray Conference*, Vol. 33 of *International Cosmic Ray Conference*, p. 2937.

CHAPTER 5

ToOpy FOR MULTI-MESSENGER ASTRONOMY

Resume: The work presented in this chapter is a publication in preparation for which I am the main author. The methodologies were elaborated and implemented by myself. The underlying algorithm of ToOpy is publicly available (see also https://github.com/arterom/ToOpy) with a setup guide provided in therein's "README.md" file. The inclined reader is encouraged to set up the conda-environment and to follow along with the examples provided in Sections 5.3.2, 5.3.3 and 5.3.4.

Contents

Previously discussed transient phenomena, e.g. AGN flares, CCSN and CBC, exhibit properties that result in the emission of various messengers and hence yield prospects with regards to the MM approach (see also Chapter 3). On one hand, there are neutrino and GW observatories, such as IceCube and LIGO/Virgo that have almost all-sky FoVs as well as satellite-based instruments, e.g. *Fermi*, *Swift* and INTEGRAL, that are able to monitor the whole sky with very low cadence, e.g. ∼1 hour for *Fermi*-GBM.

Ground-based facilities and small-dish optical telescopes that operate in the EM domain, on the other hand, are characterized by much smaller FoVs and have limited duty cycles (see also Table 2.2). In order to perform time-domain astronomy and thus operate in synergy with full-sky monitoring facilities as well as satellite-based observatories, they require elaborate strategies.

The General Coordinates Network (GCN) proves to be a powerful system, that enables the exchange of time critical information within the MM community. Its initial purpose was to quickly disseminate information about GRBs to astronomers around the world. Nowadays, the evolved GCN/Transient Astronomy Network system[1], provides real-time notification on a variety of transient phenomena, hence allowing to rapidly coordinate follow-up observations with telescopes on the ground and in space.

Catering to the inherently limited survey capacity of small FoV telescopes, and IACTs in particular, I developed a set of tools that upon receiving GCN notices, combines information from various data sources. Doing so allows isolating promising astrophysical objects and/or sky regions that could potentially harbour EM signatures for a transient event. This in return allows an IACT to swiftly react to promising alerts, therefore facilitating follow-ups of potential counterpart signals.

Going through this chapter, I will motivate the use case of a set of self-contained tools that allows the user to establish a connection to the GCN system, thereafter acting as both data broker and observation scheduler (Section 5.1). Upon establishing the methodology of all the subroutines from my algorithm in Section 5.2, I will give an overview on its performance by quantifying its response time for scheduling ToO observations as well as by elaborating on reference output (Section 5.3). I then outline in Section 5.4 the prospects for future efforts and possible implementations.

5.1 Motivation and Overview

In the particular case of GW alerts, one of the main stepping stones when attempting ToO observations can be attributed to large localization errors inferred from the underlying signal ($\sim$20–1000 deg^2) (Abbott et al.; 2020). Similar drawbacks, albeit not with such large localization errors, commonly plague efforts to follow-up IceCube, *Fermi*-GBM and *Swift*-GRB alerts. On top of that, further complications arise due to the necessity to localise EM counterparts fast enough in order to get a glimpse of their rapidly decaying signals. Since IACT systems aim at detecting signatures from SGRBs and hadronic mechanisms in jets, the aforementioned limitations are especially constricting. Hence, follow-ups of CBCs and flaring AGNs, require elaborate strategies in order to maximise the possibility to detect the EM counterpart.

Learning from the lessons of the the three observing runs of the current GW interferometers, several strategies and algorithms were proposed in the literature. Whilst there is a significant diversity of open-source tools that facilitate follow-ups, the majority can be categorized in two distinct approaches:

- ◇ **Tilling-Approach** **Andreoni et al.** (**2019**) In simple terms it can be described as a scanning

[1] https://gcn.gsfc.nasa.gov

approach for which the uncertainty region of a given alert is covered in patches whose size is based on the camera footprint of a given instrument. Hence, overall coverage is thus optimised to the FoV of the underlying telescope. Following this particular approach is especially promising for large FoV optical telescopes that can cover uncertainty area in short time spans. However, for small FoV instruments this approach might not be feasible. IACTs for example, also require to point for extended periods at the same spot in order to gather enough data. On the other hand, the next generation CTA observatory might be able to perform divergent pointing Gérard (2015) and benefit from its increased sensitivity, thus allowing to perform fast scans of the whole uncertainty regions.

- ◇ **Galaxy-Targeted Gehrels et al. (2016)** The working principle is to cross-match the localization errors of a given alert with the positions of known galaxies. Upon applying a 3-dimensional position filter, one is left with a list of potential host galaxies that might provide suitable environments in order to generate neutrinos or GWs. By taking into account various environmental and intrinsic properties of those galaxies one can elaborate additional filters that allow to further constrain the list of potential candidates. Therefore from the initial list, one can obtain a ranked list of the galaxies that most likely could harbour a given counterpart, and thus perform ToO follow-up observations based on that ranked list. The galaxy-targeted follow-up is therefore attractive to instruments with small FoVs and limited sensitivity, that would take too long to cover the full region with a tiling approach and hence can perform selected pointing on specific regions of the sky.

There are several examples of openly available algorithms that readily provide the user with pointing sequences both for the galaxy targeted approach (HOGWARTS; Salmon et al. (2020), MANGOVE; Ducoin et al. (2020)) as well as the tiling-approach (GWemopt; Almualla et al. (2020)). Since my goal is to provide the users with a personalized output, I designed the algorithm in order to implement customized ranking preferences and hence allowing the user to favour certain host galaxies over sky patches. By incorporating a personal scheduler, I furthermore allow to take into account limitations, e.g. geographic localization, FoV's size, as well as constraints such as exposure time and zenith angle, amongst others. Altogether this provides an overall seamless data processing that enables autonomous ToO follow-up operations.

5.2 Methodology

The algorithm implementing these functionalities is named ToOpy and aims at combining the functionality of a data broker and observation scheduler. The broker receives (and treats) alert notices that are injected into the GCN stream by a range of observatories, and enriches therein content with additional information from galaxy catalogs as well as contemporaneous satellite-data products, such as *Swift*, *Fermi*-LAT and *Fermi*-GBM coverage. Once promising astrophysical objects and/or sky regions are ranked in order of priority, the broker provides the scheduler with a list of galaxies or sky tiles, that based on user preferences are converted into pointing sequences for subsequent ToO observations.

The tools are contained in a single conda-environment that is based on various python packages/methods that are summarised in Table 5.1 and illustrated in Figure 5.1. The routine can be divided in two parts,

where the prior takes the role of a broker that intercepts GCN notices and thereafter processes alerts, whilst the latter acts as a scheduler that allows to obtain personalized pointing sequences for seamless ToO follow-up observations.

Broker: The broker converts localization errors for each incoming alert into a so-called Multi-Order Coverage (MOC) maps, thereafter allowing to perform quick geometrical matching between sky regions of different alert streams. Apart from very useful geometrical operation, the MOC instances also feature the possibility to directly query galaxy catalogs. This allows to obtain lists of potential host galaxies that lie within the uncertainty region. The ranking of the constituent of this list can then be performed following a variety of reasoning as well as by checking for spatio-temporal MM coincidences in the same sky regions.

Scheduler: As previously mentioned, my tool is primed toward facilitating personalized ToO-strategies. Hence, by allowing the user to set its specific limitations and preferences, the received output allows for preferential ToO scheduling of galaxies or sky tiles for any given observer.

Method	Implementation	Reference/Module
MOCs (Alerts)	alert retrieval	pyGCN
	spatial coverages	mocpy
	temporal coverages	mocpy
MOCs (Catalogs)	catalog retrieval	VizieR
	spatial coverage	mocpy
Cross-Match	MOC-based	developed
Ranking (Tiling)	probability	developed
	MM-coincidence	developed
Ranking (Targeted)	galaxy targeted	developed
	HE transients	fermipy
Ranking (Spatio-Temporal)	STMOC-based	developed
Scheduling	visibility	astroplan

Table 5.1: Reference on adopted and developed methods.

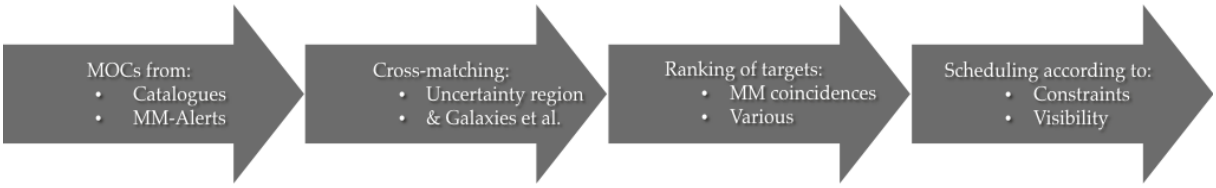

Figure 5.1: Flowchart outlining the main data flow once an alert is received.

In the following subsections, I elaborate on the flowchart in Figure 5.1 and discuss each of the steps that make up the sequence in which our tool processes incoming alerts from IceCube, LIGO/Virgo, *Swift*-BAT and *Fermi*-GBM.

5.2.1 Listening to Alert Streams via pygcn

In order to tap directly into the stream of real-time alerts, the broker-part is equipped with pyGCN[2]. This package enables the user to connect to the GCN stream, and thus allows receiving and processing of alerts from various instrumental facilities as well as space-based observatories. Once a GCN notice is intercepted, its contents are parsed into separate scripts for further processing.
Note that in principle, the GCN notices themselves already contain several data points that in principle serve as filters, e.g. values for false alarm rate, signalness, BNS-probability, etc. Hence, the user could in principle easily configure the scheduler, e.g. "if-" and "while"-loops, in order to exclude alerts at the stage of retrieval. By limiting themselves to react only to promising alerts, this would lowering the rate of triggers which would allow to balance allocated time for ToO observations corresponding to the various alert streams.

5.2.2 Conversion of Alert Contents into mocpy Objects

Once the alert content is extracted from the GCN notice and its referenced files, e.g. ".html"- and ".fits"-files, therein information is parsed into a script that with the functionality of the mocpy package Boch (2019); Baumann et al. (2020) converts the localization error of any given alert into a MOC map Fernique et al. (2019). Once these uncertainty regions are represented in a MOC instance, one can easily query various catalogs of astronomical sources through the CDS VizieR service, thus facilitating the retrieval of known astrophysical objects contained within the localization error of the alerts.

STMOC: By adding time coordinates to our MOC instance, one can promote the prior to a "**S**patio-**T**emporal" MOC (**ST**MOC). As discussed in Greco et al. (2022) a STMOC-based approach to transient alerts, can facilitate searches for kilo/macronova emissions that could happen in the near-time future of a given GW alert and/or are hidden in archival datasets. Our broker is equipped with a method to search for spatio-temporal coincidences between localization errors of *Swift*-BAT, *Fermi*-GBM and LVC alerts

5.2.3 Ranking of Targets

Upon querying catalogs therein objects whose position match the uncertainty region of a transient event are isolated for further processing. In most cases the remaining list is still to extensive and spatially spread (especially for GW alerts). In order to overcome this issue, the broker-part of our tool is designed to gather and combine as much information as possible in order to provide sequential pointing patterns that contain well-motivated host galaxies and/or sky tiles.

Ranking with Archival Catalogue Data In order to isolate the most likely host galaxies, I leverage environmental and intrinsic parameters for each candidate taking into account archival information. Whilst most data points for these cuts are contained within the previously queried galaxy catalogs, they merely contain archival data. Nevertheless with archival data alone one can use various identifiers that are contained in the respective galaxy catalogues, e.g. 4FGL-DR3 and Glade2.

[2] https://github.com/lpsinger/pygcn

◇ **Neutrino Alerts (4FGL Catalog):** After receiving a list of potential host galaxies for a given IceCube alert[3], the possibility of them entering into a flaring state, which in principle should facilitate the emission of high energetic neutrinos should be related to the variability of its host environment. One way to obtain a measure for the historical variability of a given galaxy, is contained in the variability index (aka "VarInd") as reported for sources contained in the 4FGL. Due to the lack of distance information in the 4FGL, a further query of the NED database[4] is performed in order to complement therein information. Adding this information might be crucial in the decision process of galaxy-targeted observations. This is in particular essential for IACTs, since VHE gamma-rays are absorbed due to their interaction with the EBL along their trajectory.

◇ **GW Alerts (Glade Catalogs):** The list of potential host galaxies for a given GW alert can be quite extensive. Hence even after applying a 3-dimensional position cut, which is facilitated due the distance estimates accompanying the GW triggers, setting a pointing sequence is not obvious. Following the consensus that host galaxies for SGRBs can be found in massive galaxies that have high luminosites in the optical blue band, I adopt the Glade catalogs as the main source for performing a ranking based on archival data:

- **Glade2;** For now ToOpy uses therein Absolute Blue Magnitude (BMAG) parameter to set the pointing sequence in order of decreasing luminosities.
- **"Glade+";** Intention to implement the update Glade catalog in the near-term. This would be beneficial due to the much improved coverage as well as therein novel parameter "logRate", which was computed in order to estimate the merger rates for BNS systems within individual galaxies.

◇ **GRB Alerts (Glade Catalogs):** Similar to GW alerts, the potential host galaxies that are contained in the error regions of *Swift*-BAT and *Fermi*-GBM alerts, are numerous. Unfortunately these GRB alerts do not contain distance estimates, and one has thus to wait for further distance information from the follow-up efforts of wide-field optical facilites that are able to detect the afterglow and hence establish a redshift/distance estimate.

Ranking based on the High Energy Transient Sky In order to bridge the uncertainty regarding the current state around these candidate sources, I added two methods that enable direct access to datasets from recent observations of the *Fermi*- and *Swift*-satellites. I argue that by implementing direct feedback from instruments like LAT and GBM (*Fermi*) and BAT (*Swift*) into the decision process, the scheduling of ToO observations could be carried out in full autonomy in case the high-energy sky shows spatially well constrained transient signals occurring contemporaneously to incoming IceCube and GW alerts. In the following, I outline the features of a few scientific instruments that were implemented in order to improve the ranking of pointing sequences.

[3] Based on experience from looking at many TRACK alerts, I incorporated a routine that adds the closest source (in terms of offset from the best-fit position) to the target list for those cases where no 4FGL counterpart is contained within the localization error (see also Section 6.1.2 for a rationale).

[4] https://ned.ipac.caltech.edu

◇ **Neutrino Alerts**: A major drawback of using "VarInd" as a proxy to identify potential hosts for neutrino emission, lies in the fact that it corresponds to information from the 4FGL. Hence, the actual state of the underlying AGN during the current epoch of the observation is priorly unknown. A previous attempt to overcome this uncertainty regarding the current activity of a given HE source, was to query the *Fermi* All-sky Variability Analysis (FAVA) database (Ackermann et al.; 2013). However, since the automatization of this query was not straight forward (e.g. missing routines in order to perform web-parsings that would provide direct feedback to the broker), I opted for implementing fermipy-based analysis routines of weekly datafiles provided by *Fermi*-LAT (Wood et al.; 2017). I use publicly available *Fermi*-LAT data where I focus on selected photons that are contained in the weekly photon files. For the analysis, I limit (for the time being) the analysis to a circular ROI that is centred at the position of the best fit location for any given neutrino alert, i.e. TRACK- and CASCADE-type, and has a radius of 15°. More elaborate analysis strategies, e.g. sequential ROIs, might be implemented in future releases. Adopting the instrument response functions "P8R3_SOURCE_V2", a binned likelihood analysis (0.08° binning in RA and Dec) with 8 bins per decade in energy (range 0.1–300 GeV) is performed, where correction for energy dispersion is included for all sources in the model. Furthermore, the standard quality cuts ("DATA_QUAL 0 & LAT_CONFIG==1") as well as a cut zenith ($z_{max} < 90°$) is applied in order to limit contamination from the Earth's limb. As models I use the Galactic (Acero et al.; 2016) and isotropic diffuse emission models ("gll_iem_v06.fits" and "iso_P8R3_SOURCE_V2_v1.txt", respectively,) as well as all sources listed in the 4FGL that are contained within 15° from the center of the ROI. Upon initializing the analysis with the "gta.setup()" method, I apply a sequence of standard fermipy methods:

- **gta.residmap() and gta.tsmap();** computes HE skymaps and therefore allows to check if any of the known sources in the reference catalog are in an enhanced or flaring state.
- **gta.lightcurve();** in order to compute lightcurves for individual sources.
- **gta.find_sources();** allows to search for new HE sources that are not contained in the reference catalog, e.g. excess photons from a direction that matches no previously known HE source.

◇ **GW/GRB Alerts:** In order to facilitate the follow-up of GW as well as GRB events, I implemented a methodology that searches for spatio-temporal coincidences between newly received GW/GRB notices and recent GRB alerts issued by the *Fermi*-GBM and *Swift*-BAT satellites.

Ranking based on Probabilities of RA/Dec Grid Points for GW Probability Maps In order to enable tiling observations, I overlay the uncertainty region of a GW signal with a densely spaced RA/Dec grid, e.g. 1-3 deg based on FoV. After computing[5] the probability density for each grid point, the algorithm isolates the first pointing at the most probable sky location[6]. Excluding all RA/Dec grid points that lie within the FoV of the first pointing it iteratively selects and excludes grid points in order of decreasing probability density.

[5] https://emfollow.docs.ligo.org/userguide/tutorial/multiorder_skymaps.html#probability-density-at-a-known-position
[6] https://emfollow.docs.ligo.org/userguide/tutorial/multiorder_skymaps.html#most-probable-sky-location

5.2.4 Pointing Sequences via astroplan

Once a ranked list of potential counterparts is obtained, it is essential to check check whether the sky regions of each individual object is actually observable. Depending on the geographical location of the instrument that wants to perform follow-up observations, there is the obvious criteria that ToOs from EM instruments have to be scheduled during night-time. Furthermore, most ground-based observatories are limited by the zenith angle at which the observation has to be performed, as well as its angular separation to the moon. Note that for IACTs the actual limiting factor is the intensity of the Night Sky Background (NSB) and hence the moon phase. The implementation of a constraint on NSB intensity is intended for future releases. In order to take all of these limitations and constraints into account, the scheduler is equipped with the "astroplan" module (Morris et al., 2018). This in turn allows to perform fast visibility computations for any given time-window from any given Earth location. In its own credit, this step could be considered as an additional ranking step, since high priority targets might drop out of the schedule due to unfavourable observational conditions. This occurs quite often for GW alerts, which is not surprising as they come with large localization errors (see also Example 5.3.4).

5.3 Performance and Reference Results

Since both tools (the broker and scheduler) are self-contained within a single conda-environment, ToOpy can be easily installed and run on a local machine. Once the setup is completed, the user is encouraged to modify the scheduler according to their personal preferences:

- ◇ **observatory;** Earth location from where the follow-up will be performed
- ◇ **max_zenith;** angle constraint (in degrees)
- ◇ **moon_separation;** constraint on separation from the moon (in degrees)
- ◇ **time_resolution;** exposure time for each pointing (in hours)
- ◇ **too_span;** scheduling time span to be performed for the trigger, i.e. daily, weekly or monthly.
- ◇ **Preferences for IceCube Alerts:**
  - **fermitools_refdata_path;** path to the fermitool reference datasets, e.g. 4FGL diffuse emission models.
  - **lightcurve;** boolean for running the gta.lightcurve() method (if "True" it computes the lightcurve for the source with the smallest offset from the best-fit position)
- ◇ **Preferences for GW Alerts:**
  - **instrument_FOV;** FoV of the instrument that performs the follow-up observations (in degrees)
  - **ranking;** selection of adopting a targeted or tiling mode (via corresponding string)

- **mode;** selection of whether there is user-readable diagnostic output or not

Once the constraints are fixed, the broker can start to receive and proces incoming GCN alerts of the data streams specified in Table 5.2.

Table 5.2: Currently tapped alert streams

Observatory (Messenger)	Type	ID
IceCube (Neutrino)	GOLD	174
	BRONZE	173
	CASCADE	176
Fermi-GBM (Photon)	Flight-Position	111
	Ground-Position	112
	Final-Position	115
	Subthreshold	131
LVC (GW)	LVC_PRELIMINARY	151
Swift-BAT (Photon)	SWIFT_BAT_GRB_POS_ACK	61

For the time being the broker deals with the reported data streams. Nevertheless, there are many more streams[7], which will be implemented into future releases of ToOpy. In the following, I will elaborate on the temporal response of ToOpy to fake GCN notices (see also Section 5.3.1) therefore quantifiying the performance of its ranking and scheduler methodologies to incoming alerts. The inclined user is invited to test the pipeline by following the set-up and test guide provided on github (see also https://github.com/arterom/ToOpy).

[7] https://github.com/lpsinger/pygcn/blob/main/gcn/notice_types.py

5.3.1 Alert Processing Speed

Rankings Computations The obtained time performance for the different ranking methodologies currently implemented in ToOpy is reported in Table 5.3.

Ranking Approach	Alert Stream	Time [seconds]
Targeted (Glade2 - BMAG Top10)	LVC*	11 ± 1
	Fermi-GBM**	∼11
Targeted (4FGL - VarInd Top10)	IceCube TRACK**	∼6
	IceCube CASCADE***	8 ± 1
Targeted (fermipy - 15 deg ROI)	IceCube CASCADE***	655 ± 85
Targeted (fermipy - 30 deg ROI)		3397 ± 1604†
Targeted (fermipy - LC)		∼5*60/lightcurve bin
Tiling (performance-mode)	LVC*	4 ± 2
STMOC (generation)	*Fermi*-GBM**	∼11
STMOC (generation)	*Swift*-BAT**	∼9
STMOC (crossmatch)	*Fermi*-GBM** ⋃ *Swift*-BAT**	∼5

Table 5.3: Performance of ranking for the different types of alerts processed by ToOpy.
*; The response time (mean ± standard deviation) was computed for a set of fake GW triggers (GraceID=MS230117$_{a,b,..j}$). **; The response time (approximate) was computed for single triggers, namely *Fermi*-GBM with Trignum=691590290 (see also Section 5.3.3), IceCube TRACK with IC220303A (see also Section 6.1.2) and *Swift*-BAT with Trignum=1142847 (see also Section 5.3.3). ***; The response time (mean ± standard deviation) was computed for all IceCube CASCADE triggers from 2022 (see also Table 6.1). †; fermipy analysis takes time since some ROIs contain the Galactic plane.

Visibility Computation Table 5.4 summarizes the performance for the visibility computation of the different rankings. Note that by setting a cutoff at 10 targets per ranking, the time response is of the same order for the different alert streams.

Ranking Approach	Alert Stream	Time [seconds]
Targeted (Glade2 - BMAG Top10)	LVC*	6 ± 2
	Fermi-GBM**	∼7
Targeted (4FGL - VarInd Top10)	TRACK**	∼2
	CASCADE***	8 ± 1
Tiling (performance-mode)	LVC*	5 ± 1

Table 5.4: Performance of the scheduler to elaborate pointing sequences for the different rankings.
*; The response time (mean ± standard deviation) was computed for a set of fake GW triggers (GraceID=MS230117$_{a,b,..j}$). **; The response time (approximate) was computed for single triggers, namely *Fermi*-GBM with Trignum=691590290 (see also Section 5.3.3) and IceCube TRACK with IC220303A (see also Section 6.1.2). ***; The response time (mean ± standard deviation) was computed for all IceCube CASCADE triggers from 2022 (see also Table 6.1).

Hereafter I will go step-by-step through the respective outputs for four example alerts (see also Sections 5.3.2, 5.3.3 and 5.3.4). Once again the reader is invited to follow along in order to get accustomed to the outputs provided by the tools developed for this dissertation. The reader having a working conda-environment is encouraged to follow along the beginner testing guide by calling the GUI-functionality "python testing_GUI.py" from within the home directory of its successfully deployed version of ToOpy (see also Figure 5.2). Note that the Earth location to schedule the resulting observations will be fixed to the Roque de los Muchachos (ORM) since it hosts both the MAGIC and LST-1 telescopes. Also, the next chapter contains an additional example, whose results present the findings from an actual ToO observation performed by MAGIC and LST-1 in response to a neutrino trigger (see also Sections 6.1).

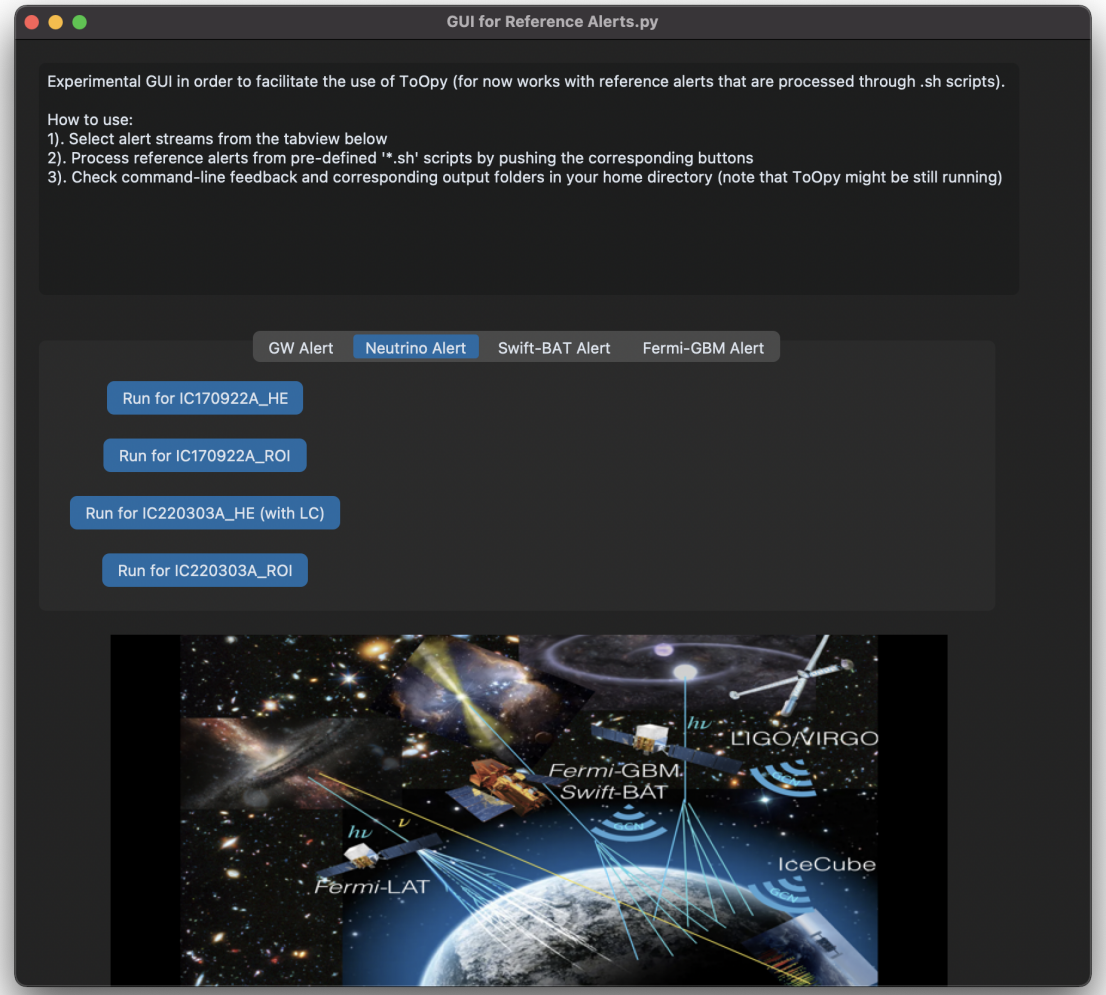

Figure 5.2: GUI for ToOpy with reference alerts from the different observatories.

5.3.2 Results for TXS 0506+056/IC-170922A Coincidence - HE Ranking

The user is encouraged to run the corresponding scripts from the "Neutrino Alert" tab in the GUI.

Step 1: Localization Error and 4FGL Galaxies: The error region for the initial alert emitted at 2017-09-22 20:54:30.43 UTC contains a single 4FGL source as shown in Figure 5.3.

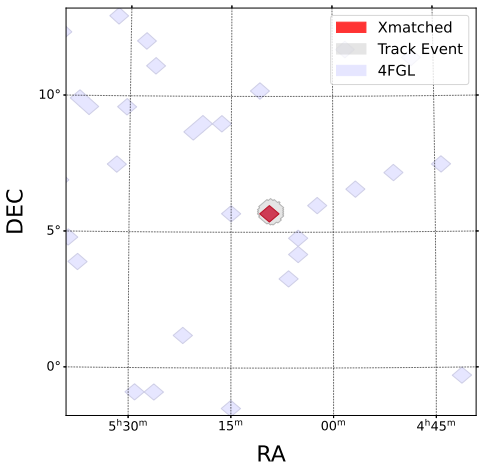

Figure 5.3: Localization error for the IceCube trigger, where the galaxy within is highlighted automatically.

Step 2.1: Archival-based Ranking 4FGL Galaxies: The source is associated with the BL Lac class object TXS 0506+056, with a reported VarInd of 1232.45374 (from 4FGL) and redshift value of 0.3365 (from NED).

Step 2.2a: HE-based Ranking 4FGL Galaxies (TS map): Having a single 4FGL object contained within the uncertainty region and having an offset of 0.08 deg from the best-fit position, results in a pointing sequence that in principle does not require further discussion. Nevertheless, this ideal situation does not always happen, e.g see also Section 6.1 in the next chapter, or especially CASCADE-type alerts that can have localization errors up to ∼20 deg. Hence in order to overcome this uncertainty regarding the actual state of crossmatched 4FGL objects, we run the fermipy analysis on a ROI of 15 deg centred at the best-fit-position. Upon inspection of the skymaps provided by the "gta.residmap()" functionality, we find that there seems to be an excess amount of HE photons from the region associated with TXS 0506+056 (see Figure 5.4).

Step 3: Scheduling of 4FGL Galaxies from ORM: Since this is a promising opportunity (due to a combination of small offset, the high archival variabilitiy as well as the increased HE flux in the week prior to the neutrino alert) we decide to inspect the output provided by the scheduler. As the user can verify TXS 0506+056 is observable at the time of the alert. Based on our constraints and location there is a ∼2 hours slot opening around 04:00 UTC. If we check the literature for the follow-up of TXS 0506+056, we indeed find in Table 1 of (Ansoldi et al.; 2018) the reported date MJD 58020.18 which corresponds to 2017-09-24 04:19:12.000 UTC, Hence indicating that the output of ToOpy is consistent with what was done for past ToO observations.

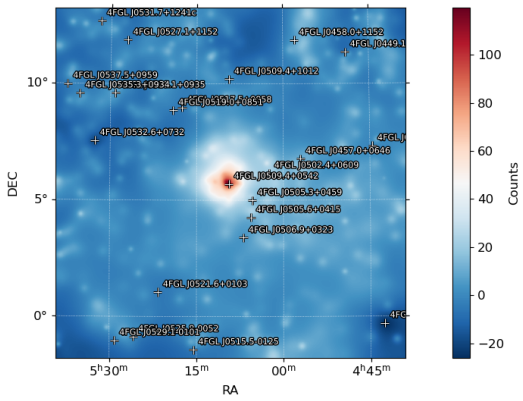

Figure 5.4: Residmap obtianed through the gta.residmap() method contained in the standard fermipy tools.

5.3.3 Results for *Fermi*-GBM/*Swift*-BAT Coincidence - STMOC Ranking

The user is encouraged to run the corresponding scripts from the "*Swift*-BAT Alert" and "*Fermi*-GBM Alert" tabs in the GUI (note that the order of execution does not matter).

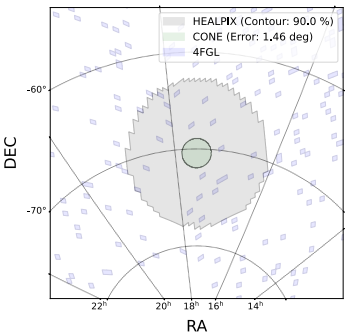

Figure 5.5: Localization error for the *Fermi*-GBM trigger.

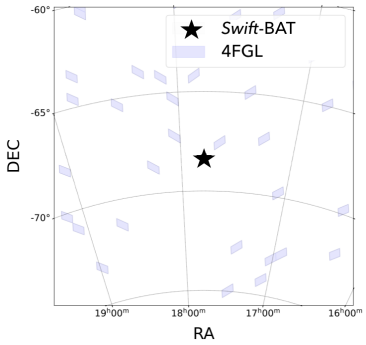

Figure 5.6: Sky location for the GRB detected by the *Swift*-BAT instrument.

Step 1: Localization Errors for GRB Triggers: At 2022-12-01 12:24:51 UTC *Fermi*-GBM registers a GRB (trignum=691590290[8]) with the spatial uncertainty shown in Figure 5.5. The location of a GRB detected by *Swift*-BAT (trignum=1142847[9]) at 2022-12-01 12:26:22 UTC is shown in Figure 5.6.

Step 2.1: HE-based Ranking STMOC: One could rank the galaxies for each GRB trigger individually and then perform ToOs based on single triggers. However, the two triggers seem to be spatially associated, and furthermore the individual triggers are separated by only 91 seconds. Note that this temporal coincidence is also reported in the trigger content of the *Fermi*-GBM notice.

In order to automatically isolate these spatio-temporal coincidences, the broker creates STMOC instances that are continuously added to an internal catalog of individual triggers from GRB and GW alerts. Upon receiving a trigger, and after the broker initiates the new STMOC, ToOpy is programmed to check if in the near-past there was a trigger that is spatially overlapping with the incoming alert (here the time-span for fulfilling temporal coincidence was set to ±100 seconds but is in general configurable). As shown in Figure 5.7 in this case ToOpy automatically found a spatio-temporal coincidence for a GRB co-detected by *Fermi*-GBM and *Swift*-BAT.

[8] https://gcn.gsfc.nasa.gov/other/691590290.fermi
[9] https://gcn.gsfc.nasa.gov/other/1142847.swift

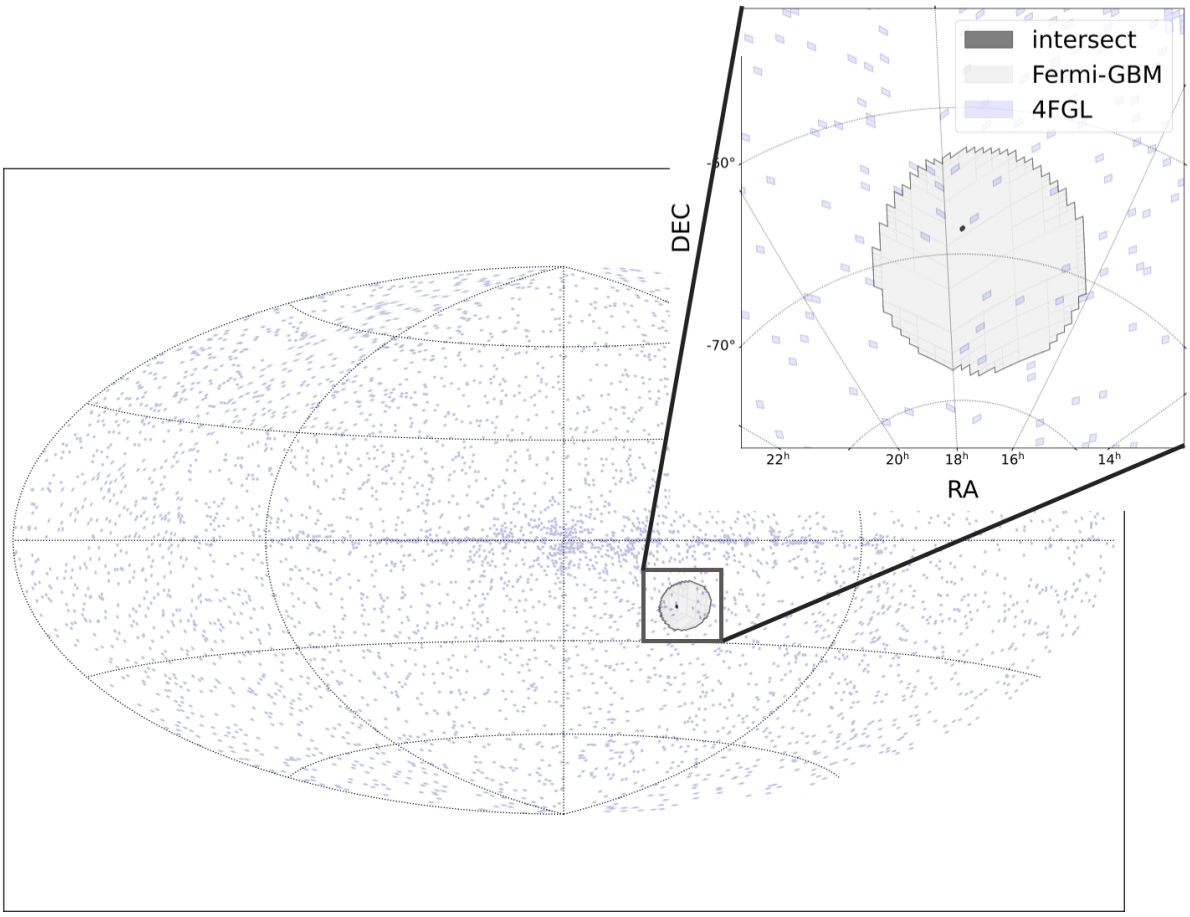

Figure 5.7: Intersection of uncertainty region associated with the individual triggers from *Fermi*-GBM and *Swift*-BAT.

Step 3: Check Observabillity and Discussion on Observational Strategy: As the user can verify, none of the galaxies within the combined uncertainty region are observable from the ORM at the time of the trigger. The user is encouraged to alter the preferences of the scheduler, i.e. lines 2-5 of the *.sh scripts, in order to check whether the sky region is observable in the near-term from ORM or a different geographical location. Since initial *Fermi*-GBM triggers are commonly updated by revisions, i.e. Flight-, Ground- and Final-Position (each distributed with an increase in latency), there could be an edge if one allows to react to initial triggers from *Fermi*-GBM (see also Figure 5.8). However, reacting to the preliminary Flight-Position trigger is accompanied with a certain risk that has to be taken into account. On one hand, following the initial notices one can react faster to coincident MM triggers if there is a clear spatio-temporal coincidence. This approach is clearly high risk/high gain but once ToOpy automatically performs web scrapping of trigger tables this could significantly reduce the search region. Nevertheless, on the other hand there is the risk that initial triggers might be retracted after more elaborate analysis and human inspection (see also results for archival crossmatching in Chapter 6).

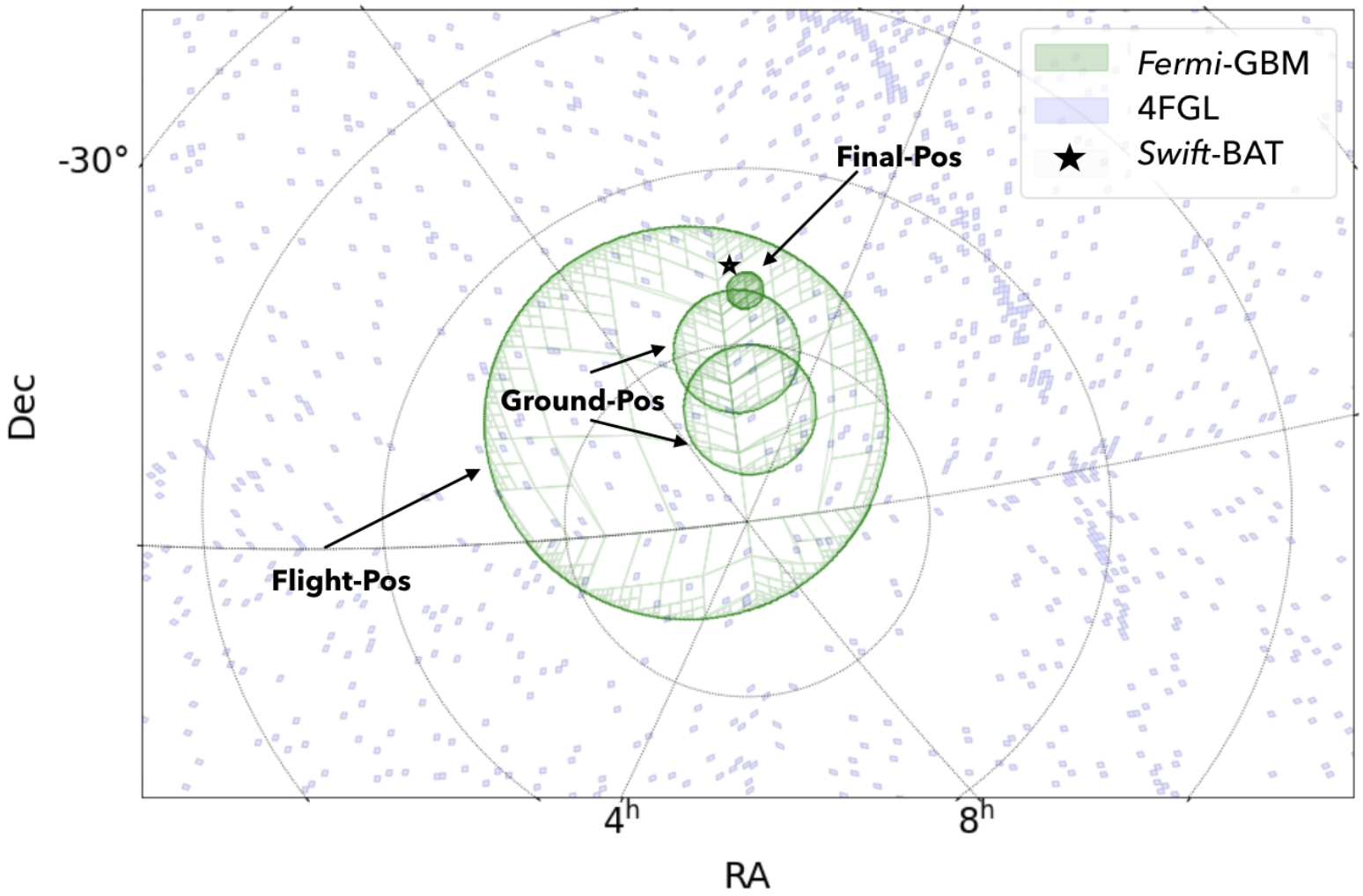

Figure 5.8: Localization errors after successive revisions of the *Fermi*-GBM trigger for this particular GRB alert. The *Fermi*-GBM triggers for this particular GRB (trignum=691590290) were collected by web scrapping the corresponding trigger table[11].

5.3.4 Results for GW Fake Alert - Tiled Ranking and Re-Scheduling

The user is encouraged to run the corresponding scripts from the "GW Alert" tab in the GUI. In this example I will elaborate on a possible response for a GW event with a large localization error (namely "MS230117q"[12] but using an instrument with a large FoV (25 degrees). The user is encourage to alter the FoV constraint and see the effect it has on the pointing selections.

Step 1: Uncertainty Region and RA&Dec Grid: The fake GW trigger is associated with a large localization error is shown in Figure 5.9.

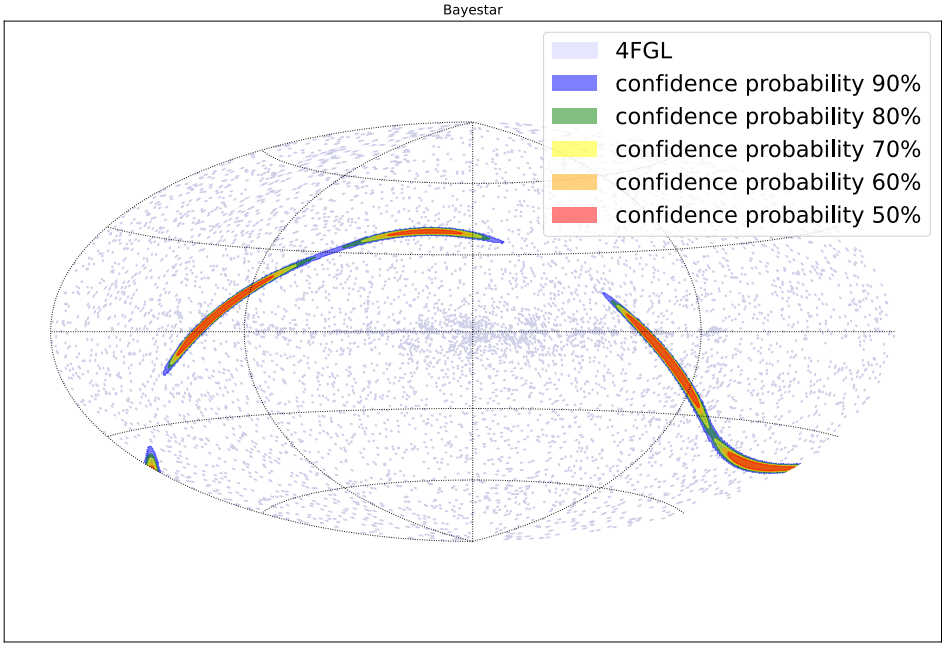

Figure 5.9: Localization error of the GW event (GraceID=MS230117q).

Step 2: Tilling-based Ranking: Following the RA/Dec grid approach, the algorithm computes the first four tiles (shown in Figure 5.10). Note that already observed grid points are excluded after each tile, and the fact that with these four pointings one can cover the bulk region of the 50% confidence probability region.

[12] https://gracedb.ligo.org/api/superevents/MS230117q

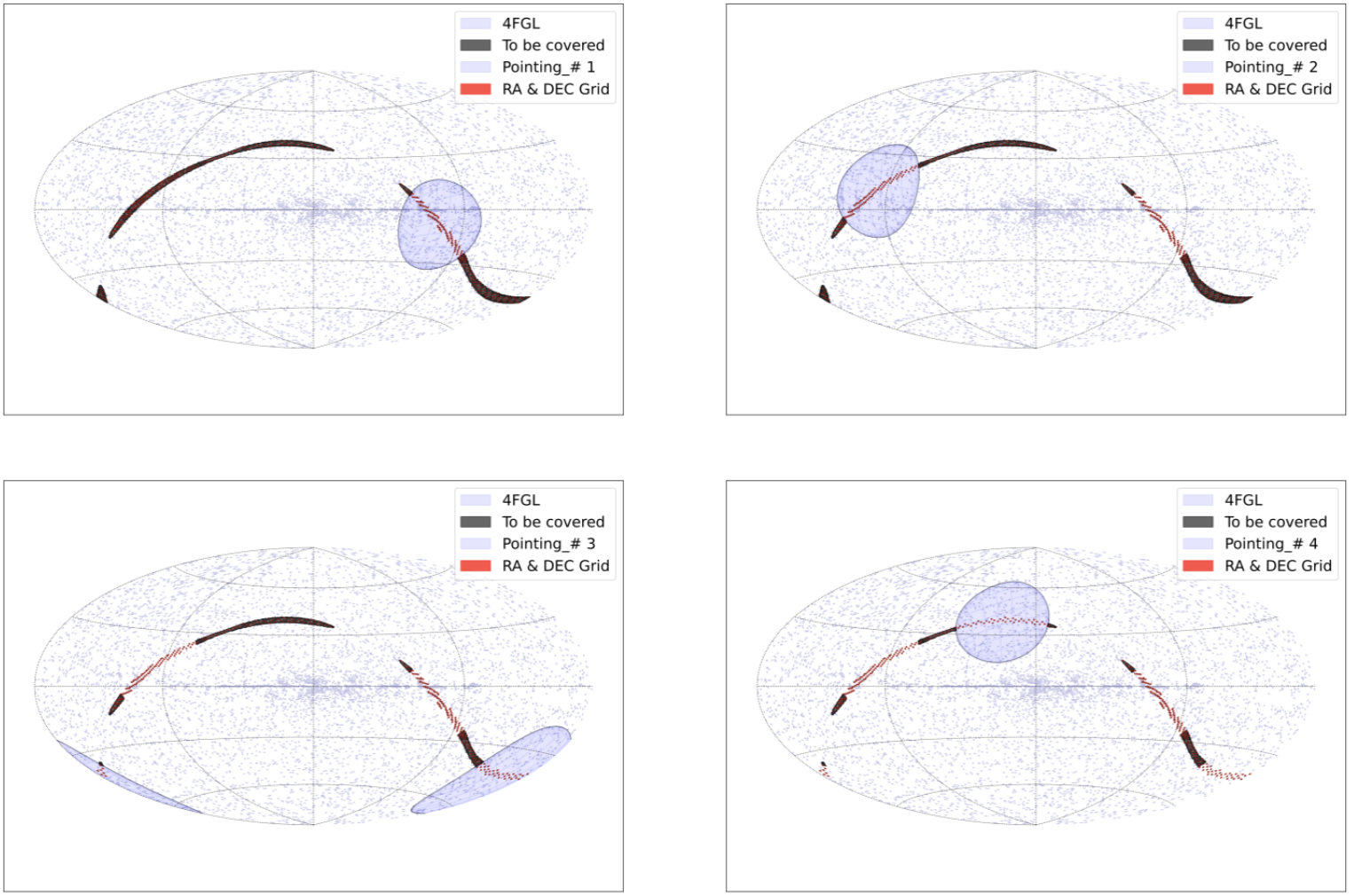

Figure 5.10: The four first tiles covering the most probable regions of the uncertainty region of the GW event.

Step 3: Scheduling of Tillings: As shown in Figure 5.11, not all pointings are observable from the selected geographic location, thus effectively requiring a re-ranking of the scheduled observations.

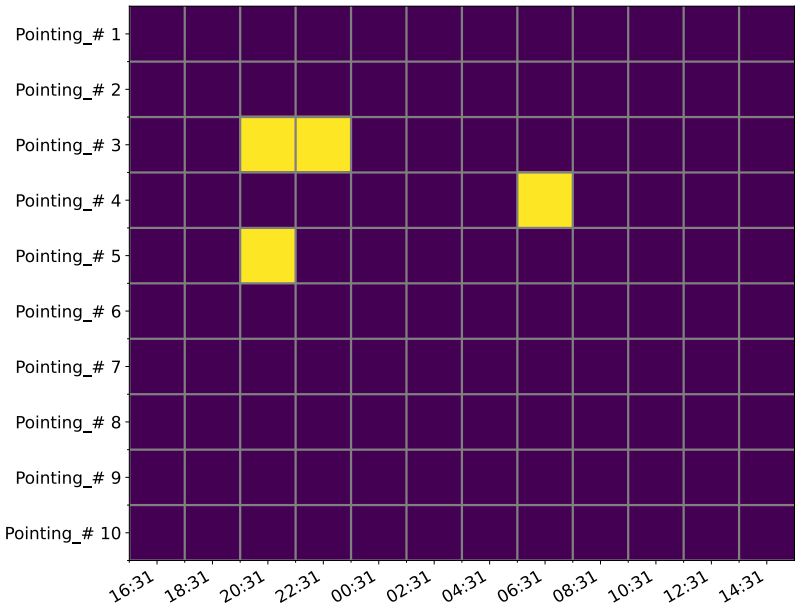

Figure 5.11: The observability for the successive tiles for an instrument having an FoV of 25 deg and located at the ORM. The y-axis shows the successive pointings whilst the x-axis denotes the starting point for each exposure slot (here 2 hours). The yellow squares denote the time slots for which all criteria of the scheduler are met, e.g. AtNightConstraint, MoonSeparationConstraint, and AltitudeConstraint (see also "astroplan" (Morris et al., 2018))

5.4 Prospects

This work can be continued in various ways, some of which I will outline in the next chapter 6. Furthermore, there are near-term extension that can be included into the tools at hand:

Inclusion of additional data streams:

- ◇ **Satellite-based:**
  - **Integral;** incorporate corresponding GRB notices to search for spatio-temporal coincidences
  - ***Fermi*-GBM;** Flight- and Ground-Position notices for lower latency reaction
  - **Telemetry;** access a priori coverage of localization errors with satellite data

◇ **Ground-based:**

- **ZTF monitoring;** obtain large FoV optical coverage
- **ZTF alerts;** access alert notices for SN triggers

◇ **Maps:**

- Add various maps in future releases of ToOpy, such as telescope surveys, galaxy maps or regions of high dust concentration located closer to the galactic plane.

Implementation of missing ranking methods:

◇ **IceCube CASCADE Alerts:**

- **Tiling Localization region;** elaborate approach similar to GW method
- **"Tiled" fermipy analyis;** enable multi-ROI analysis for faster computations

◇ ***Fermi*-GBM alerts:**

- **Tiling localization region;** elaborate tiling methods for ToO observations of *Fermi*-GBM triggers
- **Web scrapping;** in order to gain access to low latency notices from *Fermi*-GBM, i.e. Flight- and Ground-position

◇ **Multi-Satellite GRB alerts:**

- **Tiling Intersection;** elaborate tiling methods for ToO observations of spatio-temporal co-incident regions

Updating catalogs for GRB and CBC alerts

◇ **Glade+:**

- **Vizier Query;** try to resolve connection issues for quering catalogs with MOC objects
- **Fast Data Access;** maintain a catalog file within the repository of the broker and elaborate a method to obtain a fast data access

Additional constraints for scheduler

◇ **NSB Intensity;** relax the moon-separation parameter by introducing a constraint on the intensity of the NSB, e.g. based on the phase of the moon

Bibliography

Abbott et al. (2020). Prospects for observing and localizing gravitational-wave transients with advanced ligo, advanced virgo and kagra, *Living reviews in relativity* **23**(1): 1–69.

Acero, F., Ackermann, M., Ajello, M., Albert, A., Baldini, L., Ballet, J., Barbiellini, G., Bastieri, D., Bellazzini, R., Bissaldi, E. et al. (2016). Development of the model of galactic interstellar emission for standard point-source analysis of fermi large area telescope data, *The Astrophysical Journal Supplement Series* **223**(2): 26.

Ackermann, M., Ajello, M., Albert, A., Allafort, A., Antolini, E., Baldini, L., Ballet, J., Barbiellini, G., Bastieri, D., Bechtol, K. et al. (2013). The fermi all-sky variability analysis: a list of flaring gamma-ray sources and the search for transients in our galaxy, *The Astrophysical Journal* **771**(1): 57.

Almualla, M., Coughlin, M. W., Anand, S., Alqassimi, K., Guessoum, N. and Singer, L. P. (2020). Dynamic scheduling: target of opportunity observations of gravitational wave events, *Monthly Notices of the Royal Astronomical Society* **495**(4): 4366–4371.

Andreoni, I., Anand, S., Bianco, F. B., Cenko, S. B., Cowperthwaite, P. S., Coughlin, M. W., Drout, M., Golkhou, V. Z., Kaplan, D. L., Mooley, K. P. et al. (2019). A strategy for lsst to unveil a population of kilonovae without gravitational-wave triggers, *Publications of the Astronomical Society of the Pacific* **131**(1000): 068004.

Ansoldi, S., Antonelli, L. A., Arcaro, C., Baack, D., Babić, A., Banerjee, B., Bangale, P., De Almeida, U. B., Barrio, J. A., González, J. B. et al. (2018). The blazar txs 0506+ 056 associated with a high-energy neutrino: insights into extragalactic jets and cosmic-ray acceleration, *The Astrophysical Journal Letters* **863**(1): L10.

Baumann, M., Boch, T., Fernique, P., Nebot, A. and Pineau, F.-X. (2020). Space and time coverage maps in mocpy, *Astronomical Data Analysis Software and Systems XXIX* **527**: 693.

Boch, T. (2019). Mocpy, a python library to manipulate spatial coverage maps, *Astronomical data analysis software and systems XXVI* **521**: 487.

Ducoin, J., Corre, D., Leroy, N. and Le Floch, E. (2020). Optimizing gravitational waves follow-up using galaxies stellar mass, *Monthly Notices of the Royal Astronomical Society* **492**(4): 4768–4779.

Fernique, P., Boch, T., Donaldson, T., Durand, D., O'Mullane, W., Reinecke, M. and Taylor, M. (2019). Technical report, moc-healpix multi-order coverage map, version 1.1.

Gehrels, N., Cannizzo, J. K., Kanner, J., Kasliwal, M. M., Nissanke, S. and Singer, L. P. (2016). Galaxy strategy for ligo-virgo gravitational wave counterpart searches, *The Astrophysical Journal* **820**(2): 136.

Gérard, L. (2015). Divergent pointing with the cherenkov telescope array for surveys and beyond, *arXiv preprint arXiv:1508.06197* .

Greco, G., Punturo, M., Allen, M., Nebot, A., Fernique, P., Baumann, M., Pineau, F.-X., Boch, T., Derriere, S., Branchesi, M. et al. (2022). Multi order coverage data structure to plan multi-messenger observations, *Astronomy and Computing* **39**: 100547.

Morris, B. M., Tollerud, E., Sipőcz, B., Deil, C., Douglas, S. T., Medina, J. B., Vyhmeister, K., Smith, T. R., Littlefair, S., Price-Whelan, A. M. et al. (2018). Astroplan: an open source observation planning package in python, *The Astronomical Journal* **155**(3): 128.

Salmon, L., Hanlon, L., Jeffrey, R. and Martin-Carrillo, A. (2020). Web application for galaxy-targeted follow-up of electromagnetic counterparts to gravitational wave sources, *Astronomy & Astrophysics* **634**: A32.

Wood, M., Caputo, R., Charles, E., Di Mauro, M., Magill, J. and Perkins, J. (2017). Fermipy: An open-source python package for analysis of fermi-lat data.
URL: *https://arxiv.org/abs/1707.09551*

CHAPTER 6

TARGET OF OPPORTUNITY AND ARCHIVAL COUNTERPART SEARCHES

Resume: The work presented in this chapter results from applying the algorithm introduced in Chapter 5 to various alert streams: neutrino, GW and GRB. Whilst for neutrinos I deal with contemporaneous ToO counterpart searches (6.1, 6.2), the GW and GRB use cases entail access to archival data sets (6.3). The archival counterpart searches for GW are part of a publication in preparation, for which I am the main author. The inclined reader is encouraged to set up an environment and to follow along with the examples provided in Sections 6.1 and 6.2.

Contents

The starting goal to develop ToOpy was to provide small FoV ground-based instruments with a set of tools that allow them to perform automatic ToO observations of GW triggers (see also previous Chapter 5). Adopting a methodology that allows to tap directly into the stream of GCN alerts via a Broker, led to the elaboration of generalized routines that are also useful for additional alert streams, e.g. neutrino and GRB alerts. The modularity of the underlying routines, along with the incorporation of satellite-based datastreams (especially *Fermi*), allowed me to diversify the use-cases and output of ToOpy. As we will see, this turned out to be useful for triggering ToO observations with MAGIC and LST-1 on TRACK alerts from IceCube. Along this line, the newly established stream of CASCADE alerts provides since 2021 alerts of neutrino events fully contained within the IceCube detector. Since these events come with localization errors of 3-30 deg, the collaborative work required for sky and/or galaxy selection is similar to what will be needed in the CTA and O4+ era. Once again we will see that a fermipy analysis turns out to be extremely useful and could already hint towards potential host galaxies.

Apart from gaining access to these alert streams, along the way, I learned about recent efforts by the VERITAS collaboration to use archival GW event catalogs in order to look for hidden GRB signatures. This made me realize that ToOpy could be used to search for spatio-temporal correlations in archival data. Working on a methodology to deal with archival datasets, eventually resulted in the implementation of the STMOC approach into ToOpy.

I will initiate this chapter by elaborating on a first successful use case of an early prototype version of ToOpy and its success during a neutrino alert in March 2022 (Section 6.1). I then discuss in Section 6.2 the prospects for a feasible follow-up strategy for CASCADE alerts that is based on HE ranking with *Fermi*-LAT. Finally, I discuss in Section 6.3 my developed methodology and results for the search of EM counterpart signals to GW in archival datasets.

6.1 ToO Counterpart Searches for IceCube-220303A

During the developing phase of ToOpy, I had a beta version that allowed me to manually process incoming neutrino alerts issued by the IceCube observatory. On March 3rd 2022 IceCube issued a GOLD alert: IceCube-220303A, which I manually analyzed (the reader can do so by executing the "IceCube-220303A*.sh" scripts). Based on my findings I decided to get in touch with the Transient Conveners of the MAGIC collaboration, in order to incentivize them to perform follow-up observations on a specific target source. These efforts eventually contributed to the most recent observations of an AGN, e.g. OT081, by the MAGIC and LST telescopes in form of ToO observations that lasted three nights.

In the following subsections, I elaborate on the observational history of OT081 (Section 6.1.1) and then elaborate on all the pieces of information that came together and resulted in ToO observations of MAGIC and LST-1 (Section 6.1.2). After discussing the results related to the follow-up of OT081 (Section 6.1.3), I outline prospects for future ToO observations based on ToOpy.

6.1.1 Observational History of OT081

OT081 is a well-known blazar (also named PKS 1749+096 and 4C 09.57) that has been studied extensively with instruments of the entire EM domain and located at a redshift of z=0.320 ± 0.005 (Stickel et al.; 1988). It manifests variability at many energy bands and in the past has shown significant fluctuations in brightness on timescales of minutes, which might stem from changes with respect to the rate at which matter is accreted onto the central SMBH. Having long been studied by instruments such as *Fermi* and the Very Long Baseline Array (VLBA), in July 2016 after *Fermi*-LAT detected a HE flare a MWL follow-up campaign resulted in its first detection at VHE by H.E.S.S. and MAGIC (Seglar-Arroyo et al.; 2022). The authors argue that while a single one-zone SSC model does not reproduce the broadband emission, adoption of a lepto-hadronic model does (see also discussion for the SED modeling of VER J0521+211 in Section 4.4.3). Hence, OT081 is an interesting target for a MM approach in order to study the emission of photons and neutrinos from potential hadronic components in the jet of blazars.

6.1.2 IceCube-220303A GOLD TRACK Alert

As mentioned in the introduction, on March 3rd the IceCube observatory detected a neutrino event, 2022-03-03 18:00:07.62 UTC, which was automatically disseminated as a GOLD TRACK alert into the GCN stream. At that time ToOpy was not running on a dedicated machine and hence I manually analyzed the alert. The obtained outputs will be presented in the following, and perhaps contributed towards the most recent observations of OT081 by the MAGIC and LST telescopes in form of ToO observations that lasted for three nights.

Initial Trigger - Revision 0: The initial notice was issued at 2022-03-03 18:01:13 UTC and as seen in Figure 6.1 did not contain any crossmatched sources from the 4FGL within the error region of 0.53 deg. Hence due to the automatic addition of the closest possible source, the first trigger resulted in a single candidate source "4FGL J1745.5+1017" located at an offset of ∼1.2 deg from the best-fit position of the alert

Revised Trigger - Revision 1: Processing the revised alert (issued at 2022-03-03 20:47:41 UTC) resulted in an ∼ 0.3 deg shift of the initial best-fit position along with a widening of the initial localization error (see also Figure 6.2). Reevaluating the output from the broker still resulted in having no cross matched sources from the 4FGL. Nevertheless, due to the shift in the best-fit position, the closest source was now changed to "4FGL J1751.5+0938" located at an offset of ∼1.8 deg from the best-fit position of the alert.

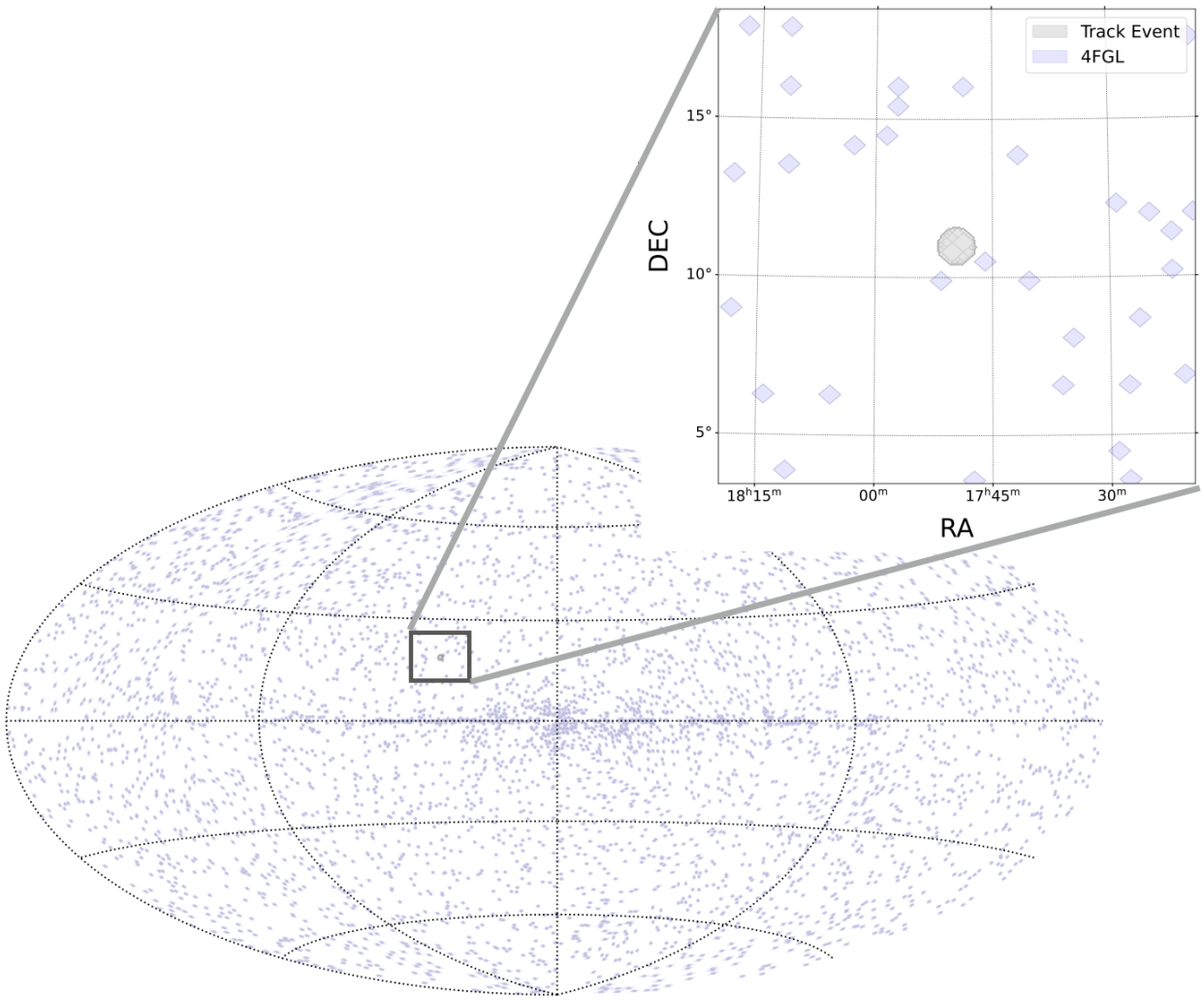

Figure 6.1: Initial alert with its localization error of 0.53 deg for IC220303A.

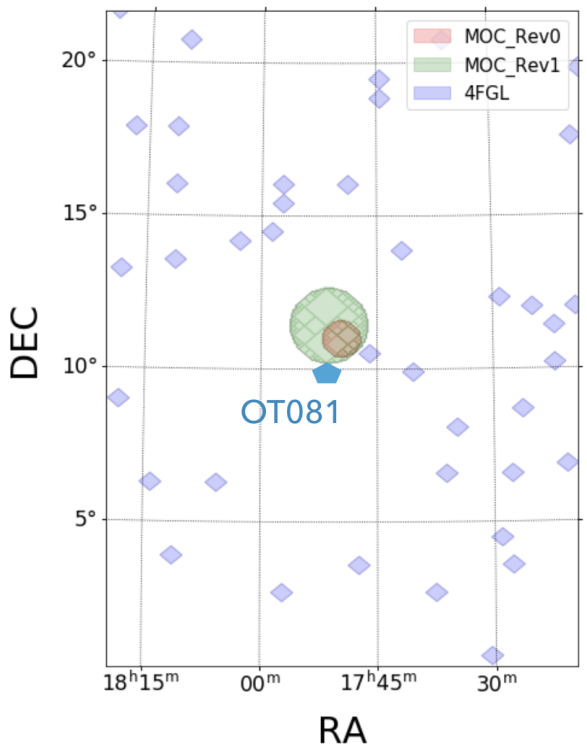

Figure 6.2: Zoom on the uncertainty region of IC220303A, where the first two revisions are superimposed.

VarInd Ranking: Hence in this particular case, after the two revisions we have each time two different galaxy targets at different offsets with respect to the best-fit position:

◇ **Rev 0 - 4FGL J1745.5+1017**

- **VarInd;** 4.073183
- **Associated Source;** PSR J1745+1017
- **Class;** PSR
- **offset;** 1.20144208821474 deg
- **Redshift;** N/A

◇ **Rev 1 - 4FGL J1751.5+0938**

- **VarInd;** 884.581543
- **Associated Source;** OT081 (also known as PKS 1749+096 and 4C 09.57)
- **Class;** BL Lac
- **offset;** 1.77593933451072 deg
- **Redshift;** 0.322

Observability: As shown in Figure 6.3 both sources were observable at the same time and after the revised trigger there was plenty of time (∼8 hours) to gather information in order to discuss if a ToO observation should be triggered and where one would want to point, e.g. the best-fit position, the blazar, the PSR or another in between position allowing to cover more of the interesting region. At the time it took me some time to elaborate all bits and pieces but now the user can execute the "IceCube-220303A_HE.sh" script and within ∼600 seconds one should have a pretty good motivation to target OT081 (apart from the biased introduction of this Section).

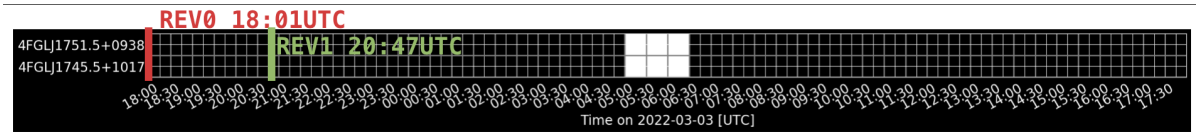

Figure 6.3: Output of the scheduler showing that both sources are observable at the same time (the white squares mark the epochs where all the user constraints are met). The respective times for the IceCube triggers are marked accordingly.

***Fermi*-LAT:** Let's now discuss how we could motivate a specific ToO pointing strategy.
Analyzing the weekly file of *Fermi*-LAT (week 717 for this specific alert) and upon running the standard fermipy methods outlined in the previous chapter, it became apparent that 4FGL J1751.5+0938 was showing a slight excess in flux levels at HE (see also Figure 6.4).

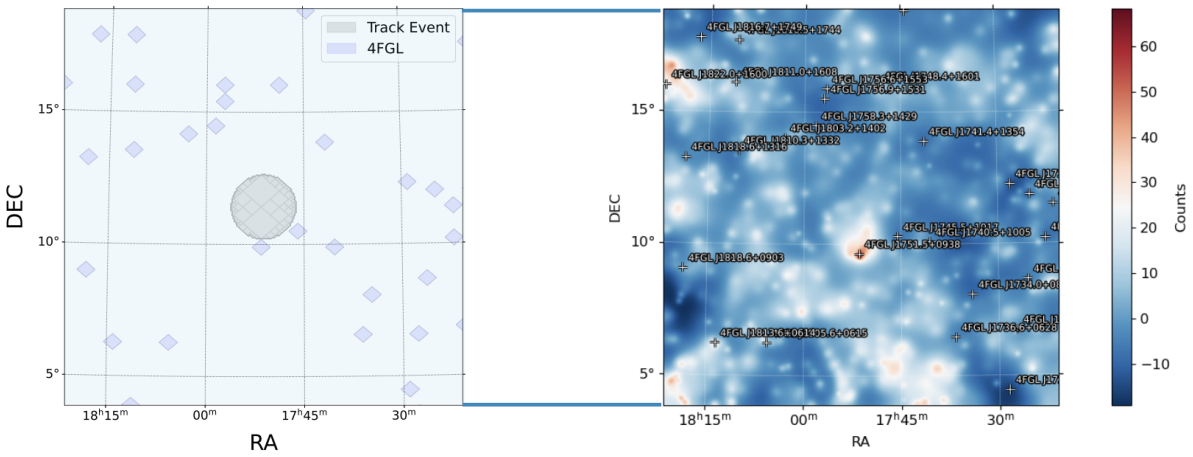

Figure 6.4: Zoom on the uncertainty region of IC220303A. The **left plot** shows the localization error for the final IceCube trigger distribution and the **right plot** shows the HE skymap of the same region obtained with a fermipy-based analysis of the weekly data file from *Fermi*-LAT.

Since the HE skymap was computed on a weekly basis, it is interesting to check if this higher flux was a generic state that lasted the entire week, or if this weekly enhancement stemmed from a short-lived state, e.g. a flare, temporally closer to the neutrino alert trigger. Upon manually computing the LC it

was seen that this flux enhancement was manifesting itself two days prior to the neutrino alert as shown in Figure 6.5.

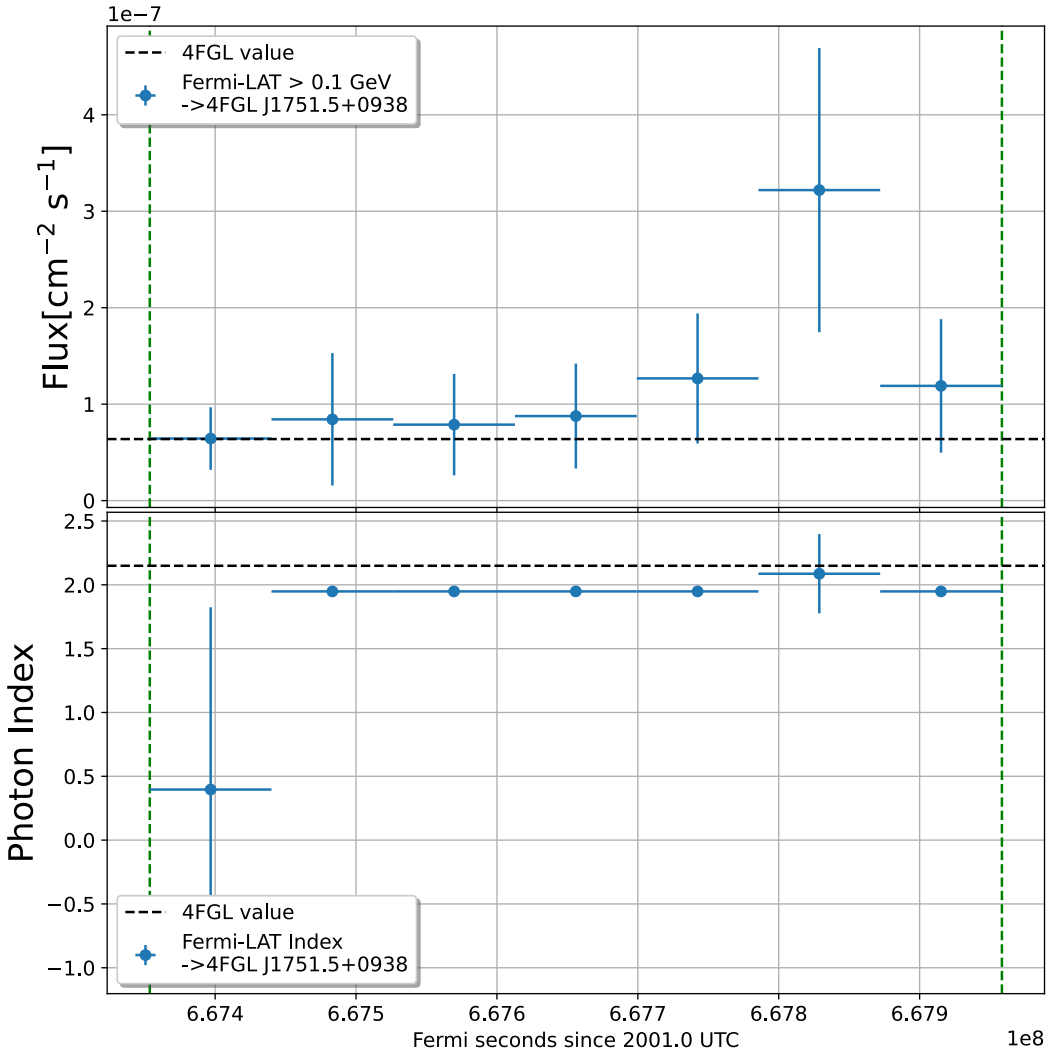

Figure 6.5: The result when generating a daily-binned lightcurve for 4FGL J1751.5+0938 using the weekly file. As can be seen the flux enhancement in HE seems to peak on the second to last day of the week, i.e. two days prior to the neutrino trigger (see also Figure 6.3).

6.1.3 ToO Observations on OT081 following IceCube-220303A

The combination of all these factors, i.e. high archival variability, transient HE state, and good observability, led me to alert the MAGIC and LST collaboration in order in order to initiate ToO observations on OT081. Since the localization error region of IC220303A was observable in the second half of the night,

MAGIC+LST initiate follow-up observations for ∼2 hours, initially pointing at the best-fit position of IC-220303A and then at the position of OT081 (∼1 hr each).

The next morning, before the data could be transferred to the servers where the first analysis steps are automatically performed, another GCN notice related to IC220303A was issued at 22-03-04 07:46:26 UTC. Therein, the MASTER-Net team reported an optical high state in the TeV blazar 4C 09.57 10 hours after the trigger time of IC220303A[1]. Based on this report, two additional nights of ToO observations were scheduled. Whilst MAGIC could not gather data during the second night (due to atmospheric conditions) LST managed to take data on all three nights (see also Figure 6.6).

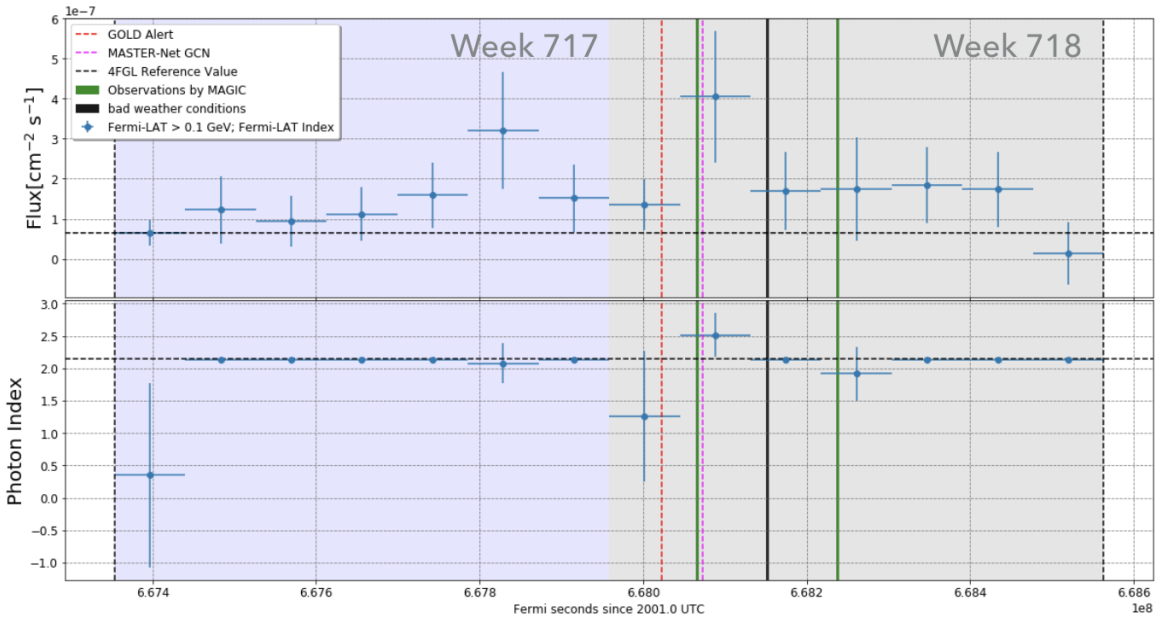

Figure 6.6: The daily-binned lightcurve of source 4FGL J1751.5+0938 in the two weeks around the alert. The vertical lines denote the timing of information received: neutrino trigger, MAGIC observations, and Master-Net GCN notice. As can be seen, MAGIC and LST observed on three successive nights (MAGIC observations on the second night were interrupted because of strong wind).

6.1.4 Conclusions and Prospects

A fast analysis by the "Flare Advocates" on duty for the observational period showed for neither MAGIC nor LST any significant VHE excess emission from data taken at the best-fit position of IC220303A nor at the position of OT081. Although no VHE emission was detected, it is clear that the rapid intervention allowed for a reaction prior to the GCN notice from MASTER-Net. Hence even though this time we did not manage to find a spatio-temporal association of two separate messengers, the circumstances around this particular ToO observations demonstrate the validity of the approach of ToOpy for future use-cases.

[1] https://gcn.gsfc.nasa.gov/other/icecube_220303A.gcn3

6.2 Targeted Strategy for CASCADE Alerts

As mentioned in the introduction of this chapter, IceCube opened at the beginning of 2021 a new stream of alerts that disseminates single cascade events to the astronomical community. The main difference between CASCADE- and TRACK-alerts is the event signature recorded by the IceCube detector (see also Figure 6.7):

- ◇ **TRACK Alerts:** When a high-energy neutrino enters the ice medium of the IceCube detector, it can interact with therein nuclei and generate muons. A muon that travels through the ice, leaves a track of light, which can be detected by the sensors of the detector. TRACK alerts provide information about the direction and energy of the neutrino, as well as the estimated position of the source in the sky.
- ◇ **CASCADE Alerts:** Similar to the case of the TRACK alert, a neutrino reaches the IceCube detector. But instead of passing completely through the detector, it deposits its entire energy within the medium and hence remains contained within the detector. Thanks to improvements in event classification this allows the possibility to reject tracks, and thus reduce the background of atmospheric muons and neutrinos, this selection of events leads to very high astrophysical purity, i.e. $> 85\%$ in the standard case.

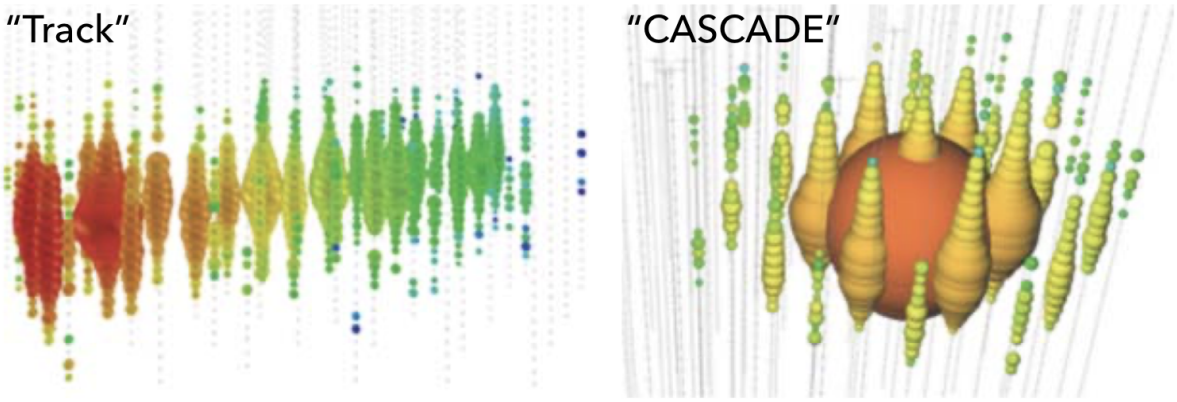

Figure 6.7: Examples of signatures from events recorded by IceCube. The **left plot** shows an example of a TRACK-like event and the **right plot** shows CASCADE shower-like event. The spheres mark individual DOMs, whose size is based on the received Cerenkov light intensity and color represents the arrival times of photons, with the earliest colored in red while the latest are colored in blue. Image Credit: (Kowalski et al.; 2017)

Both types of alerts are important because they allow astronomers and astrophysicists to quickly follow-up on the detection of a high-energy neutrino with other instruments, in order to try to identify the source of the neutrino and to study the physical processes that produced it. The CASCADE alerts are characterized by a large localization error of the order of 3-30 deg. Hence their follow-up by small FoV instruments has similar issues as for GW, which in return motivates the elaboration of tiling strategies. However, a galaxy targeted approach remains as a viable alternative especially for those cases where

contemporaneous HE flares are registered by the *Fermi*-LAT instrument. Hence, in the following I will discuss the findings from applying ToOpy to the CASCADE alerts and thereafter provide a catalog of HE candidate sources for each CASCADE trigger.

6.2.1 CASCADE Alert Catalog of HE Analysis

Unlike the ToO trigger for the GOLD TRACK alert discussed in Section 6.1, as of the writing of this manuscript none of the CASCADE alerts resulted in ToO observations by MAGIC or LST. As of April 2023 there are a total of 19 CASCADE alerts emitted. In the following, I will elaborate on a few of these alerts and how a fermipy based analysis performed in a ROI of 15 deg and centered at the best-fit position highlights galaxy targets or specific sky regions of high interest for potential ToOs. Table 6.1 then sumarizes the 19 CASCADE alerts along with potential host candidates found by ToOpy. The reader having a working environment is encouraged to follow along by putting the broker into listening mode with the given "*.xml" template files for each CASCADE alert (see also "README.md" file on https://github.com/arterom/ToOpy for further guidance).

January 2021 (IceCubeCascade-210121b): As shown in Figure 6.8 *Fermi*-LAT records an excess of HE photons from the direction of "4FGL J1408.9-0751". The queried 4FGL catalog tells us that this object is associated with the FSRQ-type blazar PKS B1406-076, with a large VarInd of 1392.43689 and located at a redshift of z∼1.494.

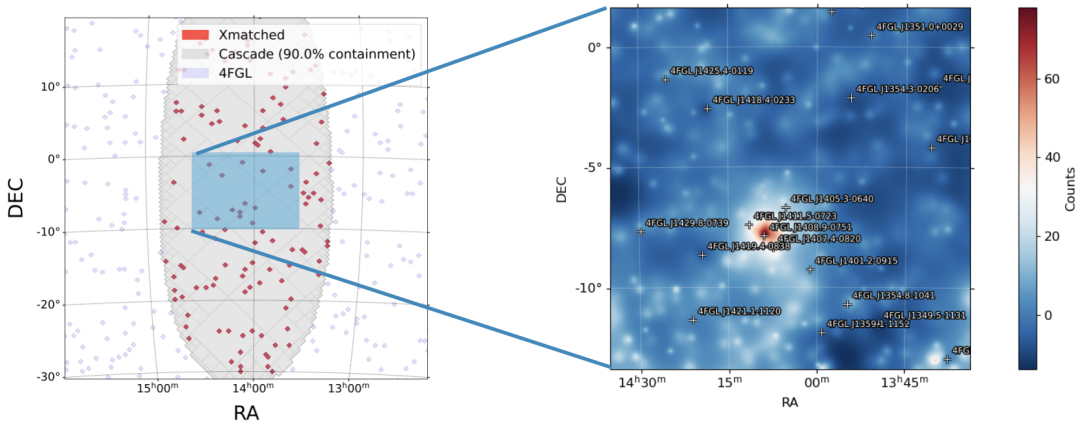

Figure 6.8: Zoom on the uncertainty region of IceCubeCascade-210121b. The **left plot** shows the localization error of the neutrino origin and the **right plot** shows for the highlighted region a HE skymap obtained through fermipy-based analysis of the weekly data file from *Fermi*-LAT. Note the HE excess recorded at the position of 4FGL J1408.9-0751.

March 2021 (IceCubeCascade-210329a): As shown in Figure 6.9 *Fermi*-LAT records an excess amount of HE photons from the direction where according the *Fermi* catalog there seems to be no known source candidate. As a general note it is important to understand that this can happen due to performing the analysis with a ROI model that does not include a source that is lying right at the edge of the region.

The excess HE photons from that region might be misinterpreted as a new source candidate by the gta.find_sources() method (albeit not for this case due to a too TS value).

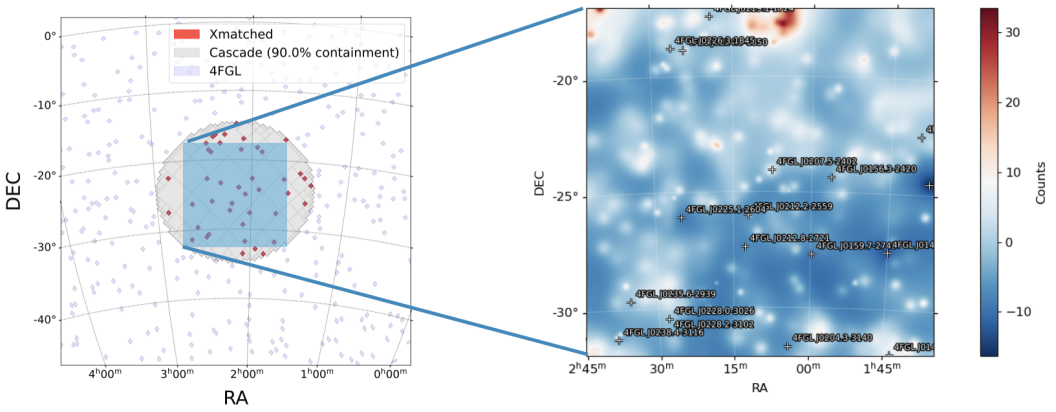

Figure 6.9: Zoom on the uncertainty region of IceCubeCascade-210329a. The **left plot** shows the localization error of the neutrino origin and the **right plot** shows for the highlighted region a HE skymap obtained through fermipy-based analysis of the weekly data file from *Fermi*-LAT.

April 2021 (IceCubeCascade-210416a): As shown in Figure 6.10 *Fermi*-LAT records an excess amount of HE photons from the direction of "4FGL J1256.1-0547". The queried 4FGL catalog tells us that this object is associated with the FSRQ-type blazar 3C 279, with a large VarInd of 29785.23633 and located at a redshift of z∼0.5362.

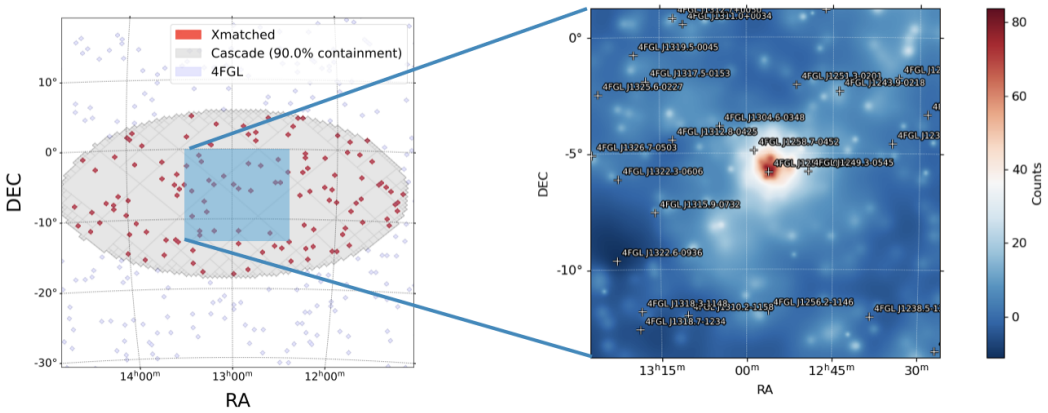

Figure 6.10: Zoom on the uncertainty region of IceCubeCascade-210416a. The **left plot** shows the localization error of the neutrino origin and the **right plot** shows for the highlighted region a HE skymap obtained through fermipy-based analysis of the weekly data file from *Fermi*-LAT. Note the HE excess recorded at the position of 4FGL J1256.1-0547.

EventNumber	Epoch	RA	Dec	Error90	# Sources	Candidate					
	[UTC]	[deg]	[deg]	[deg]		4FGL	Assoc (Class)	VarInd	redshift	offset	
38931474	23/04/30 08:42:02.63	23.9720	+38.9953	79.99	1664	J0112.8+3208	4C +31.03 (FSRQ)	1211.00964	0.603	8.294	
43811235	23/04/17 20:04:38.42	252.9321	-58.6351	9.03	73	-	-	-	-	-	-
1524801	23/03/29 20:30:08.31	133.4575	-36.7572	7.41	38	-	-	-	-	-	
43987982	23/01/09 11:12:11.29	174.8091	+45.3298	7.07	21	-	-	-	-	-	
30229466	22/12/29 22:57:12.76	27.2437	+36.8047	6.01	12	J0112.8+3208	4C +31.03 (FSRQ)	1211.00964	0.603	8.773 (beyond)	
67425471	22/10/18 21:13:59.70	90.8799	+37.5748	17.43	109	-	-	-	-	-	
22247606	22/09/03 01:46:39.59	109.0181	+4.6516	34.45	317	J0738.1+1742	PKS 0735+17 (BL Lac)	208.41606	0.45	14.129	
60401984	22/08/26 21:38:13.69	81.9293	+29.7022	20.77	146	-	-	-	-	-	
25590129	22/08/01 04:08:34.26	150.1126	-9.1693	12.90	49	-	-	-	-	-	
7950373	22/07/28 08:20:30.29	258.8350	-22.6512	8.00	80	-	-	-	-	-	
63259630	22/06/25 14:14:38.53	179.3921	-4.1645	5.86	14	-	-	-	-	-	
6590287	22/06/02 08:06:02.26	49.9691	-63.7976	14.52	115	J0303.6-6211	PKS 0302-623 (FSRQ)	255.52426	1.351	2.440	
4249774	22/05/27 20:27:01.77	226.1220	+4.8579	8.01	19	-	-	-	-	-	
40906130	21/12/10 21:38:16.30	142.6953	+16.0864	105.24	1492	-	-	-	-	-	
6354173	21/11/28 02:43:07.79	26.9641	+0.7524	18.96	148	J0108.6+0134	4C +01.02(FSRQ)	7107.27686	2.099	9.828	
58376130	21/09/26 05:26:10.94	249.4993	-35.7347	10.18	121	-	-	-	-	-	
31863828	21/04/16 01:58:00.70	194.1867	-6.2888	19.85	128	J1256.1-0547	3C 279 (FSRQ)	29785.23633	0.5362	0.521	
69399950	21/03/29 16:40:29.22	32.4624	-24.5896	11.32	43	-	-	-	-	-	
80902176	21/01/21 02:55:00.76	211.1333	-5.8941	20.93	135	J1408.9-0751	PKS B1406-076 (FSRQ)	1392.43689	1.494	2.248	

Table 6.1: Catalog of public CASCADE alerts along with output generated from ToOpy. Columns: (1) the EventNumber of the CASCADE alert; (2) Date (yy/mm/dd) and the time (hh:mm:ss.ms) of the event detection; (3) RA location of the event (J2000 epoch) in units of degrees; (4) Dec location of the event (J2000 epoch) in units of degrees; (5) Error90 is the location uncertainty (including radius, statistical and systematic errors, and computed at 90% containment) in units of degrees; (6) Number of 4FGL objects contained within the Error90 localization region; (7-11) information on potential host candidates that were obtained based on HE reference analysis with contemporaneous *Fermi*-LAT data as performed by ToOpy.

6.2.2 Conclusions and Prospects

Based on the detailed examples provided for the previous set of alerts I argue in favour of the usefulness of a HE-based reference analysis to find a potential counterpart. Even though CASCADE alerts are characterized by a large localization error, with up to hundreds of potential galaxy targets, our findings suggest that based on a HE reference analysis one could in principle select specific galaxy targets from within larger pools of counterparts.

As discussed for the CASCADE alert from March 21, my approach of choosing 15 deg ROIs centered at the best-fit positions needs to be improved in future releases, either by setting an additional parameter for ROI size or enabling tiled ROIs. The computational cost for both approaches should, however, be studied in order to guarantee correct performances and timely responses.

Even though the results in this section are biased in favour of assuming a strong connection between gamma-ray emitters and neutrino events (see also discussion in the following Chapter 7), I argue that this approach is still useful. Benefiting from the survey capacity of the *Fermi*-LAT instrument we see that for some of the CASCADE alerts the neutrino trigger was accompanied by a contemporaneous hotspot in the HE sky. Perhaps this bias can be relaxed once we manage to incorporate additional survey data from optical instruments, e.g. ZTF and LSST, into future releases of ToOpy.

On this note, these efforts are highly relevant due to the high astrophysical probability associated with CASCADE-type alerts, as well as their inherently large localization error, which in principle could also be covered by tiling observations. Hence, efforts to deal with CASCADE alerts thus also represent an excellent test bench for GW follow-ups.

6.3 Archival Counterpart Searches for GW Transient Signals

Even though the detection rate of CBCs has significantly increased for the third observing run (O3) of the LVC, the observations led to the report of eight NSBH and six BNS candidate events, without any confirmed EM counterparts yet. Hence GW170817 remains to this day in the spotlight as it is the only CBC detected along with its GRB counterpart GRB170817A.

Based on improvements in the data processing and the analysis methods, the LVC started to release various catalogs that summarize GW event triggers from the different observing runs, e.g. a sub-threshold GW dataset from the first observing run (Magee et al.; 2019), the Gravitational Wave Transient Catalog 2.1 (GWTC-2.1) based on the results of the first half of the third observing run (O3a) (Abbott et al.; 2021a) and the Gravitational Wave Transient Catalog 3 (GWTC-3) based on the results of the second half of the third observing run (O3b) (Abbott et al.; 2021b). Therein the LVC provided the astronomical community with event triggers that not only contain confident detections but also candidate events. These candidates are of lower statistical significance and buried in noisy data thus rendering the parameter estimation less accurate which in turn leads to a worse localization. Nevertheless, one of the

goals for distributing these catalogs is that based on additional potential GW triggers, astronomers could contribute to confident detections of GWs from BNS systems by detecting spatio-temporal coincidences with other types of transient signals in the EM domain (or neutrinos as a matter of fact). Eventually, this could lead to new multi-messenger discoveries, therefore adding new co-detections. Furthermore, since there are many more low-significance events than high-significance ones, the chances of finding a rare multi-messenger event improve, which is an additional reason to look at weaker signals.

Benefiting from the public release of these catalogs, I used their rich samples to search for hidden MM coincidences in a multitude of archival datasets. Previous efforts in using these catalogs include archival searches as reported by the VERITAS collaboration (Adams et al.; 2021). The authors elaborated a strategy to search for coincident observations in their VHE gamma-ray datasets and sub-threshold GW datasets from the first observing run (Magee et al.; 2019). In another publication (Hamburg et al.; 2020) performed offline searches in *Fermi*-GBM data in order to detect coincidences with CBC signals during the first and second observing runs.

Looking for routines that could be incorporated into ToOpy and to improve its ranking of sky regions, I learned about the efforts of the VERITAS collaboration and got motivated to elaborate an algorithm that based on ToOpy's MOC method (see also Section 5.2) would allow to perform spatio-temporal cross matches with archival datasets. My particular strategy consisted in using archival data from *Fermi*-GBM triggers and sub-threshold events from candidate CBC catalogs in order to facilitate novel detection of HE gamma-ray signatures potentially associated with a CBC.
Hence, in Section 6.3.1 I will outline the MM datasets e.g. sample of GW candidates and trigger table of GBM alerts, that were used to conduct this study. In Section 6.3.2, I then introduce my method that allows searching for spatio-temporal coincidences in combined MM alert streams. In Section 6.3.3 I will address the known association of GW170817 and GRB170817A and then discuss the results obtained when applying my algorithm to archival datasets of sub-threshold GW candidates and *Fermi*-GBM alerts. Section 6.3.4 concludes on this work and outlines possible future investigations, which includes also the prospect of using additional archival datasets that could contribute to the detection of coincidences between different messenger particles.

6.3.1 Observations and Data Analysis

As discussed in the introductory chapters of this thesis, the signals from the inspiraling and coalescence phase of BNS systems are expected to result in GW and GRB signals that are detectable by a range of observatories. Benefiting from the release of additional triggers, contained within catalogs of candidate GW events, as well as the public availability of GRB trigger data from satellite-based survey instruments, in the following sub-sections, I introduce the two datasets that will be used for my search of novel MM coincidences.

GW Catalogs By applying various search pipelines, e.g. PyCBC (Usman et al.; 2016) and GstLAL (Messick et al.; 2017), to strain data of the LVC interferometers, astronomers manage to isolate signals from CBC events hidden within the detector noise. Candidate events that were gathered from the three observing runs into catalogs are summarized in Table 6.2 and represent our sample of GW events used for this work. Overall there are 1132 triggers from the various catalogs corresponding to the different observing runs of the GW interferometers. Note, that there are many more triggers contained in the catalogs GWTC-2.1 and GWTC-3 but I exclude all events from pipelines that do not yield coincidences at all.

Observing Run/ Catalog	Epoch	$\#_{Trigger}$ Candidate GW Events	$\#_{Trigger}$ GBM-Fligth	$\#_{Trigger}$ GBM-SubTreshold
O1 SubT BNS	Sep 2015-Jan 2016	103	619	0*
O1&O2 GWTC-1	Nov 2016-Aug 2017	11**	2396	156*
O3a GWTC-2.1	Apr 2019-Nov 2019	734	308	289
O3b GWTC-3	Nov 2019-Mar 2020	284	201	193

Table 6.2: GW and GRB datasets for this work. Columns: (1) Observing Run and catalog used, (2) Epoch, (3) Number of triggers contained in the GW sample, (4) Number of *Fermi*-GBM triggers (Flight-Position) during the respective observing runs, (5) Number of *Fermi*-GBM triggers (SubTreshold) during the respective observing runs.
***;** The SubTreshold trigger stream was not established prior to 2017-04-16
****;** These are confident detections

High-Energy Gamma Rays and *Fermi*-GBM Triggers For this study, we collected all *Fermi*-GBM event triggers recorded during the times when the GW interferometers were taking data by web scrapping their detection date from the corresponding trigger table[2] as well as the corresponding sub-threshold trigger table [3]. The dataset was then filtered to cover the time ranges of the observing runs and the number of events found is summarized in the last two columns of Table 6.2.

6.3.2 Methodology

STMOC Method: Adopting the MOC methodology I elaborated for ToOpy, I generalized it in order to generate STMOC objects. This facilitated my search for spatio-temporal coincidences in archival trigger tables of GW and GBM events. As requirements to identify spatio-temporal coincidences, I require that for a given trigger pair there are both i) a spatial overlap within the 90% confidence regions of the localization errors and ii) two spatially overlapping events that coincide within one minute of t_c,

[2] https://gcn.gsfc.nasa.gov/fermi_grbs.html
[3] https://gcn.gsfc.nasa.gov/fermi_gbm_subthresh_archive.html

i.e. a time window of -30 $\leq t_c \leq$ +30 seconds, where t_c corresponds to the time of coalescence for a given GW trigger. Note that this value was chosen based on the results from performing checks with bootstrapped data sets as described in the following paragaph.

Bootstrapping: In order to obtain a measure of how often one can expect accidental spatio-temporal crossmatches for triggers in a given datasets, I adopted the following methodology in order to obtain bootstrapped version of the same data:

- ◇ **Step I:** Choose one random event from the *Fermi*-GBM triggers and add it to a list.
- ◇ **Step II:** Repeat step for all *Fermi*-GBM triggers and allow for duplicates, i.e. performing a sampling with replacement in order to generate a new dataset.
- ◇ **Step III:** Compute for the new dataset the number of spatio-temporal coincidences and add it to a histogram.
- ◇ **Step IV:** Start over steps I to III 1000 times.

Note that in Step I, one can either keep the positional and temporal information of each trigger integer, or one can split these two quantities and recombine them afterwards randomly. The results from keeping them homogeneous will be illustrated using blue histograms of Figure 6.16 whereas the splitted case is represented by the use of red histograms.

Hotspot-Screener: Upon applying the STMOC method to the dataset described in Table 6.2, I also investigate whether for any of the resulting spatio-temporal associations, there is any notable HE emission from within the shared uncertainty region of the GW- and GBM triggers. In order to perform this screening I analyze contemporaneous *Fermi*-LAT data. My analysis is primarily based on weekly files around the time of the CBC trigger, hence allowing to detect flaring activity at HE. In case that there is a hint of a hotspot, I then gather more data around the trigger date in order to detect new candidate sources via the fermipy-method "gta.findsources()", which allows to detect new candidate sources of HE emission. Once isolated these source candidates then allow me to generate customized models[4] which in turn enable us to use data samples from the Pass 8 SOURCE class data (Atwood et al.; 2013) in order to analyze long-term trends. In order to obtain the long-term HE gamma-ray light curves of potential counterpart candidates, we perform dedicated likelihood analyses with monthly binned *Fermi*-LAT data sets. If there are repeated transient signals from the same sky position, this indicates a reoccurring event whilst in the case of the absence of repetitions this would favor a potential detection of a CBC at HE.

[4] https://fermipy.readthedocs.io/en/latest/model.html

6.3.3 Results and Discussions

Prior to discussing the results that we obtain by applying our methods to the dataset in Table 6.2, we will elaborate on the GW170817 and GRB170817A association.

Sanity check GW170817/GRB170817A The pair GW170817/GRB170817A provides a valuable sanity check for this analysis pipeline. Since the underlying triggers satisfy both conditions for identifying spatio-temporal coincidence, the algorithm must recover this particular pair of triggers, which it did as shown in Figure 6.11. But not only only did it match the two involved triggers, it also gave me valuable insight into dealing with the revision of *Fermi*-GBM triggers. The notice with the lowest latency, i.e. the Flight Position alert, assigns this particular trigger a 97% probability of being associated with a transient GRB signal and contains the localization of the confirmed host galaxy in its error region. The three successive revisions for the Final Position notice intriguingly do not contain the confirmed host galaxy NGC4993 within their respective 90% containment region. Furthermore, the last revision does not even spatially overlap with the GW localization error anymore.
Regarding the contemporaneous *Fermi*-LAT data, we find no evidence for any HE signature (see also Figure 6.12). Nevertheless, this is expected since the *Fermi*-LAT instruments were not operational due to the spacecraft's passage through the South Atlantic Anomaly (notice that the GBM instruments would have turned off ∼2 minutes after the CBC trigger (Thompson and Wilson-Hodge; 2022)).

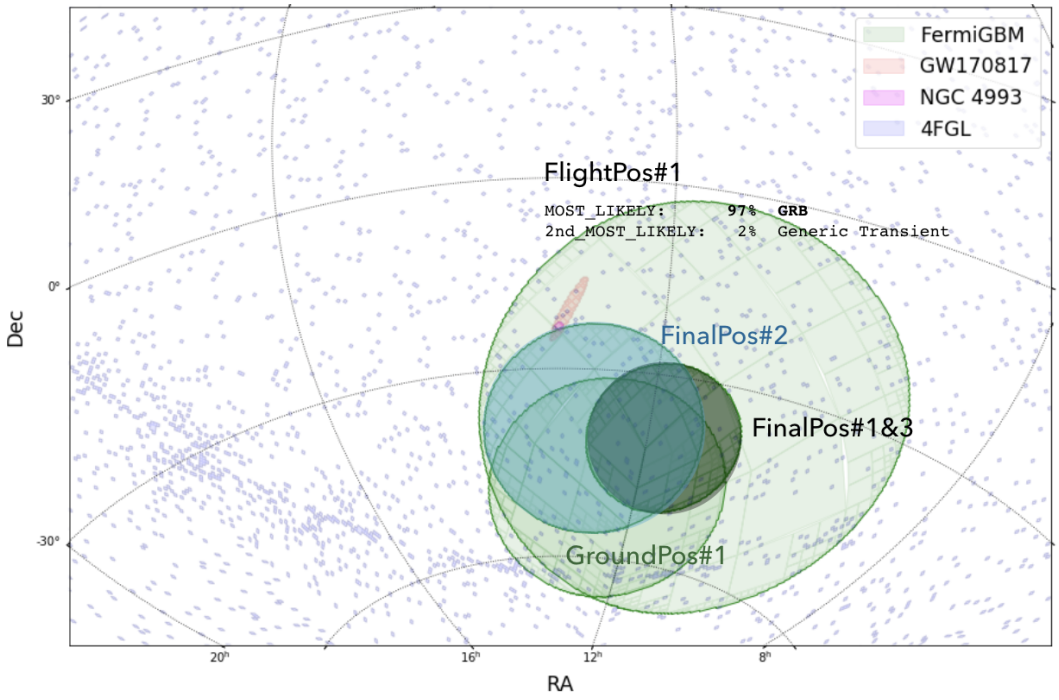

Figure 6.11: Successive localization errors for the revisions of the triggers associated with a the transient event GRB170817A recorded by *Fermi*-GBM 1.74 ± 0.05 seconds after the GW170817 event trigger from the second observing run of the LVC.

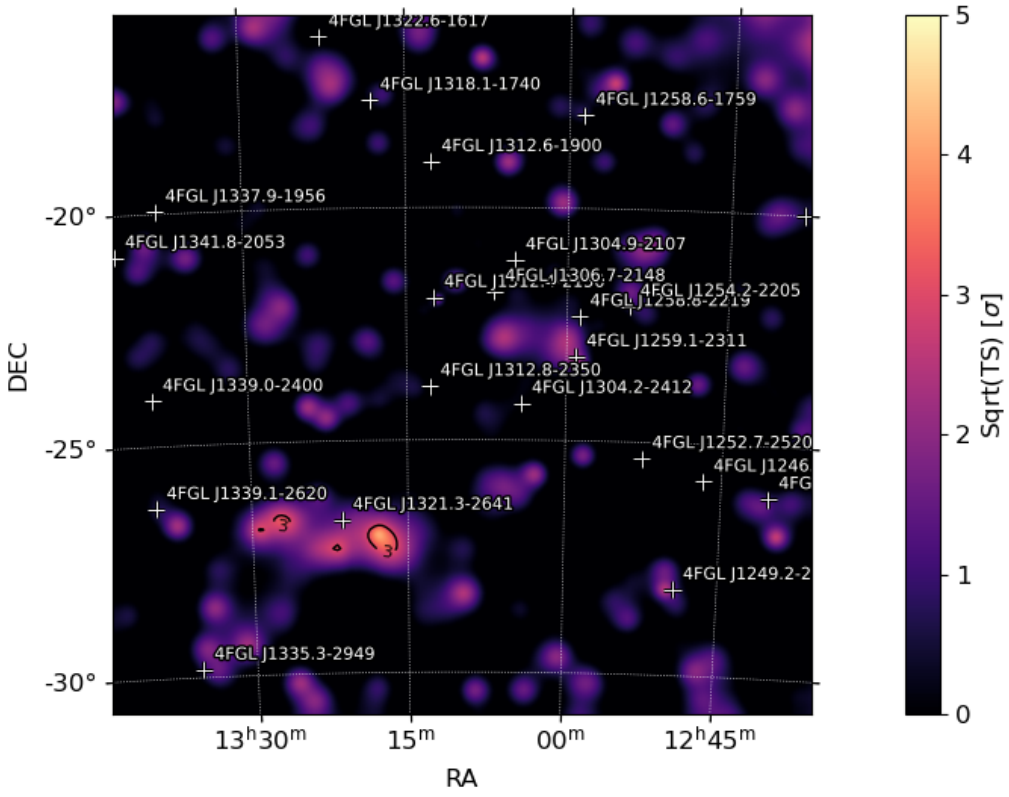

Figure 6.12: Sanity check of the "hotspot-screener" method with the pair GW170817/GRB170817A. The position of NGC4993 (R.A. [J2000]: 197.448776 Dec. [J2000]: -23.383831) is chosen as the center of the 15 deg ROI for which I then perform a fermipy anylsis.

Spatio-Temporal Coincidences from subthreshold GW Events and *Fermi*-GBM Triggers Upon applying our "STMOC" method to the dataset from Table 6.2 we obtained four coincidences between *Fermi*-GBM Triggers and sub-threshold GW triggers from the first and third observing run of the GW interferometers. Figure 6.13 gives an overview of these four spatio-temporal coincidences we found and in the following, we go briefly through each trigger pair:

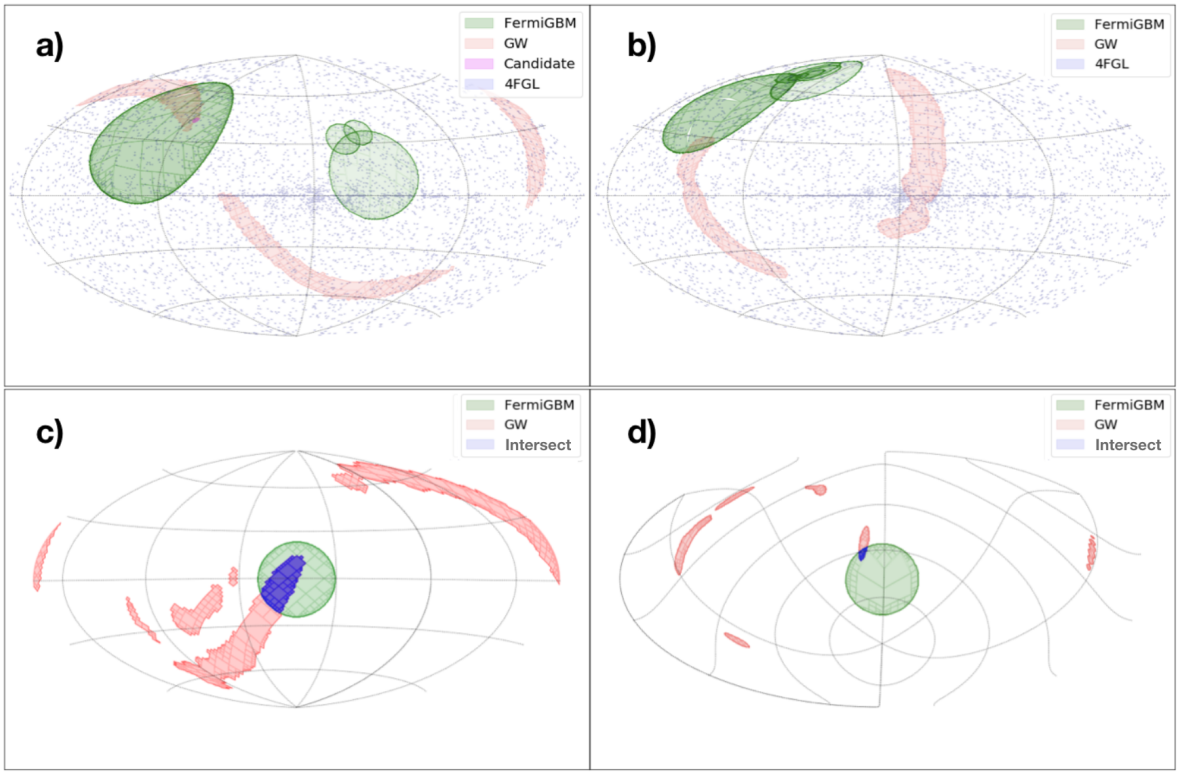

Figure 6.13: Overview of the four spatio-termporal coincidences between *Fermi*-GBM and candidate GW events found with the STMOC method.

- **a) O1 & Flight Position Alert:** The individual triggers relate as follows: $t_{FermiGBM} = t_{GW}+28$sec. As we can see in Figure 6.14 the initial Flight-Position alert assigned a 75% probability for a GRB transient classification, whilst the revision of the trigger resulted in an association with a solar flare. Nevertheless, in this case the "hotspot-screener" method resulted in the detection of a HE candidate within the common localization errors (we will revisit this below). Note that for this *Fermi*-Trigger there is no Final- or Ground-Position reported.
- **b) O3a & Flight Position Alert:** The individual triggers relate as follows: $t_{FermiGBM} = t_{GW}+21$sec. As we can see in Figure 6.15 the best-fit position from the initial Flight Position is once again overruled by revised triggers and the spatial association is erased. In this particular case in favour of a likely GRB counterpart with a best-fit located at a large offset with respect to the initial trigger.
- **c) O3a & SubTreshold Alert:** The individual triggers relate as follows: $t_{FermiGBM} = t_{GW}+28$sec. The "hotspot-screener" method did not reveal any excess HE signatures from within the region of spatial overlap.
- **d) O3b & SubTreshold Alert:** The individual triggers relate as follows: $t_{FermiGBM} = t_{GW}-26$sec. From a physical point of view, the situation that the GRB precedes a CBC seems unphysical. To be fair, there might be other transient phenomena at play that are beyond our current understanding.

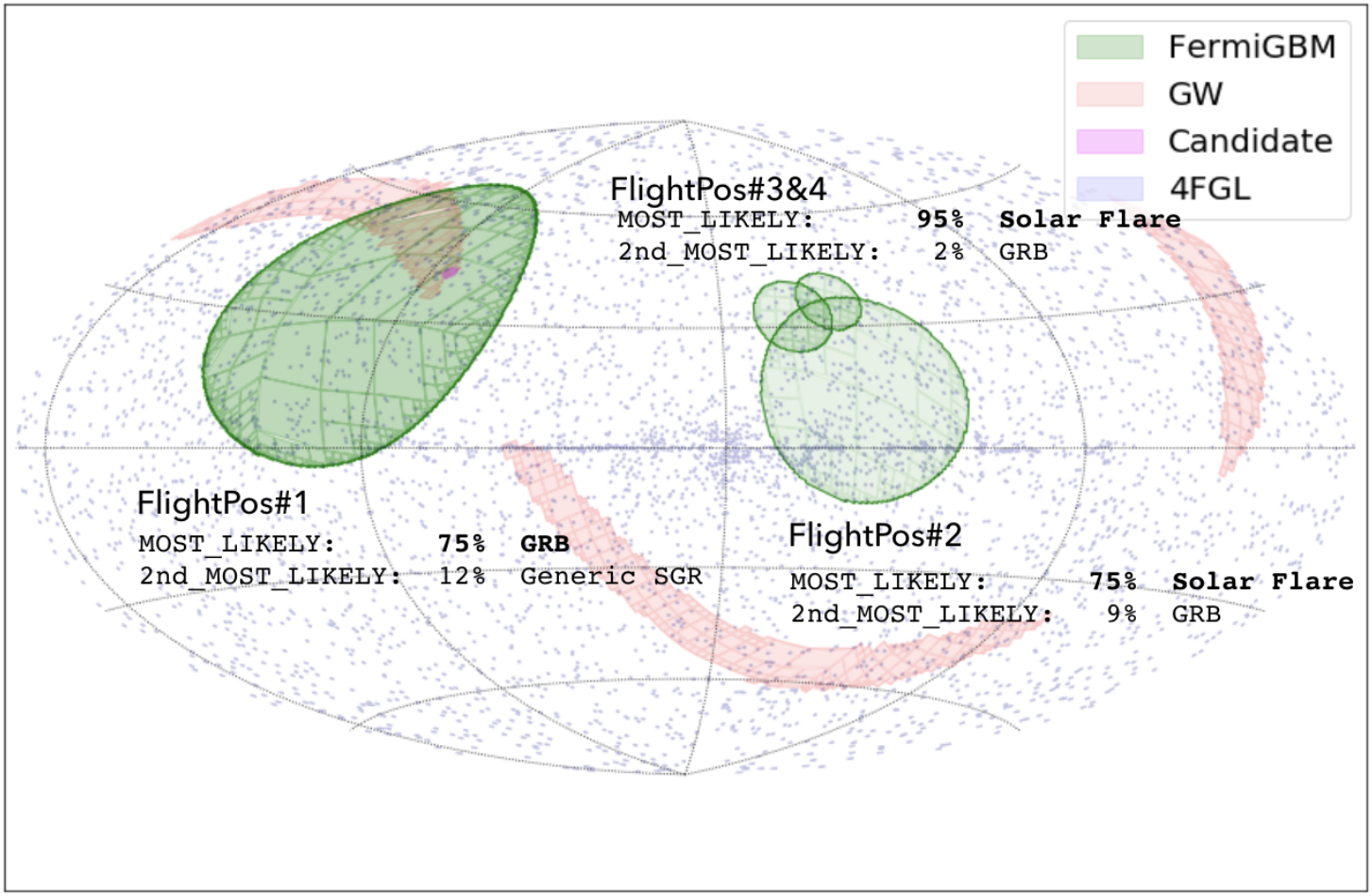

Figure 6.14: Successive localization errors for the revisions of the triggers associated with a transient event detected by *Fermi*-GBM 28 seconds after the GW event trigger from the first observing run of the LIGO detectors.

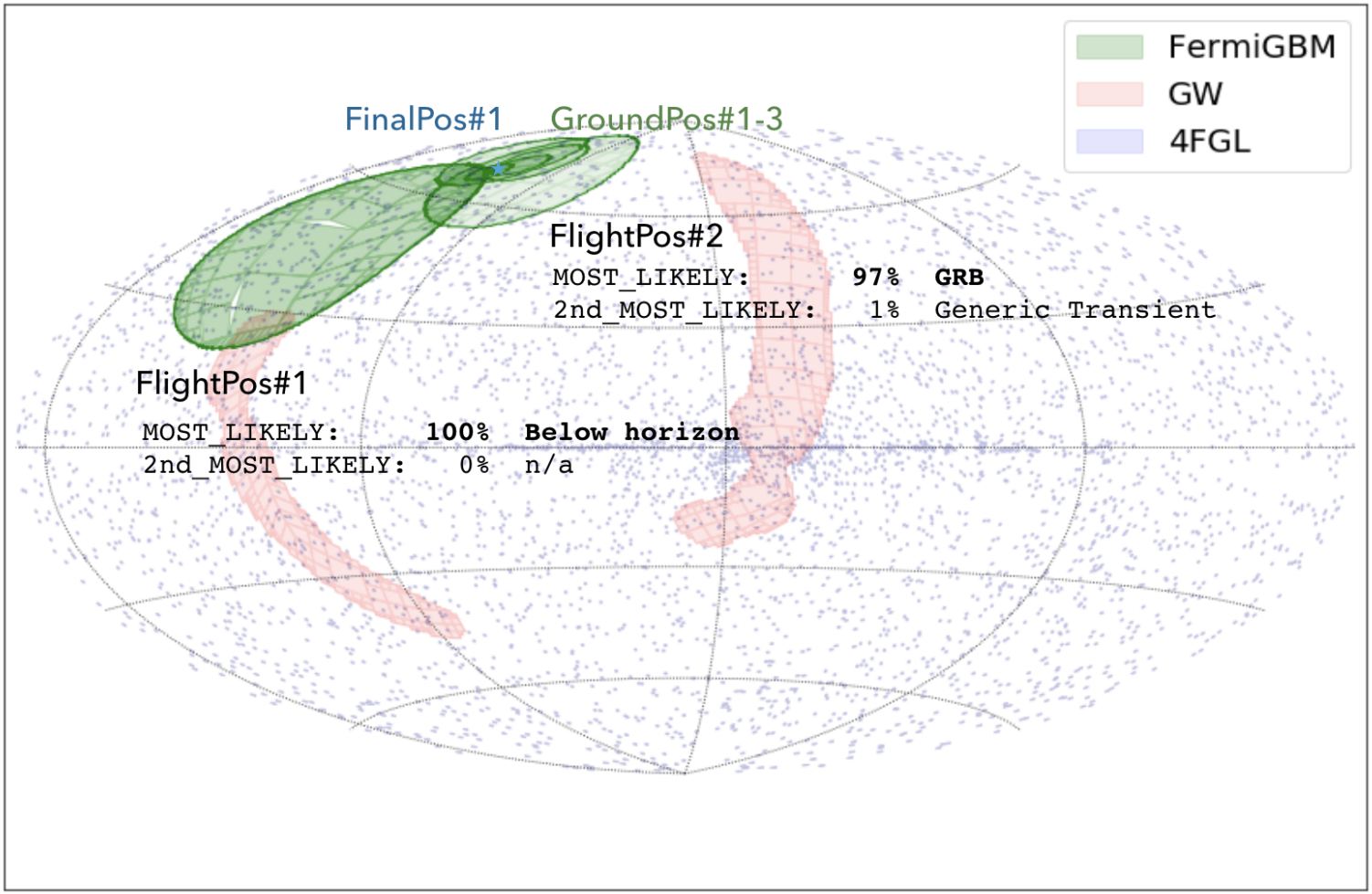

Figure 6.15: Successive localization errors for the revisions of the triggers associated with a transient event detected by *Fermi*-GBM 21 seconds after the GW event trigger from the third observing run of the LVC.

Bootstrapped Data Sets The result from searching for spatio-temporal coincidences in bootstrapped datasets is shown for 1000 realizations thereof in Figure 6.16.

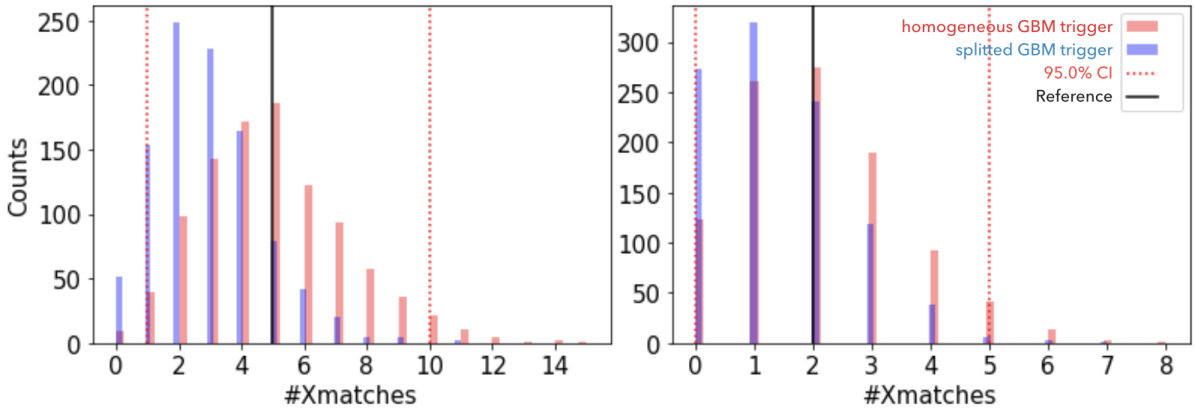

Figure 6.16: Histograms showing the number of obtained spatio-temporal coincidences with 1000 bootstrapped datasets. The **left plot** shows the number of found coincidences when using all triggers from *Fermi*-GBM, e.g. Flight-, Ground-, Final- and Subtreshold-alerts. The **right plot** shows the number of found coincidences when using only the last revision of the alerts, i.e. Final- and Subtreshold-notice from *Fermi*-GBM. The reference amount of coincidences found in the original dataset are marked by a black line and the 95% CI of coincidences one obtains with the bootstrapped dataset (here only homogeneous) is marked by a red dotted line.

As one can see, the amount of spatio-temporal coincidences one obtains in the original dataset (five in the case of keeping all *Fermi*-GBM revisions and two in the case of only considering the newest *Fermi*-GBM notice) are easily reproducible by using bootstrapped datasets. This is shown by the reference values (black lines) being contained in the 95% CI of the bootstrapped distributions (red (homogeneous) and blue (splitted) histograms). Hence the four found spatio-temporal crossmatches might be simply due to randomness and not physically relevant. This indicates towards the real data not yielding a significantly larger number of coincidences than in the bootstrapped version thereof. Therefore we can not argue in favour of saying that the four found coincidences are events beyond random coincidences.

Hotspot-Screener for O1 and Flight Position Alert To further investigate the found spatio-temporal crossmatches, I performed a *Fermi*-LAT analysis for each trigger pair separately and inspect the overlapping regions for potential hotspot signatures. From all coincidences (a-d) only the first shows a promising hint of HE excess emission for the week that covers the triggers. Even though the revisions of the *Fermi*-GBM trigger eventually nullify the spatial crossmatch, this HE candidate event deserves further attention. Gathering enough weekly *Fermi*-LAT data in order to apply the "gta.find_sources()" method I managed to isolate the coordinates of a source candidate in the HE skymap, thus allowing to add an additional source to a custom model (see also Figure 6.17). Note also that the weekly-binned light curve is promising, even though the HE emission seems to precede the GW trigger by two weeks.

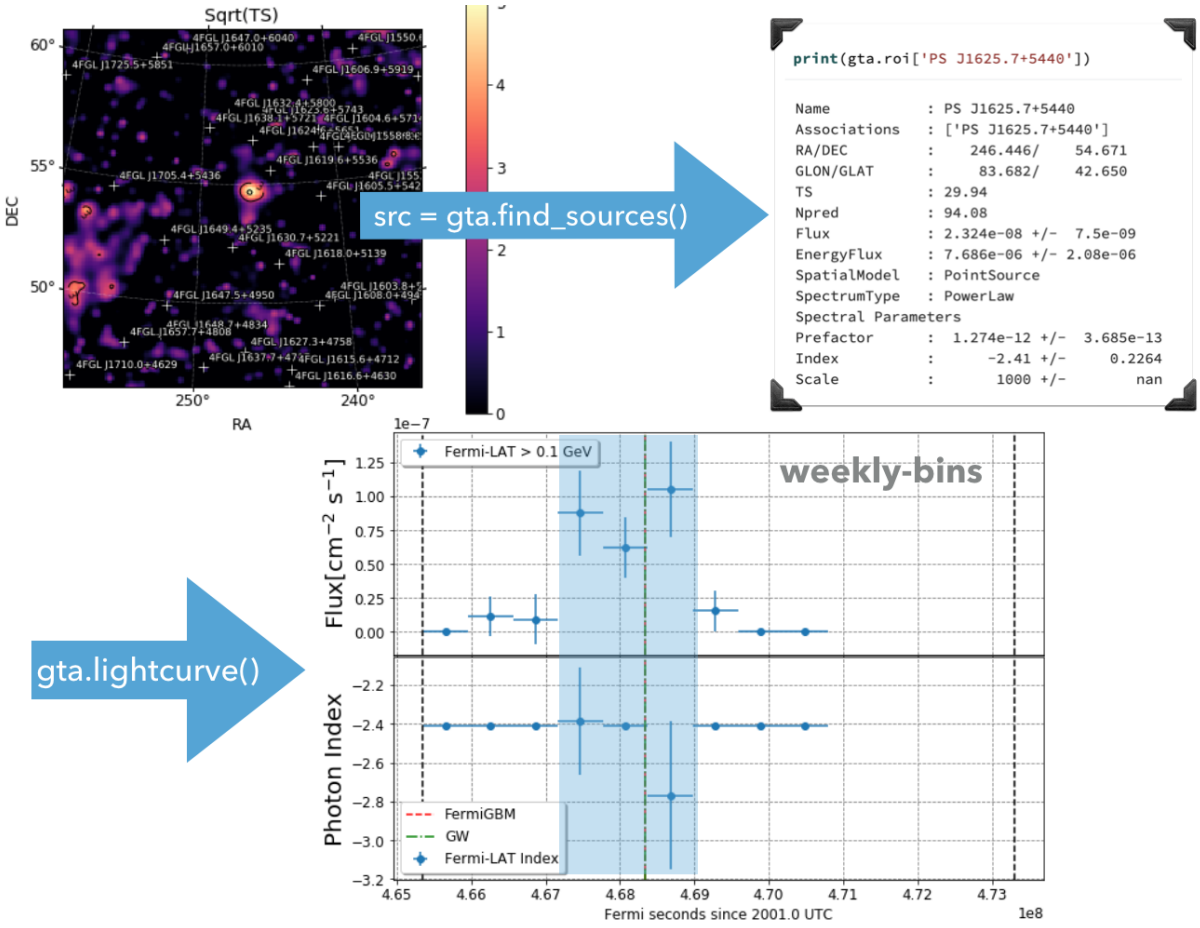

Figure 6.17: Gathering enough data allows to apply the "gta.find_sources()" method and thereafter isolate a new source candidate PS J1625.7+5440. The **top left plot** shows the result from the "hotspot-screener" method indicating a clear excess at the centre of the ROI. The **top right plot** are the source parameters found by the "gta.find_sources()" method. The **lower plot** shows the light curve (weekly-binned) for the newly obtained source candidate.

Having built my custom model, I then analyzed 10 years of data and verified by computing a light curve (monthly-binned) that the HE flare around the GW trigger is a non-repeating transient event (see also Figure 6.18).

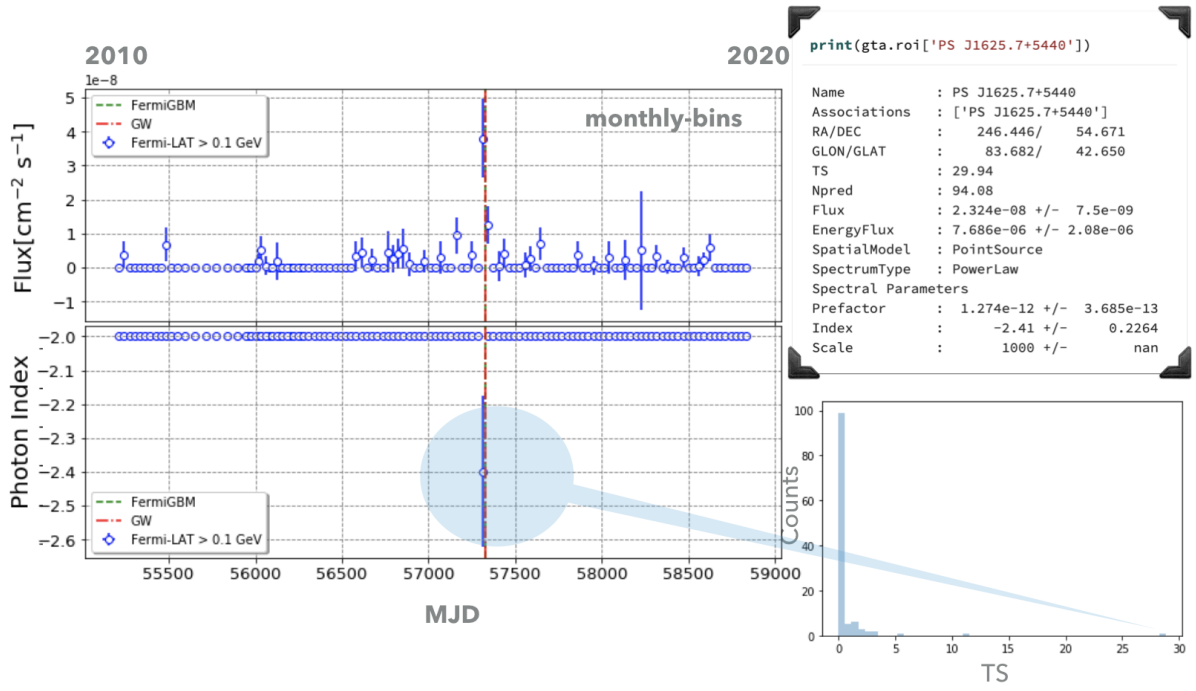

Figure 6.18: Long-term lightcurve, here 10 years, for my candidate PS J1625.7+5440. The data is monthly-binned with a single confident detection, i.e. TS>25, during the month that contains the GW trigger. The **left plot** shows the light curve (monthly-binned) for PS J1625.7+5440. The **top right plot** describes the source paramters of PS J1625.7+5440 and the **bottom right plot** shows a histogram of the TS-value for each lightcurve bin.

6.3.4 Conclusions and Prospects

My results on GBM counterparts to LVC triggers report four coincident triggers when allowing time spans of ±30 seconds around the trigger time of the GW signal. Nevertheless, given that after revisions of the initial GRB triggers, the coincidences for the two significant GBM events vanished, it is doubtful that these coincidences correspond to real astrophysical associations. Also as learned through bootstrapping, finding four spatio-temporal associations is consistent with what one would expect from simple random chance. Nevertheless, for one of these events, a hotspot of HE gamma-ray emission can be found in a contemporaneous Fermi-LAT data set, and checking the long-term flux (10 years) at the position of the hotspot reveals a single flare of HE photons around the time of the GW trigger. This may hint at a real correlation but it would still need monitoring data from other instruments, such as optical telescopes, to extract actual information.

Prospects for Searches in Additional Archival Datasets There are many more datasets in which we could search for EM counterpart signatures using the same algorithm we described in the previous section. These datasets include, amongst many others:

- ◇ **BNS mergers in *Swift*-BAT:** Promising in case of a spatio-temporal association due to the excellent localization error of 3 arcmin (0.05 degree) radius.
- ◇ **Other space-borne instruments:** For example INTEGRAL.
- ◇ **Coincidences of GRBs in *Swift*-BAT and *Fermi*-GBM:** Promising in case of a spatio-temporal association due to its excellent localization region of 3 arcmin radius.
- ◇ **VHE Transient signatures in archival MAGIC data:** Search for spatio-temporal coincidences of low latency trigger data, such as *Fermi*-GBM Subtreshold-type or candidate GW events, in archival datasets of MAGIC (similar to what VERITAS did but extended to other low latency triggers).

Bibliography

Abbott, R., Abbott, T., Acernese, F., Ackley, K., Adams, C., Adhikari, N., Adhikari, R., Adya, V., Affeldt, C., Agarwal, D. et al. (2021a). Gwtc-2.1: Deep extended catalog of compact binary coalescences observed by ligo and virgo during the first half of the third observing run, *arXiv preprint arXiv:2108.01045* .

Abbott, R., Abbott, T., Acernese, F., Ackley, K., Adams, C., Adhikari, N., Adhikari, R., Adya, V., Affeldt, C., Agarwal, D. et al. (2021b). Gwtc-3: compact binary coalescences observed by ligo and virgo during the second part of the third observing run, *arXiv preprint arXiv:2111.03606* .

Adams, C., Benbow, W., Brill, A., Buckley, J., Capasso, M., Christiansen, J., Chromey, A., Daniel, M., Errando, M., Falcone, A. et al. (2021). An archival search for neutron-star mergers in gravitational waves and very-high-energy gamma rays, *The Astrophysical Journal* **918**(2): 66.

Atwood, W., Albert, A., Baldini, L., Tinivella, M., Bregeon, J., Pesce-Rollins, M., Sgrò, C., Bruel, P., Charles, E., Drlica-Wagner, A. et al. (2013). Pass 8: toward the full realization of the fermi-lat scientific potential, *arXiv preprint arXiv:1303.3514* .

Hamburg, R., Fletcher, C., Burns, E., Goldstein, A., Bissaldi, E., Briggs, M., Cleveland, W., Giles, M., Hui, C., Kocevski, D. et al. (2020). A joint fermi-gbm and ligo/virgo analysis of compact binary mergers from the first and second gravitational-wave observing runs, *The Astrophysical Journal* **893**(2): 100.

Kowalski, M., Collaboration, I. et al. (2017). Neutrino astronomy with icecube and beyond, *Journal of Physics: Conference Series*, Vol. 888, IOP Publishing, p. 012007.

Magee, R., Fong, H., Caudill, S., Messick, C., Cannon, K., Godwin, P., Hanna, C., Kapadia, S., Meacher, D., Mohite, S. R. et al. (2019). Sub-threshold binary neutron star search in advanced ligo's first observing run, *The Astrophysical Journal Letters* **878**(1): L17.

Messick, C., Blackburn, K., Brady, P., Brockill, P., Cannon, K., Cariou, R., Caudill, S., Chamberlin, S. J., Creighton, J. D. E., Everett, R., Hanna, C., Keppel, D., Lang, R. N., Li, T. G. F., Meacher, D., Nielsen, A., Pankow, C., Privitera, S., Qi, H., Sachdev, S., Sadeghian, L., Singer, L., Thomas,

E. G., Wade, L., Wade, M., Weinstein, A. and Wiesner, K. (2017). Analysis framework for the prompt discovery of compact binary mergers in gravitational-wave data, **95**(4): 042001.

Seglar-Arroyo, M., Sanchez, D., Esteban Gutierrez, A., Agudo, I., Ciprini, S., Filippenko, A., Hovatta, T., Jermak, H., Jorstad, S., Kopatskaya, E. et al. (2022). Magic and hess detect vhe gamma rays from the blazar ot 081 for the first time: a deep multiwavelength study, *POS PROCEEDINGS OF SCIENCE* **395**.

Stickel, M., Fried, J. and Kuehr, H. (1988). The redshifts of the bl lac objects 1749+ 096 and 2254+ 074., *Astronomy and Astrophysics* **191**: L16–L18.

Thompson, D. J. and Wilson-Hodge, C. A. (2022). Fermi gamma-ray space telescope, *Handbook of X-ray and Gamma-ray Astrophysics* .

Usman, S. A., Nitz, A. H., Harry, I. W., Biwer, C. M., Brown, D. A., Cabero, M., Capano, C. D., Dal Canton, T., Dent, T., Fairhurst, S., Kehl, M. S., Keppel, D., Krishnan, B., Lenon, A., Lundgren, A., Nielsen, A. B., Pekowsky, L. P., Pfeiffer, H. P., Saulson, P. R., West, M. and Willis, J. L. (2016). The PyCBC search for gravitational waves from compact binary coalescence, *Classical and Quantum Gravity* **33**(21): 215004.

CHAPTER 7

HIGH ENERGY NEUTRINO GAMMA FOLLOW UP LIST

Resume: The work presented in this chapter was performed during my stay at the Institute for Cosmic Ray Research (ICRR) in Tokyo, Japan. Together with K. Noda and A. Fiasson we elaborated an updated GFU list for follow-ups with the LSTs.

Contents

As mentioned in the introductory chapters of this manuscript, there are well-founded reasons why the study of blazar jets and therein physics could be boosted by studying VHE gamma rays and HE neutrino signatures. In section 3.1.3 we briefly touched upon a follow-up program that was set up by the IceCube observatory in cooperation with IACTs of the third generation, namely FACT, H.E.S.S., MAGIC, and VERITAS. The goal for this specific program is to facilitate quick ToO observations on neutrino alerts sent by the IceCube observatory, and it comes in two distinct approaches:

- **Singlet events:** follow-up of single high-energy neutrino candidate events with attributed signalness implying that they are of astrophysical origin of different probability (GOLD, BRONZE, CASCADE).

◇ **Multiplet events:** follow-up on previously known HE gamma-ray sources that lie within the uncertainty region of clusters of neutrino events that occur on time scales of seconds up to 180 days.

Whilst feasible strategies and tools to follow up **singlet events** were outlined previously in Chapter 5 (and thereafter successfully applied in Sections 6.1 and 6.2), the case of **multiplet events** requires further elaboration. I will initiate this chapter by outlining the ingredients used to build a current version of a GFU list (Section 7.1). Upon motivating in Section 7.2 the need for a revised list, I will elaborate on our ingredients and respective approaches in order to generate a new list that combines sources from three catalogs: 4FGL-DR3 (Section 7.3.1), TeVCat (Section 7.3.2) and Glade+ (Section 7.3.3). Upon merging the source candidates of the three selections, I present our new candidate list in Section 7.4 and outline prospects for upcoming efforts.

7.1 Current GFU List used by 3rd Generation IACTs

The GFU program was initialized in 2012 with all third-generation IACTs participating. The list of objects monitored for possible associations with neutrino clusters were selected out of the 3FGL and 3FHL catalogs based upon the following criteria detailed in Satalecka et al. (2021):

- Extragalactic source with known redshift and z $\leq$ 1.0
- 3FGL: variability index $>$ 77.2; 3FHL: variability $>$ 1 based on Bayesian blocks
- Culmination at the IACT site within a chosen zenith angle limit (usually $<$ 45 deg)
- Assuming that the source can produce a gamma-ray flare with a 10-fold increase over the average Fermi-LAT flux, the extrapolated flux above 100GeV has to exceed the IACT 5 σ sensitivity for observation times between 2.5 h to 5 h.
- Adding all extragalactic sources detected by IACTs along with the Galactic Centre and the Crab Nebula.

7.2 Motivation for an updated GFU List

The previous GFU list was initialized from the 3FGL (4 years of data of *Fermi*-LAT, 100 MeV-300 GeV, 3033 sources) and 3FHL (7 years of data of *Fermi*-LAT, E $>$ 10 GeV, 1556 sources) catalogs. Since these two catalogs are outdated in comparison to the newest 4FGL-DR3 (12 years of data of *Fermi*-LAT, 50 MeV - 1 TeV, 6658 sources), a revision seems appropriate at this point. Up until now there are only two known extragalactic neutrino emitters and they are very different: TXS 0506+056 is a blazar and highly variable source whilst NGC 1068 is a Seyfert galaxy[1] that is a steady source detected at HE by *Fermi*-LAT but not at VHE. Hence, limiting ourselves only to the known gamma emitters from the Fermi

[1]Both blazars and Seyfert galaxies are AGNs that emit strong radiation across the EM domain. However, whilst blazars are characterized by high accretion rates and hence significant variability and strong radio emission, Seyfert galaxies are accreting matter at a lower rate and are characterized by their strong emission lines in their optical spectra.

catalogs does not seem the best strategy or approach anymore. This, in return, gives rise to the need to open up the idea to observe neutrino events that are not constrained to be located around gamma-ray emitters but also other sources/targets.

7.3 Towards an New GFU List

Needless to say that the collaboration with IceCube collaboration should be continued given the interest and potential discoveries that may arise from it. However, in order for the next generation of gamma-ray telescopes to achieve the best possible results when it comes to reacting to neutrino triggers from multiplet alerts, the candidates sources or targets for the GFU should be reevaluated. We argue that we need to start from scratch with new catalogs and a revised strategy. Otherwise, the current LST-1 (and future LSTs) will be constrained to follow-up the same triggers that are currently received by the 3rd generation instrument and at best we might only detect a few more sources in the coming decade which are not enough to elucidate the question of the neutrino emitters. The catalogs we used and the respective cuts we applied to select the final GFU list are listed in the following:

◇ **4FGL-DR3:**

- **i) Observability :** culmination at the site observatory with zenith < 45 deg
- **ii) $10{*}\mathbf{F}_{VHE,extrap.}$ > Cerenkov telescope sensitivity :** extrapolated VHE flux (x10) surpassing IACT sensitivity.
- **iii) Known redshift:** querying NED database for sources obtained in step ii).
- **iv) $10{*}\mathbf{F}_{VHE,extrap.+EBL}$ > Cerenkov telescope :** extrapolated VHE flux (x10) surpassing IACT sensitivity but accounting for EBL attenuation (computed using the redshift and the Dominguez model (Dominguez et al.; 2011)).

Note that compared to the current GFU list (see also Section 7.1) we discarded the variability cut after lessons learned from NGC 1068.

◇ **TeVCat (?):**

- **i) Observability :** culmination at the ORM with zenith < 45 deg
- **ii) various filters:** to exclude specific sources, e.g. galactic targets, non-repeating transients, duplicate entries, double counts within 4FGL-DR3, unIDs, SNR and PWN.

◇ **GLADE+ (?):**

- **i) Reported BNS merger rate :** in order to only consider those galaxies for which the authors report a parameter that serves as an estimate of the BNS merger rate.
- **ii) BMAG and BNS merger rate cut:** using the reported values of NGC 4993 as reference in order to apply cuts on BMAG and BNS merger rate.

- **ii) Distance Cut:** using the reported value of NGC 4993 as reference to apply cuts on distance.
- **iii) Observabillity :** culmination at the ORM with zenith < 45 deg.
- **iv) Offsets:** remove indiviudal galaxies from pairs that are too close (here we used > 1 deg).

We use the reported parameters for NGC 4993 as reference cuts in order to reduce the bulk of potential candidate sources and to keep the more massive galaxies.

In the following Sections, we will introduce the three catalogs: 4FGL-DR3 (Section 7.3.1), Glade+ (Section 7.3.3), TeVCat (Section 7.3.2). Going through each of those, we will elaborate on our approach and the cuts listed above that we apply in order to select specific sources that we will then add to our new GFU candidate list.

7.3.1 4FGL-DR3

The third data release of the fourth Fermi-LAT catalog (4FGL-DR3) contains 6658 sources detected in the energy range from 50 MeV to 1 TeV and whose coverage is plotted in Figure 7.1.

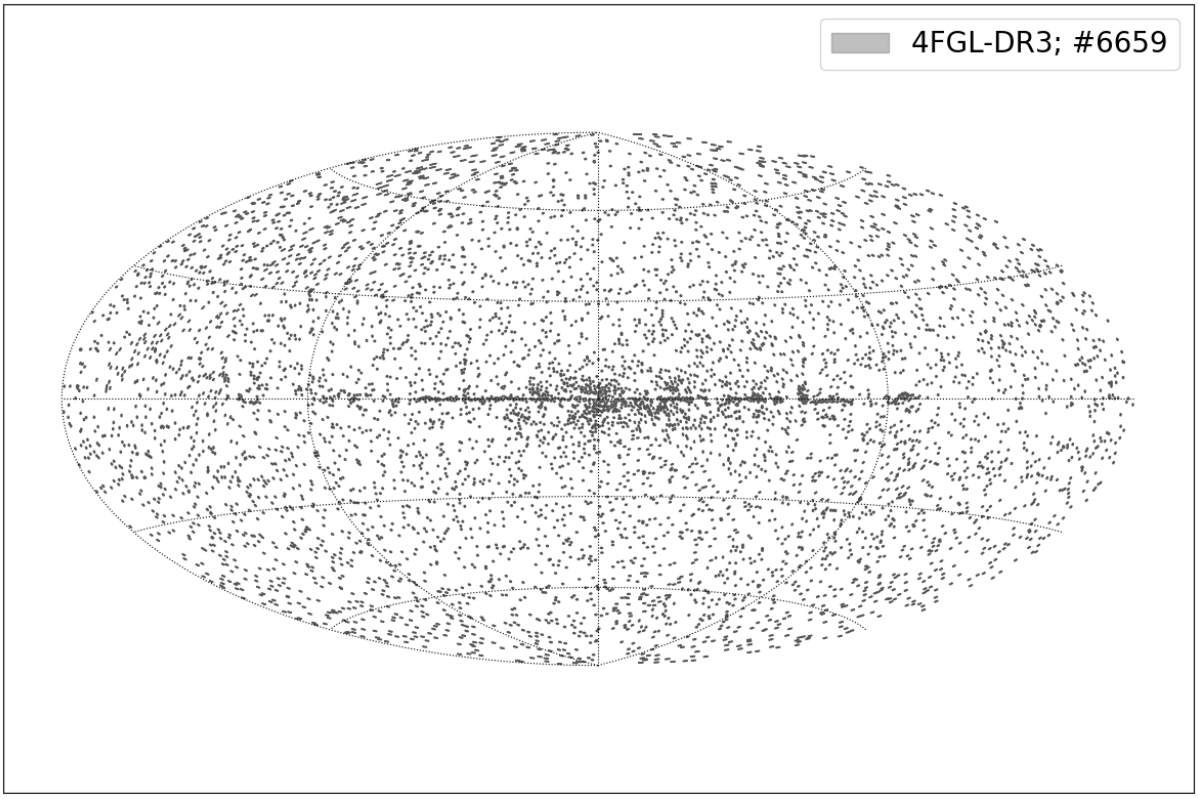

Figure 7.1: Sky coverage of the 4FGL-DR3 catalog in galactic coordinates.

Observability by astroplan In order to check the visibility of the sources, we used the "astroplan" package. Those that are visible based on constraints of visibility from ORM (the site of MAGIC and LST-1) are marked accordingly in Figure 7.2

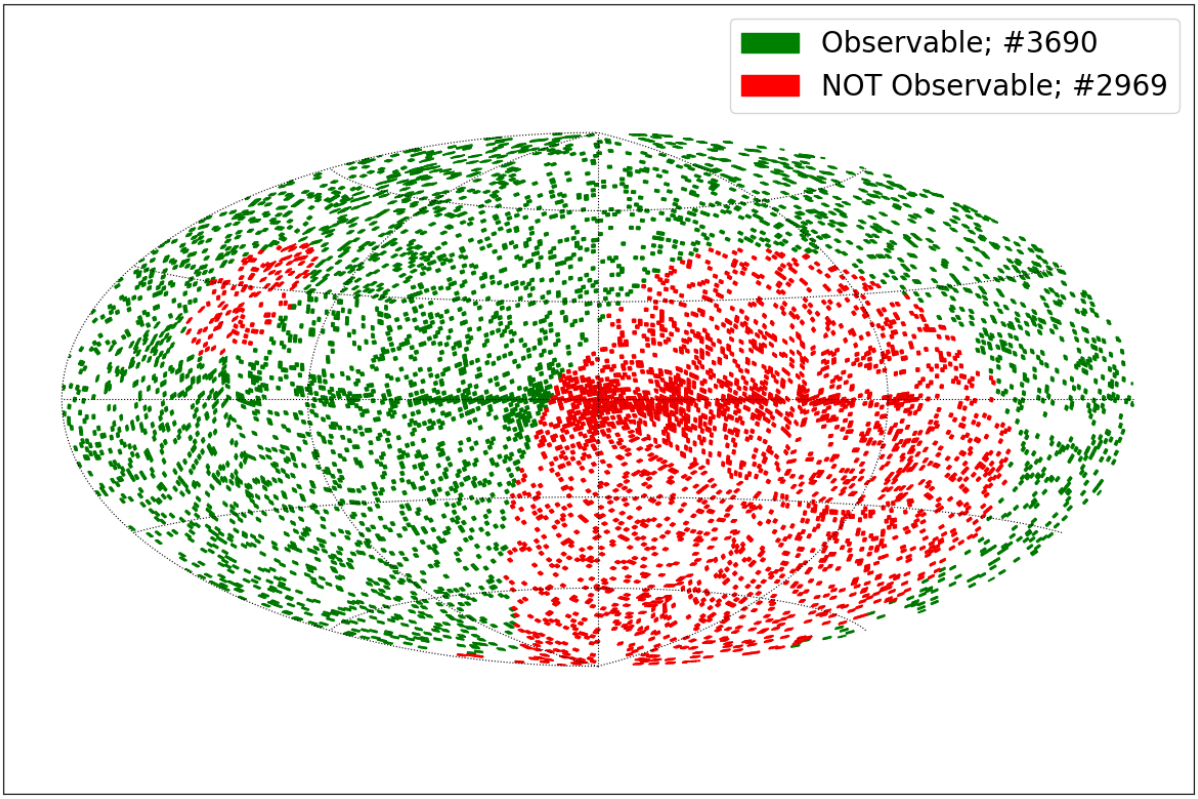

Figure 7.2: Sources from the 4FGL-DR3 catalog that are visible at the ORM with a culmination within culmination within zenith < 45 deg.

Extrapolated VHE Flux (10x) In order to check whether the previously obtained sources could emit high enough fluxes of VHE photons in order for the sources to be detectable by IACTs, I elaborated a method to perform a flux extrapolation based on the source spectral parameters derived from HE Fermi-LAT data for which I used spectral parameters for the PWL and LP models reported in the 4FGL-DR3 catalog.

Testing our method on the Crab Nebula, we found that using an LP model (pink curve in Figure 7.3) would lead to an exlusion from our candidate list, whereas the extrapolation with a PWL model (blue curve in Figure 7.3) resulted in the prediction of a VHE flux slightly below the actual recovered flux (red curve in Figure 7.3) by the MAGIC instrument. Balancing the two models we decided to prefer the PWL model rather than missing out on potential candidates that would have been detected but were excluded a priory. The prize however being the possibility of ending up with candidates that might have an intrinsic spectrum that falls below our sensitivity. Our findings are also visually illustrated in Figure 7.4). This step reduces our initial sample of pool of candidates from 3690 to 696 sources.

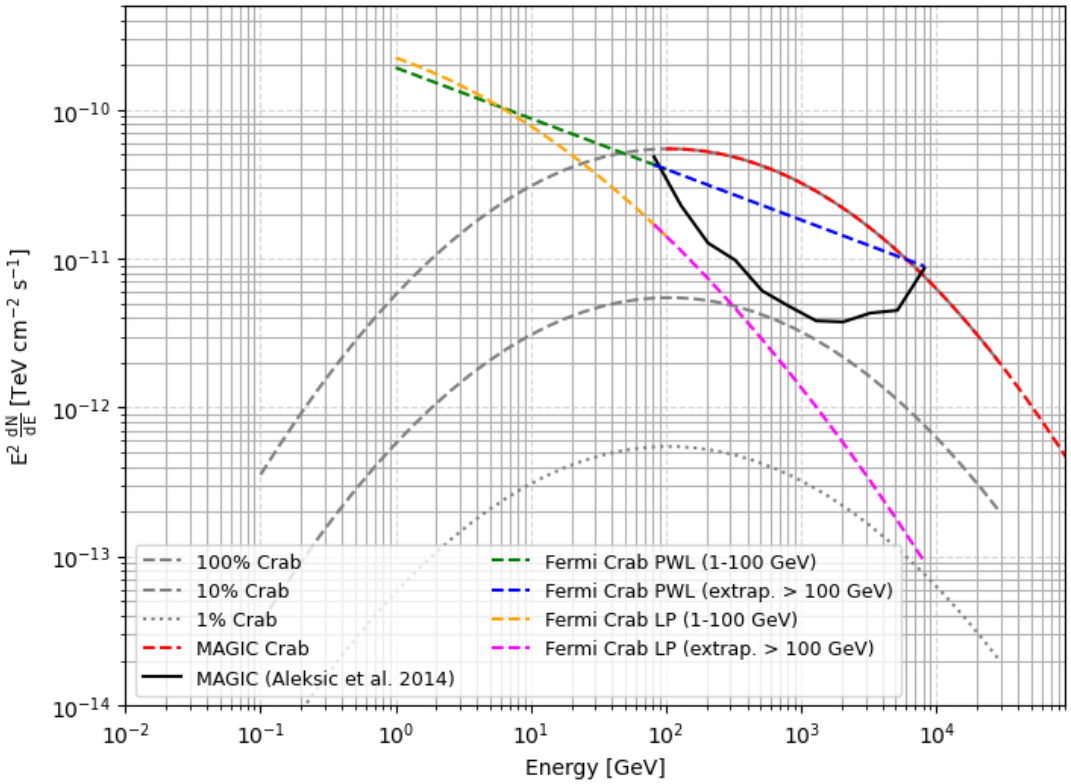

Figure 7.3: Results when performing the flux extrapolation from HE to VHE using parameters reported in the *Fermi*-LAT catalog 4FG for the Crab Nebula.

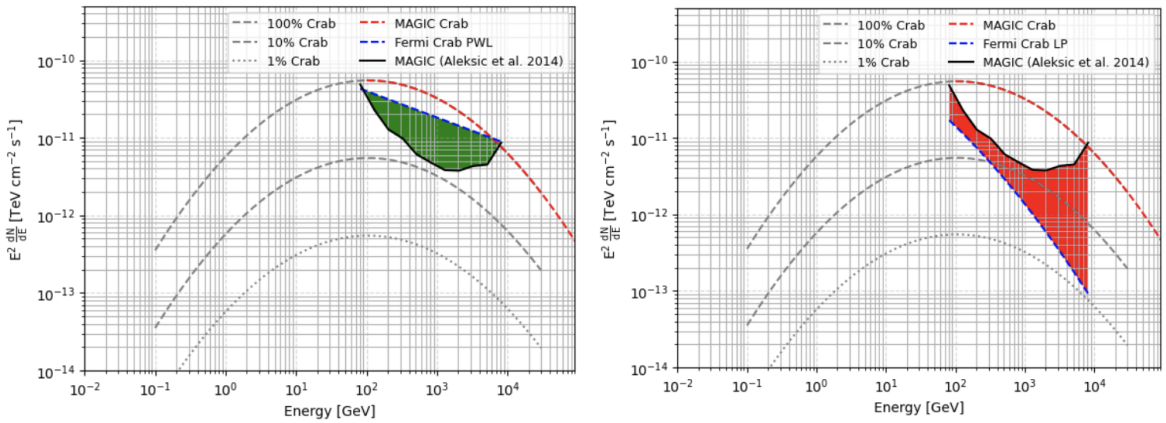

Figure 7.4: Confirmation that the condition "Flux > Sensitivity" is satisfied for the Crab Nebula when using a PWL extrapolation (**left plot**) while it's not satisfied in the case of a LP extrapolation (**right plot**.

Extrapolated VHE Flux (10x) + EBL attenuation Since the 4FGL catalog does not contain any estimate on the distance of its constituents, we have to enrich our previously obtained sample by crossmatching therein sources with the NED database. Since the majority of 4FGL sources lack associated counterparts this reduces[2] our list to 398 sources. With the remaining list we repeat the comparison of VHE flux with IACT sensitivy but this time accounting for EBL absorption as well (see also Figure 7.5 for an example of the impact of the EBL on VHE photons). This step reduces our sample to 110 source candidates.

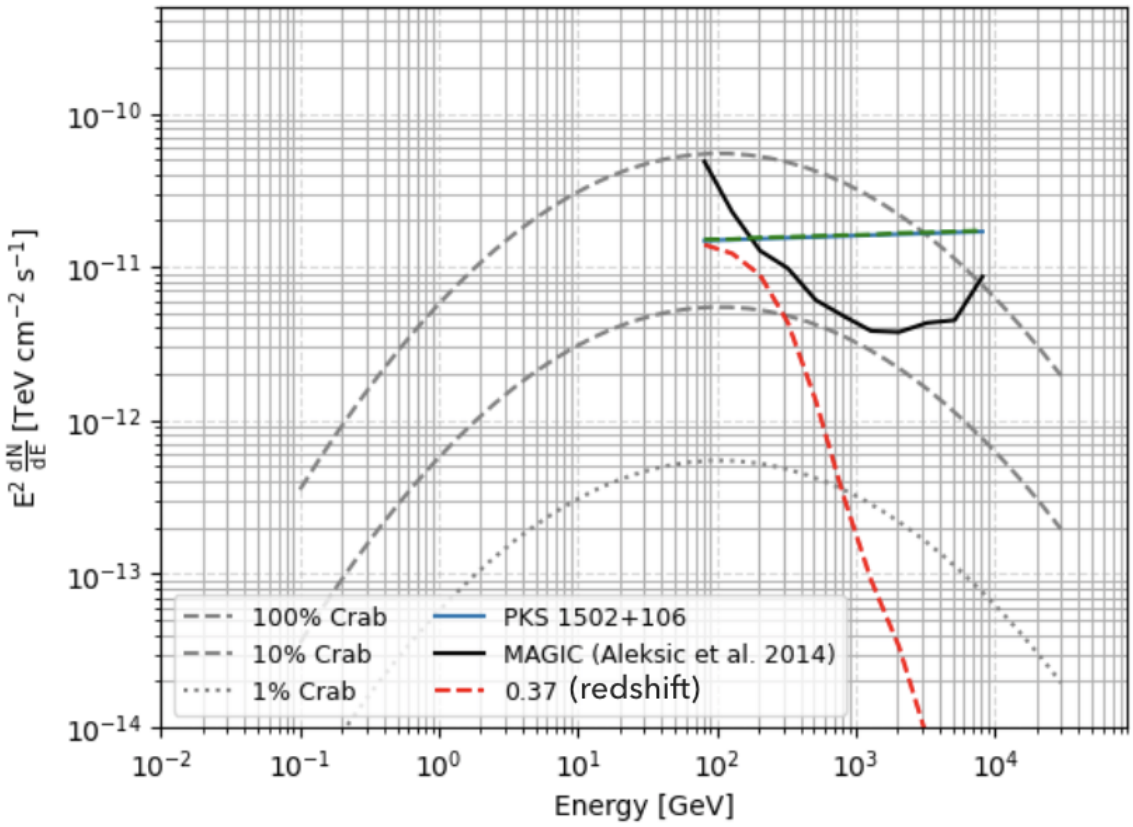

Figure 7.5: Visual confirmation that the condition of "10xFlux > Sensitivity" is initially satisfied for "PKS 1502+106" (green line). Since it is located at a redshift of z=0.37, the VHE photon flux is attenuated along its trajectory. The recorded flux at the location of the observer (red line) is computed from the intrinsic flux at the origin where one accounts for attenuation along its trajectory. The Dominguez et al. (2011) model was used for the EBL.

[2]Perhaps the excluded 298 sources could be added as a separate list, where we assume a fixed redshift or even without considering EBL absorption at all.

Contributions from 4FGL to GFU List In the end the contribution from 4FGL to the new GFU list entails 110 gamma-ray emitters and their sky distribution is shown in Figure 7.6.

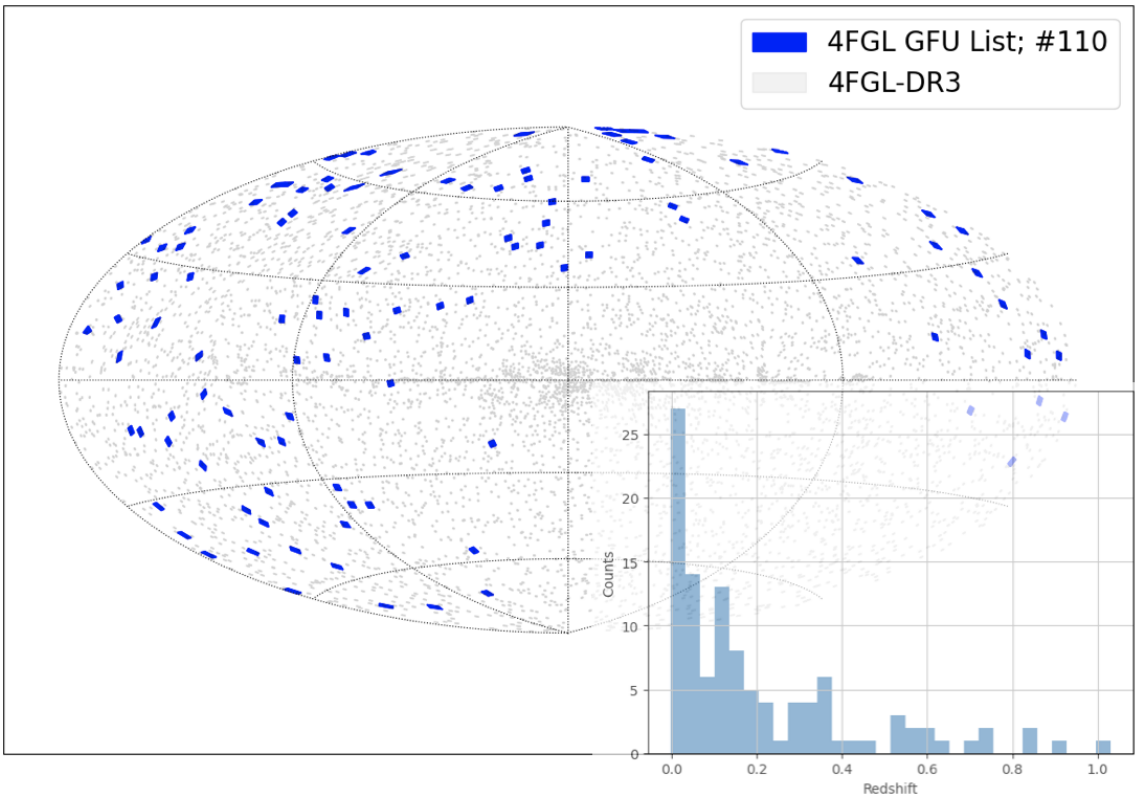

Figure 7.6: Sky distribution of the 110 gamma-ray emitters in the new GFU list after filtering the 4FGL-DR3 catalog. Their redshift distribution is shown in the in the bottom right histogram.

7.3.2 TeVCat

TeVCat is a catalog of VHE gamma-ray sources that was initiated in 2008 and as of October 2022 counted 280[3] sources. Most of them were detected by the 3rd generation of IACTs, and in particular MAGIC, HESS and VERITAS. The sky distribution of its constituents is shown in Figure 7.7.

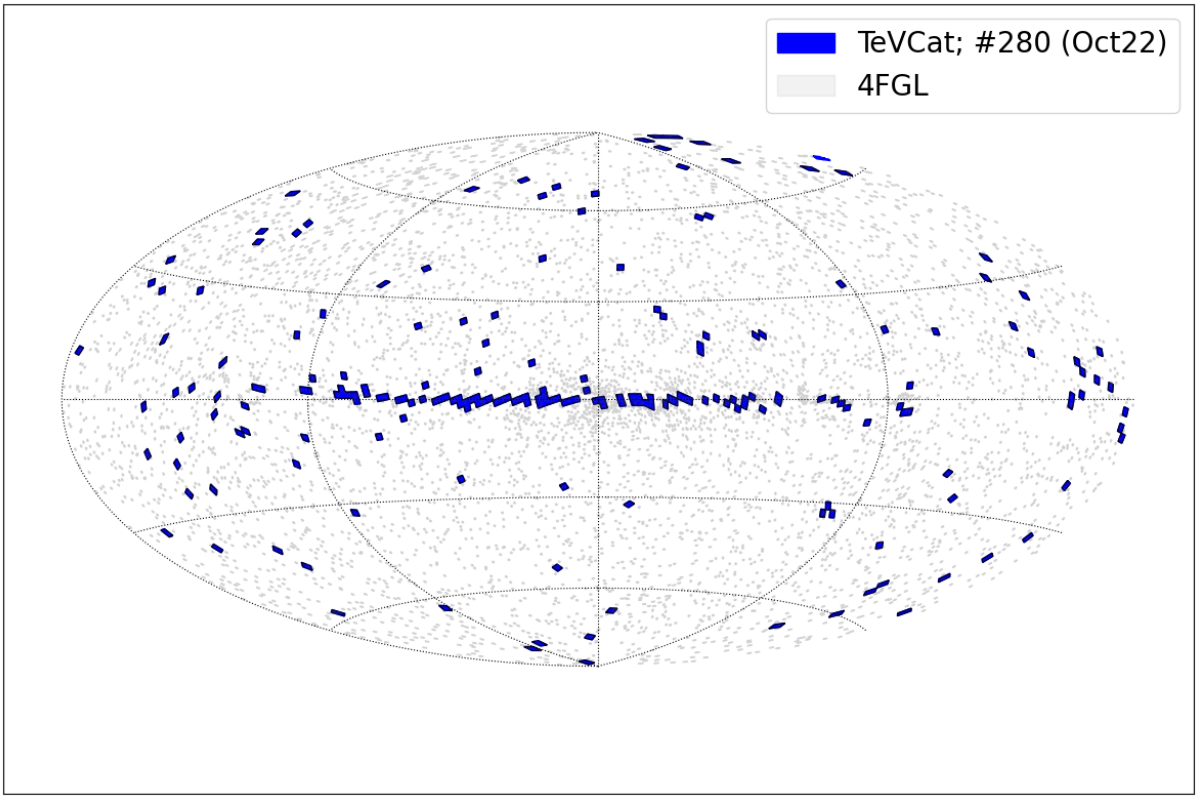

Figure 7.7: Sky coverage of the TeVCat catalog in galactic coordinates.

Applied Filters In the following, we list the filters that were applied in order to isolate 29 sources that we added to the pool of gamma-emitters of our new GFU list.

- ◇ **Observability:** culmination at the ORM with zenith < 45 deg, resulting in removing 101 sources from the list.
- ◇ **Exclude galactic objects:** $|\text{lat}| > 2.5$ deg, resulting in removing 81 more sources from the list.
- ◇ **Exclude non-repeating transients:** GRBs and Novae, resulting in removing 7 more sources from the list

Sources that are filtered by these cuts are shown in Figure 7.8.

[3]Number of sources contained in TeVCat the month we queried the catalog in order to start this study.

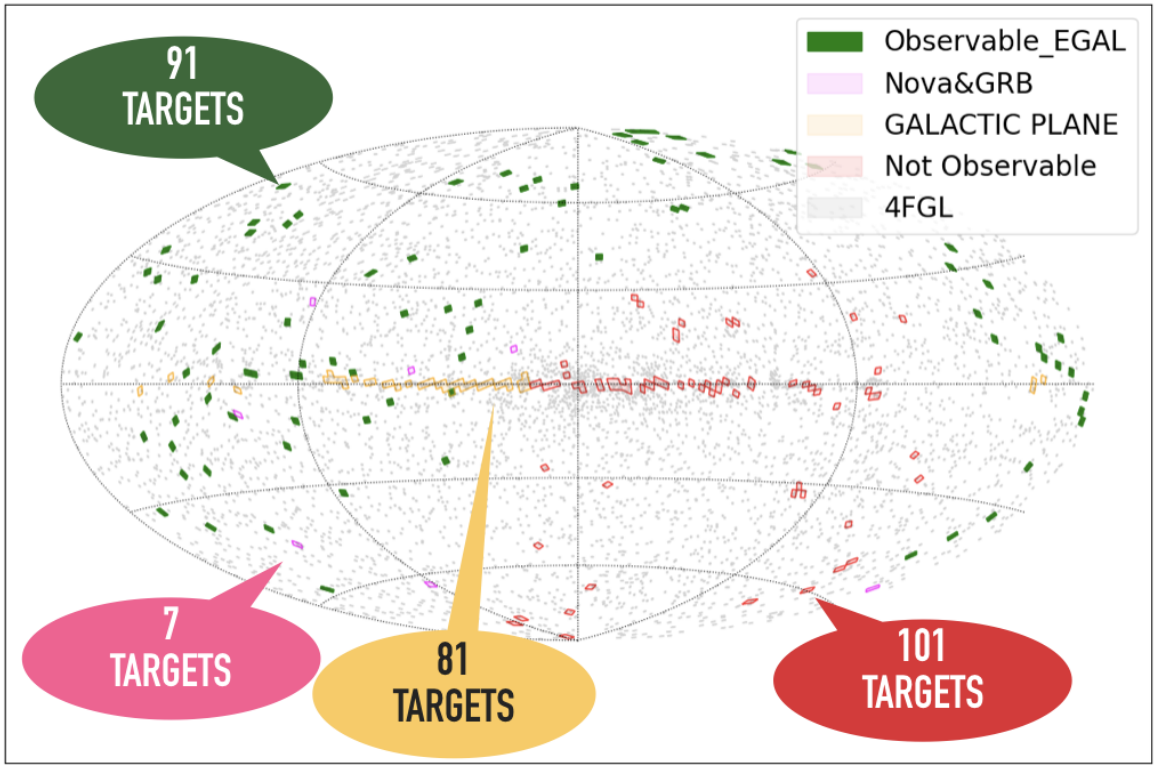

Figure 7.8: Sky coverage of the TeVCat in galactic coordinates. The sources removed by the different filters are marked with different colors.

◇ **Further reductions of the remaining 91 candidate targets:**

- **duplicates:** exclude duplicate entries for pulsars and nebulae, resulting in removing 6 more sources from the list
- **doubble counts:** exclude sources already contained in our 4FGL-DR3 sample, resulting in removing 46 more sources from the list
- **unIDs and galactic SNR/PWN:** removed unidentified and steady objects like SNR and PWN, resulting in removing 10 more sources from the list

In the end, the contribution from TeVCat to our new GFU list is reduced to 29 sources.

7.3.3 GLADE+

In order to obtain a GFU list that reduces the bias from known HE gamma-ray emitters we use the data from the GLADE+ catalog. Since the full catalog contains $\sim$ 22.5 million galaxies, as well as $\sim$750,000 quasars, we need to apply filters in order to isolate viable candidates for our list. Since simple cuts in the distance did not yield reasonable numbers of candidates, we decided to filter the catalog in order to isolate only those galaxies for which the authors obtained an estimate for the BNS merger rate via their stellar mass[4]. The decision to only use those was done in order to reduce the number of sources in the most conservative manner and more importantly to be able to effectively isolate the most massive candidate galaxies. Hence, we managed to reduced the initial source pool to $\sim$3.2 million galaxies (see also Figure 7.9).

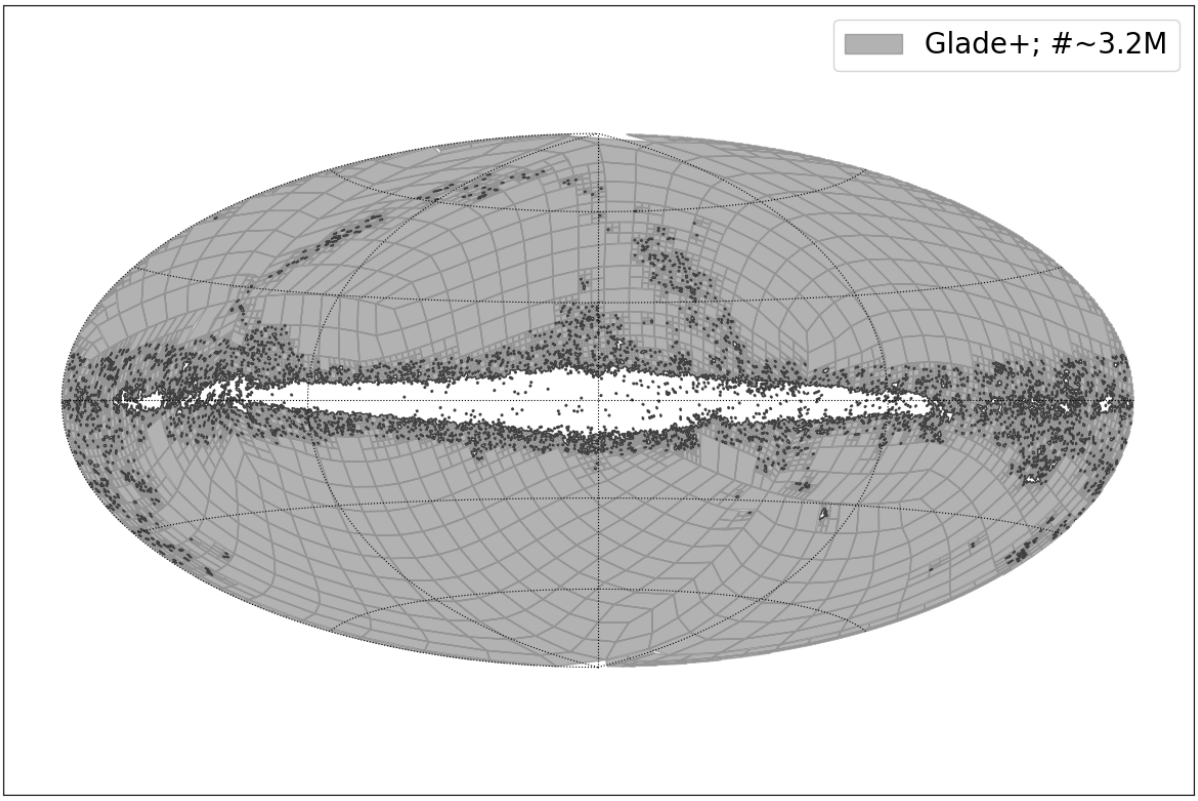

Figure 7.9: Sky coverage of the filtered GLADE+ catalog in galactic coordinates. The applied filter reduces the catalog to only consider those for which the authors could compute an estimate for the BNS merger.

[4] https://github.com/MariaPalfi/Stellar_masses_for_GLADE/blob/main/Stellar_mass_estimation_short20%version2.ipynb

Applying reference cuts from NGC 4993 As mentioned we used the parameters from NGC 4993 as reference as it is the host galaxy where GW170817 was located. Based on its reference values we first applied cuts to the BNS merger rate estimates and BMAG. This allowed us to isolate the most massive galaxies, i.e. those having a higher optical blue luminosity than NGC 4933 and higher probability to be a potential host galaxies of BNS systems than NGC 4933. In Figure 7.10 this subset of ∼570k candidates corresponds to the zone in the lower right.

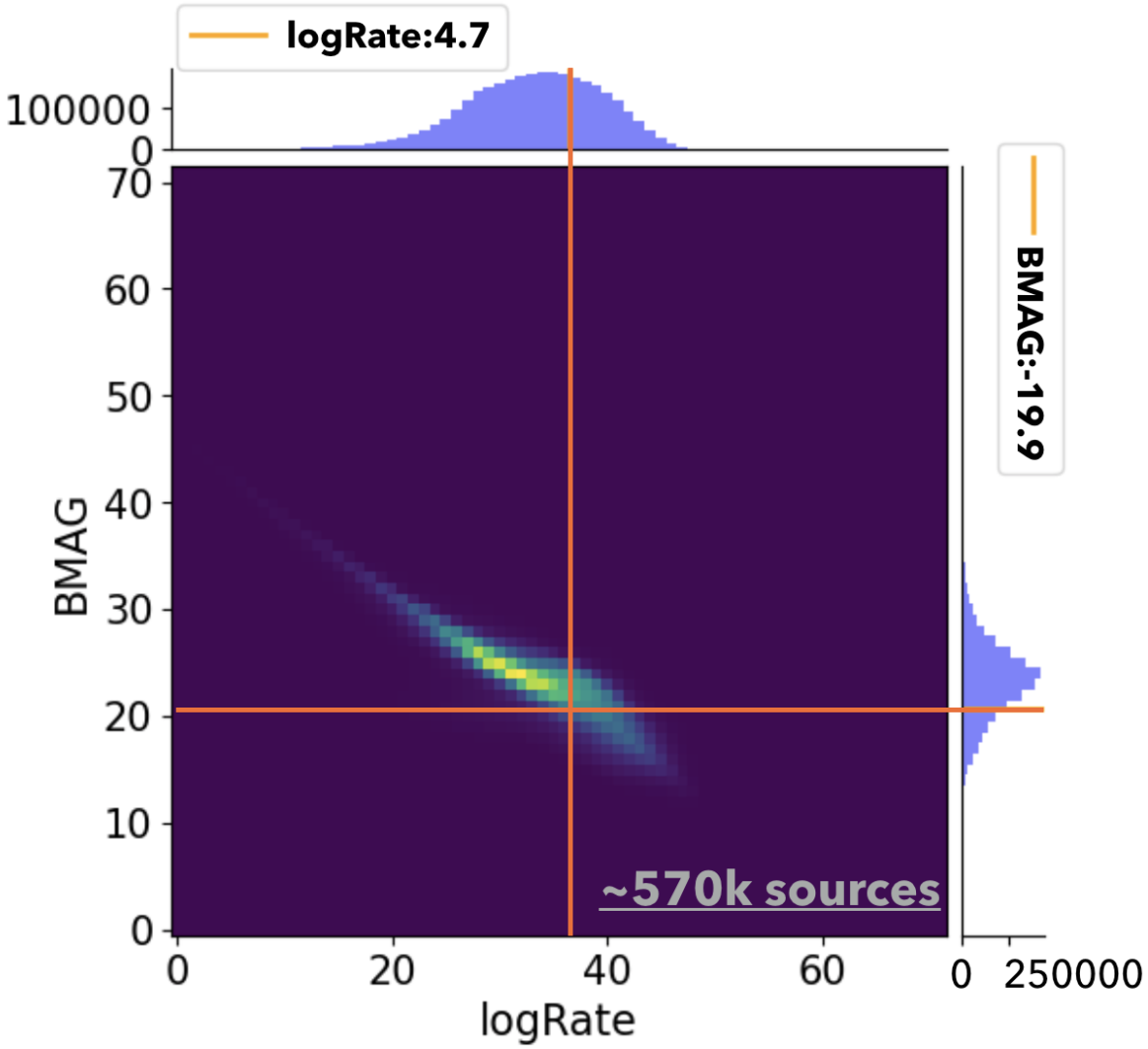

Figure 7.10: 2D histogram for the parameter value distributions of BMAG and BNS merger rate estimates. The reference values of NGC 4993 are marked by orange lines.

Applying reference cuts from NGC 4993 Cont'D Since the first cuts resulted in still too many candidates we need to apply an additional cut in distance. In order to isolate nearby galaxies we thus use as reference value the distance of NGC 4933 as a maximum value (see also Figure 7.11). Applying this cut reduces the number of candidates to 224 galaxies.

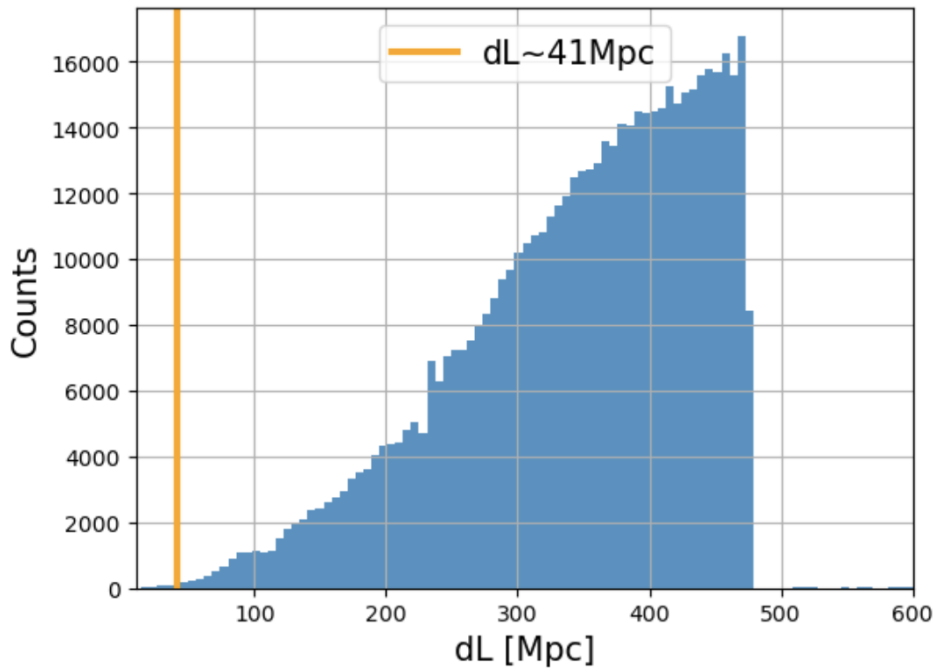

Figure 7.11: 1D histogram of the luminosity distance distribution of the galaxies in the lower right zone of Figure 7.10. The reference distance value of NGC 4993 is marked by an orange line.

Observability and offset-cuts for GLADE+ targets The galaxies that result from the three previous cuts are further filtered by checking their respective observability. This resulted in 94 galaxies being observable from ORM which are shown in the upper plot of Figure 7.12. Based on feedback from my collaborators, we improved our selection of GLADE+ targets by avoiding the accumulation of sources with too small angular separation. Our approach was to isolate pairs that are too close (we used < 1 deg) and thereafter remove for each pair that particular source that reports a lower BNS merger rate probability. Our new list of targets that contains 73 galaxies is shown in the lower plots of Figure 7.12.

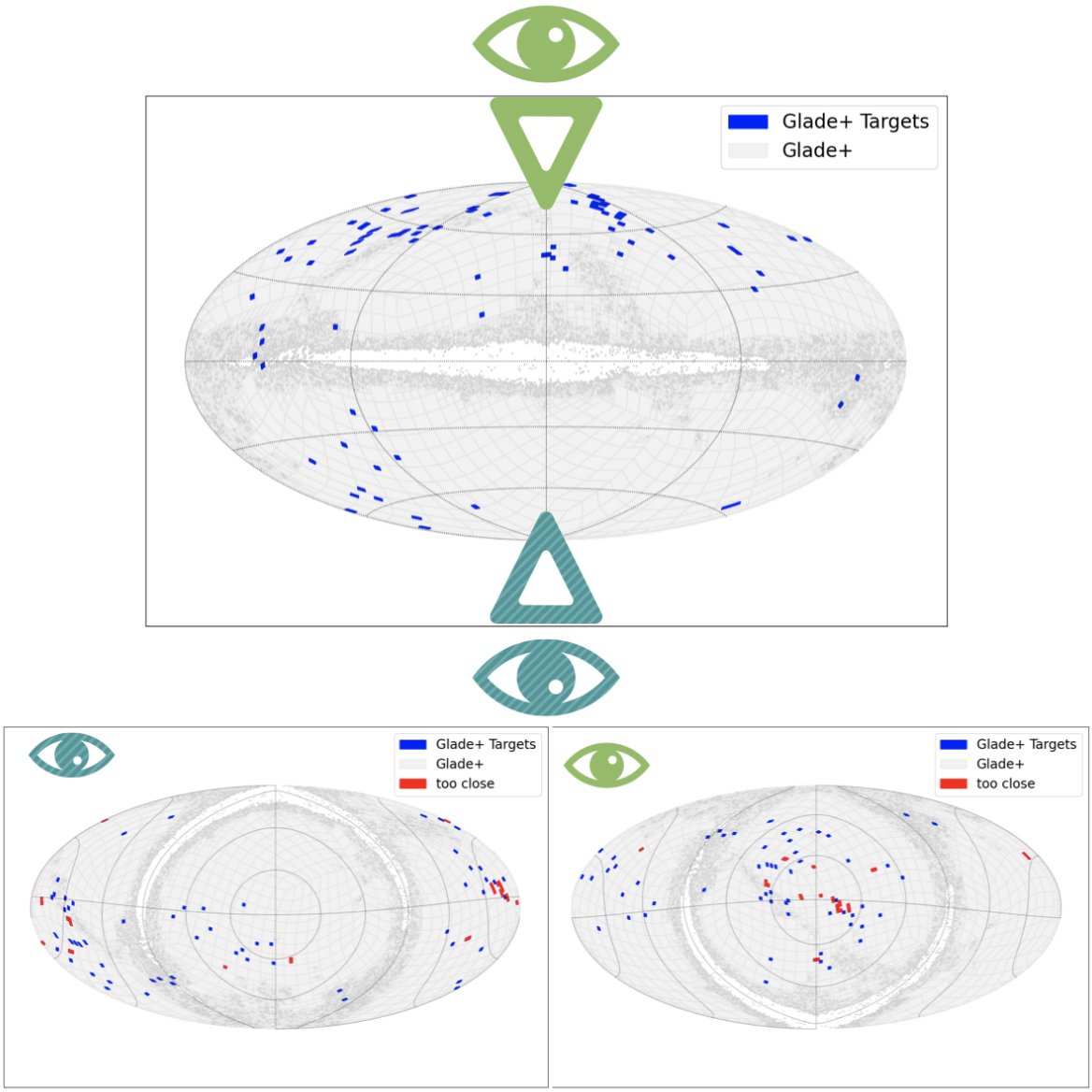

Figure 7.12: Sky coverage of our selected galaxies from GLADE+ in galactic coordinates. The **upper plot** shows 94 candidate galaxies after applying an observability cut for the ORM whereas the **lower plot** shows the galaxy distribution centered on -90 lat and +90 lat respectively and as depicted by the differently colored "eyes". Note that galaxies that are closer than 1 deg are highlighted in red.

7.4 Conclusions and Prospects

7.4.1 Conclusions

We presented our newly elaborated GFU list that is composed of sources from three separate catalogs:

- ◇ **#139:** Gamma-ray emitters
  - **#110:** 4FGL objects
  - **#29:** TeVCat objects
- ◇ **#73:** Nearby galaxies
  - **#73:** GLADE+ objects

The constituents of the individual catalogs were filtered according to multiple criteria, which results in a GFU list that entails 212 targets and whose distribution is shown in Figure 7.13. This represents a 20% increase compared to the 178 sources contained in the currently implemented GFU list for MAGIC.

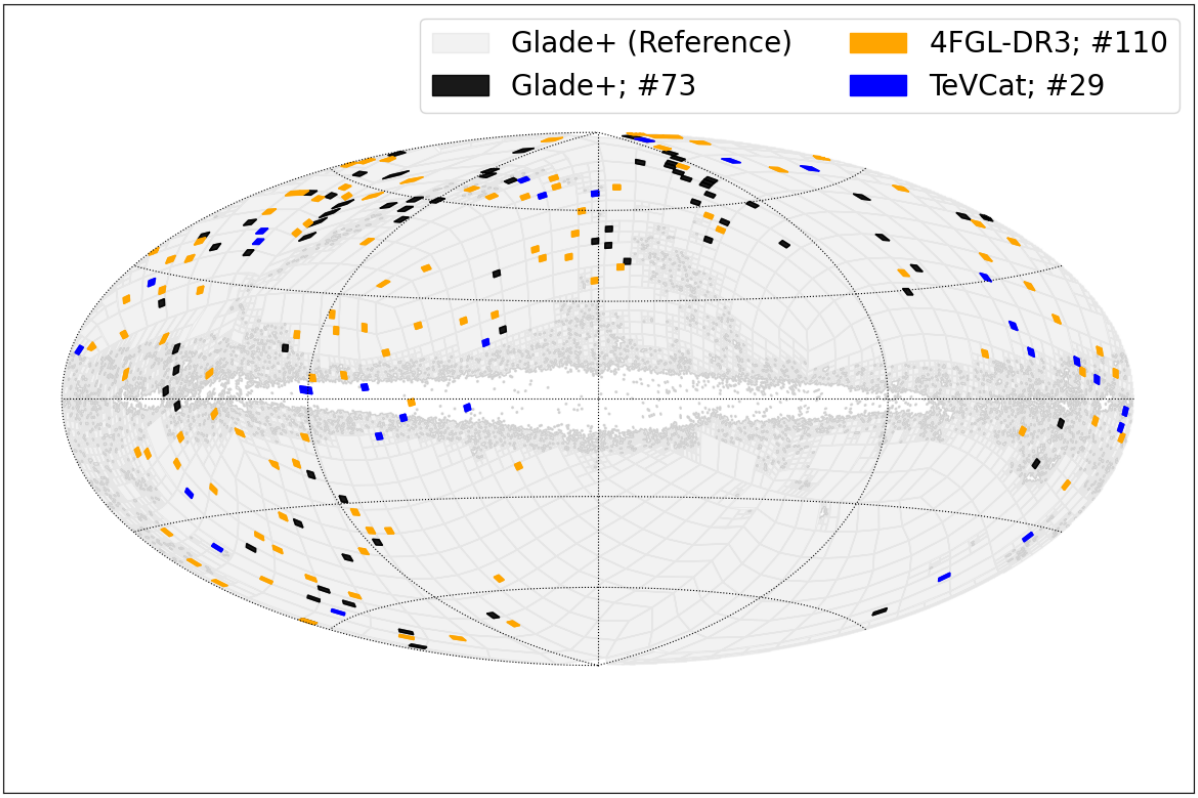

Figure 7.13: Sky coverage of our new GFU list that merges candidates from the three catalogs; #73 GLADE+, #110 4FGL-DR3, #29 TeVCat

7.4.2 Prospects

Our proposal for a revised GFU source list originates from the fact that LST signed about a year ago a memorandum of understanding with IceCube in order to receive its own alerts for multiplet events. Since time is a critical factor when attempting follow-ups on neutrino triggers, the LST collaboration is in favour of establishing a direct communication with IceCube for these GFU alerts. At the same time there is an ongoing discussion in order to provide IceCube with a new revised GFU source list, e.g. the one discussed in this chapter.
Upon circulating our new GFU list within the LST collaboration, we implemented the received feedback, e.g. included TeVCat and checked offsets for GLADE+ sources. Upon receiving a blessing from the LST management, we proceeded by getting in touch with the IceCube collaboration. The discussions are still ongoing but it seems that there are general efforts underway to improve the GFU list for all currently operating IACTs.

Bibliography

Dominguez, A., Primack, J. R., Rosario, D., Prada, F., Gilmore, R., Faber, S., Koo, D., Somerville, R., Pérez-Torres, M., Pérez-González, P. et al. (2011). Extragalactic background light inferred from aegis galaxy-sed-type fractions, *Monthly Notices of the Royal Astronomical Society* **410**(4): 2556–2578.

Satalecka, K., Bernardini, E., Dorner, D., Mezek, G. K. and Jin, W. (2021). Searching for vhe gamma-ray emission associated with icecube neutrino alerts using fact, hess, magic, and veritas, *arXiv preprint arXiv:2109.04350* .

CHAPTER 8

CONCLUSIONS AND OUTLOOK

Resume: The work performed in the framework of this dissertation, could be broadly divided into technical and scientific research. Activities in both domains were carried out as member of the MAGIC collaboration as well as the LST sub-consortium of CTA. Whilst technical efforts were mainly conducted in order to facilitate strategies for EM counterpart searches of MM alerts, the scientific research elaborates on obtained results from MWL and MM associations in various datasets.

Contents

Going through the manuscript, the introductory chapters aimed at providing the reader with a general overview of high-energy astrophysics, including relevant physical mechanisms and connections between different cosmic messengers. Upon elaborating on a few selected transient astrophysical sources, this set the stage for the subsequent chapters, which were devoted to the original research performed in this dissertation. Sections 8.1 and 8.2 provide conclusions and possible outlooks for the technical and scientific research reported in this manuscript.

8.1 Technical Research Activity - Conclusions and Outlook

With respect to the technical research activity, the goal was to develop a tool that could provide IACT systems with efficient follow-up strategies for any given transient phenomena. Since transients are generally serendipitous and characterized by quickly fading emissions at VHE (especially in the case of GRBs), a quick response is crucial to detect them. A python-based tool, ToOpy, was designed and initially developed to deal with real-time GW alerts from the LVC. Aiming at leveraging contemporaneous/archival datasets, ToOpy was extended with new functionalities in order for it to have access to additional alert/-data streams from facilities such as IceCube, *Fermi*, and *Swift*. These extensions to the responsiveness of ToOpy along with the incorporation of user-preferences shape its core modular design and therefore

render it suitable and performant for a wide range of use cases.
ToOpy is now distributed as open-source software on Github (see also https://github.com/arterom/ToOpy) and can be easily deployed in order to listen to real-time alerts and/or search for spatio-temporal coincidences in archival datasets as well as to elaborate a galaxy target list for neutrino multiplet events. The technical contributions presented in this dissertation have the potential to advance the field of high-energy astronomy by improving the efficiency and accuracy of observation planning. Given the novel detections of spatio-temporal coincidences in archival GW and GRB datasets, the prospects of having ToOpy listening to merger signatures during the fourth observing run of the GW interferometers look promising.

The technical efforts that were commenced in the framework of this dissertation can be extended in the future, and in the following, they are classified according to their short- and long-term prospects:

◇ Short-term development, to be finalized by the end of 2023:

- Deployment of ToOpy into the command chain of an IACT. Note that the MAGIC collaboration is planning to perform technical tests in order to implement a tiling strategy for GW alerts into the automatic response of their telescopes.

◇ Long-term improvements to be elaborated within the next year:

- Various extensions to the broker of ToOpy, such as accessing new data streams (see also Section 5.4 for a breakdown of the envisioned extensions).
- Strengthening and establishing new connections between members of the MM community, i.e. IceCube with the GFU list, ZTF with SN monitoring program, etc..

8.2 Physics Research Activity - Conclusions and Outlook

The TeV blazar VER J0521+211 was observed in the context of an extensive MWL campaign by MAGIC and other instruments after VERITAS reported flaring activity. The modeling of the broadband SED shows that the emission can be explained by either leptonic or hadronic acceleration models. Both models manage to explain the temporal evolution of the broadband emission by assuming a few co-evolving parameters, and the latter model even proposes upper limits for neutrino fluxes that are interesting for future MM studies.

The possibility to collect pieces of information, i.e. novel and archival, from multiple messengers (MM-context) or energies (MWL-context) allows a better understanding of the phenomena that power astrophysical transients. Whilst dealing with archival data entail searching, correlating and even analyzing large datasets, access to novel information requires having optimized observational strategies in place to react accordingly. In this sense, ToOpy has shown to be an efficient tool for both avenues. On one hand, when it comes to archival searches, ToOpy recovers the two major cornerstones of MM astronomy, i.e. the spatio-temporal coincidences of TXS 0506+056/IC-170922A as well as GRB170817A/GW170817.

Furthermore ToOpy provides efficient routines that allow to crossmatch extensive GRB trigger tables with catalogs of GW candidate events and CASCADE-type neutrino triggers with contemporaneous *Fermi*-LAT monitoring data. *Having only scratched the surface of potential spatio-temporal associations, the prospects of having ToOpy connected to additional data streams, i.e. optical monitoring data from the ZTF and/or other transient event trigger tables, look promising for the short-term future.*
On the other hand, when it comes to efficiently access novel information, ToOpy is designed to tackle the inherent uncertainty regarding where one should point small FoV telescopes in response to a given MM alert. Indeed, ToOpy was the trigger for ToO observations that were performed during March of 2021 by both the MAGIC and the LST-1 telescopes. Reacting to an IceCube TRACK alert, both IACT systems targeted the TeV blazar OT081, whose enhanced state was later confirmed by instruments operating at optical wavelengths. This response was achieved by coupling galaxy catalogs to contemporaneous HE coverage (perhaps optical coverage in the future as well) and thereafter executing pointing strategies on host galaxies (or sky tiles). For the GW case, a methodology is in place for upcoming runs of GW instruments and has been validated with catalog events from previous runs.
Further strategies to respond to MM triggers have also been put in place in ToOpy:

- **i) Neutrino multiplet alerts;** targeting a specific host galaxy from a pre-selected GFU list would be well-motivated if there is prompt feedback from analyzing contemporaneous *Fermi*-LAT data.
- **ii) Neutrino CASCADE alerts;** promising host galaxies from within a large uncertainty area could be targeted if they show flaring activity as obtained through a scan of the HE sky.
- **iii) GW and/or GRB alerts;** target sky regions could be well constrained by having contemporaneous *Swift*-BAT and or *Fermi*-GBM triggers. This would effectively reduce the localization error from a GW (or GRB) trigger to tiles that can easily be covered by the small FoV of IACT instruments.

APPENDIX A

LST CAMERA COMMISSIONING

Resume: The technical work presented in this chapter is my contribution to the commissioning of the camera of the LST-1 installed at the ORM.

Contents

My main contribution to the LST camera commissioning was to elaborate python-based macros that would facilitate the analysis of camera calibration routines. The inclined reader is encouraged to read the dissertation of Leyre Nogués (Appendix A[1]) in order to gain a concise introduction to the study of rates for the LST cameras. In the following I will elaborate on my contributions for the commissioning of the LST1 camera in operation at the Roque de los Muchachos, Canary Islands, Spain.

A.1 Contribution to the LST1-Camera Commissioning Document

My contributions to the commissioning of the LST1 camera entail making sure that the trigger system of the camera is configured correctly in order to assure homogeneity in the response of the camera to test pulses from controlled laboratory settings. Note that the content of the following section is reproduced from my contributions to the camera commissioning document (Subsection "L0/L1 rate scans with HV=0").

[1] https://magic.mpp.mpg.de/backend/publication/show/442

A.1.1 Deliverable Goal

The goal is to check the consistency in terms of homogeneity and linearity for the trigger response of individual modules to an electronic signal over the full camera. This is assessed by performing rate scans, i.e. recording the rate as a function of the trigger discriminator level, with controlled input pulses (from the pulse test injection) as well as only electronic noise. This provides then a viable cross-check for the individual pixel response in each cluster (pixels for L0-levels) as well as the response of the trigger regions (L1-level) for different configurations (adders and modes). In order to obtain both a qualitative and quantitative confirmation for overall consistency in trigger response, the results are visually inspected (see figures in the following subsections) and also evaluated by means of linear regression (see results in Table A.1). The following list outlines the necessary plots in order to provide visual confirmation of consistency:

- Overlay of L0 and L1 rate scans with electronic noise only, with limits for the acceptable noise (see Figures A.1, A.4).
- Overlay of L0 and L1 rate scans with test pulse of known amplitude, with limits for the acceptable discriminator level (see Figures A.1, A.4).
- Overlay of baseline dispersions for L0 and L1 rate scans (see Figures A.2, A.5).
- L0 and L1 threshold at 50% for each pulse amplitude (see Figures A.3, A.6).
- Overlay of L1 rate scans with electronic noise only and test pulse of known amplitudes without applied baseline correction (see Figure A.7).

A.1.2 Deliverable Procedure

The test procedure requires to perform rate scans for the different trigger levels and their corresponding configurations:

- L0 rate scans for every individual pixel with only electronic noise as well as test pulses of different known amplitudes.
- L1 rate scans for every module and adder with only electronic noise as well as test pulses of different known amplitudes. The L1 scans are repeated for different configurations of the adders, in particular the Local Mode in which each module only gets the L0 from itself, and the Mode 3, which is the one used for observations and for which each module evaluates the L0 information from 2 regions of three modules.

Rate scans for each trigger level were obtained on several occasions:

- The bulk of L0 and L1 rate scans was obtained during observing nights on the 15th and 16th of September 2020.
- Due to rate spikes in L0-scans, additional scans were taken on the 14th and 19th of December 2020. The origin of these spikes remains unknown. However, a first follow-up study ruled out possible

drawbacks on regular camera operations, since these spikes occur during a single time-bin for each of the affected pixels, and generally only seem to occur when there is no high voltage applied.

- An additional L1 rate scan was performed on the 11th of February 2021 in order to substitute an occasionally poor data sample (L1, Local Mode, adder B, Input amplitude 10).

The data was parsed into standalone python code and further processed in order to obtain the following plots and results.

A.1.3 Deliverable Results

Study of L0 level Figure A.1 shows superimposed L0 rate scans with electronic noise only (left), and when subjected to a test pulse of input amplitude gain 20 (right). It is worth noticing that the X-axis shows the iscriminator threshold (DT) value once the estimated value of DT for the baseline position, which is around 512, for each individual pixel is subtracted. The baseline dispersion for individual pixel groups is shown in Figure A.2 for both electronic noise only (left) and input amplitude gain 20 (right). Once the baseline correction is applied, one can see that trigger from electronic noise becomes negligible once the DT is about 20 units larger than the baseline. In another study it was shown that the rates induced by the NSB for this DT levels exceed 30 KHz and hence the effect of the electronic noise during data taking is completely negligible. For the rate scans when a pulse test with amplitude 20 is injected, the range for which the pulse does not trigger anymore is within about 20 DT units for most of the pixels. There are 7 pixels that show a clear lower DT value at which the pulse does not trigger anymore. Since the L0 discriminator is only used for the detection of stars in the pixel FoV, this non optimal performance has very limited implications in the camera performance. Figure A.3 shows the distribution of DTL0 values for all considered input amplitudes (left) and when corrected for its baseline and normalized by gain 7 (right). To evaluate the relative dispersion for the different amplitudes in the left plot, it should be considered that the baseline is at about a DT of 512 **(see also Figure A.2)**. One can observe that the relative dispersion for the non-normalised case decreases from about 70 % to 10% indicating that they are mainly induced by the baseline dispersion. The normalisation to those values obtained with a test pulse of amplitude 7 also to calibrate out both the baseline dispersion and possible different gains. The remaining relative dispersion is at the level of 5%. Finally, the values from the distributions in Figure A.3 (mean and standard deviation) are used to perform a linear regression whose parameters are summarized in Table A.1 (note that the intercept obtained by the fitting is in good agreement with the baseline dispersions in Figure A.2). The fit is done taking into account that the relation between the set amplitude and the actual amplitude of the test pulse is logarithmic and it shows a good linearity at 10% level.

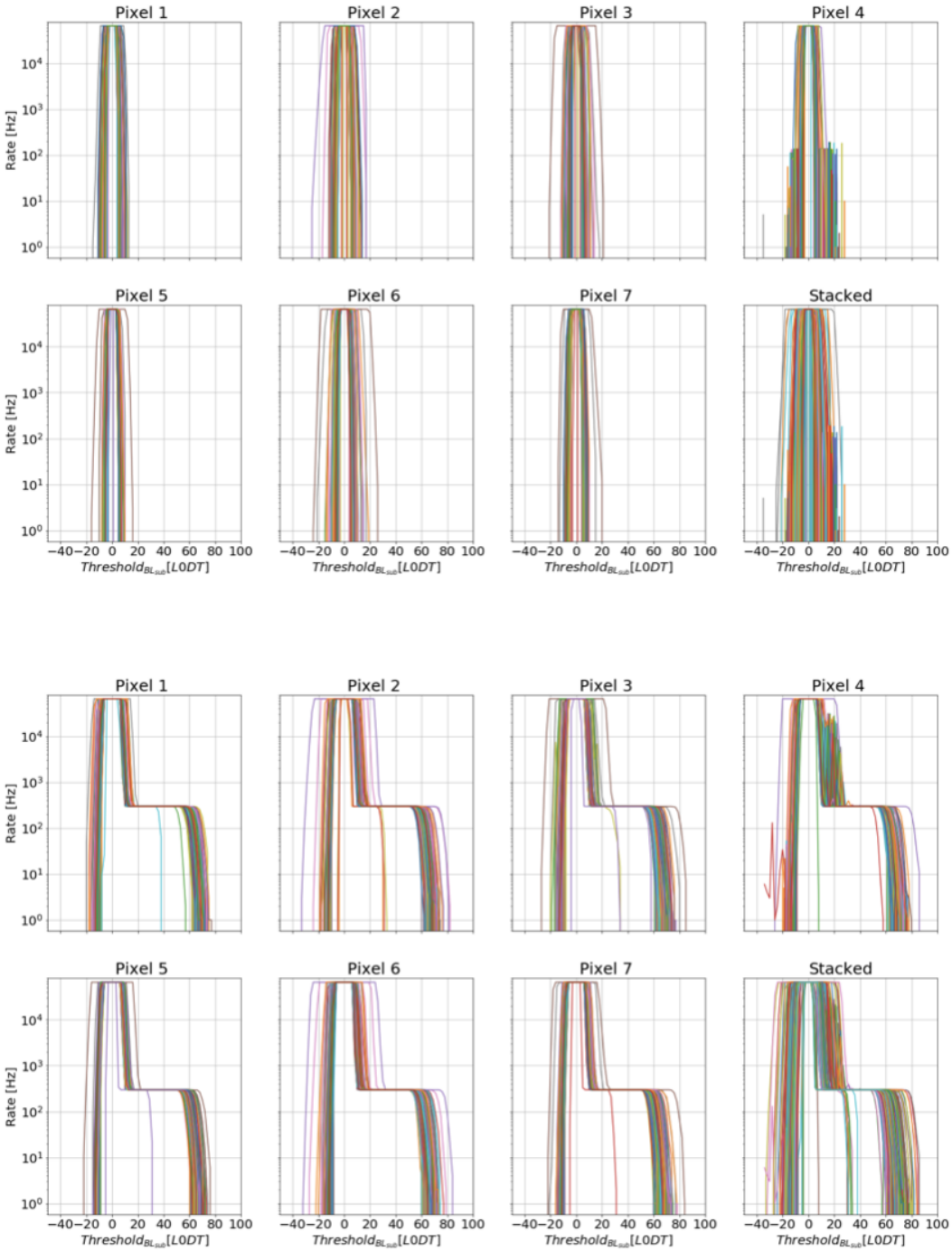

Figure A.1: **Top plot:** Overlay of L0 rate scans with electronic noise only. **Bottom plot:** Overlay of L0 rate scans subjected to a test pulse of input amplitude gain 20. In both figures there are at least 264 modules superimposed (1 missing due to a hardware issue in one of the modules during the process of obtaining rate scans).

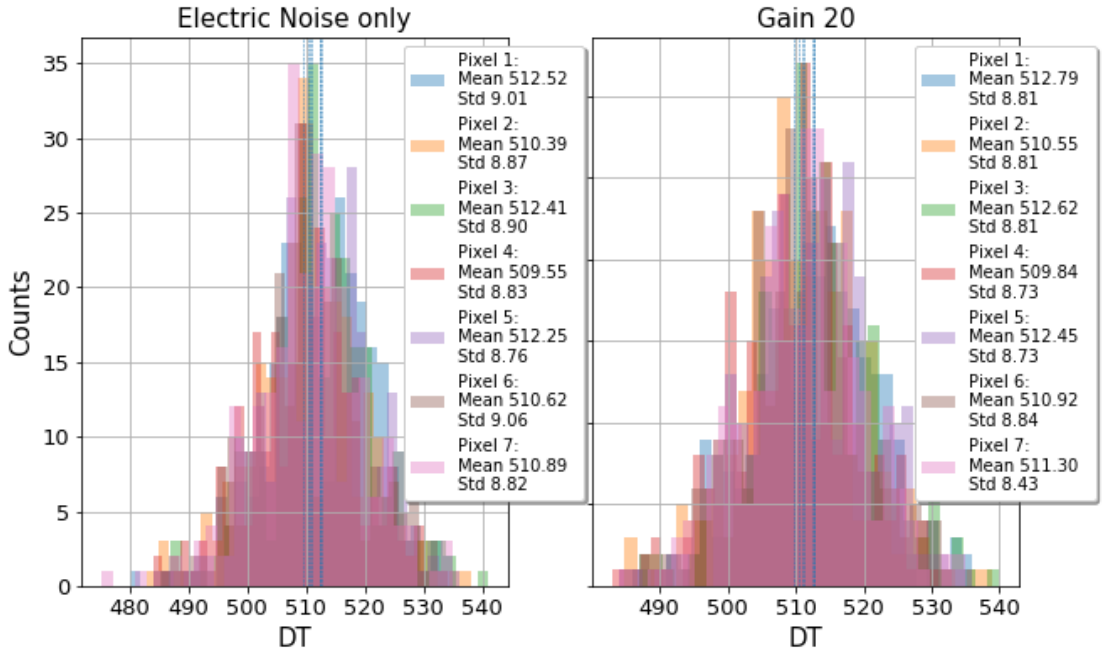

Figure A.2: **Left plot:** Pixel-wise baseline dispersion with electronic noise only. **Right plot:** Pixel-wise baseline dispersion when subjected to a test pulse of input amplitude gain 20. As can be seen the dispersion is not affected by the test pulse injection.

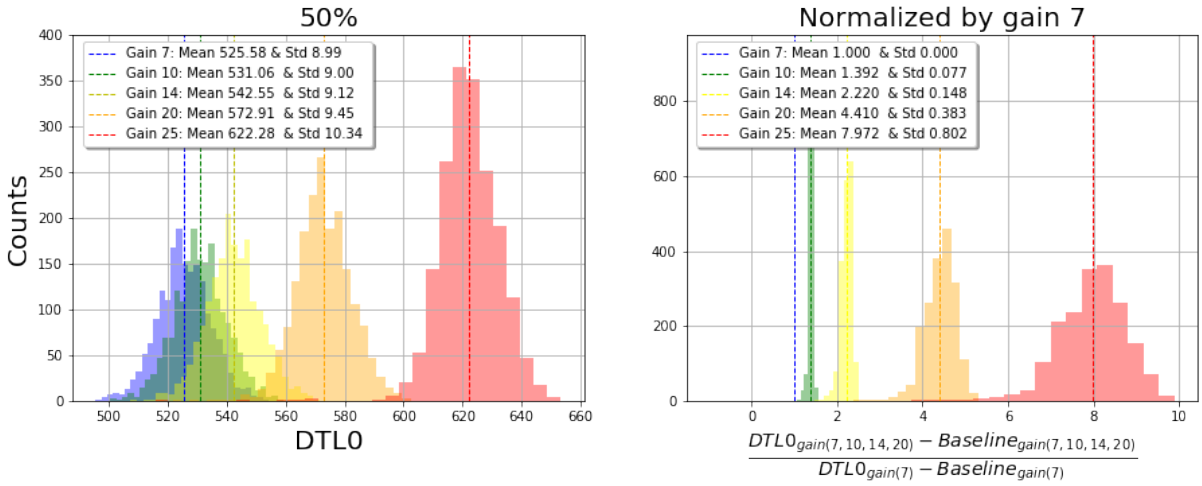

Figure A.3: **Left plot:** Distribution of L0 threshold at 50% for each pulse amplitude. **Right plot:** Distribution of L0 threshold at 50% for each pulse amplitude when corrected for its baseline and normalized by gain 7.

Study of L1 level Figure A.4 shows for an exemplary configuration (adder A in local mode) the superimposition of L1 rate scans with electronic noise only as well as when subjected to test pulses of increasing input amplitudes (the presence of secondary plateaus as visible in the second row of Figure A.4 remains currently under investigation). Again the X-axis shows the DT value after subtracting the baseline position located around 10.70, whose underlying dispersion is summarized in Figure A.5. It can be observed that for the highest test pulse amplitude (20), the DT value for which the test pulse does not trigger anymore goes beyond the dynamic range of the DT (0 to 255 for the L1). Figure A.6 shows the distribution of DTL1 values for all considered input amplitudes **(left)** and when corrected for its baseline and normalized by gain 7 **(right)**. The relative dispersion is about 10%, except for the case of the test pulse amplitude 20. The values from the distributions in Figure A.6 (mean and standard deviation) are used to perform a linear regression, whose parameters are summarized in Table A.1 for all adders and configurations. Values that are too close or beyond the dynamic range of the DT are not used. Once the data points for test pulse amplitude 20 are excluded from the fit (showing saturation), it can be noted that the intercept point obtained through the fit is in good agreement with its corresponding baseline dispersion in Figure A.5. Considering the regression parameters in Table A.1, one can deduce that the trigger response at L1 trigger level remains stable for all the configurations that were employed in this study (Local Mode and Mode 3) and they have a good linearity at 10% level. It is worth to mention that not all rate-scans show the same rate behaviour, i.e. for some scans the first peak is not well defined. Since the baseline is deduced from intersections with the rate-scan patterns, we only only use combinations of modules for which the baseline could be established (these are then shown in the plots and used for the fits). For reference Figure A.7 shows the superimposition of L1 rate scans from all available modules and without their respective baseline corrections. The results do not differ significantly if modules for which the baseline cannot be estimated, because the rising edge before the noise is below the DT range, are included.

Level	Config	Adder	Slope	Intercept	Nr_M
L0	Pixels	-	6.21 ± 0.04	511.40 ± 0.32	263
L1	Local	A	20.64 ± 0.05	10.79 ± 0.16	235
L1	Local	B	20.61 ± 0.24	11.17 ± 0.77	234
L1	Mode 3	A	20.70 ± 0.03	10.62 ± 0.09	235
L1	Mode 3	B	20.65 ± 0.02	11.18 ± 0.06	234

Table A.1: Summary of parameters (values $\pm$ error) when performing a linear regression on the mean and the standard of underlying distributions of DTL0- and DTL1-values as shown in Figures A.3, A.6. Note that whilst for the L0-level all gains can be used for the fit, this is not the case for the L1-level, which excludes gain 20 and 25 data points due to saturation effects. The values in column "Nr_M" indicates on how many modules the linear regression was performed.

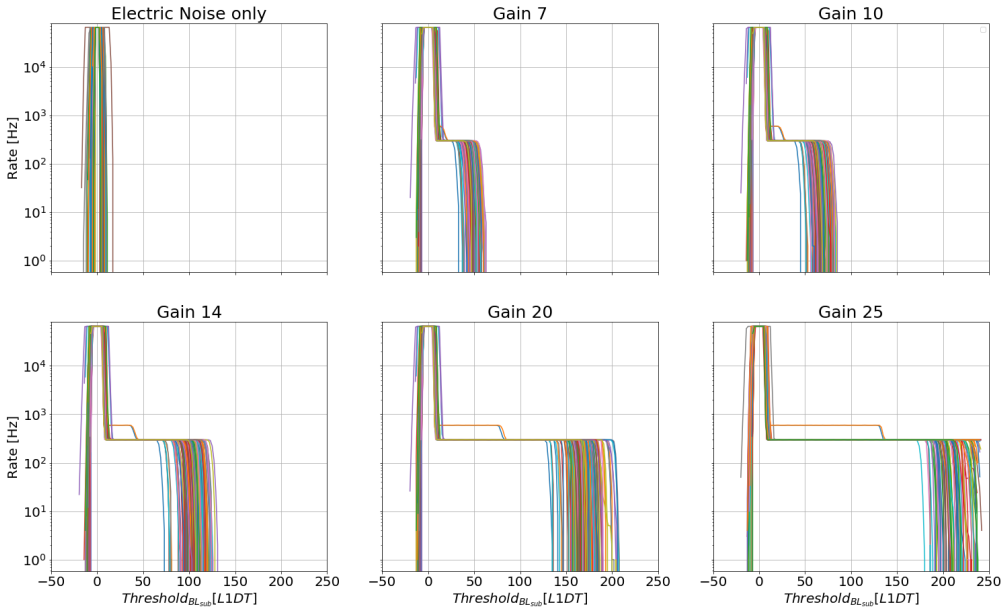

Figure A.4: Overlay of L1 rate scans with electronic noise only as well as when subjected to test pulses of increasing input amplitudes for adder A in local mode configuration. In each of the sub-figures there are 179 baseline corrected modules superimposed (except for cases "electric noise only" and "Gain 25", which display 153 and 213 modules, respectively). This limitation is related to a long-standing issue of not being able to obtain the baseline for various modules.

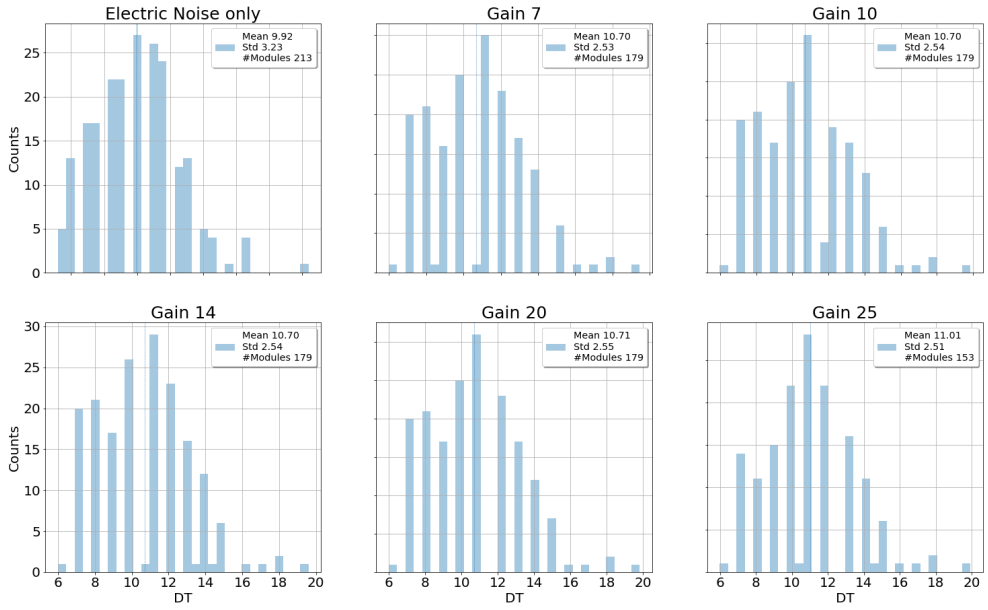

Figure A.5: Baseline dispersion for L1 rate scans with electronic noise only as well as when subjected to test pulses of increasing input amplitudes for adder A in local mode configuration. The dispersion in the series remains fixed to a mean of 10.70 as well as comparable standard deviations for each of the input amplitudes, except for the cases "electric noise only" and "gain 25", which is due to larger and lower count, respectively, that are contributing to the dispersion.

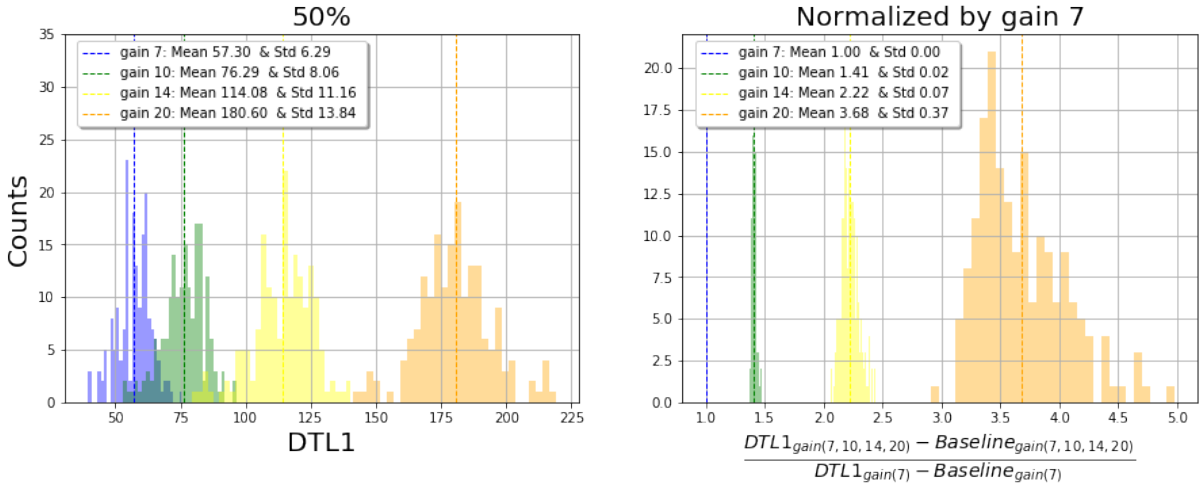

Figure A.6: **Left plot:** Distribution of L1 threshold at 50% for each pulse amplitude. **Right plot:** Distribution of L1 threshold at 50% for each pulse amplitude when corrected for its baseline and normalized by gain 7.

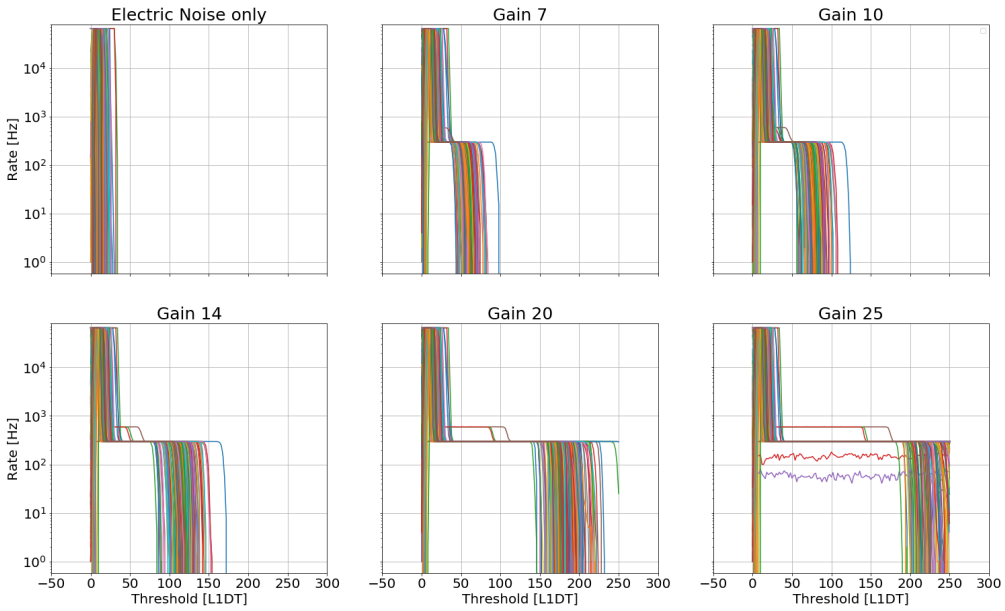

Figure A.7: Overlay of L1 rate scans with electronic noise only as well as when subjected to test pulses of increasing input amplitudes for adder A in local mode configuration. In each of the sub-figures there are 265 modules superimposed and no baseline correction is applied.

LIST OF FIGURES

LIST OF TABLES

Aartsen, M., Ackermann, M., Adams, J., Aguilar, J. A., Ahlers, M., Ahrens, M., Altmann, D., Andeen, K., Anderson, T., Ansseau, I. et al. (2018). Astrophysical neutrinos and cosmic rays observed by icecube, *Advances in Space Research* **62**(10): 2902–2930.

Aartsen, M. G. et al. (2020). Time-Integrated Neutrino Source Searches with 10 Years of IceCube Data, *Phys. Rev. Lett.* **124**(5): 051103.

Aasi, J., Abbott, B., Abbott, R., Abbott, T., Abernathy, M., Ackley, K., Adams, C., Adams, T., Addesso, P., Adhikari, R. et al. (2015). Advanced ligo, *Classical and quantum gravity* **32**(7): 074001.

Abbott, B. P., Abbott, R., Abbott, T., Abernathy, M., Acernese, F., Ackley, K., Adams, C., Adams, T., Addesso, P., Adhikari, R. et al. (2016). Gw150914: The advanced ligo detectors in the era of first discoveries, *Physical review letters* **116**(13): 131103.

Abbott, B. P., Abbott, R., Abbott, T., Acernese, F., Ackley, K., Adams, C., Adams, T., Addesso, P., Adhikari, R., Adya, V. et al. (2017). Gravitational waves and gamma-rays from a binary neutron star merger: Gw170817 and grb 170817a, *The Astrophysical Journal Letters* **848**(2): L13.

Abbott, R., Abbott, T., Acernese, F., Ackley, K., Adams, C., Adhikari, N., Adhikari, R., Adya, V., Affeldt, C., Agarwal, D. et al. (2021a). Gwtc-2.1: Deep extended catalog of compact binary coalescences observed by ligo and virgo during the first half of the third observing run, *arXiv preprint arXiv:2108.01045* .

Abbott, R., Abbott, T., Acernese, F., Ackley, K., Adams, C., Adhikari, N., Adhikari, R., Adya, V., Affeldt, C., Agarwal, D. et al. (2021b). Gwtc-3: compact binary coalescences observed by ligo and virgo during the second part of the third observing run, *arXiv preprint arXiv:2111.03606* .

Abbott et al. (2020a). Gw190425: Observation of a compact binary coalescence with total mass 3.4 m, *The Astrophysical Journal* **892**(1): L3.

Abbott et al. (2020b). Prospects for observing and localizing gravitational-wave transients with advanced ligo, advanced virgo and kagra, *Living reviews in relativity* **23**(1): 1–69.

Abdollahi, S., Acero, F., Ackermann, M., Ajello, M., Atwood, W., Axelsson, M., Baldini, L., Ballet, J., Barbiellini, G., Bastieri, D. et al. (2020). Fermi large area telescope fourth source catalog, *ApJS* **247**(1): 33.

Acciari, V. A., Ansoldi, S., Antonelli, L. A., Arbet Engels, A., Baack, D., Babić, A., Banerjee, B., Barres de Almeida, U., Barrio, J. A. and et al. (2020). Testing two-component models on very high-energy gamma-ray-emitting bl lac objects, *Astronomy Astrophysics* **640**: A132.
URL: *http://dx.doi.org/10.1051/0004-6361/202037811*

Acciari, V. A. e. a. (2019). Measurement of the extragalactic background light using MAGIC and Fermi-LAT gamma-ray observations of blazars up to z = 1, **486**(3): 4233–4251.

Acernese, F. a., Agathos, M., Agatsuma, K., Aisa, D., Allemandou, N., Allocca, A., Amarni, J., Astone, P., Balestri, G., Ballardin, G. et al. (2014). Advanced virgo: a second-generation interferometric gravitational wave detector, *Classical and Quantum Gravity* **32**(2): 024001.

Acero, F., Ackermann, M., Ajello, M., Albert, A., Baldini, L., Ballet, J., Barbiellini, G., Bastieri, D., Bellazzini, R., Bissaldi, E. et al. (2016). Development of the model of galactic interstellar emission for standard point-source analysis of fermi large area telescope data, *The Astrophysical Journal Supplement Series* **223**(2): 26.

Ackermann, M., Ajello, M., Albert, A., Allafort, A., Antolini, E., Baldini, L., Ballet, J., Barbiellini, G., Bastieri, D., Bechtol, K. et al. (2013). The fermi all-sky variability analysis: a list of flaring gamma-ray sources and the search for transients in our galaxy, *The Astrophysical Journal* **771**(1): 57.

Adams, C., Benbow, W., Brill, A., Buckley, J., Capasso, M., Christiansen, J., Chromey, A., Daniel, M., Errando, M., Falcone, A. et al. (2021). An archival search for neutron-star mergers in gravitational waves and very-high-energy gamma rays, *The Astrophysical Journal* **918**(2): 66.

Aharonian, F. A. (2004). *Very High Energy Cosmic Gamma Radiation Physics*, World Scientific Publishing Company.

Ahnen, M., Ansoldi, S., Antonelli, L., Arcaro, C., Babić, A., Banerjee, B., Bangale, P., Barres de Almeida, U., Barrio, J., Becerra González, J. and et al. (2017). Performance of the magic telescopes under moonlight, *Astroparticle Physics* **94**: 29–41.
URL: *http://dx.doi.org/10.1016/j.astropartphys.2017.08.001*

Aleksić, J., Ansoldi, S., Antonelli, L. A., Antoranz, P., Babic, A., Bangale, P., Barceló, M., Barrio, J., González, J. B., Bednarek, W. et al. (2016). The major upgrade of the magic telescopes, part ii: A performance study using observations of the crab nebula, *Astroparticle Physics* **72**: 76–94.

Almualla, M., Coughlin, M. W., Anand, S., Alqassimi, K., Guessoum, N. and Singer, L. P. (2020). Dynamic scheduling: target of opportunity observations of gravitational wave events, *Monthly Notices of the Royal Astronomical Society* **495**(4): 4366–4371.

Andreoni, I., Anand, S., Bianco, F. B., Cenko, S. B., Cowperthwaite, P. S., Coughlin, M. W., Drout, M., Golkhou, V. Z., Kaplan, D. L., Mooley, K. P. et al. (2019). A strategy for lsst to unveil a population of kilonovae without gravitational-wave triggers, *Publications of the Astronomical Society of the Pacific* **131**(1000): 068004.

Angelis, A. D. and Pimenta, M. (2018). *Introduction to Astroparticle Physics*, Springer.

Ansoldi, S., Antonelli, L. A., Arcaro, C., Baack, D., Babić, A., Banerjee, B., Bangale, P., De Almeida, U. B., Barrio, J. A., González, J. B. et al. (2018). The blazar txs 0506+ 056 associated with a high-energy neutrino: insights into extragalactic jets and cosmic-ray acceleration, *The Astrophysical Journal Letters* **863**(1): L10.

Archambault, S., Arlen, T., Aune, T., Behera, B., Beilicke, M., Benbow, W., Bird, R., Bouvier, A., Buckley, J., Bugaev, V. et al. (2013). Discovery of a new tev gamma-ray source: Ver j0521+ 211, *ApJ* **776**(2): 69.

Atwood, W., Abdo, A. A., Ackermann, M., Althouse, W., Anderson, B., Axelsson, M., Baldini, L., Ballet, J., Band, D., Barbiellini, G. et al. (2009). The large area telescope on the fermi gamma-ray space telescope mission, *ApJ* **697**(2): 1071.

Atwood, W., Albert, A., Baldini, L., Tinivella, M., Bregeon, J., Pesce-Rollins, M., Sgrò, C., Bruel, P., Charles, E., Drlica-Wagner, A. et al. (2013). Pass 8: toward the full realization of the fermi-lat scientific potential, *arXiv preprint arXiv:1303.3514* .

Bartos, I., Brady, P. and Márka, S. (2013). How gravitational-wave observations can shape the gamma-ray burst paradigm, *Classical and Quantum Gravity* **30**.

Baumann, M., Boch, T., Fernique, P., Nebot, A. and Pineau, F.-X. (2020). Space and time coverage maps in mocpy, *Astronomical Data Analysis Software and Systems XXIX* **527**: 693.

Beckmann, V. and Shrader, C. R. (2013). The agn phenomenon: open issues, *arXiv preprint arXiv:1302.1397* .

Blandford, R. D. and Znajek, R. L. (1977). Electromagnetic extraction of energy from kerr black holes, *Monthly Notices of the Royal Astronomical Society* **179**(3): 433–456.

Blümer, J., Engel, R. and Hörandel, J. R. (2009). Cosmic rays from the knee to the highest energies, *Progress in Particle and Nuclear Physics* **63**(2): 293–338.

Boch, T. (2019). Mocpy, a python library to manipulate spatial coverage maps, *Astronomical data analysis software and systems XXVI* **521**: 487.

Breeveld, A., Curran, P., Hoversten, E., Koch, S., Landsman, W., Marshall, F., Page, M., Poole, T., Roming, P., Smith, P. et al. (2010). Further calibration of the swift ultraviolet/optical telescope, *MNRAS* **406**(3): 1687–1700.

Burrows, D. N., Hill, J. E., Nousek, J. A., Wells, A. A., Chincarini, G., Abbey, A. F., Beardmore, A. P., Bosworth, J., Bräuninger, H. W., Burkert, W., Campana, S., Capalbi, M., Chang, W., Citterio, O., Freyberg, M. J., Giommi, P., Hartner, G. D., Killough, R., Kittle, B., Klar, R., Mangels, C., McMeekin, M., Miles, B. J., Moretti, A., Mori, K., Morris, D. C., Mukerjee, K., Osborne, J. P., Short, A. D. T., Tagliaferri, G., Tamburelli, F., Watson, D. J., Willingale, R. and Zugger, M. E. (2004). The Swift X-Ray Telescope, *in* K. A. Flanagan and O. H. W. Siegmund (eds), *X-Ray and Gamma-Ray Instrumentation for Astronomy XIII*, Vol. 5165 of , pp. 201–216.

Collaboration, P. A., Aab, A., Abreu, P., Aglietta, M., Al Samarai, I., Albuquerque, I., Allekotte, I., Almela, A., Alvarez Castillo, J., Alvarez-Muñiz, J. et al. (2017). Observation of a large-scale anisotropy in the arrival directions of cosmic rays above 8× 1018 ev, *Science* **357**(6357): 1266–1270.

Collaboration*†, I., Abbasi, R., Ackermann, M., Adams, J., Aguilar, J., Ahlers, M., Ahrens, M., Alameddine, J., Alispach, C., Alves Jr, A. et al. (2022). Evidence for neutrino emission from the nearby active galaxy ngc 1068, *Science* **378**(6619): 538–543.

Crothers, S. J. (2016). A critical analysis of ligo's recent detection of gravitational waves caused by merging black holes, *Hadronic Journal* **39**: 1.

D'Avanzo, P. (2015). Short gamma-ray bursts: A review, *Journal of High Energy Astrophysics* **7**: 73–80.

Dominguez, A., Primack, J. R., Rosario, D., Prada, F., Gilmore, R., Faber, S., Koo, D., Somerville, R., Pérez-Torres, M., Pérez-González, P. et al. (2011). Extragalactic background light inferred from aegis galaxy-sed-type fractions, *Monthly Notices of the Royal Astronomical Society* **410**(4): 2556–2578.

Ducoin, J., Corre, D., Leroy, N. and Le Floch, E. (2020). Optimizing gravitational waves follow-up using galaxies stellar mass, *Monthly Notices of the Royal Astronomical Society* **492**(4): 4768–4779.

EHT-Collaboration et al. (2019). First m87 event horizon telescope results. ii. array and instrumentation, *arXiv preprint arXiv:1906.11239* .

Engel, K., Lewis, T., Muzio, M. S., Venters, T. M., Ahlers, M., Albert, A., Allen, A., Solares, H. A. A., Anandagoda, S., Andersen, T. et al. (2022). Advancing the landscape of multimessenger science in the next decade, *arXiv preprint arXiv:2203.10074* .

Erdoğdu, P., Huchra, J. P., Lahav, O., Colless, M., Cutri, R. M., Falco, E., George, T., Jarrett, T., Jones, D. H., Kochanek, C. S. et al. (2006). The dipole anisotropy of the 2 micron all-sky redshift survey, *Monthly Notices of the Royal Astronomical Society* **368**(4): 1515–1526.

Fallah Ramazani, V., Lindfors, E. and Nilsson, K. (2017). Empirical multi-wavelength prediction method for very high energy gamma-ray emitting BL Lacertae objects, **608**: A68.

Fernique, P., Boch, T., Donaldson, T., Durand, D., O'Mullane, W., Reinecke, M. and Taylor, M. (2019). Technical report, moc-healpix multi-order coverage map, version 1.1.

Frontera, F. (2019). The key role of bepposax in the grb history, *Rendiconti Lincei. Scienze Fisiche e Naturali* **30**(Suppl 1): 171–184.

Fruck, C. and Gaug, M. (2015). Atmospheric monitoring in magic and data corrections.

Gao, S., Pohl, M. and Winter, W. (2017). On the direct correlation between gamma-rays and pev neutrinos from blazars, *ApJ* **843**(2): 109.

Gehrels, N., Cannizzo, J. K., Kanner, J., Kasliwal, M. M., Nissanke, S. and Singer, L. P. (2016). Galaxy strategy for ligo-virgo gravitational wave counterpart searches, *The Astrophysical Journal* **820**(2): 136.

Gérard, L. (2015). Divergent pointing with the cherenkov telescope array for surveys and beyond, *arXiv preprint arXiv:1508.06197* .

Ghisellini, G., Righi, C., Costamante, L. and Tavecchio, F. (2017). The Fermi blazar sequence, *Monthly Notices of the Royal Astronomical Society* **469**(1): 255–266.
URL: *https://doi.org/10.1093/mnras/stx806*

Goldman, I., Aharonov, Y., Alexander, G. and Nussinov, S. (1988). Implications of the supernova sn1987a neutrino signals, *Physical review letters* **60**(18): 1789.

Greco, G., Punturo, M., Allen, M., Nebot, A., Fernique, P., Baumann, M., Pineau, F.-X., Boch, T., Derriere, S., Branchesi, M. et al. (2022). Multi order coverage data structure to plan multi-messenger observations, *Astronomy and Computing* **39**: 100547.

Grupen, C. (2005). *Astroparticle Physics*, Springer.

Hailey, C. J., Mori, K., Bauer, F. E., Berkowitz, M. E., Hong, J. and Hord, B. J. (2018). A density cusp of quiescent x-ray binaries in the central parsec of the galaxy, *Nature* **556**(7699): 70–73.

Hamburg, R., Fletcher, C., Burns, E., Goldstein, A., Bissaldi, E., Briggs, M., Cleveland, W., Giles, M., Hui, C., Kocevski, D. et al. (2020). A joint fermi-gbm and ligo/virgo analysis of compact binary mergers from the first and second gravitational-wave observing runs, *The Astrophysical Journal* **893**(2): 100.

Jorstad, S. and Marscher, A. (2016). The vlba-bu-blazar multi-wavelength monitoring program, *Galaxies* **4**(4).
URL: *https://www.mdpi.com/2075-4434/4/4/47*

Kowalski, M., Collaboration, I. et al. (2017). Neutrino astronomy with icecube and beyond, *Journal of Physics: Conference Series*, Vol. 888, IOP Publishing, p. 012007.

Li, W., Filippenko, A. V., Chornock, R. and Jha, S. (2003). The katzman automatic imaging telescope gamma-ray burst alert system, and observations of GRB 020813, *Publications of the Astronomical Society of the Pacific* **115**(809): 844–853.
URL: *https://doi.org/10.1086/376432*

Lindfors, E., Hovatta, T., Nilsson, K., Reinthal, R., Ramazani, V. F., Pavlidou, V., Max-Moerbeck, W., Richards, J., Berdyugin, A., Takalo, L. et al. (2016). Optical and radio variability of the northern vhe gamma-ray emitting bl lacertae objects, *Astronomy & Astrophysics* **593**: A98.

Lister, M. L., Aller, M. F., Aller, H. D., Hodge, M. A., Homan, D. C., Kovalev, Y. Y., Pushkarev, A. B. and Savolainen, T. (2018). MOJAVE. XV. VLBA 15 GHz Total Intensity and Polarization Maps of 437 Parsec-scale AGN Jets from 1996 to 2017, **234**(1): 12.

Longair, M. S. (1992). *Astrophysics*, Cambridge University Press.

Lopez-Coto, R., Moralejo, A., Artero, M., Baquero, A., Bernardos, M., Contreras, J., Di Pierro, F., García, E., Kerszberg, D., López-Moya, M. et al. (2021). Physics performance of the large-sized telescope prototype of the cherenkov telescope array, *arXiv preprint arXiv:2109.03515* .

MacFadyen, A. and Woosley, S. (1999). Collapsars: Gamma-ray bursts and explosions in "failed supernovae", *The Astrophysical Journal* **524**(1): 262.

Magee, R., Chatterjee, D., Singer, L. P., Sachdev, S., Kovalam, M., Mo, G., Anderson, S., Brady, P., Brockill, P., Cannon, K. et al. (2021). First demonstration of early warning gravitational-wave alerts, *The Astrophysical Journal Letters* **910**(2): L21.

Magee, R., Fong, H., Caudill, S., Messick, C., Cannon, K., Godwin, P., Hanna, C., Kapadia, S., Meacher, D., Mohite, S. R. et al. (2019). Sub-threshold binary neutron star search in advanced ligo's first observing run, *The Astrophysical Journal Letters* **878**(1): L17.

Meegan, C., Lichti, G., Bhat, P., Bissaldi, E., Briggs, M. S., Connaughton, V., Diehl, R., Fishman, G., Greiner, J., Hoover, A. S. et al. (2009). The fermi gamma-ray burst monitor, *The Astrophysical Journal* **702**(1): 791.

Messick, C., Blackburn, K., Brady, P., Brockill, P., Cannon, K., Cariou, R., Caudill, S., Chamberlin, S. J., Creighton, J. D. E., Everett, R., Hanna, C., Keppel, D., Lang, R. N., Li, T. G. F., Meacher, D., Nielsen, A., Pankow, C., Privitera, S., Qi, H., Sachdev, S., Sadeghian, L., Singer, L., Thomas, E. G., Wade, L., Wade, M., Weinstein, A. and Wiesner, K. (2017). Analysis framework for the prompt discovery of compact binary mergers in gravitational-wave data, **95**(4): 042001.

Moore, C. J., Cole, R. H. and Berry, C. P. (2014). Gravitational-wave sensitivity curves, *Classical and Quantum Gravity* **32**(1): 015014.

Morris, B. M., Tollerud, E., Sipőcz, B., Deil, C., Douglas, S. T., Medina, J. B., Vyhmeister, K., Smith, T. R., Littlefair, S., Price-Whelan, A. M. et al. (2018). Astroplan: an open source observation planning package in python, *The Astronomical Journal* **155**(3): 128.

Nakamura, K., Horiuchi, S., Tanaka, M., Hayama, K., Takiwaki, T. and Kotake, K. (2016). Multimessenger signals of long-term core-collapse supernova simulations: synergetic observation strategies, *Monthly Notices of the Royal Astronomical Society* **461**(3): 3296–3313.

Nilsson, K., Lindfors, E., Takalo, L. O., Reinthal, R., Berdyugin, A., Sillanpää, A., Ciprini, S., Halkola, A., Heinämäki, P., Hovatta, T., Kadenius, V., Nurmi, P., Ostorero, L., Pasanen, M., Rekola, R., Saarinen, J., Sainio, J., Tuominen, T., Villforth, C., Vornanen, T. and Zaprudin, B. (2018). Long-term optical monitoring of TeV emitting blazars. I. Data analysis, **620**: A185.

Padovani, P., Alexander, D., Assef, R., De Marco, B., Giommi, P., Hickox, R., Richards, G., Smolčić, V., Hatziminaoglou, E., Mainieri, V. et al. (2017). Active galactic nuclei: what's in a name?, *The Astronomy and Astrophysics Review* **25**: 1–91.

Paiano, S., Landoni, M., Falomo, R., Treves, A., Scarpa, R. and Righi, C. (2017). On the redshift of tev bl lac objects, *ApJ* **837**(2): 144.

Palmer, D. M. (2020). A forest of bursts from sgr 1935+ 2154, *The Astronomer's Telegram* **13675**: 1.

Penrose, R. and Floyd, R. (1971). Extraction of rotational energy from a black hole, *Nature Physical Science* **229**: 177–179.

Poole, T., Breeveld, A., Page, M., Landsman, W., Holland, S., Roming, P., Kuin, N., Brown, P., Gronwall, C., Hunsberger, S. et al. (2008). Photometric calibration of the swift ultraviolet/optical telescope, *MNRAS* **383**(2): 627–645.

Prokoph, H., Schultz, C. and Da Vela, P. (2015). Time-resolved multiwavelength observations of the blazar VER J0521+211 from radio to gamma-ray energies, *34th International Cosmic Ray Conference (ICRC2015)*, Vol. 34 of *International Cosmic Ray Conference*, p. 864.

Richards, J. L., Max-Moerbeck, W., Pavlidou, V., King, O. G., Pearson, T. J., Readhead, A. C., Reeves, R., Shepherd, M. C., Stevenson, M. A., Weintraub, L. C. et al. (2011). Blazars in the fermi era: the ovro 40 m telescope monitoring program, *ApJS* **194**(2): 29.

Salmon, L., Hanlon, L., Jeffrey, R. and Martin-Carrillo, A. (2020). Web application for galaxy-targeted follow-up of electromagnetic counterparts to gravitational wave sources, *Astronomy & Astrophysics* **634**: A32.

Satalecka, K., Bernardini, E., Dorner, D., Mezek, G. K. and Jin, W. (2021). Searching for vhe gamma-ray emission associated with icecube neutrino alerts using fact, hess, magic, and veritas, *arXiv preprint arXiv:2109.04350* .

Schlafly, E. F. and Finkbeiner, D. P. (2011). Measuring reddening with sloan digital sky survey stellar spectra and recalibrating sfd, *ApJ* **737**(2): 103.

Seglar-Arroyo, M., Sanchez, D., Esteban Gutierrez, A., Agudo, I., Ciprini, S., Filippenko, A., Hovatta, T., Jermak, H., Jorstad, S., Kopatskaya, E. et al. (2022). Magic and hess detect vhe gamma rays from the blazar ot 081 for the first time: a deep multiwavelength study, *POS PROCEEDINGS OF SCIENCE* **395**.

Stickel, M., Fried, J. and Kuehr, H. (1988). The redshifts of the bl lac objects 1749+ 096 and 2254+ 074., *Astronomy and Astrophysics* **191**: L16–L18.

Takalo, L. O., Nilsson, K., Lindfors, E., Sillanpää, A., Berdyugin, A. and Pasanen, M. (2008). Tuorla Blazar Monitoring Program, *in* F. A. Aharonian, W. Hofmann and F. Rieger (eds), *American Institute of Physics Conference Series*, Vol. 1085 of *American Institute of Physics Conference Series*, pp. 705–707.

Teräsranta, H., Tornikoski, M., Mujunen, A., Karlamaa, K., Valtonen, T., Henelius, N., Urpo, S., Lainela, M., Pursimo, T., Nilsson, K. et al. (1998). Fifteen years monitoring of extragalactic radio sources at 22, 37 and 87 ghz, *A&AS* **132**(3): 305–331.

Thompson, D. J. (2019). The fourth fermi lat source catalog (4fgl), *AAS/High Energy Astrophysics Division* **17**: 109–33.

Thompson, D. J. and Wilson-Hodge, C. A. (2022). Fermi gamma-ray space telescope, *Handbook of X-ray and Gamma-ray Astrophysics* .

Urban, A. L. (2016). *Monsters in the dark: High energy signatures of black hole formation with multi-messenger astronomy*, PhD thesis, The University of Wisconsin-Milwaukee.

Urry, C. M. and Padovani, P. (1995). Unified schemes for radio-loud active galactic nuclei, *Publications of the Astronomical Society of the Pacific* **107**(715): 803.

Usman, S. A., Nitz, A. H., Harry, I. W., Biwer, C. M., Brown, D. A., Cabero, M., Capano, C. D., Dal Canton, T., Dent, T., Fairhurst, S., Kehl, M. S., Keppel, D., Krishnan, B., Lenon, A., Lundgren, A., Nielsen, A. B., Pekowsky, L. P., Pfeiffer, H. P., Saulson, P. R., West, M. and Willis, J. L. (2016).

The PyCBC search for gravitational waves from compact binary coalescence, *Classical and Quantum Gravity* **33**(21): 215004.

VERITAS&MAGIC et al. (2022). Multiwavelength observations of the blazar ver j0521+ 211 during an elevated tev gamma-ray state, *arXiv preprint arXiv:2205.02808* .

Wang, B., Zhu, Z., Li, A. and Zhao, W. (2020). Comprehensive analysis of the tidal effect in gravitational waves and implication for cosmology, *The Astrophysical Journal Supplement Series* **250**: 6.

Willingale, R., Starling, R. L. C., Beardmore, A. P., Tanvir, N. R. and O'Brien, P. T. (2013). Calibration of X-ray absorption in our Galaxy, **431**(1): 394–404.

Wood, M., Caputo, R., Charles, E., Di Mauro, M., Magill, J. and Perkins, J. (2017). Fermipy: An open-source python package for analysis of fermi-lat data.
URL: *https://arxiv.org/abs/1707.09551*

Zanin, R., Carmona, E., Sitarek, J., Colin, P., Frantzen, K., Gaug, M., Lombardi, S., Lopez, M., Moralejo, A., Satalecka, K., Scapin, V. and Stamatescu, V. (2013). MARS, The MAGIC Analysis and Reconstruction Software, *International Cosmic Ray Conference*, Vol. 33 of *International Cosmic Ray Conference*, p. 2937.